New insights for femtosecond spectroscopy

From transient absorption to
2-dimensional spectroscopy in the UV spectral domain

Nils Krebs

Dissertation
an der Fakultät für Physik
der Ludwig-Maximilians-Universität
München

vorgelegt von
Nils Krebs
aus München

München, im August 2013

Erstgutachter: Prof. Dr. E. Riedle
Zweitgutachter: Prof. Dr. Matthias Kling

Tag der mündlichen Prüfung: 16.10.2013

Kurzfassung

In der Ultrakurzzeitspektroskopie wird die Änderung der Eigenschaften von Licht durch die Interaktion mit Materie gemessen, um fotoinduzierte Prozesse auf der Femtosekunden- und sogar Attosekundenzeitskala zu untersuchen. Eine höhere Zeitauflösung führt zu einer schlechteren spektralen Auflösung, da ein kürzerer Impuls ein breiteres Spektrum hat und simultan mehrere Absorptionsbanden der untersuchten molekularen Probe anregt. Diese lassen sich dann nicht mehr separat untersuchen. Zweidimensionale (2D) Spektroskopie hat die Eigenschaft, dass die spektrale Auflösung unabhängig von der Zeitauflösung ist. Diese Technik wurde aber erst vor kurzem erfolgreich im ultravioletten (UV) Spektralbereich realisiert und ist von großem Interesse für Untersuchungen in der Biologie, Chemie und den Materialwissenschaften.

Im *technischen Teil dieser Dissertation* werden experimentelle Verbesserungen für die Ultrakurzzeitspektroskopie beschrieben, die später in einem 2D-UV Aufbau implementiert wurden. In einem kollinearen 2D Aufbau werden zwei Anrege-Impulse mit variablem Zeitabstand und einstellbarer Phase benötigt. Ein akusto-optischer dispersiver Filter wurde benutzt, um eine einzigartige Quelle von frei wählbaren Impulsformen mit Substrukturen von 20 fs Dauer, abstimmbarer Zentralwellenlänge (250 – 400 nm) und Energien zwischen 50 und 200 nJ, zu realisieren. Dies sind bis heute die kürzesten direkt im UV geformten Laserimpulse und ermöglichen die Untersuchung und Kontrolle von lichtinduzierten Prozessen. Eine Reduzierung der Impulslänge wurde mittels spektraler Verbreiterung aufgrund von Selbstphasenmodulation in einem Festkörper erreicht. Eine Verkürzung der Impulsdauer um einem Faktor von 1.5 für 20 fs lange Laserimpulse (und bis zu 3 für > 150 fs) ist möglich. Um eine einfache Methode zur Messung der Impulsdauer im UV zu haben, wurde ein Intensitätsautokorrelator entwickelt, der auf Zwei-Photonen-Absorption basiert. Die Eliminierung der Intensitätsfluktuationen des Abfragelichts durch Einzel-Laserimpuls-Referenzierung wurde für die spektral aufgelöste Breitbandabfrage implementiert. Das Rauschen des Messsignals und damit auch die benötigte Messdauer können damit um einen Faktor bis zu 10 reduziert werden.

Ein neuartiger kollinearer 2D-UV Aufbau wurde mit Hilfe eines UV Impulsformers realisiert. Die erreichte Bandbreite der Anregung im UV beträgt 25 nm bei 316 nm Zentralwellenlänge. Als Abfrage wurden breitbandige Superkontinuum-Weißlichter (250 – 720 nm) benutzt. Die Messdauer für ein 2D Spektrum beträgt lediglich 4 Minuten und ermöglicht die Untersuchung von unbeständigen Proben. Ein spezielles Auswertungsverfahren ermöglicht die Berechnung von anregungswellenlängenabhängigen Quantenausbeuten und ermöglicht, komplexe fotoinduzierte Prozesse auf molekularer Ebene zu verstehen.

Im *spektroskopischen Teil dieser Dissertation* wurden mit Hilfe von Femtosekunden transienter Spektroskopie lichtinduzierte Eigenschaften und Dynamiken von Molekülen untersucht, die im UV und Sichtbarem absorbieren. Zum Beispiel konnte die anfängliche Dynamik des Bindungsbruchs von Benzhydrylchlorid, ein wichtiges Intermediat in der organischen Chemie, als ballistische Wellenpaketsbewegung auf den elektronischen Potentialflächen identifiziert werden. Zwei konische Durchschneidungen ermöglichen die Entstehung von Radikalpaaren in 76 fs oder von Ionenpaaren in 124 fs.

Mit Hilfe des 2D-UV Aufbaus wurde die Energiedissipation in Pyrene untersucht. Die Anregung des zweiten elektronischen Zustands (S_2) führt zu einer ultraschnellen internen Konversion zum S_1 Zustands in 85 fs. Eine impulsive Anregung der Schwingungsmoden des S_1 Zustands erfolgt aufgrund von starken Schwingungskopplungen. Diese Beobachtungen zeigen die Kohärenz der internen Konversion, die ein wichtiger Deaktivierungsprozess in vielen Biomolekülen, z.B. DNA, ist.

Anregungswellenlängenabhängige Reaktionsausbeuten wurden für die Ringöffnungsreaktion eines Chromen Moleküls bestimmt. Sowohl die Ausbeute als auch die Reaktionsgeschwindigkeit auf der ps Zeitskala hängen von der angeregten Schwingungsbande ab. Dieses Verhalten ist wichtig für die Entschlüsselung der Moleküldynamik und erlaubt die optimale Wahl einer Anregungswellenlänge, um die Verwendung von Chromenen als optischer Schalter zu verbessern.

Die Neuheiten des 2D-UV Aufbaus erlauben nun, die Absorptionseigenschaften und Dynamiken von aromatischen Nukleinsäuren in Proteinen sowie auch von DNA zu untersuchen, und ermöglichen, einen substanziellen Beitrag zum Verständnis von Fotoschäden in lebenden Organismen zu liefern.

Short summary

In the field of ultrafast spectroscopy, changes of light caused by light-matter interaction are used to unravel photo-induced processes on the femtosecond or even attosecond time scale. Better time resolution comes with the expense of decreasing spectral resolution. A shorter pulse will be broader in spectrum and excites more features of the investigated molecular species which can no longer be observed separately. With two-dimensional (2D) spectroscopy, the spectral resolution is made independent from pulse duration. Only recently successful experiments in the ultraviolet (UV) spectral domain have been realized due to the challenging technical requirements but are of great value in biology, chemistry and material sciences.

In the *technical part of this thesis*, new experimental developments for ultrafast spectroscopy are described that converge in the realization of broadband 2D-UV spectroscopy. To build a collinear 2D setup, double pump pulses with variable interpulse delay and phase are needed. An acousto-optical dispersive filter was used to produce a unique UV light source which renders possible fully tunable pulses between 250 – 400 nm with pulse durations down to sub-20 fs and energies between 50 to 200 nJ. These pulses are the shortest pulses shaped directly in the UV so far and the energies are more than sufficient to investigate and coherently control ultrafast molecular dynamics. Spectral broadening by self-phase modulation in a bulk material further reduces the achieved pulse durations, with reduction of a factor of 1.5 for pulses around 20 fs and up to 3 for > 150 fs pulses. To have an easy to handle method to measure the pulse length and swiftly optimize the compression with the pulse shaper, an autocorrelator based on two-photon absorption was developed. Single-shot referencing of the probe intensity fluctuations was implemented for spectrally resolved broadband detection, reducing the noise level in any transient measurement, and thus the measurement time by a factor of up to 10.

The effort to produce ultrashort and tunable UV-pulses collimate in their application in an innovative shaper assisted 2D-UV setup. It employs UV pump pulses with 25 nm bandwidth at 316 nm and a broadband supercontinuum white light for probing between 250 – 720 nm. The acquisition time of only 4 minutes for one 2D spectrum allows investigating even fragile UV absorbing biomolecules. A data evaluation procedure was devised retrieving excitation-frequency resolved quantum yields from a 2D measurement, helping to understand complex photochemical reactions on the microscopic level.

In the *spectroscopic part of this thesis*, femtosecond transient spectroscopy was used to investigate photophysical properties and photo-induced dynamics of molecules absorbing in the UV and visible. As an example, the initial dynamics of the bond cleavage of benzhydryl chloride, which is an important reactive intermediate in organic chemistry, was found to be determined by a ballistic wavepacket motion on the potential energy landscape through two conical intersections happening in 76 fs (radical pair formation) and 124 fs (ion pair formation).

The excitation-frequency resolution of the 2D-UV setup was used to measure intramolecular energy dissipation in pyrene. The internal conversion to the lowest excited electronic state (S_1) after excitation of the S_2 state was determined to happen in 85 fs. An impulsive excitation of the S_1 vibronic modes occurs. The results allow a detailed insight into the coherent vibrational coupling involved in internal conversion that is an important deactivation channel in many molecules, e.g. DNA.

Excitation-frequency resolved reaction yields were determined for the ring-opening reaction of chromene in solution. The efficiency as well as the reaction dynamics on the ps time scale vary with the excited vibronic mode. Such dependence is not only of interest for unravelling the intramolecular processes but also to choose the correct activation light when using chromenes as photoswitches in all optical devices.

The novelties of the 2D-UV setup allow addressing the absorption and ultrafast dynamics of aromatic amino acids in proteins and DNA bases and will give a substantial contribution to the understanding of photo-damage in living organisms.

Publications

This thesis is based on the following publications. They form the basis of chapter 3.1 (publication 2) and chapter 3.2 (publication 3), and are reprinted in the appendices B.1 (publication 1) and B.2 to B.5 (publications 4 to 7).

1 **Two dimensional Fourier transform spectroscopy in the UV with sub-20 fs pump pulses and 250 – 720 nm supercontinuum probe**
N. Krebs, I. Pugliesi, J. Hauer, and E. Riedle
Accepted for publication in New Journal of Physics (2013).

2 **Ultrafast photochemical reaction with two product channels: wavepacket motion through two distinct conical intersections**
C. F. Sailer, N. Krebs, B. P. Fingerhut, R. de Vivie-Riedle, and E. Riedle
To be submitted to Physical Review Letters.

3 **Detection of coherent vibrational dynamics of perylene orange in solution by strong-pulse double-pump coherent spectroscopy**
M. Gelin, N. Krebs, E. Riedle, and W. Domcke
In preparation.

4 **Pulse compression of ultrashort UV pulses by self-phase modulation in bulk material**
N. Krebs, I. Pugliesi, and E. Riedle
Applied Sciences **3**, 153 - 167 (2013).

5 **Convenient pulse length measurement of sub-20-fs pulses down to the deep UV via two-photon absorption in bulk material**
C. Homann, N. Krebs, and E. Riedle
Applied Physics B **104**, 783 - 791 (2011).

6 **Shaped sub-20 fs UV Pulses: Handling Spatio-Temporal Coupling**
N. Krebs, R. A. Probst, and E. Riedle
Ultrafast Phenomena XVII, M. Chergui, D. Jonas, E. Riedle, R.W. Schoenlein, A. Taylor, eds. (Oxford University Press, Inc., New York 2011), 814 - 816.

7 **Sub-20 fs pulses shaped directly in the UV by an acousto-optic programmable dispersive filter**
N. Krebs, R. A. Probst, and E. Riedle
Optics Express **18**, 6164–6171 (2010).

Contents

1. Introduction and outline

The increasing understanding of the properties and functions of photoactive chemical and biological systems is strongly related to the technical developments and advances made in the field of spectroscopy. Optical spectroscopy records changes of light caused by light-matter interaction. The interpretation of these modulations allows for conclusions about the properties of matter itself [Muk95]. Beginning with pure optical techniques to measure the steady-state absorption and emission properties, nowadays a variety of advanced time-resolved spectroscopic techniques are available.

The technical progress was strongly supported by the development of coherent light sources advancing with the invention of the laser in 1960 [Mai60]. High intensity coherent light sources are used in the field of nonlinear optics and enabled the generation of ultrashort laser pulses that have pulse durations in the femtosecond (10^{-15} s) [DeM66, Sha74, Sib12 (recent review)] or even attosecond (10^{-18} s) regime [Hen01]. These ultrashort pulsed light sources are widely used in ultrafast time-resolved spectroscopy, allowing the observation of light-induced intra- and intermolecular processes on the time scale of the motion of atoms and electrons [Kli08].

Femtosecond transient absorption spectroscopy, also referred to as femtosecond pump-probe spectroscopy, is one of the most common tools to investigate ultrafast photochemical reactions [Dan87, Ern01].

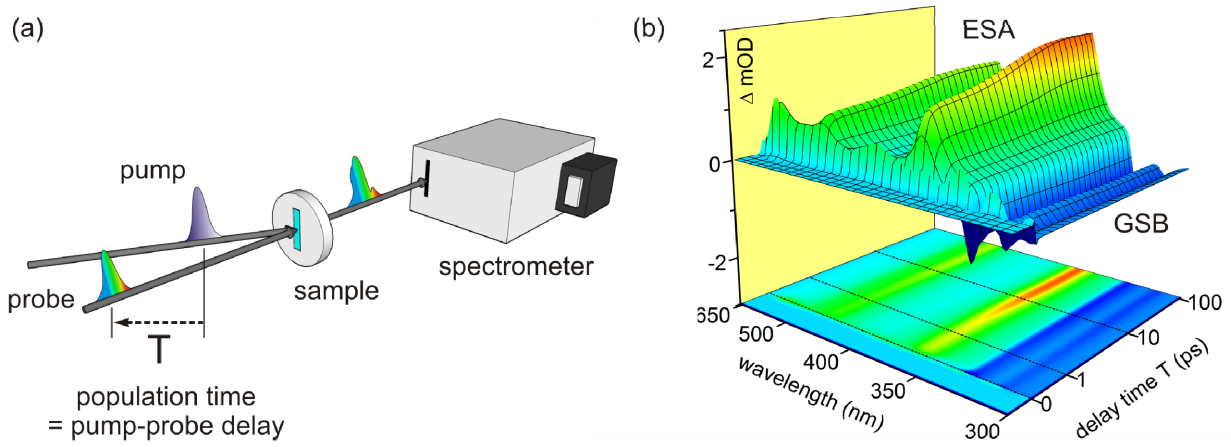

Fig. 1.1. (a) Schematic representation of transient absorption (pump-probe) spectroscopy. (b) UV-light-induced changes in optical density (ΔOD) of pyrene showing dynamics of the S_1 excited state absorption (ESA) and ground state bleach (GSB) contribution.

This pure optical technique measures the excited state dynamics of a sample upon irradiation with an ultrashort pump pulse (Fig. 1.1a) [Muk90]. A second ultrashort probe pulse that is delayed with respect to the pump pulse, monitors the change of the optical density (ΔOD) induced by pumping. By recording spectra for different pump-probe delays a molecular movie of the light-induced dynamics is retrieved. The pump-induced transient signatures, typically appearing at different probe frequencies, allow for the interpretation of the ultrafast processes on the molecular level. In state-of-the-art transient spectroscopy the probe pulse is measured spectrally resolved, covering a broad spectral range. The measured transient absorption spectrum then resolves the time and the probe frequency.

More sophisticated methods are needed to gain deeper insights into light-induced molecular processes which are not accessible with conventional transient absorption spectroscopy. One of the most promising tools is 2-dimensional (2D) spectroscopy. Simply speaking, 2D spectroscopy can be understood as the extension of transient absorption spectroscopy by the additional dimension of the excitation frequency resolution [Fae99, Jon03]. 2D spectroscopy allows to investigate electronic or vibrational couplings [Bri05, Cho08], to measure molecular dynamics influenced by the solvent [Fae99], to resolve molecular dynamics of photochemical and photobiological systems that have congested absorption spectra like proteins or amino acids [Mid09], and to perform chemical exchange measurements [Ogi09].

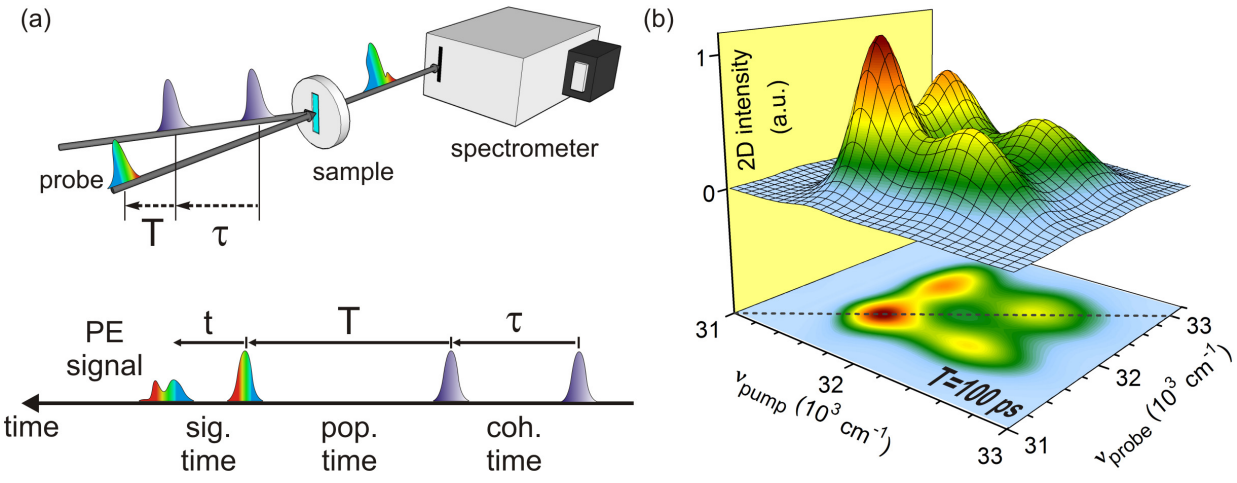

Fig. 1.2. (a) Schematic representation of collinear 2-dimensional spectroscopy; PE: Photon echo; (b) 2D-UV measurement of the ground state bleach contribution of pyrene for a population time T of 100 ps. Details see text.

2D spectroscopy can be experimentally realized in the (partially) collinear geometry, also referred to as shaper-assisted geometry (Fig. 1.2a) [Shi09]. Two collinear pump pulses with a defined carrier envelope phase relation excite the molecule. A third noncollinear probe pulse,

which is delayed with respect to the second pump pulse (population time or pump-probe delay T), probes the molecular response and is typically spectrally resolved to retrieve the probe frequency axis. By scanning the interpulse delay between the two pump pulses (coherence time τ), the excitation (pump) frequency axis is afterwards retrieved by Fourier transformation along τ. Then the 2D measurement resolves the time, the probe frequency and the pump frequency.

When starting this thesis, 2D experiments had been done with IR [Ham98] and visible pulses [Bri04a]. However, 2D spectroscopy had not been realized experimentally in the UV at all. A large variety of photoactive molecules has their absorption as well as their optically detectable signatures in the UV spectral domain, e.g., aromatic amino acids [Mid09]. It was therefore of great interest to realize 2D-UV spectroscopy to solve open questions in the understanding of UV light-induced molecular processes [Can11].

In this thesis, 2D-UV spectroscopy is realized in the partial collinear geometry. The steps to realize high-quality 2D-UV measurements are: 1) Generation of clean sub-20 fs shaped UV pulses that have sufficient bandwidth to address absorptive features of UV absorbing molecules. 2) Implementation of the shaped UV pulses in a collinear 2D experiment that allows rapid and robust measurements. 3) Development of correct data acquisition and post processing procedures enabling a quantitative analysis of the 2D measurements.

The most promising techniques that allow the generation of arbitrary pulse shapes in the UV are direct shaping of UV pulses by acousto-optical pulse shapers [Rot05, Pea07] or an 4-f setup based on movable micromirrors [Ron09, Hac03, Möh09]. The reported pulse durations are so far limited to 30 – 100 fs. A newly available acousto-optical dispersive filter (AOPDF) [Cou06] allows amplitude and phase shaping in the whole UV spectral domain from 240 – 420 nm. So far, only pulses with more than 50 fs have been demonstrated with this shaper [Web10]. To achieve shorter pulses that are compressed to nearly their Fourier limit of less than 20 fs, one has to explicitly consider the spatio-temporal coupling inherent in all shaping devices.

Despite the direct generation of sub-15 fs UV by frequency upconversion in nonlinear crystals [Bau04a, Zha09] or gases [Bac96, Rei10, Kid11] it is of great interest to have a technique that allows to reduce the pulse duration of the UV pulses after their generation. The nonlinear process of self-phase modulation (SPM) allows spectral broadening. SPM has been successfully applied in gases [Nag09, Gho11]. However, high input pulse energies up to several hundred µJ are required due to the low nonlinearity of the gas. Bulk materials in contrast offer medium to high nonlinearities and are suitable candidates for nonlinear phase modulations of few µJ UV pulses. The shortening of IR and visible pulses by SPM in bulk materials has been realized

successfully in the 1980s [Pet89] but has not been realized in the UV. Pulse shortening by SPM in bulk material offers a convenient technique to improve the temporal and spectral detection range of a 2D-UV experiment.

In an actual 2D-UV experiment it is desirable to have a fast way to optimize the temporal compression of the UV pump pulses with the pulse shaper on a day-to-day basis. To find the optimal compression it is sufficient to minimize the measured pulse duration until finding the optimal spectral phase function applied by the pulse shaper. The most convenient way to determine the pulse duration is done by measuring the intensity autocorrelation. However, to develop an UV-autocorrelator a nonlinear process in the UV is needed. Two-photon absorption in bulk materials has the potential to do so.

To measure light-induced dynamics with 2D-UV spectroscopy, multiple population times have to be measured, and for each one, the coherence time has to be scanned. This makes a complete 2D experiment a lot more time consuming as compared to conventional transient absorption spectroscopy. Therefore, a high signal-to-noise ratio is favorable, which allows reducing the averaging time needed due to the intensity fluctuations of the laser. Absorbance changes down to 10^{-6} can be resolved in transient absorption measurements by additionally measuring the probe intensity fluctuations. However, the probe pulse was spectrally integrated on a photodiode [Sch08]. The adaptation of this technique for spectrally resolved broadband detection poses a great advantage for 2D measurements.

Pulse shaper-assisted 2D spectroscopy has been first implemented in the IR [DeF07, Gru07] and later on in the visible [Mye08]. Despite the general statement that 2D spectroscopy measures directly the amplitude of the light-induced third-order polarization $P^{(3)}$ (which is related to the third-order susceptibility $\chi^{(3)}$ of the sample), most of the reported data in the literature is of different character when related to $P^{(3)}$. Often a systematic and detailed description of the actual data acquisition and analysis procedures is missing. In particular the amplitude of nearly all reported 2D spectra is given as arbitrary units, unfortunately not allowing a quantitative comparison or interpretation of the results. It is therefore of great importance to develop a fundamental understanding of the origin of the signals measured in 2D spectroscopy to develop the correct data acquisition and evaluation procedure. Then it is possible to retrieve 2D amplitudes that are quantitatively related to physical properties of interest, e.g., the amount of molecules in a given excited state. Quantitative 2D measurements have a great potential to investigate, e.g., excitation-frequency dependent molecular processes.

The present thesis describes the development and experimental realization of broadband 2D-UV spectroscopy and the technical prerequisites necessary to do so. Additionally, technical modifications of conventional transient absorption experiments are described. These techniques are used to clarify ultrafast light-induced molecular processes not investigated before.

In Chap. 2 the technical developments needed for broadband 2D-UV spectroscopy are described. The generation of clean shaped UV pulses with an AOPDF is described in Chap. 2.1 & 2.2 and a convenient way for their temporal compression in Chap. 2.3. The improvement of the measurement accuracy by elimination of the intensity fluctuations of the spectrally resolved probe is highlighted in Chap. 2.3.

The spectroscopic results presented in Chap. 3 are an excursion to the investigation of ultrafast molecular processes measured by transient absorption spectroscopy. In Chap. 3.1 the light-induced bond cleavage of benzhydryl chloride is investigated. Chap. 3.2 deals with the question whether strong-field double-pump-single-probe spectroscopy can retrieve additional information about the molecular dynamics of the laser dye perylene orange compared to the weak-field excitation. In Chap. 3.3 the experimental setup of Chap. 3.2 is adapted for the UV to investigate the light-induced proton transfer in 2-(2'-hydroxyphenyl)benzothiazole (HBT).

The technical development of collinear 2D-UV spectroscopy is explained in Chap. 4. At first a general introduction to 2D spectroscopy and the most relevant mathematical formalism is given (Chap. 4.1). In Chap. 4.2 the experimental setup and the data acquisition and evaluation procedure is described in detail. The measurement procedure when using the AOPDF and a prism based CCD spectrometer to detect the probe, which can be a supercontinuum white light, is explained. In Chap. 4.3 the fundamental question about the "quantitativity" of the 2D signal is posed. It is shown that the retrieved 2D amplitudes here are proportional to the change in optical density which is proportional to the population in a given state.

With the newly developed broadband 2D-UV setup, light-induced molecular processes of UV absorbing molecules are discussed in Chap. 5. The excitation-frequency dependent photo-chemistry of the internal conversion of pyrene (Chap. 5.1) and the ring-opening reaction of chromene (Chap. 5.2) are studied.

A summary of the results and proposals for future experiments are given at the end of this thesis (Chap. 6).

2. Generation and characterization of ultrashort UV pulses

The generation of ultrashort UV pulses with sufficiently short pulse duration is the natural prerequisite for the successful realization of femtosecond transient spectroscopy in the UV spectral domain. Additionally, full control of the spectral amplitude and phase of the UV pulses, e.g., by the aid of a pulse shaper, opens up the possibility to generate arbitrarily shaped pulses needed for coherent control or clean double pulses with variable interpulse delay and phase needed for 2D-UV spectroscopy.

In the following chapter the results for the generation of shaped ultrashort UV pulses with an acousto-optical pulse shaper are given. As an excursion, a referencing scheme is described that allows increasing the signal-to-noise ratio for transient absorption or 2D spectroscopy. In total, all the technical developments are implemented in the 2D-UV measurements described in Chap. 4 &5.

2.1 Sub-20fs pulses shaped with an acousto-optical pulse shaper

Full control of the spectral amplitude and phase of UV pulses can be achieved by using pulse shapers either in visible/IR part of the beam prior to the frequency conversion to the UV [Sch06, Par09] or directly in the UV [Pea07, Möh09, Ron09]. Due to the spatio-temporal coupling common for all pulse shapers [Wei00, Tan05, Vau06, Fre10, McC11, Bri11], the implementation of a pulse shaper is far from simple but can only be done with a correct understanding of the shaper's working principles. When handling spatio-temporal effects it is favorable to shape the pulses directly in the UV because one avoids additional spatio-temporal effects originating in the frequency conversion process, e.g., when shaping in the visible part of the beam. For the UV spectral domain techniques to generate shaped pulses directly in the UV are much more sophisticated and only recently commercial systems got available [Hac03, Cou06]. However, at the beginning of this thesis the shortest pulses demonstrated with a pulse shaper directly in the UV had a pulse length of about 50 fs [Web10].

Combined with a source of ultrashort UV pulses we are able to generate tunable UV (250-400 nm) pulses with sub-20 fs substructure with an AOPDF (Dazzler^{TM}, Fastlite [Cou06]). The results are described in the following publication (appendix B.5):

Sub-20 fs pulses shaped directly in the UV by an acousto-optic programmable dispersive filter

N. Krebs, R.A. Probst, E. Riedle

Optic Express **18**, 6164-6171 (2010).

To compensate for the spatio-temporal coupling of the AOPDF the working principle of the shaping device has to be understood, which is therefore explained briefly in the following. In the AOPDF, the incident beam is diffracted on an density grating induced by an acoustic wave in a potassium dihydrogen phosphate (KDP) crystal. Due to the phase matching condition each diffracted optical frequency corresponds to only one acoustic frequency. The amplitude of the diffracted light is directly proportional to the acoustic power. When diffracted, the polarization of the incident light is rotated from the fast extraordinary to the slow ordinary axis of the crystal (Fig. 2.1.1a). By designing a specific acoustic wave, different frequencies can be diffracted at different positions in the crystal and the group delay and amplitudes of the individual optical frequencies can be adjusted. The different spectral components of the incident light that are diffracted along the crystal leave the shaper parallel with respect to each other but spatially shifted. This is shown in Fig. 2.1.1b for the generation of a double pulse. This group-delay-dependent displacement of the shaped pulse is the only spatio-temporal coupling observed in the AOPDF [McB11]. The angle between the incident and the diffracted beam is about 10°.

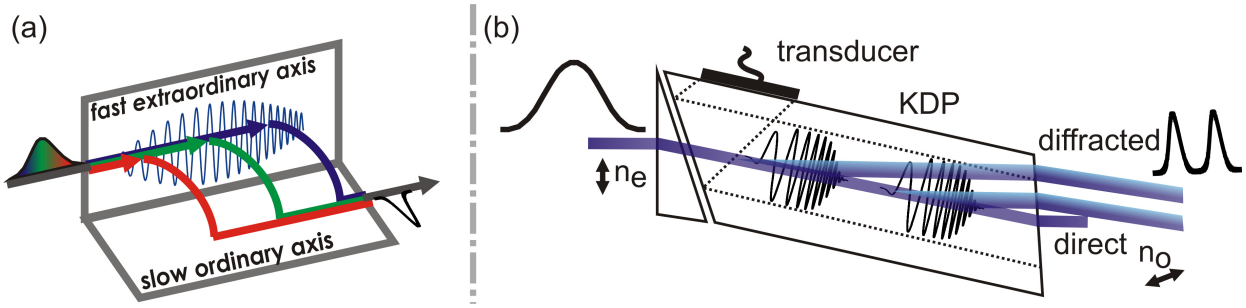

Fig. 2.1.1. Working principle of the acousto-optical dispersive filter. (a) When diffracted along the crystal, the optical frequencies obtain different group delay. (b) Spatio-temporal coupling manifests in the parallel displacement of the diffracted light, e.g., the subpulses of a double pulse.

This lateral shift leads to a distorted pulse when the diffracted beam is focused. Consider a perfectly focusing element with a focusing length f which focuses a triple pulse generated by

the AOPDF. The three pulses will be laterally shifted and can be treated as geometric rays. The parallel beams will spatially overlap at the distance f after the focusing element (Fig. 2.1.2). However, for a Gaussian input beam to the AOPDF, each diffracted part of the beam has to be treated as a Gaussian beam when focused. The position of the Gaussian focus after the lens depends on the Gaussian beam parameter of the pulse to be focused and is not located in general at the distance f. In the paraxial approximation a Gaussian beam can be described along the propagation distance x by the complex beam parameter q(x) [Mes99]:

$$\frac{1}{q(x)} = \frac{1}{R(x)} + i\frac{2}{kw^2(x)}. \qquad (2.1.1)$$

R(x) is the beam curvature, w(x) is the beam radius and k is the wave vector. For an optical beam (wavelength λ) with an intermediate beam waist (IBW) w_0 at the distance x_0 in front of the lens and an incident Rayleigh length $z_0 = \pi w_0^2/\lambda$, the beam parameter $q(x_1)$ at the distance x_1 after the lens is given by:

$$q(x_1) = -i\frac{z_0 f^2}{(x_0 - f)^2 + z_0^2} - \frac{f\left(x_0^2 - x_0 f + z_0^2\right)}{(x_0 - f)^2 + z_0^2} + x_1. \qquad (2.1.2)$$

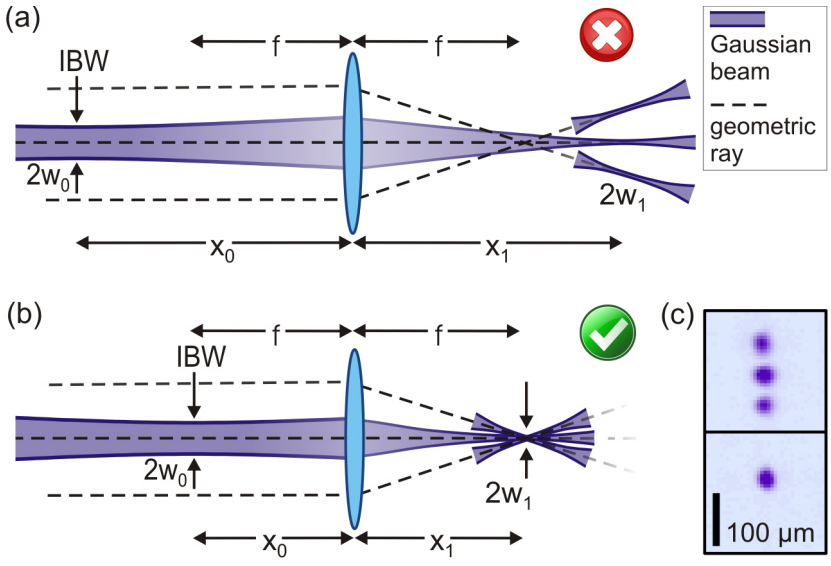

Fig. 2.1.2. Focusing of three Gaussian beams with incorrect (a) and correct (b) positioning of the intermediate beam waist (IBW). When the distance of the IBW corresponds to the focal length f, the Gaussian loci of the three beams spatially overlap as can be seen in the measured beam profiles of the Gaussian loci (c).

As can be seen from Eq. 2.1.1, at the position of a Gaussian focus where the beam curvature is infinite, $q(x_1)$ has to be purely imaginary. Therefore the last two terms of Eq. 2.1.2 have to compensate each other. The position x_1 of the Gaussian focus after the lens then reads as [Kle86]:

$$x_1 = f + \frac{f^2 (x_0 - f)}{(x_0 - f)^2 + z_0^2}. \qquad (2.1.3)$$

To superimpose the Gaussian with the geometric focus ($x_1 = f$), two solutions are possible. The first one is to place the IBW at the position of the lens ($x_0 = 0$) and to fulfill the condition $z_0^2 \gg f^3$. This condition for the Rayleigh length is not practicable in most of the experiments in the UV. The other solution which we use is to place the IBW at the distance f in front of the lens ($x_0 = f$). Then the Gaussian focus is superimposed with the geometric focus as can be seen in Fig. 2.1.2b.

Experimentally we use a telescope consisting of two thin lenses in front of the AOPDF to place the IBW of the shaped beam at a distance f in front of the last focusing element. The dispersion of the two lenses can be directly compensated for by the AOPDF. For focusing, a spherical mirror is used. The correct choice of the experimental geometry ($x_0 = f$) guarantees that all the diffracted light is well combined in the focus. In this way clean ultrashort shaped UV pulses can be achieved with the AOPDF.

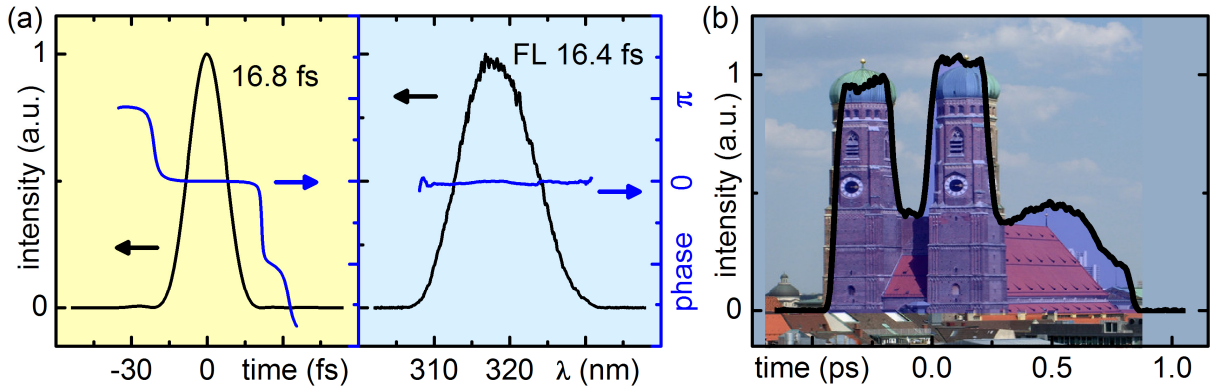

Fig. 2.1.3. ZAP-SPIDER measurement of a nearly Fourier limited 16.8 fs pulse at 319 nm. (b) Cross-correlation of a chirped pulse centered at 260 nm imitating the "Frauenkirche" in the time domain.

To demonstrate the ability of our setup to generate ultrashort shaped femtosecond pulses we first compressed the frequency doubled output of a noncollinear optical parametric amplifier (NOPA) [Rie00, Cer03] close to its Fourier limit of 16.8 fs (Fig. 2.1.3). Optimal compression of the pulses can be achieved by measuring the spectral phase with zero-additional-phase spectral phase interferometry for direct electric-field reconstruction (ZAP-SPIDER) [Bau04b] and compensation with the pulse shaper. Alternatively the optimal phase function can be found while monitoring the pulse length when measuring the cross-correlation with an ultrashort visible pulse or with the aid of an UV autocorrelator (for details see Chap. 2.3). When the necessary phase function for optimal compression is found, the AOPDF can generate arbitrarily shaped pulses. As an example we generated UV pulses which resemble the shape of the "Frauenkirche" in the time domain (Fig. 2.1.3b) measured by cross-correlation with a visible pulse.

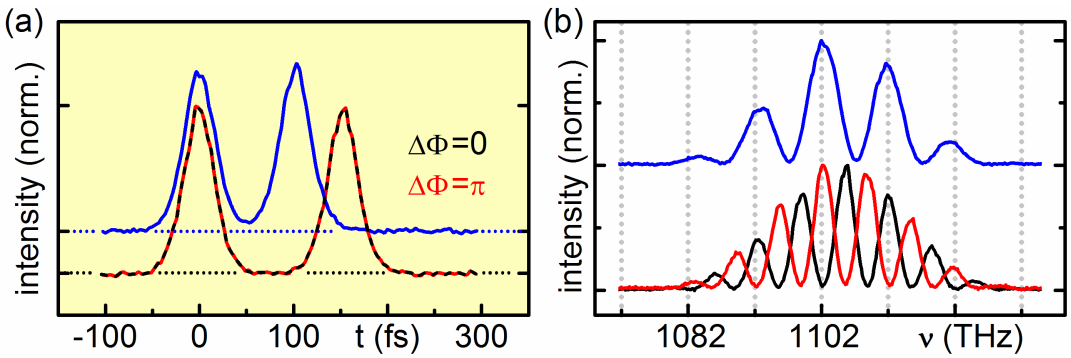

Fig. 2.1.4. Cross correlations (a) and spectra (b) of double pulses at 260 nm with 100 fs (blue) and 150 fs (black) interpulse delay. ΔΦ is the relative phase of the carrier wave of the two pulses. The subpulses for a delay of 150 fs are in-phase (ΔΦ=0, black spectrum), and opposite in phase (ΔΦ=π, red spectrum).

With this setup phase coherent double pulses, necessary as the pump in 2D collinear spectroscopy, are readily available. Double pulses with a central wavelength of 260 nm with an interpulse delay of 100 and 150 fs are shown in Fig. 2.1.4a. The doubles pulses are free from satellite pulses which is most important for their application in 2D spectroscopy. This result is in contrast to results reported in the literature for double pulses generated with the aid of pixelated devices like LCD based pulse shapers in the visible [Wei00] or after frequency conversion of visible pulses into the UV [Par09]. For the double pulses separated by 100 fs (shown in blue) the resulting spectrum is modulated with 10 THz spacing. The pulse spacing of

150 fs decreases the spectral period (Fig. 2.1.4b). The relative phase of the two subpulses with respect to the carrier wave determines the position of the fringes: for in-phase pulses there is a maximum at the center of the spectrum (black curve) while for pulses with opposite phase two equal height maxima are found symmetrically displaced (red curve).

The phase coherent double pulses with variable interpulse delay and phase can readily be used as pump pulses for 2D-UV spectroscopy. Their implementations in a 2D-UV experiment are described in Chap. 4.

2.2 Pulse compression by self-phase modulation in bulk material

When an experimental setup is designed and built, the UV source chosen limits the minimal achievable pulse duration and can typically only be changed with major modifications of the optical components used. Therefore it is desirable to have a convenient way of further shortening the available UV pulses which can be implemented in an existing setup later on. We found that pulse compression by SPM in bulk material can, alongside successful applications early in the 1980s for the visible [Rol88], also be used in the UV spectral domain. When the correct experimental conditions are met, we can achieve a reduction of the pulse length of 20-fs pulses by a factor of 1.5 and observe an even stronger pulse reduction for longer pulses. The correct conditions for pulse compression of UV pulses together with the results are given in the following publication (appendix B.2):

> **Pulse compression of ultrashort UV pulses by self-phase modulation in bulk material**
>
> N. Krebs, I. Pugliesi, E. Riedle
>
> Applied Sciences. **3**, 153 - 167 (2013).

An intense laser pulse propagating through a bulk material induces a dynamic refractive index change due to the third-order nonlinearity (Kerr nonlinearity n_2). The intensity dependent refractive index is defined by $n(t) = n_0 + n_2 \cdot I(t)$. The resulting effects are self-focusing, self-steepening and SPM. The change in intensity at the leading and trailing edge of the pulse itself leads to a nonlinear frequency shift $\delta\omega(t)$ of the instantaneous frequencies along the propagation distance x according to:

$$\delta\omega(t) = -n_2 \cdot x \cdot \left(\frac{dI(t)}{dt} \right). \qquad (2.2.1)$$

For the common case of positive n_2 this effect leads to a red-shift of the frequencies at the leading edge of the pulse and a blue-shift at the trailing edge (Fig. 2.2.1a). For positively chirped or chirp free pulses SPM therefore generates new frequency components and the pulse spectrum is broadened. For negatively chirped pulses, the spectrum is narrowed (Fig. 2.2.1b).

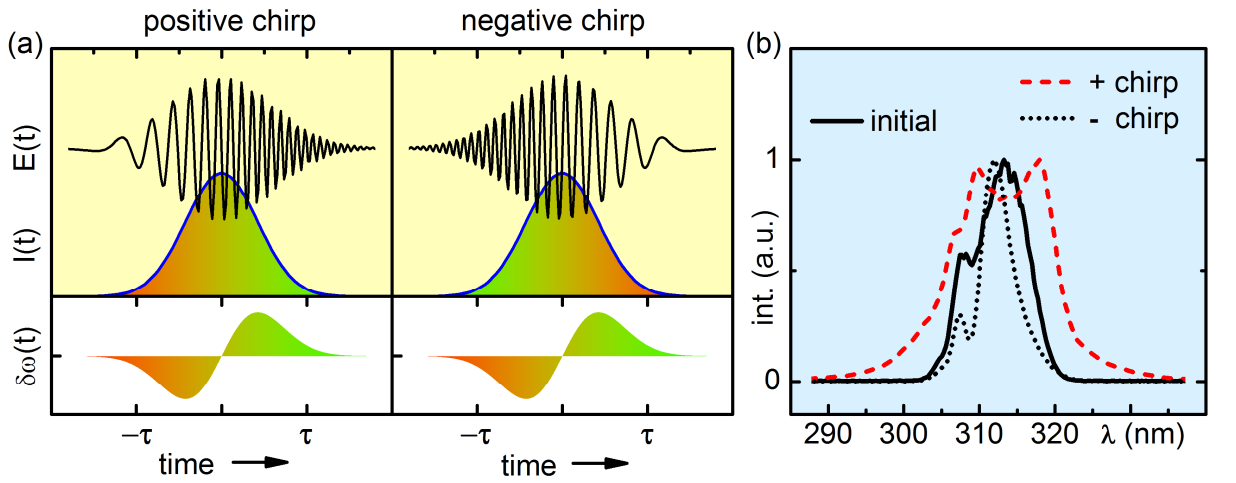

Fig. 2.2.1. **(a)** Illustration of the nonlinear frequency shift by self-phase modulation of chirped pulses. (b) Measurement of the spectral broadening by SPM in a 1 mm thick CaF_2 crystal for positive (~260 fs^2) and negative (-60 fs^2) chirped pulses centered at 312 nm.

When using SPM in bulk material for spectral broadening of UV pulses two major effects have to be considered: 1) Strong dispersion of the material in the UV leads to a reduction of the peak intensity and thus the amount of the accumulated nonlinear frequency shift while the pulse propagates in the medium. 2) Self-focusing has to be kept to a moderate level to avoid spatial beam distortions. Experimentally and by simulations we found that maximum spectral broadening is achieved for thin (≤ 1 mm) crystals with peak intensities just low enough to guarantee that the self-focus lies about 25 % after the crystal thickness. Additionally high n_2 values are favorable. We found that despite the fact that CaF_2 has a smaller n_2 value than other materials, a 1 mm thick CaF_2 crystal gives the most promising results in terms of beam quality and experimental handling.

Experimentally, we focused ultrashort UV pulses with energies of a few µJ into a 1 mm thick CaF_2 crystal with a thin fused silica lens. For a given pulse energy, the peak intensity of the pulse inside the crystal was adjusted by moving the crystal along the convergent beam towards the focus until the optimal conditions without beam distortions are found (see Fig. 2.2.2a). A second lens after the crystal recollimates the beam and can also be used to compensate for the change in divergence by moderate self-focusing in the crystal.

To demonstrate the compressibility of the spectrally broadened pulses we used a combination of a UV prism compressor (UV-PC) and an AOPDF and characterized the compressed pulses with a ZAP-SPIDER [Bau04b]. We found that a flat spectral phase can be achieved when the inner part of the beam is selected by an aperture after the SPM stage. This is done because SPM can lead to different frequency chirps across the transversal beam profile related to the spatial intensity profile, e.g., Gaussian shaped [Rol88]. The overall energy efficiency of the SPM stage is then typically > 80 %. Under the optimal conditions we could reduce the pulse length of pulses centered at 273 nm and 312 nm by a factor of 1.4 and 1.5, respectively. The results are shown in Fig. 2.2.2. We also compressed the 120 fs long third-harmonic of the CPAs fundamental by a combination of a SPM stage and an UV-PC to 53 fs. This shows that for longer pulse durations even higher compression factors are feasible, even without the use of a pulse shaper.

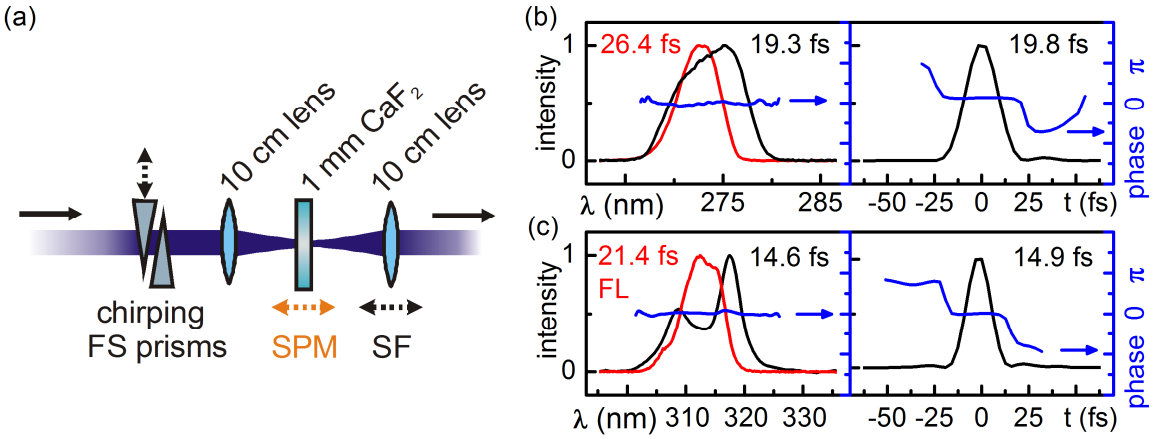

Fig. 2.2.2. Sketch of the experimental components needed for spectral broadening of UV pulses. ZAP-SPIDER measurements of typical compressed UV pulses centered at 273 nm and 312 nm obtained for input energies of 0.7 µJ in a 2 mm thick CaF_2 crystal (b) and 2.1 µJ in a 1 mm thick CaF_2 crystal (c) (red line: input pulse, black line: output pulse, blue line: spectral and temporal phase)

When comparing the achieved pulse durations of UV pulses by SPM in bulk material with the results reported in the literature, the pulses reported here have comparable or longer durations. Straightforward frequency upconversion of short visible pulses in non-linear crystals already allows for the generation of sub-20 fs UV pulses [Sch06] and 30 fs pulses down to 189 nm [Hom12]. The phase-matching bandwidth can be increased by advanced angular dispersion

methods leading to sub-10 fs pulses [Bau04a, Zha09]. Cross-phase modulation in gas filled fibers has also been used to generate pulse lengths of 25 fs [Noa05] or 8 fs [Dur99]. Third harmonic generation of the fundamental pulses at around 800 nm provide even 3-fs pulses in a Neon filled gas cell [Rei10]. However, these techniques require an elaborate experimental implementation.

A reduction of the duration of given UV pulses can also be achieved by SPM in gaseous media. In gas filled hollow fibers pulses as short as 20 fs centered at 268 nm [Gho11] and 25 fs centered at 248 nm [Nag09] were obtained. However, these techniques need high input UV pulse energies up to several hundreds of μJ.

The concept of UV pulse compression of few μJ pulses by SPM in bulk material has the advantage that only a few additional optical components are needed and it can easily be incorporated into an existing setup. Additionally this technique is applicable for the whole UV spectral domain without changing the optical components. It is therefore optimally suited for the combination with tunable UV pulse sources, e.g., generated by frequency upconversion of visible NOPA pulses. This makes SPM in bulk an attractive method for, e.g., spectroscopic applications, which require simple parts for a reliable long term operation.

The benefit of SPM broadened pulses for 2D spectroscopy (see Chap. 4) lies in the gain of the spectral bandwidth which directly increases the available detection window and the increased temporal resolution due to the shorter pulse duration achievable.

2.3 On-the-fly pulse characterization and compression with an UV autocorrelator

Along with the generation of ultrashort UV pulses comes the need of their characterization on a day-to-day basis. There are well established techniques for the full spectral and temporal characterization of UV pulses like SPIDER [Iac98, Bau04b, And08] or cross-correlation frequency-resolved optical gating (X-FROG) [Gie99]. However these techniques are experimentally demanding and are not always needed. When a pulse shaper is used to compress the pulses it is often sufficient to minimize the pulse duration to find the optimal spectral phase function that compensates for any dispersion. The most convenient and robust technique to measure the pulse length is the intensity autocorrelation. In the visible second-harmonic generation (SHG) is commonly used but not implementable for the UV due to the lack of suitable nonlinear crystals. Two-photon absorption in bulk material can however serve as the nonlinearity necessary to measure intensity autocorrelations over a large spectral range. Despite various efforts to measure ultrashort pulses with two-photon absorption in water [Reu97] or diamond [Dad91] there has not been a systematic study of the promising capability of two-photon absorption in crystals to characterize femtosecond UV pulses. We therefore developed a UV autocorrelator (UV-AC) based on two-photon absorption in thin crystals which is described in detail in the following publication (appendix B.3):

> **Convenient pulse length measurement of sub-20-fs pulses down to the deep UV via two-photon absorption in bulk material**
>
> C. Homann, N. Krebs, E. Riedle
>
> Applied Physics B **104**, 783-791 (2011).

Our pump-probe approach to measure the intensity autocorrelation relies on the depletion of a weak fraction of the UV pulse (probe) by the strong remaining part (pump) when temporal and spatial overlap in a thin two-photon absorbing crystal (Fig. 2.3.1) prevails. For probing the reflection of thin (160 µm thick) uncoated fused silica cover slip is used. An identical slip introduces the same chirp into the reflected probe beam and the reflected part of the second slip is used for referencing out the intensity fluctuations. Fused silica is appropriate for the whole UV spectral domain without severely affecting the pulse length of pulses longer than tens of femtosecond.

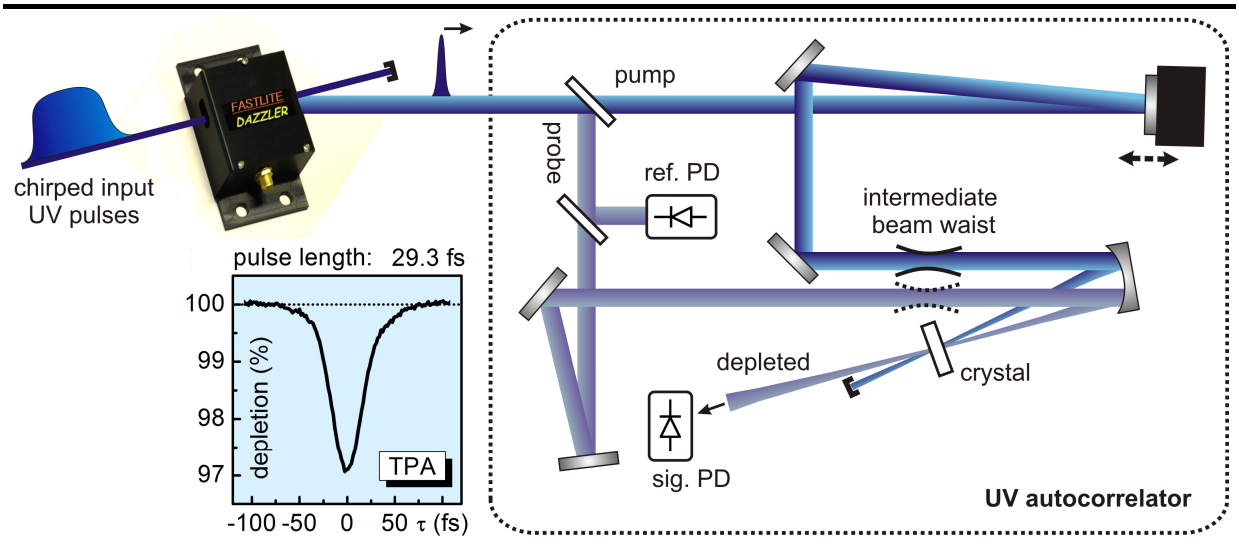

Fig. 2.3.1. Experimental realization of optimal pulse compression with the AOPDF in conjunction with an UV autocorrelator. The layout of the UV autocorrelator based on two-photon absorption (TPA) in a thin crystal is shown on the right. The intensity autocorrelation is retrieved by looking at the depletion of the probe pulse (lower left part).

When the UV-AC is used to find the optimal compression of UV pulses in an experiment, the two cover slips can also be replaced by elements of the experiment, e.g., the windows of a vacuum chamber, to mimic their dispersion. The referencing scheme significantly increases the signal-to-noise ratio and enables to measure pulses with energies down to a few nJ. With the UV-AC we can measure sub-20 fs pulses and UV pulses with a central wavelength in the range of 190 – 400 nm and can be extended to the visible spectral domain when using adequate two-photon absorbing crystals.

In the lower left part of Fig. 2.3.1 the autocorrelation trace of a 30 fs pulse centered at 308 nm (15 nJ energy) measured in a 100 µm thick gadolinium gallium garnet (GGG) crystal is shown. The smooth autocorrelation trace indicates the high signal-to-noise ratio in the order of 10^{-3} for a depletion amplitude of about 3 %.

It is worth noting that the UV-AC depicted in Fig. 2.3.1 can also be operated in the self-diffraction (SD) mode where the intensity of the self-diffracted beam is measured. This beam occurs because the two pulses generate an interference grating in the crystal on which the beam itself is diffracted. The self-diffracted part of the pump beam is then emitted in the direction of $k_{selfdiff}=2k_{pump}-k_{probe}$. Self-diffraction (SD) is commonly used in SD-FROG experiments to

measure ultrashort pulses [Nig89, Tre00]. However this technique can only be used if sufficient pulse energies are available (typically > 50 - 100 nJ). The resulting third-order autocorrelation trace indicates pulse asymmetry [Lev94] and can therefore help to decipher different orders of the chirp present in the pulse that can be fed back to the pulse shaper, when implemented. However, as will be seen further on, it is typically sufficient to characterize only the pulse length with the two-photon absorption autocorrelator to achieve nearly Fourier limited pulses with the AOPDF.

When an UV pulse shaper is used the optimal compression can be found on-the-fly without the need for experimentally more demanding methods like ZAP-SPIDER or the cross-correlation with an additional short visible pulse. As sketched in Fig. 2.3.1 the output of an AOPDF can directly be sent into the autocorrelator. The only prerequisite is that the intermediate beam waist of the shaped beam has to be placed one focusing length in front of the focusing mirror of the UV-AC, as described in the previous chapter. This can readily be achieved, because the UV-AC can be freely moved on the laboratory table to ensure the correct distance with respect to the AOPDF.

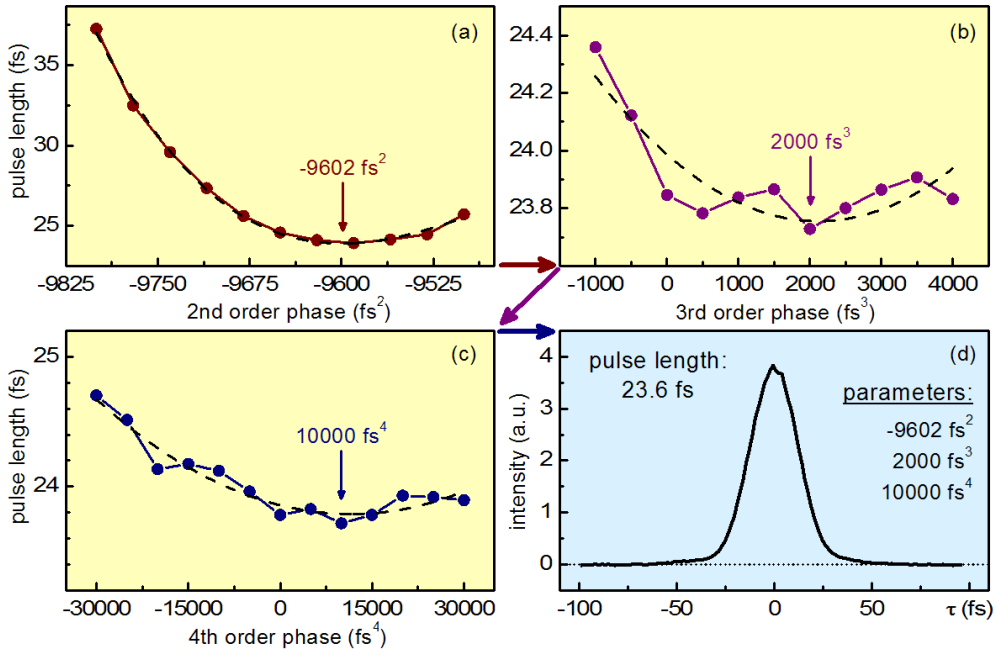

Fig. 2.3.2. On-the-fly pulse compression of the output of the AOPDF with the aid of the UV-AC. The 2nd (a), 3rd (b), 4th (c) order spectral phase is scanned with the pulse shaper and the optimal phase parameters found by minimizing the pulse length measured with the UV-AC. The dotted lines are a guide for the eye.

To find the optimal compression with the AOPDF the 2nd, 3rd and 4th order spectral phase applied by the AOPDF is scanned while the pulse length is measured simultaneously. Typically, manually scanning of the 2nd to 4th order spectral phase one after another and each time taking the optimal spectral phase value for the next higher-order phase is enough to achieve nearly Fourier limited pulses. If a more automated system is desired, a more sophisticated scanning scheme, e.g., by using a genetic algorithm as commonly used for 4-f-LCD based pulse shapers in the visible [Bau97], can be used.In Fig. 2.3.2 the spectral phase scans are shown for a 150 nJ pulse centered at 308 nm which is measured by self-diffraction in a 173 μm thick α-BBO crystal. This pulse was moderately broadened by SPM in a 1 mm thick CaF_2 crystal (for details see Chap. 2.2) with an initial Fourier limit of about 27 fs. Compression down to 23.6 fs (21 fs Fourier Limit) was achieved in about 10 minutes on a day-to-day basis.

After compression the UV pulses can then readily be used for ultrafast spectroscopy or to generate shaped UV pulses by adapting the spectral amplitude and phase with the AOPDF.

2.4 Increased signal-to-noise ratio by single-shot spectral referencing

In ultrafast transient pump-probe spectroscopy the observable of interest is the change in the spectral intensity distribution of the probe pulse due to pumping. The sources of noise in such a pump-probe experiment have different origins. They can originate from electronic noise induced by the data acquisition electronics or from intensity fluctuations of the laser pulses. For the transient pump-probe setups used in this study, the electronic noise is dominated by the shot noise limit of the probe detector [Meg09]. The probe detector is a CCD based prism spectrograph operating on the 1 kHz laser repetition rate. The resulting shot noise limit corresponding to the fullwell capacity of the CCD reading register is $1.3 \cdot 10^{-3}$ [Meg09]. This value is still well below the shot-to-shot fluctuations of the laser pulses which are in the order of 10^{-2}. Both, the probe as well as the pump pulses generate noise in the transient pump-probe spectra measured. The pump pulse does not contribute to the noise in linear fashion, but has to be weighted with the induced transmission change [Sch08]. However, when the change in optical density is less than a few percent, the contribution of the pump noise is somewhat smaller than the contribution from the probe intensity fluctuations [Meg09].

Averaging of multiple laser shots should increase the quality of the measured data as for statistical processes the signal-to-noise ratio should increase with the square root of the averaging time. However, the intensity fluctuations originating from the laser system have been shown to be not purely statistical but are typically dominated by low frequency contributions [Bra09, Sch08]. This is also the case for broadband probing with a supercontinuum white light generated by focusing the laser fundamental into a moving CaF_2 disc [Meg09].

To counteract this nonstatistical behavior of the probe intensity fluctuations two experimental designs are possible. The most conventional way is to use a chopper in the pump beam and measure the spectral intensity of consecutive probe pulses with and without pump [Sch08, Meg09], which will be called shot-to-shot referencing further on. This procedure is justified due to the high shot-to-shot intensity correlation of the laser and the transient absorbance changes that can clearly be resolved are in the order of $1 \cdot 10^{-4}$ OD [Meg09]. This limit can be overcome by measuring additionally the intensity of an identical copy of the probe without being transmitted through the excited area of the sample. This procedure is called single-shot referencing further on. For this technique it was shown that transient absorbance changes in the order of 10^{-6} OD can be resolved when the probe is measured spectrally integrated on a

photodiode detector [Sch08]. Recently, single-shot-referencing has been shown to achieve a sensitivity, also named confidence interval, for spectrally resolved transient absorption measurements of $2.5 \cdot 10^{-5}$ OD [Dob10].

In this section the single-shot spectral referencing scheme is adapted for broadband detection with a supercontinuum probe by using an additional reference spectrometer. A state-of-the-art transient spectrometer (for experimental details see also [Meg09]) was upgraded by a second identical prism based CCD spectrometer (Fig. 2.4.1a). The probe pulse is split into two parts with a broadband beam splitter. The beam splitter was a metal coated fused silica plate with an optical density for the transmitted beam of 0.5. This leads to an intensity ratio of roughly 33:33:33 (transmitted : reflected : absorbed). The part of the probe beam which is reflected on the metal-coated front surface is sent through the sample. After recollimation with a metal-coated spherical mirror the beam is dispersed with a fused silica prism and focused on the signal CCD (FFT sensor, S7030-0906, Hamamatsu) with another spherical mirror. The focusing length of the last spherical mirror (f = -250 mm) was selected such that the complete spectrum of the dispersed probe covers the whole horizontal elongation of the CCD sensor (~1.25 cm / 512 pixels). The transmitted part is directly sent into the reference spectrometer, which is an identical copy of the signal spectrometer. The spectral intensity for every laser shot is measured simultaneously with the two CCDs at the full 1 kHz laser repetition rate.

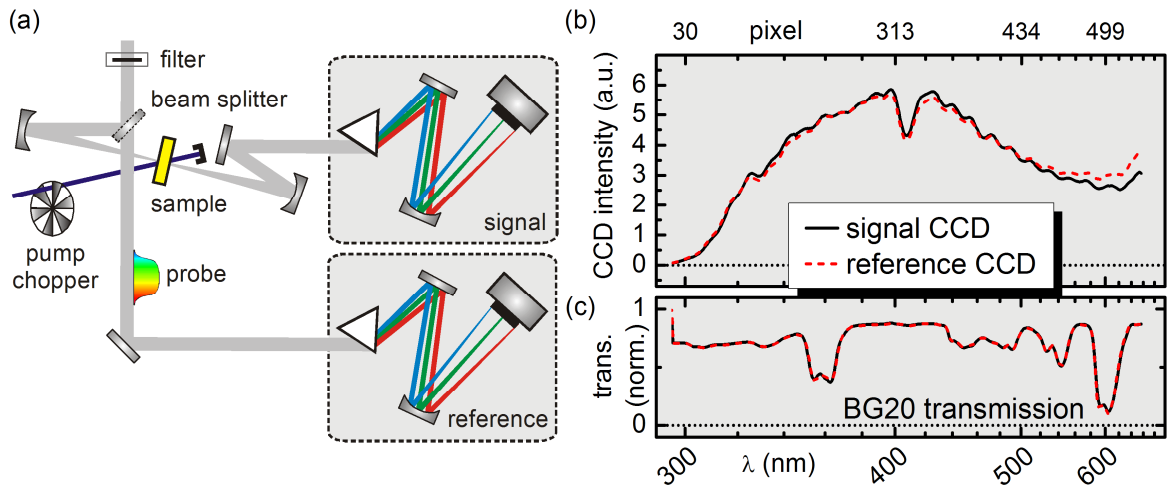

Fig. 2.4.1. (a) Schematic of the double CCD referencing scheme. The probe is split by a broadband beam splitter and measured in two identical prism based single-shot spectrometers. (b) Spectral intensity measured with the signal and reference CCD. (c) Characteristic transmission of a color filter (BG20) placed in the probe beam.

For optimal single-shot referencing the wavelength calibration of the two spectrometers should ideally be identical, e.g., by mapping the signal and reference wavelengths on the same pixel numbers. This can be done by placing a color filter into the probe beam in front of the beam splitter (Fig. 2.4.1c). The transmission features of the filter can then be used to precisely adjust the reference spectrometer until the modulations on the two detected spectra overlap at identical pixel numbers for the two CCDs. Adjusting the reference spectrometer is done by moving the CCD horizontally along the direction which is orthogonal to the incoming light and parallel to the optical table. This movement shifts the wavelength calibration. Tilting the CCD along its vertical axis allows tuning the wavelength spreading.

The color filter in the probe beam also allows performing the wavelength calibration as described in [Meg09]. Briefly, when the transmission features of the color filter are known, the respective wavelength can then be assigned to the pixel numbers where they appear on the signal CCD.

A more universal procedure to adjust the probe spectrometer analogue to the signal spectrometers can be done by placing a thin transparent material in only one half of the probe beam. Then, two identical but temporally delayed copies of the probe pulse are generated which lead to interference modulations in the spectral domain measured with the spectrometers. This procedure does also work for narrowband probe pulses with only a few nm bandwidths and is of great value for the UV spectral domain.

It is worth noting here, that the wavelength calibration of the two spectrometers has not to be exactly the same. Due to the high correlation of the amplitude fluctuations of neighboring wavelength components of the white light, even slightly detuning both spectrometers with respect to each other still allows for good single-shot referencing results. The spectral width of these correlations strongly depend on the daily performance of the white light and also change for different spectral regions of the white light. As a guideline for an upper limit of the allowed detuning, we found that a shift of up to 5 nm for a white light (300 – 650 nm) spanning the whole CCD sensor did not increase the resulting noise.

In Fig. 2.4.1b the intensity of a single-filament CaF_2 white light measured with the two CCDs is shown. With optimal alignment very good similarity of the two measured spectra is achieved. For optimal single-shot referencing it is sufficient that the wavelength calibration is identical, the spectral intensity distribution must not be identical.

A quantitative comparison between the traditional shot-to-shot referencing and the single-shot referencing method is described in the following. To do so, the intensity fluctuation of the probe and the shot-to-shot intensity correlation is calculated. The intensity fluctuation of the probe can be calculated by the root-mean-square value (RMS) given by

$$\mathrm{RMS} = \frac{\sigma_s}{\bar{s}} = \frac{\sqrt{\sum_n (s_i - \bar{s})^2}}{\sqrt{n}\,\bar{s}}, \tag{2.4.1}$$

where $\bar{s}$ is the mean value of the individual pulse intensities s_i and σ_s is the standard deviation. It describes the amount of the quadratic deviations of the intensity from the mean value and is 0 if there are no intensity fluctuations. The RMS value for every probe wavelength of a supercontinuum white light is shown in Fig. 2.4.2a and is the same in both spectrometers. It is on the order of 1 % intensity fluctuation [Bra10] and is higher for lower spectral intensities as the electronic noise becomes dominant [Meg09]. Without any referencing method this would also be the signal-to-noise ratio of the measurement. By using the shot-to-shot referencing scheme the signal-to-noise value is increased because this method benefits from the high intensity correlation between consecutive laser shots. Then the signal-to-noise ratio is increased by a factor that is related to the shot-to-shot correlation value.

A quantitative value that describes the correlation between two laser shots, e.g., between consecutive laser shots or between the signal and reference detector, is the Pearson-coefficient γ. The correlation between the signal s_i (the primary laser shot) and reference intensity r_i (the consecutive laser shot) at one CCD pixel measured for n laser shots is given by:

$$\gamma = \frac{\left(\sum_n r_i s_i\right) - n\bar{r}\,\bar{s}}{(n-1)\sigma_r \sigma_s}, \tag{2.4.2}$$

where $\bar{s}, \bar{r}$ are the mean values and σ_s, σ_s are the standard deviations [Dob10]. This value describes the similarity of the two selected intensities and reaches 1 for perfect correlation. In Fig. 2.4.2b the person coefficient, calculated for the different probe wavelengths, is shown for the consecutive laser shots (γ_{cons}) and for the signal to reference correlation (γ_{ref}). For shot-to-shot referencing with only one CCD, the mean correlation for the whole spectra is 0.56 while the correlation for single-shot referencing γ_{ref} is 0.978. This difference in the retrieved correlation shows that single-shot referencing can increase the signal-to-noise ratio significantly

when used in transient spectroscopy, and is remarkably better than shot-to-shot referencing.

This merit can be directly seen when calculating the RMS value for the referenced signal intensity, namely s_i/r_i (Fig. 2.4.2a). For such a value the RMS value drops below 0.2 %. The residual RMS is due to electronic noise which also explains the increased RMS values where the spectral intensity is low. The RMS value for the shot-to-shot referenced data drops only by a factor of about 30 % (data not shown).

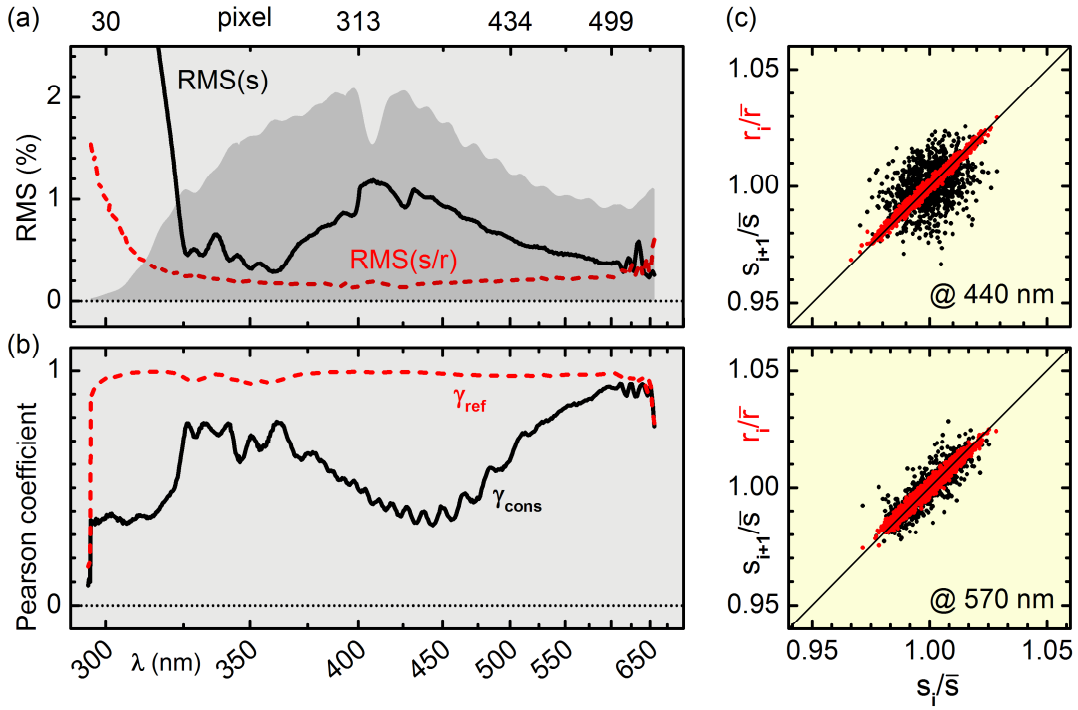

Fig. 2.4.2. (a) Spectrally resolved RMS values calculated for 2000 consecutive laser shots for the intensity of the signal CCD (black) and for signal divided by reference intensity (red). (b) Pearson correlation coefficient for shot-to-shot referencing (black) and single-shot referencing (red). (c) Plot of the normalized intensity (divided by the mean intensity) for consecutive laser shots ($s_{i+1} \leftrightarrow s_i$, black) and for the same laser shot but measured at the signal (s_i) and reference (r_i) spectrometers ($s_i \leftrightarrow r_i$, red) for different probe wavelengths.

The maximum value of γ_{ref} is about 0.995. This value is better than the reported value of 0.992 in Ref. [Dob10]. This is because we use single-filament white light which has for itself a better noise with a RMS of typically less than 1 % (Fig. 2.4.2a) compared to the multi-filament white light reported (RMS is 9.6 % [Dob10]). A graphical illustration of the Pearson coefficient can

be done by plotting pairs of measured intensities as dots in a graph with the normalized intensities as the x and y axis (Fig. 2.4.2c). The diagonal line corresponds to perfect correlation g = 1. The plot shows that the signal and reference spectrometer intensities correlate strongly for the selected wavelength while the pairs of consecutive laser shots correlate less as they are located also in the off diagonal area.

To use the high correlation of the single-shot referencing scheme in a transient pump probe experiment the pump induced transmission change I^*/I_0 is calculated for each probe wavelength as given in Eq. 2.4.3.

$$\frac{I^*}{I_0} = \frac{Sig_0}{Ref_0} \cdot \left(\frac{Sig^*}{Ref^*} \right)^{-1} . \qquad (2.4.3)$$

The signal intensity with Sig* and without pump Sig_0 is divided by the reference intensity Ref* and Ref_0 for each laser shot [Sch08]. Then the intensity fluctuations of the probe are eliminated and the residual RMS of typically less than 0.2 % can be attributed to electronic noise [Meg09]. Note, that it is also possible to measure transient spectra by calculating only Sig*/Ref* because the reference pulse is not influenced by the pump. By measuring Sig_0/Ref_0 once before starting the transient measurement, the transmission change can be calculated for all pump-probe delays. This technique would avoid chopping and every laser shot can be used and thus the measurement time can be reduced. However, long time drifts of the count rates of the two CCDs, e.g., by heating of the electronics, can lead to systematic deviations of the transient spectra. From I^*/I_0 the induced change in optical density can be calculated by

$$\Delta OD = -\log\left(\frac{I^*}{I_0} \right). \qquad (2.4.4)$$

The strong benefit of referencing besides a higher signal-to-noise ratio is the elimination of systematic *ghost* signals observed in shot-to-shot referenced transient spectra. These modulations span over broad spectral regions and have typically amplitudes which are bigger than the electronic noise observed for neighboring detection pixels. These *ghost* signals originate from systematic intensity fluctuations of the probe in the time span of the averaging time. Therefore these *ghost* signals can be misinterpreted as a *real* sample response for weakly absorbing samples. They are present even when many (> 5000) laser shots are used for averaging. The single-shot referencing scheme eliminates these *ghost* signals. To demonstrate

this, the transient absorption spectrum of malachite green dissolved in ethanol was measured.

The transient spectra for a delay of about 10 ps were calculated as an average of 1500 laser shots and plotted once with and without referencing (Fig. 2.4.3a). The black curve is the expected transient for 10 ps that is derived by scaling the strong transient spectrum for 1 ps with a value that is derived by taking the temporal behavior of the molecular signal into account. Additionally, from the complete pump-probe delay scan (data not shown) it can be concluded, that the transient signal amplitude at about 10 ps is nearly constant for the different delays shown in the figure (red, green and blue curve). Therefore, the deviations of the transients from expected shape (black curve) are dominated by systematic deviations (*ghost* signals) that are clearly larger for the conventional shot-to-shot referencing technique when compared to the referenced measurement. The systematic deviations are even larger than the electronic noise which is visible as the amplitude modulations for neighboring wavelength pixels. As a result, the typical detection sensitivity of the instrument averaged over the whole spectral range is enhanced by a factor of 5 from $9.9 \cdot 10^{-5}$ to $2.1 \cdot 10^{-5}$ OD by using single-shot referencing (Fig. 2.4.3b). This value is slightly better than the value reported in the literature for multi-filament white light probing of $2.5 \cdot 10^{-5}$ OD [Dob10]. With the same laser and a similar setup using only one CCD, detection sensitivities of $7.6 \cdot 10^{-5}$ OD are achievable [Meg09].

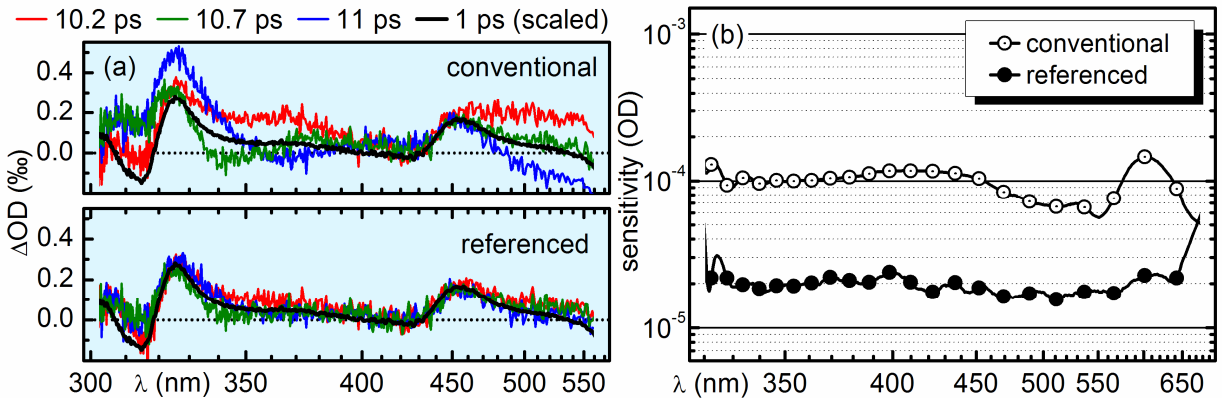

Fig. 2.4.3. (a) Measured transient spectra of malachite green for different pump-probe delays. For conventional pump probe measurements (upper panel) strong amplitude fluctuations of the transient spectra on top of weak pixel-to-pixel electronic noise are observed which are eliminated by referencing. (b) Detection sensitivities. The average sensitivities are $9.9 \cdot 10^{-5}$ OD for the conventional shot-to-shot and $2.1 \cdot 10^{-5}$ OD for the new single-shot referencing scheme.

The *ghost* signals observed here for white light supercontinuum probing are even more severe when using a frequency upconverted NOPA pulse as the spectrally resolved probe pulse. Such an UV pulse has a noise which is typically in the order of 1.5 % RMS and additionally shows changes in the shape of the spectrum on a shot-to-shot basis, which can distort the measured transients. However, by using single-shot-referencing a reduction of *ghost* signals and an increased sensitivity are achieved that equal the results presented here for white light probing.

The referencing technique can easily be incorporated into an existing pump-probe setup and is minimal invasive by only implementing a beam splitter into the existing probe beam. This technique allows measuring weak transient signals and can significantly reduce the overall measurement time when fragile samples are investigated or time consuming techniques like 2D spectroscopy are performed.

3. Molecular processes investigated with transient absorption spectroscopy

Femtosecond transient absorption spectroscopy is a versatile tool to investigate ultrafast light-induced molecular processes and reactions. However, there is no universal experiment tool to investigate all different types of molecules. Typically, the experimental configuration has to be adapted to match the particular requirements of the system under investigation, e.g., to achieve sufficient temporal resolution or to cover the spectral domain where the molecule is optically addressable.

The following chapter describes the results on the ultrafast light-induced photoreactions and dynamics of different photoactive molecules. The experimental setups used to do so have been developed in the course of my thesis to investigate specific properties of the individual molecular systems.

3.1 Ultrashort UV-pump-UV-probe spectroscopy of DPMC

Introduction. The optical excitation of valence electrons in atoms leads to long lived excited states that can only relax by fluorescence. In polyatomic molecules the extra degrees of freedom provided by the nuclear motion allow for nonradiative decay where part or all of the excitation energy is converted to vibrations. The geometric distortion leads to points in the 3N-6 dimensional vibrational space (N atoms in the molecule) where states with differing electronic configuration cross and the energy gap vanishes. Strictly speaking, the non-crossing rule of diatomics is not valid for larger systems and the displacement along nonsymmetric coupling modes leads to a conical intersection (CoIn) [Oli00, Yar01, Dom04]. In the vicinity of the CoIn the Born-Oppenheimer separation breaks down completely and highly efficient and rapid photodissociation [Har01] or isomerization can take place [Mad11].

Experimentally, the presence and effectiveness of a CoIn is detected as femtosecond decay of the optical signature attributed to the excited state or the equally fast recovery of the ground state absorption. For a photochemical process the newly appearing product signal serves as indication. The detection and interpretation gets more complex as more than one CoIn is involved. Theory has shown convincing examples for this situation and it now seems to be rather the rule than the exception [Yar01, Oli00, Nen10]. Once the existence of CoIns is accepted, the next step is to move away from the description of the ultrafast process in terms of

populations toward the motion of a vibronic wavepacket from the Franck-Condon point toward the CoIn and beyond. This has recently been demonstrated in a particularly comprehensible study of the isomerization of rhodopsin [Pol10].

For many chemical processes not only the channels of return to the ground state and a single product like a ring opened structure exist, but two or more product channels. In a classical kinetic description (rate model) one expects a decay of the excited state signal with $\tau = 1/(k_{IC} + k_1 + k_2)$ where k_1 and k_2 are the effective product formation rates and k_{IC} is the internal conversion rate. The products are expected to appear equally fast and the ratio of products is given by $r = k_1 / k_2$. From the theoretical point of view the question arises whether one or two CoIns are responsible. To clarify this experimentally, the sole determination of the ultrafast rates is not sufficient. Additional and more specific signatures have to be found.

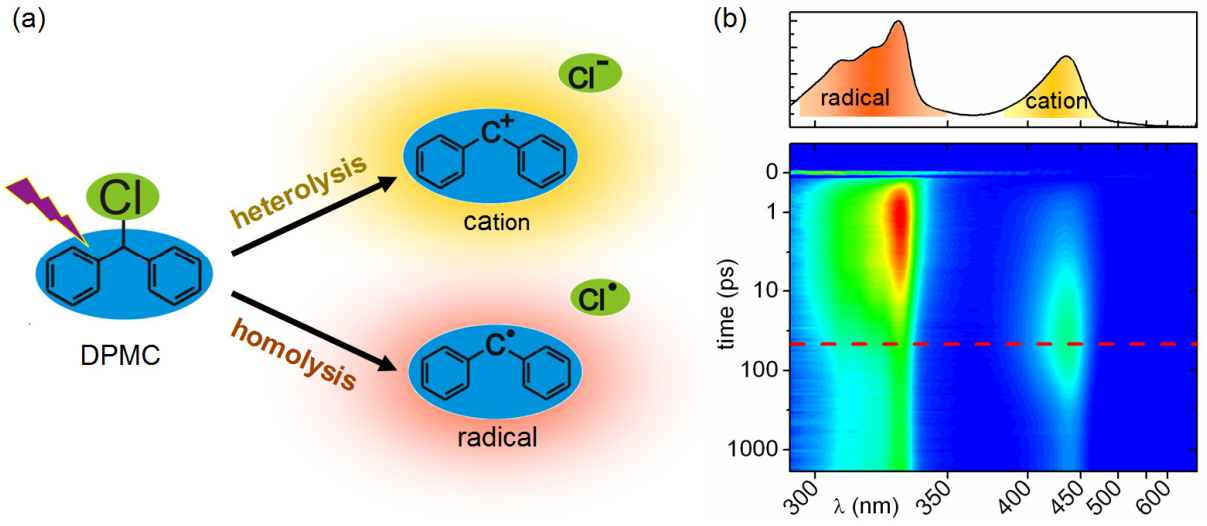

Fig. 3.1.1. Light-induced bond cleavage of benzhydryl chloride (DPMC). (a) Illustration of the homolytic and heterolytic reaction channels of DPMC after UV irradiation. (b) Broadband transient absorption measurement showing two distinct absorption signatures belonging to the benzhydryl radical (327 nm) and benzhydryl cation (430 nm).

A photoreaction with two distinct product states is the light-induced bond-cleavage of diarylmethyl chlorides which we investigated by transient absorption spectroscopy with sub-40 fs temporal resolution. The results are described in this chapter. After excitation with UV light, the bond-cleavage of benzhydryl chloride (DPMC) in solution is known to either proceed homolytically (benzhydryl radical + chlorine radical) or heterolytically (benzhydryl cation + chlorine anion) (Fig. 3.1.1a). Broadband transient absorption measurements with high

but still limited temporal resolution show that both processes occur in well under 1 ps and the benzhydryl moieties can be easily distinguished spectroscopically (Fig. 3.1.1b) [Fin08, Fin12, Sai13].

DPMC absorbs at 270 nm and below by excitation in the phenyl rings. The bond between the central sp^3 hybridized carbon and the chlorine is eventually broken. If the bond electrons are shared between the fragments (homolysis), the benzhydryl radical with a strong absorption peaking at 327 nm results. If both electrons go to the chlorine (heterolysis), the benzhydryl cation with an absorption centered at 435 nm emerges. The two signal contributions can uniquely and unambiguously decipher the complex dynamics and can be used to finally show that one of two distinct CoIns is responsible for each reaction channel.

To investigate the ultrafast bond-cleavage process itself transient absorption measurements with high temporal resolution are needed to resolve the dynamics in the first hundreds of femtoseconds. Therefore we developed a new two-color pump-probe experiment with sub-40 fs temporal resolution and absolute time-zero calibration. The design of the experimental setup is described in the following.

Experimental setup. A schematic of the experimental setup is shown in Fig. 3.1.2. As primary light source a regenerative Ti:Sa amplifier system (CPA 2001; Clark MXR) was used. For the pump and probe pulse generation two noncollinear optical parametric amplifiers (NOPA) [Rie00] were employed. The NOPA which delivers the pump pulses operates at 540 nm. The pump wavelength of 270 nm is then generated by second harmonic generation in a 35 µm thin BBO crystal. Precompression of the pulses in a prism compressor in the visible beam ensures that the pulses have a temporal width of the FWHM of about 29 fs at the position of the sample after propagation through all dispersive materials. The pulse length was measured by an UV-autocorrelator [Hom11]. Analogously, the probe pulses are generated by frequency doubling in a 62 µm thick BBO crystal and compression is again achieved by a prism compressor in the visible. The pulse length was measured to about 30 fs and 45 fs for pulses centered at 327 nm and 430 nm, respectively.

The spot sizes for the pump beam at the sample position was about 76 µm FWHM with a pulse energy of about 200 nJ. About 2 % of the DPMC molecules dissolved in acetonitrile were excited. The large molar extinction coefficient of the fragments (about 50,000 L/mol/cm as compared to 500 L/mol/cm for DPMC) leads to a sizable absorption change at the respective wavelength of each benzhydryl fragment. The probe was about 45 µm in size and had a pulse

energy up to a few nJ. A mechanical delay line (M-014.D01, Physik Instrumente) with a minimal incremental motion of 0.1 µm affords the delay between the pump and probe pulses.

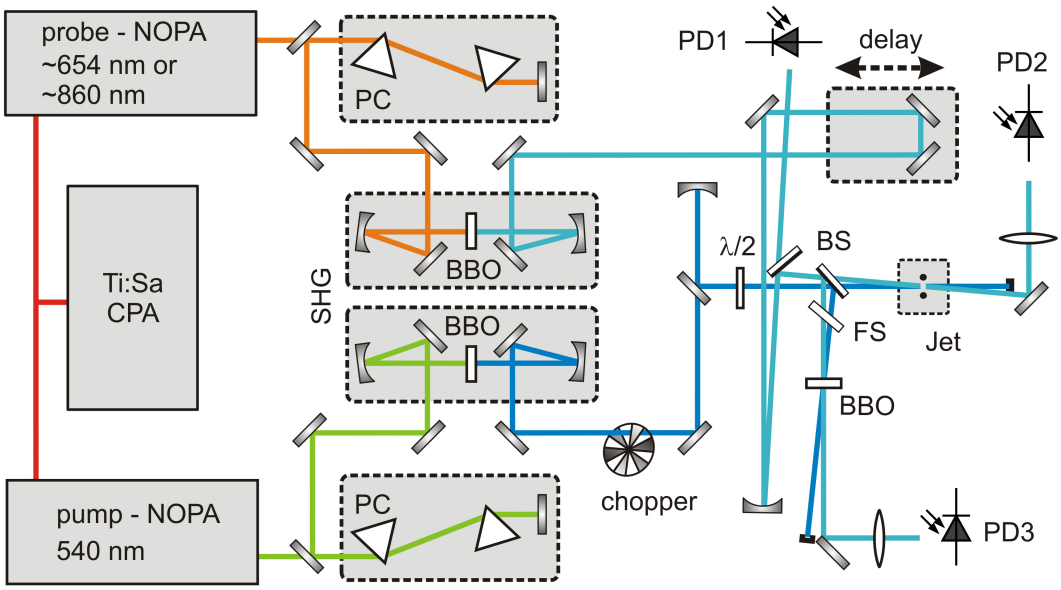

Fig. 3.1.2. Scheme of the two-color pump-probe setup. NOPA: noncollinear optical parametric amplifier; PC: prism compressor; SHG: second harmonic generation; Chopper; BS: beam splitter; FS: fused-silica plate; PD: photo-diode.

The probe intensity fluctuations were measured with a fraction of the probe before transmission through the sample. The change in transmission with and without pump, measured with the photodiode after the sample, was then divided by the probe reference diode signal as described in [Sch08]. This single-shot referencing scheme is analogous to the one developed for broadband transient absorption measurements described in Chap. 2.4. To minimize dispersion and coherent artifacts, the sample was a free flowing jet with a thickness of about 50 µm [Lai06]. The decrease of the molecular concentration due to evaporation of the solvent was continuously monitored by an absorption spectrometer of our own design that is incorporated into the jet's circuit. A computer controlled pump then refilled the necessary pure solvent to keep the concentration constant.

The absolute zero-time delay, i.e. the timing when the temporal peak of the Gaussian shaped pump and probe pulse are incident in the sample at the same time, was determined as follows. An additional reference pump-probe branch was generated by splitting a fraction of the probe and the pump beam with a dielectrically coated fused silica UV beam splitter in front of the sample. As the beams are focused before impinging on the beam splitter this generates an identical pump-probe overlapping region as for the transmitted beams. A compensation plate

identical to the beam splitter, but without dielectric coating, compensates for the difference in dispersion for the two branches.

In the reference pump-probe branch the cross-correlation between the pump and probe pulse was measured via two-photon absorption in a 100 µm thick BBO. The sample branch and the reference branch measurement were recorded in parallel for all measurements. The reference branch cross-correlation can then be used to link the time delay between multiple measurements where only the sample in the jet is changed. The procedure to retrieve the absolute time-zero delay is shown in Fig. 3.1.3. Prior to each measurement of the molecular solution the pure solvent artifact was measured in the jet. To link the two successive measurements the two reference arm cross-correlations are then temporally shifted by at most a few fs to achieve optimal overlap. The pure solvent artifact signal is then correctly overlaid with the molecule measurement in time. This procedure allows us to determine the absolute zero-time delay with a precision better than 4 fs and the amount and temporal profile of the solvent contribution for the molecule measurement.

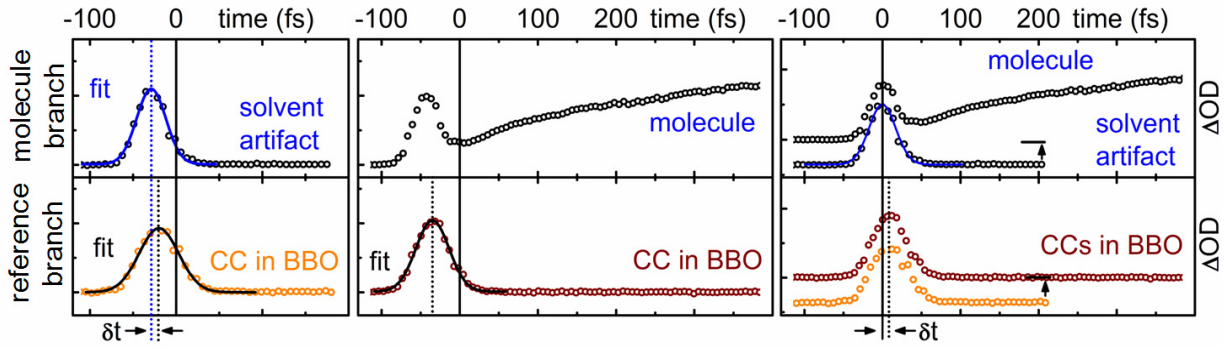

Fig. 3.1.3. Scheme for the determination of the absolute time-zero delay (t=0). The reference branch (lower) is overlaid for the pure solvent (left) and molecule (middle) measurement (lower right). This allows comparing the two measurements with absolute timing precision of better than 4 fs. The time-zero for the molecule measurement is then given by the peak of the pure solvent artifact which is shifted to the reference branch by a slight value of δt.

Data modeling and analysis. To model the signal evolution quantitatively the measured temporal development of the transient absorption signals were fitted with the model described in the following. Several processes and the resulting possible optical transitions contribute to the transient absorption signal measured after UV excitation of DPMC in acetonitrile. The measured signals can be separated into two types of contributions. One the one side, the

contributions arising only at the temporal overlap of the pump and probe pulses and on the other side the contributions arising from the pump light-induced molecular dynamics containing the desired information of the bond-cleavage itself.

The Jablonski diagram of DPMC and the benzhydryl radical as the main photoproduct is shown in Fig. 3.1.4. It depicts the temporal evolution of the optical signal at the maximum wavelength of the radical band. For temporal overlap of the pump and probe pulses, additionally to a coherent, non-resonant two-photon absorption from the solute, the two-photon absorption of DPMC is present ①. The pump pulse generates a wavepacket in the S_1 state of DPMC. The probe pulse can now be depleted by the $S_n \leftarrow S_1$ transition that gives rise to a short-lived excited state absorption (ESA) directly after UV excitation ②. The wavepacket evolves towards the first conical intersection (CoIn) and after a time delay of Δt_{bc} (bond cleavage time) the CoIn is reached. Here, the major part of the wavepacket couples to the potential energy surface which leads to a radical pair and the ESA vanishes. The newly formed benzhydryl radicals are in the electronic ground state and can be detected via the $D_5 \leftarrow D_0$ transition, namely the product absorption ③. Then there is a strong increase of the benzhydryl cation and radical absorption with a time constant of ~ 300 fs due to planarization and solvation [Fin12] ④. An analogous discussion can be made for the cation channel.

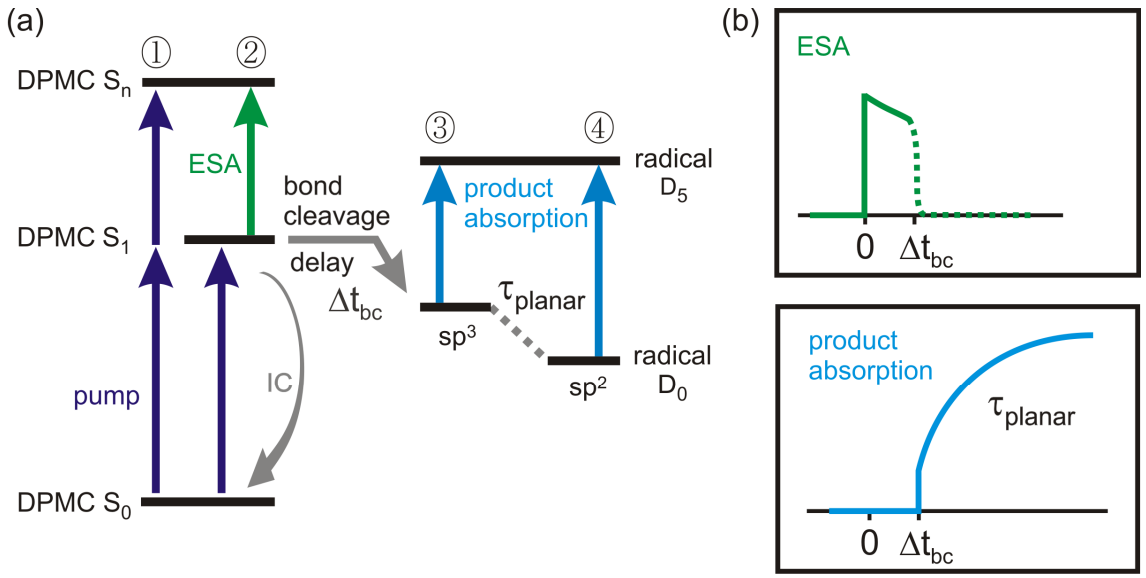

Fig. 3.1.4. (a) Jablonski diagram showing the involved transitions and processes after UV irradiation of DPMC in acetonitrile when the radical channel is probed. (b) Scheme of the corresponding transient absorption signal for the same transitions and processes.

The measured time-dependent transient absorption changes were fitted with a LabView routine which is slightly modified compared to the one described in Ref. [Meg09, Loc03]. The fit function F(t) can account for signal contributions starting with time-zero as well as for contributions starting with a temporal delay Δt_{bc} with respect to time-zero:

$$F(t) = IRF(t) \otimes \left\{ A_{coherent}\,\delta(t) + \theta(t) \cdot \theta(\Delta t_{bc} - t) \left[A_{ESA,\infty} + A_{ESA} \exp\left(-\frac{t}{\tau_{ESA}} \right) \right] + \theta(t - \Delta t_{bc}) \cdot \left[A_{product,\,initial} + A_{planar} \left(1 - \exp\left(-\frac{t - \Delta t_{bc}}{\tau_{planar}} \right) \right) \right] \right\}. \tag{3.1.1}$$

The kernel of the fit function consists of a δ function centered at t = 0 with amplitude $A_{coherent}$ which accounts for the coherent signal contribution of the molecule. A constant and a fast decaying absorption which is multiplied by two step functions Θ(t) and Θ(Δt_{bc}-t) reproduces the instantaneous ESA with a possible small decay due to the wavepacket motion and the sudden disappearance of the ESA at t = Δt_{bc} when the CoIns are reached. Then the kernel contains a constant and a rising absorption which are multiplied by the step function Θ(Δt_{bc}-t). This accounts for the delayed dynamics of the photoproducts (i.e., benzhydryl radical and cation). It reproduces the absorption of the unrelaxed photofragments after their generation at t = Δt_{bc} and the signal rise due to planarization and solvation. Further on, a delayed exponential dynamics can also be fitted (not shown in Eq. 3.1.1). It is needed to account for the evolution of the signal on the tens to hundreds of picoseconds scale due to electron transfer and geminate recombination [Sai13] and rotational relaxation. The kernel is convoluted with the instrumental response function (IRF(t)) to account for the finite temporal evolution of the experiment. The IRF(t) is a Gaussian function with the temporal FWHM given by the width of the cross-correlation measured in the pure solvent.

As mentioned earlier, part of the measured transient absorption signal after UV excitation of DPMC in acetonitrile or FDPMC in methanol is due to two-photon absorption in the solvent [Lor02]. Therefore the signal of the neat solvent was always measured before a measurement of the solution. However, in order to subtract the signal of the solvent from the data it has to be scaled properly, since the pump is depleted by the absorption from DPMC. The OD of the solution in the experiment was 0.11 for DPMC. This leads to a typical scaling factor for the two-photon absorption signal in neat solvent of 0.88 in the case of DPMC.

Results. At first, the two-color pump-probe setup was used to measure DPMC dissolved in acetonitrile. The absorption spectrum of DPMC as well as the pump and probe spectra are shown in Fig. 3.1.5a. The probe spectra have central frequencies that match the respective light-induced product absorption at 327 nm (radical) and 430 nm (cation). The time dependence of the transient absorption of both products is shown in Fig. 3.1.5b. Through careful monitoring of the beam sizes, sample concentration and pulse energies not only a picture of the temporal behavior but even the quantitative yields can be extracted [Sai13].

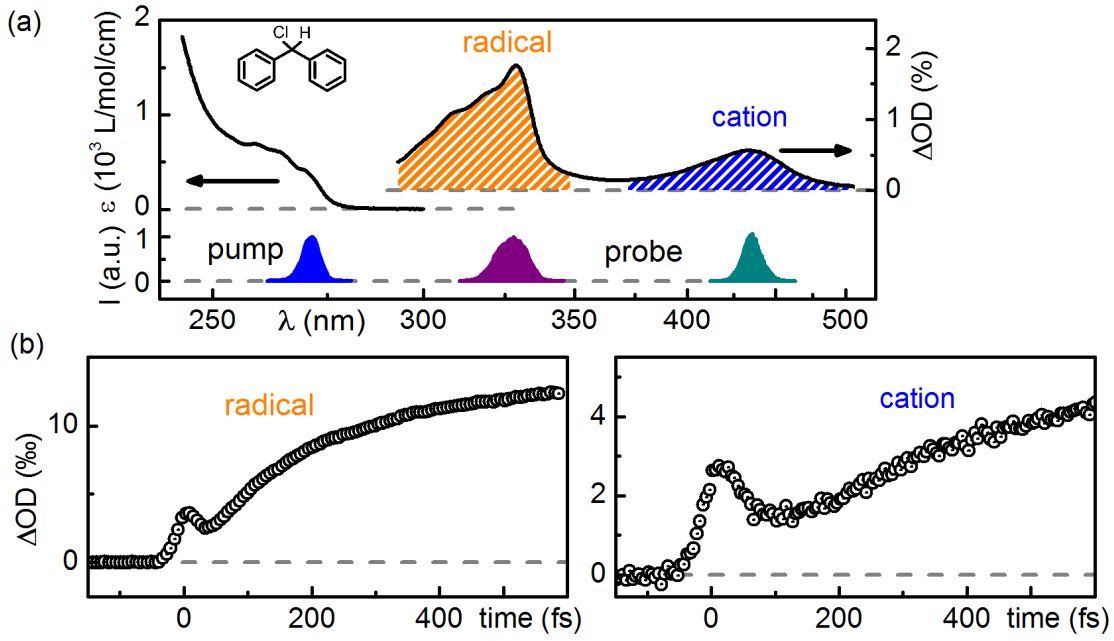

Fig. 3.1.5. (a) Absorption spectrum of DPMC in acetonitrile (left) and its transient absorption spectrum (right) 5 ps after 270 nm excitation. The spectrum of the pump and the probe pulses are shown below. (b) Transient absorption (black circles) after UV excitation of DPMC in acetonitrile at a) 327 nm (benzhydryl radical) and b) 436 nm (benzhydryl cation).

The result of fitting the measured time dependent transient absorption of DPMC (Fig. 3.1.5b) is shown in Fig. 3.1.6. For proper modeling the 20 ps electron transfer (ET) within the radical pairs that depletes the radical population and increases the cation population is included [Sai13]. The effective 300 fs increase of both signals has been previously shown to originate from both planarizations of the benzhydryls after the bond cleavage and from solvation [Fin12]. The different molecular contributions, for which the sum does perfectly match the measured data, are also plotted separately.

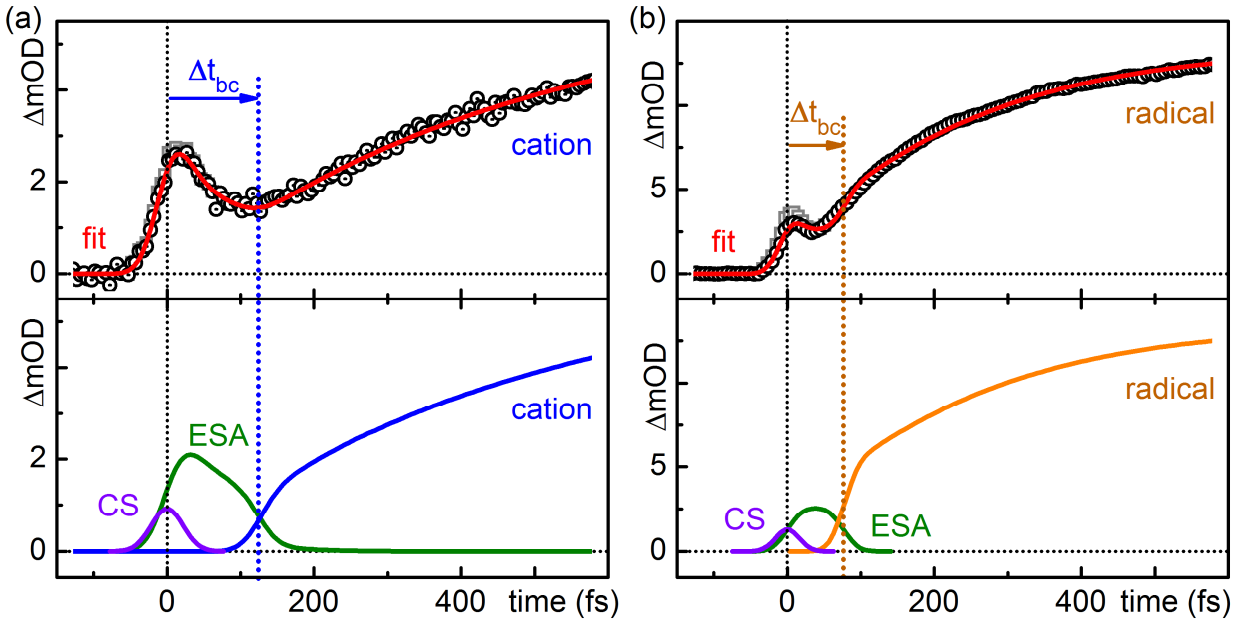

Fig. 3.1.6. Transient absorption (black circles) after UV excitation of DPMC in acetonitrile. Probed at 327 nm (benzhydryl radical) and 436 nm (benzhydryl cation) (b). The coherent signal from the solvent is subtracted from the raw data (open grey squares) to yield the pure molecular signal. The fit is shown in red. The single fit contributions are depicted below. The product absorption from the cation and radical are shown in blue and orange. ESA: excited state absorption. CS: coherent signal from the molecule.

Roughly 40 % of the excited DPMC dissociates homolytically. The transient signal rises with the cross-correlation (CC) of the pump and probe pulse (38 fs FWHM) and falls off within the next tens of femtoseconds (see Fig. 3.1.6a). After correction of the raw data (grey squares) by the properly scaled solvent contribution even the pure molecular signal (black circles) still contains a Gaussian shaped contribution centered exactly at delay zero. This contribution is assigned to the coherent, nonresonant two-photon absorption of the molecule. This interaction depletes the probe pulse as long as the pump-probe delay is within the CC convoluted with the electronic dephasing time of DPMC of likely a few tens of femtoseconds [Big91, Nib91].

The remaining population part of the early molecular signal is proportional to the integral of the pump-probe CC as population in the S_1 state is accumulated from the initial polarization and the subsequent electronic dephasing. The signal strength is due to the excited state absorption (ESA) in the Franck-Condon (FC) region. Immediately after the pump pulse the wavepacket accelerates away from the FC point and the signal changes weakly. At a delay Δt_{bc} = 76 fs the

signal increases significantly within the time resolution. Finally it increases further with a quasi-exponential behavior and a time constant of 270 fs.

Only about 2 % of the excited DPMC dissociates heterolytically and leads to a weak but well detectable transient absorption signal at 435 nm. The temporal behavior is analogous to the radical signal with two exceptions: the delay is now 124 fs and the signal increases much more at later times. The increase from 76 to 124 fs for the delay in signal increase is the decisive difference between the homolytic and the heterolytic channel. Already the clearly non-exponential signal increase in the first 150 fs and even more the different times for the two distinct product channels deviate not only quantitatively but conceptually from the expectation of a rate model with two processes drawing from the same reservoir.

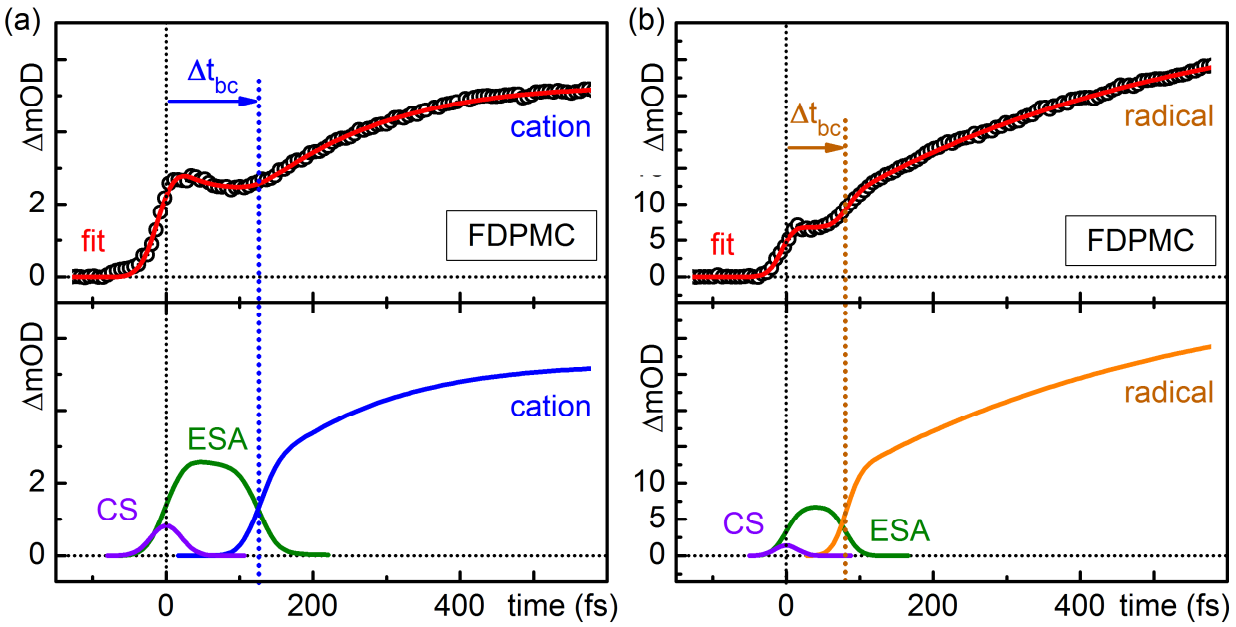

Fig. 3.1.7 Transient absorption (black circles) after UV excitation of FDPMC in methanol. Probed at 327 nm (benzhydryl radical) (a) and 427 nm (benzhydryl cation) (b). The coherent signal from the solvent is subtracted. The fit is shown in red. . The single fit contributions are depicted below. The product absorption from the cation and radical are shown in blue and orange. ESA: excited state absorption. CS: coherent signal from the molecule.

The ET in the radical pair is only possible if the cation is better stabilized than the radical. Therefore preliminary experiments with the transient absorption setup [Meg09] were performed. It is found, that in methanol the ET does not contribute effectively to the cation generation. DPMC itself is not stable in methanol, but properly substituted derivatives are

[Den06]. The monofluoro-substituted benzhydryl chloride (FDPMC) was chosen for additional measurements in methanol. The measured results (Fig. 3.1.7) reveal that the general behavior is quite similar to DPMC and that the slowly increasing component due to ET which is visible on the ps time scale is indeed absent in the cation signal. FDPMC thus allows an even more unambiguous interpretation. As the same features are observed in DPMC and FDPMC, it can readily be concluded that the bond cleavage is neither altered by the substitution nor the solvent. It is purely a property of the molecular core. Most importantly, delay times of 81 and 126 fs were found for the two delays, which are equal to the times found for DPMC within the experimental precision.

Ab initio calculations. From the experimental evidence the involvement of conical intersections (CoIn) in the bond cleavage dynamics can only be inferred indirectly due to the ultrafast reaction times. All ab initio calculations described in the following have been done in the group of Prof. Dr. Regina de Vivie-Riedle (Ludwig-Maximilians-Universität in Munich, Germany). In a first quantum chemical investigation of DPMC the importance of CoIns for the cation channel was already demonstrated [Fin08]. Their calculations now include more electronic states to differentiate between homolysis and heterolysis and to quantitatively interpret the experimental observations. Calculations were performed on the CASSCF level of theory for the ground and the first five excited singlet states along the bond cleavage coordinate $R_{C\text{-}Cl}$. They were followed by a multi-reference second order perturbation treatment (MRPT2) [Cel00] to obtain accurate excitation energies. All other coordinates were relaxed at each position of $R_{C\text{-}Cl}$. The potential energy curves are shown in Fig. 3.1.8. The optical excitation is allowed in both phenyl rings and leads to the degenerate S_1 and $S_{1'}$ states with $\pi\pi^*$ character (black and blue lines). Close to the FC-point both states are crossed by the repulsive S_2 and $S_{2'}$ states, whose electronic structure corresponds to transitions from the Cl lone pair np_x or np_z to the π^* system of the phenyl ring (orange line representing both states). The leading configurations of the S_3 state are of $\pi\pi^*$ and $\pi\sigma^*$ character. Due to the σ^* contribution the S_3 state is also repulsive.

To highlight the significance of the S_2 and $S_{2'}$ states they are represented in the diabatic description, all others in the adiabatic description. Coupling among all states is needed to describe the dynamic situation properly. As a result two spatially separated CoIns are found. The first corresponds to bond cleavage into the radical pair and the second into the ion pair. The existence of CoIns does not yet warrant an effective and ultrafast process, but it provides the possibility. Only dynamical calculations can clarify this question [Dom04, All12].

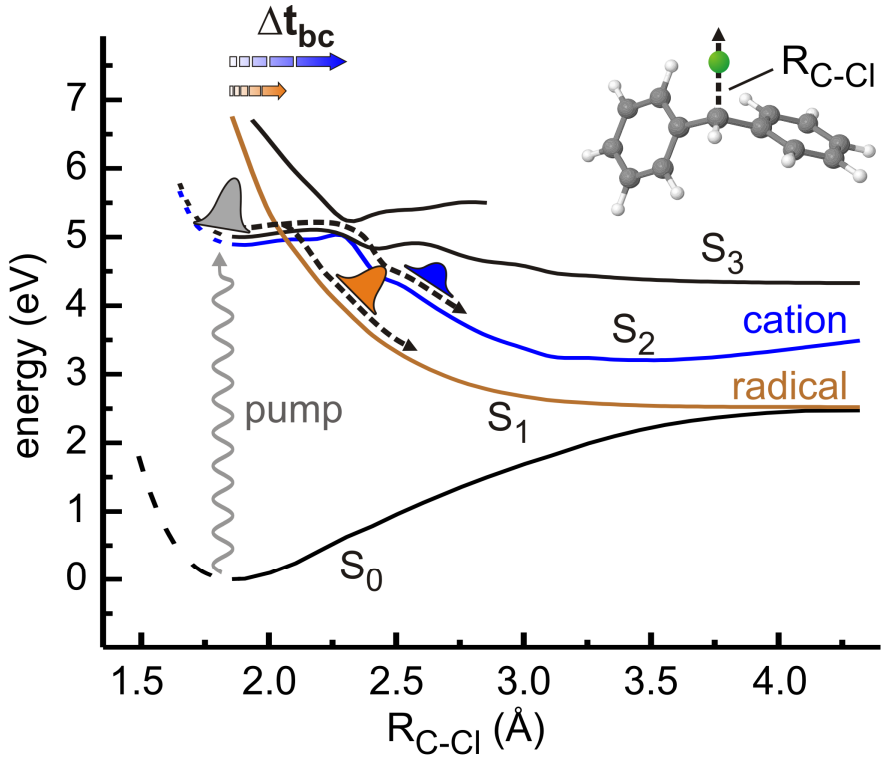

Fig. 3.1.8 Potential energy curves along the ground state minimum energy path vs. C–Cl-distance $R_{C\text{-}Cl}$ calculated on the CASSCF level of theory. Shown are the ground state S_0, the excited states S_1 (blue turning orange), $S_{1'}$ (black), S_2 and $S_{2'}$ (orange turning blue) and S_3.

For the CoIn leading to the radical pair, nonadiabatic on-the-fly molecular dynamic simulations were performed by the theoreticians [Bar07, Fin12]. The transition from the originally excited states S1 and S1' to the repulsive radical pair states is treated by surface hoping [Tul90] where transitions are possible when two states approach closely in energy and the nonadiabatic coupling becomes large. Of the 52 trajectories roughly a quarter show bond cleavage subsequent to a nonadiabatic ππ* → np_z-π* transition. This compares well to the 40 % found experimentally.

The potential energies of the electronic states for a typical trajectory are shown as Fig. 3.1.9a. As the DPMC vibrates after the UV excitation, part of the available energy is transferred to kinetic energy of the atoms and the potential energy of the various states changes.

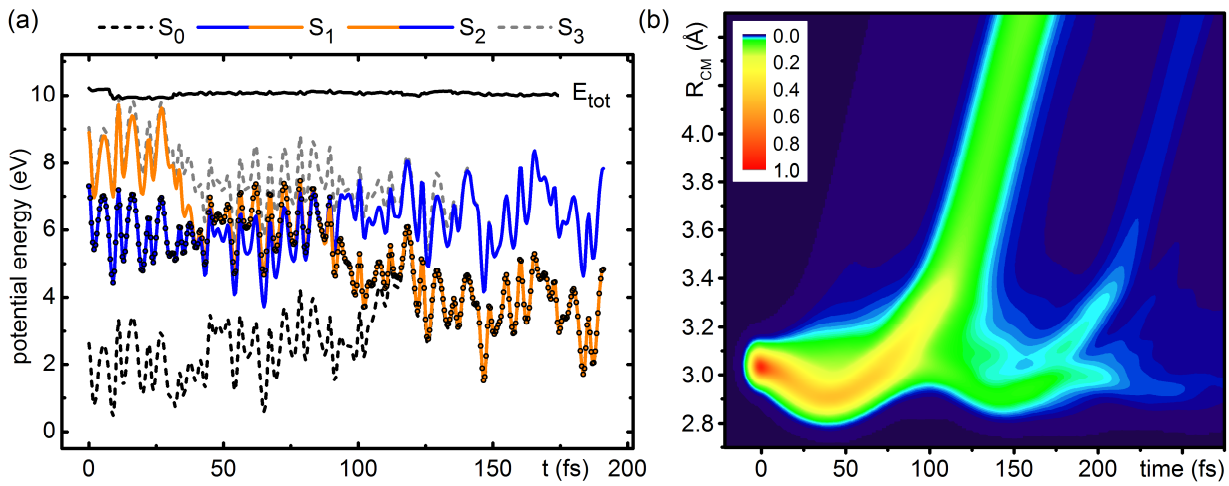

Fig. 3.1.9 Theoretical calculations performed by collaborating theoreticians (Group of Prof. R. de Vivie-Riedle. LMU Munich, Germany). (a) Exemplary trajectory for the bond cleavage process in DPMC. Shown are the electronic energies of the ground state S_0 (black), the excited state S_1 (blue turning orange), S_2 (orange turning blue) and S_3 (gray-dashed). S_3 corresponds to S_2' in the FC region, i.e. during the first 35 fs. After the conical intersection S_1/S_2 is passed, the leading configuration of the S_1 state is a $n_p\sigma^*$ configuration directly correlated to the radical formation channel. S_2 and S_3 (S_2') change their character to $\pi\pi^*$ and $\pi\sigma^*$ configurations at the same time. (b) Time evolution of the wavepacket in the adiabatic S_1 state after excitation with an ultrafast pulse. The time evolution of the wavepacket was followed on two dimensional potential energy curves spanned by two reactive coordinates R_{CM} and ϕ; for details see [Fin08]. The two-dimensional wavepacket is projected onto the bond cleavage coordinate R_{CM} and the time evolution is shown as false-color plot with the wavepacket's amplitude encoded in the color code.

In the trajectory the first CoIn is reached after 45 fs (joining of blue and orange lines). The energies stay closely matched up to about 100 fs when the nonadibatically populated state acquires repulsive character and the curve crossing is finally accomplished. The molecular system follows the orange curve that slopes downward and separates from the blue curve. The evolving electronic character of the system correlates with the radical bond cleavage channel. The time scale of the calculated cleavage is in the same range as the 76 fs found experimentally.

In line with the small probability of 2 % for heterolysis already found experimentally, no evidence for ionic bond cleavage from the set of trajectories can be found. Therefore 2D quantum dynamical calculations were performed by the theoreticians with a reduced set of

electronic states. The optical excitation was confined to one phenyl ring and the repulsive $S_2/S_{2'}$ states leading to the radicals were omitted to allow propagation of the wavepacket towards the second CoIn. As in the previous investigation [Fin08], the two reactive coordinates R_{CM} and ϕ are used. R_{CM} is the distance between the center of mass of the benzhydryl fragment and the Cl atom. The polar angle ϕ is defined relative to the center of mass of the whole molecule and describes the bending of the Cl atom towards one of the phenyl rings.

The wavepacket first moves to nominally smaller R_{CM} values (see Fig. 3.1.9b). This is due to the multidimensional character of the full motion. At about 110 fs the main part of the wavepacket accelerates to larger values of R_{CM} and reaches a constant speed. The point of acceleration corresponds to the passing of the second CoIn. This CoIn is responsible for the ionic bond cleavage. Again, the experimental value of 124 fs is very close to the result of the 2D wavepacket propagation.

The two dynamical calculations show that both channels given by the two CoIns are indeed active on the ultrafast time scale. They lead to the two distinct products, the benzhydryl radical and the benzhydryl cation. It is most likely from the potential topology that the radical is produced at a slightly earlier time than the cation.

Conclusion. The following overall picture of the photo-initiated processes in DPMC evolves. The system (wavepacket) accelerates from the FC-point upon optical excitation, but it stays in the shallow minimum for some tens of femtoseconds. The atomic motion is not describable by a single normal mode, but a truly multidimensional motion develops. At close to 100 fs the weak potential barrier is crossed and now the homolytic bond cleavage happens. The experiment suggests a time of 80 fs for the appearance of the radical pair in the electronic ground state. The remaining part of the wavepacket in the excited state proceeds to the second CoIn and at 125 fs ion pairs are generated. This cooperative picture of highest temporal resolution and sensitivity measurements, thorough analysis and high level quantum chemical and dynamical calculation clearly establishes that the ultrafast photochemistry with two product channels is due to wavepacket motion through two distinct conical intersections. The relative reaction yield depends on the detailed motion of the wavepacket and the position of the CoIns. A traditional rate model of two competing stochastic processes cannot explain the dynamics and branching ratio. For many other systems with two ultrafast appearing products, a similar behavior can be expected and a deviation from the traditional rate models will be needed for a correct description.

3.2 Strong-pulse double-pump coherent spectroscopy of perylene orange

Introduction. Transient pump-probe spectroscopy is a four-wave mixing (4WM) process that measures the third-order susceptibility $\chi^{(3)}$ of the system under investigation. The first two interactions with the electric field of the pump pulse generates excited molecules while the third interaction with the probe field generates the 4th signal wave that is either in phase (stimulated emission and ground state bleach contribution) or out of phase (excited stat absorption) with the probe field. 4WM time-resolved spectroscopy pump-probe spectroscopy is nowadays widely employed to explore the electronic and/or vibrational dynamics of molecular chromophores [Muk95, Zim97, Ren01, Osk08]. The main goal of these experiments is to probe the material system and to learn about its intrinsic (unperturbed by external fields) dynamics. Therefore, comparatively weak laser pulses are traditionally used in 4WM spectroscopy. Nevertheless, a number of interesting new effects have been detected in 4WM experiments when pulse intensities beyond the weak-pulse limit and therefore beyond the third-order response were employed.

For example, the transient absorption [Bit94, Ric08, Syt11] and the fluorescence quantum yield [Sch96, Ric07] of light-harvesting complexes revealed a nontrivial dependence on the intensity of the pump pulse. Vibrational wavepackets in multiple electronic states of $CH_2I_2^+$ have been detected in a strong-field ionization pump-probe experiment [Gei10]. Strong-pulse phenomena were also observed in 4WM experiments. The most important experiments are the nonlinear heterodyning in femtosecond rotational degenerate 4WM [Mat03], pulse-strength-dependent three-pulse photon echo peak-shift of semiconducting single-walled carbon nanotubes [Gra08], manipulation of Liouville pathways in multiply resonant coherent multidimensional spectroscopy [Wri11], observation of triexciton quantum coherences in quantum wells [Tur10]. Experimental strong-field control of the molecular population transfer [Ger96, Bar97, Sch11a] and other photophysical and photochemical processes (see [Sch11a, Rab00, Wol11, Ohm09, Sil09, Pro11] and references therein) has been demonstrated. Single molecule femtosecond spectroscopy requires also strong pulses [Hil11].

In principle, a whole series of nonlinear 4WM, 6WM, ..., NWM measurements can be performed within a single experiment using a pair (or triple) of strong and phase-locked pump pulses. By increasing the strength of the pulses, the contributions from 6WM and higher order processes into the measured signal can be amplified [Kue09, Kue11]. Experiments with strong phase-locked pulses are hoped to allow us to retrieve more information on the material system than traditional weak-pulse 4WM techniques. On the other hand, the complexity of strong-pulse

responses makes their interpretation challenging and requires adequate theoretical support.

In the following chapter the investigation of the strong-pulse double-pump single-probe (2P1P) signal for the molecular dye perylene orange (PO) in solution with sub-13 fs visible pump pulses is described. Our experiment is conceptually related to the pioneering time-domain "double-slit" experiment of Scherer et al [Sch91, Sch92]. Since publication of these seminal papers, similar experiments have been performed on alkali atoms and polyatomic molecules (see [Ohm09, Cin08] and references therein), sometimes in the strong-pulse regime (see [Sch11a] and references therein). The present work can be viewed as a generalization of these studies to polyatomic molecules with multiple Franck-Condon (FC)-active modes in the condensed phase.

Experimental setup. The experimental setup is depicted in Fig. 3.2.3a. The two pump pulses are generated by a NOPA [Rie00]. The spectrum is centered at 530 nm and is compressed by a combination of a prism compressor and Brewster-angled chirped mirrors [Bau06]. This combination can compensate nearly all orders of dispersion introduced by the optical components between the NOPA and the sample. The pulse length was measured by an autocorrelator [Koz04] to 11.7 fs (FWHM), which is within 6 % of the Fourier limit.

In order to generate pairs of phase-locked pulses with a variable time delay, we use a Michelson interferometer (MI). The beam splitter is a 2.5 mm thin fused silica substrate with a broadband dielectric coating. The reflectivity is about 60 %. A similar substrate, but without coating, is used in the other arm to introduce the same amount of dispersion in both arms. The overall intensity ratio of the two pump pulses is 50:50. The delay is dynamically adjusted by moving the end mirror with a piezo-electric displacement stage in order to control the interpulse delay Δt. Rapid scanning is beneficial for reducing noise; this is why a sawtooth driving voltage is used to scan a full delay range of about 175 fs in about 6 s.

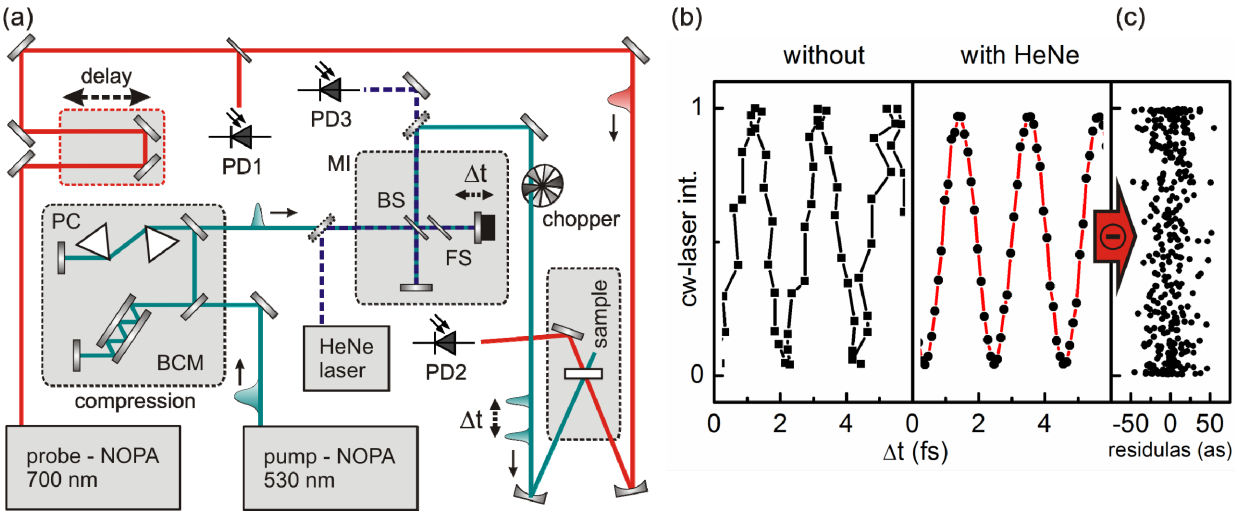

Fig. 3.2.2. Double-pump single-probe (2P1P) setup. (a) Schematic of the experimental setup. MI: Michelson interferometer; NOPA: noncollinear optical parametric amplifier; PC: prism compressor; BCM: Brewster angled chirped mirrors; BS: beam splitter; FS: fused-silica plate; PD: photo-diode. (b) Measurement of the interference of a second HeNe laser after the Michelson interferometer. Calibration of the time delay by the piezo's internal sensor (left) and with the aid of the calibration HeNe laser (right). (b) Deviations to an exact sinus are smaller than 20 as standard deviation.

The effective delay Δt was experimentally determined for each single laser pulse at 1 kHz repetition rate. This is achieved by combining the readings from the transducer's resistive displacement sensor with an interferometric measurement by a monochromatic calibration laser. The resistive sensor is accurate enough to determine the delay with a resolution of 0.3 fs, which is however not yet enough for a Fourier transform spectroscopy at visible frequencies. In order to improve the delay reading, we use a continuous-wave HeNe laser, which is incorporated into the Michelson interferometer in parallel, but laterally shifted by 2 mm with respect to the femtosecond laser beam. Both beams pass the identical optical components. The interferometric signal of the HeNe laser provides a sinusoidal pattern which allows determining changes of the delay. It is, however, required to identify the correct interferometric order. This is achieved by using the resistive sensor of the piezo-electric transducer, which is less accurate but capable of unambiguously identifying in which order of the interferometric signal the delay currently is. In total, this procedure provides a measurement of the femtosecond pulse pair's delay with an accuracy better than 50 as for every single laser shot.

We experimentally checked this procedure by using a second monochromatic laser (630 nm) instead of the femtosecond pulses. Fig. 3.2.2b shows the results. In the left part of Fig. 3.2.3b

the second laser's interference is plotted if only the resistive sensor is used; a significant noise contribution on top of Δt is evident. With the full procedure described above, an almost perfect interferogram is obtained (right part of Fig. 3.2.2b). The deviations to the perfectly sinusoidal pattern are plotted in Fig. 3.2.2c and amount to less than 20 as (standard deviation) over many minutes.

After the interferometer, the femtosecond pulse pair is focused into a flowing cell with a solution of the perylene dye. The two pulses are used as pump pulses with precisely determined temporal spacing and thereby relative optical phase. The pump pulse energy was adjusted with a metallic variable attenuator to cover the transition from weak to strong pulse interaction. Perylene orange was purchased from Exciton and dissolved in ethylacetate (99.8 % pure, Sigma Aldrich) with an optical density (OD) of 0.1 at the absorption maximum of 530 nm in a 120 μm thick home built flow cell [Meg09].

In order to probe the amount of excited molecules, a second femtosecond pulse from another NOPA is used at a delay of 5.5 ps with respect to the pump pulse that is not delayed by the piezo. The spectrum of the probe pulse is centered at 700 nm. There, the dye is transparent, but a strong absorption occurs in case of excited molecules. To provide a precise measurement of the transient absorption, the probe pulse intensity is measured before and after transmission through the flow cell with two photodiodes. In addition, every second pump pulse pair is blocked with a mechanical chopper wheel. In total, this allows excluding many components of the laser noise and provides a measurement of transient absorption with an accuracy of better than 10^{-5} [Sch08].

Spectroscopic characteristics of perylene orange. Perylene dyes are of particular interest in various applications like laser dyes [Rah97], light absorber and energy-transfer molecules in solar cells [Jan00, Rei01]. They are extraordinary suited due to a strong absorption in the visible, high fluorescence quantum yield ($\Phi_F \sim 100$ % [Rah97]) and high photo stability [Tan06a]. For the use as fluorescence molecules, saturable absorbers or as all-optical switches it is of special interest to understand the electronic level structure and photodynamics of the molecule.

The absorption and emission spectra of PO dissolved in ethylacetate is shown in Fig. 3.2.1a. The absorption spectrum shows a peaked structure that mimics the vibrational mode structure of the first electronic state S_1. The fluorescence spectrum is the mirror image of the absorption spectra indicating that the vibrational structure of the ground state is very similar to the S_1 state.

In addition the spectra are nearly independent on the solvent used. The small Stokes shift between the absorption and emission spectrum leads to the conclusion that due to their symmetry these molecules exhibit no significant static dipole moment neither in the electronic ground nor in the excited state.

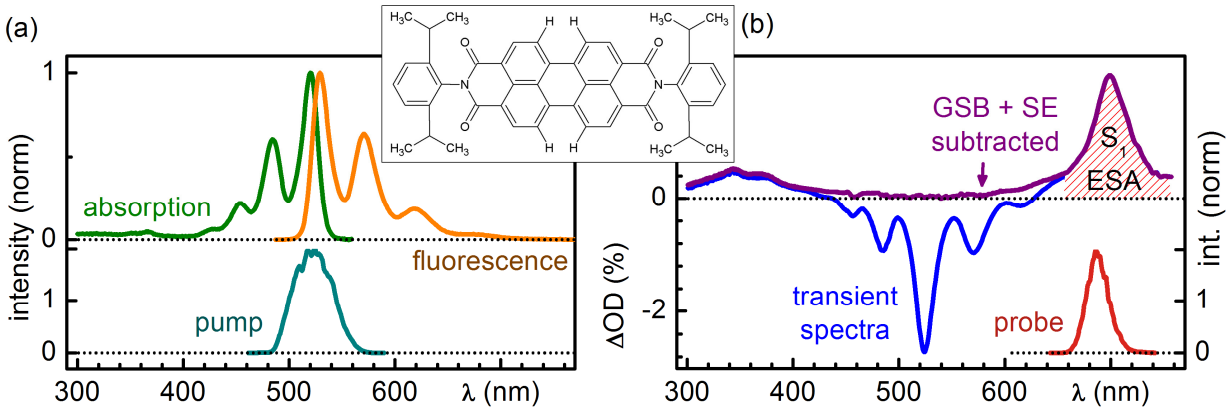

Fig. 3.2.1. Spectroscopic characteristics of perylene orange (PO). (a) The spectral intensity distribution of the pump overlays with both the absorption and emission spectra of PO. (b) Transient absorption measurement of PO dissolved in ethylacetate for a pump-probe delay of 200 ps. When the ground state bleach (GSB) and stimulated emission (SE) contribution is subtracted from the transient spectra, minor excited state absorption (ESA) remains at the pump wavelength. The probe spectral intensity distribution overlaps with the strong S_1 ESA contribution.

The pump spectral intensity distribution is tuned to the wavelength of the peak of the lowest vibrational mode of the S_1 state. The check if there is a significant excited state absorption in the vicinity of the probe wavelength after excitation, a transient absorption measurement with broadband white light supercontinuum probing [Meg05] was performed. The transient spectrum for a pump probe delay of 200 ps is shown in Fig. 3.2.1b (blue line). After excitation into the S_1 level PO shows excited state absorption bands in the UV as well as at 700 nm. The negative ΔOD in the spectral range of 400 – 650 nm is assigned to a combination of ground state bleach and stimulated emission. This signal contribution stays constant for the hundreds of ps measured in the experiment which is in perfect agreement with the excited state lifetimes of a few ns reported in the literature [Kal01].

To elucidate whether there is a significant amount of excited state absorption in the spectral region of the pump pulse the steady state absorption and emission spectra, equally scaled in intensity, were subtracted from the transient spectrum and the residual spectrum is shown in

Fig. 3.2.1b (purple line). This procedure is justified because for long delays the PO molecules are vibrational relaxed and are trapped in the S_1 state [Kal01]. From the residual spectrum it can be concluded that there is only a negligible excited state absorption from the S_1 state to higher lying electronic states present at 530 nm. This result is important for the strong-pump pulses applied later on because it shows that multiphoton processes strongly favor a pump-dump cycle (to the ground state) over an excitation to higher lying electronic states. This is in agreement with quantum chemical calculations endorsing that PO can be seen as an electronic two-level system (S_1 and S_0) when absorbing in the visible spectral region [Ald07].

Simulation background. Theoretical simulations where performed by Dr. Maxim Gelin in the group of Prof. Dr. Wolfgang Domcke (Technische Universität Munich, Germany) that allow to link the signal contributions of the measurements to the molecular dynamics of PO. Calculations in the strong-field limit are far more delicate than calculations in the weak field limit. It is nowadays common to use simplifications of the quantum mechanical light-matter interaction. When comparing the experimental with the theoretical results these simplifications have to be kept in mind. Therefore, a short review of the most important parameters used in the calculations is given in the following.

The theoretical formalism to simulate the 2P1P results is described only conceptually in the following. The chromophore is assumed to be an electronic two-level system with the two dominant FC-active vibrational modes. The Hamiltonian describing the total system consist of the bath (environment) Hamiltonian, the chromophore Hamiltonian and an interaction Hamiltonian. The dynamics of the primary system (chromophore) is described by the density matrix formalism that allows incorporating the light-mater interaction in a master equation [Ren01]. The 2P1P signal is treated within the strong-pulse doorway-window approximation [Gel11a]. The 2P1P signal is measured as a function of the interpulse delay Δt of the two pump pulses. It is proportional to the long-time population of the first excited electronic state. The signal amplitude is therefore equivalent to the total (frequency-integrated) fluorescence from the excited state [Sch91, Gel02]. The signal can then be divided into population and coherence contributions,

$$S(\Delta t) = S^{(p)}(\Delta t) + S^{(c)}(\Delta t)\,. \qquad (3.2.1)$$

Δt is the delay between the two pump pulses. $S^{(p)}(\Delta t)$ reflects the dynamics of vibrational wave packets in the ground and excited state and describes the sum of the intensities arising from these two states. This contribution yields the strong-pump strong-probe signal considered in

[Gel11b] and does not require phase-locked pulses. This contribution exhibits (for underdamped FC-active modes) pronounced beatings due to vibrational wavepacket motion.

$S^{(c)}(\Delta t)$ reflects the time evolution of the coherences between the ground and excited state and describes the interference of the signals arising from these two states. It is responsible for the evolution of electronic coherences and vanishes when the two pump pulses are not phase-locked. $S^{(c)}(\Delta t)$ exhibits fast oscillations with the optical frequency of the pump ω_p, depending on the phase difference $\Delta\Phi$ between the pulses, and is sensitive to the optical dephasing.

To identify the FC-active vibrations in the S_1 state of PO, the equilibrium geometries and harmonic vibrational frequencies in the S_0 and S_1 states were determined by density functional theory (DFT) calculations with the BP86 functional and the SVP basis set using the TURBOMOLE package [Ahl89]. As indicated by the DFT results, two FC-active underdamped vibrational modes are included in the Hamiltonian describing the system. The vibrational Hamiltonians are assumed to be harmonic. The vibrational frequencies are taken as $\tilde{\nu}_1$ = 534 cm^{-1} (0.066 eV, vibrational period of 62.4 fs) and $\tilde{\nu}_2$ = 1260 cm^{-1} (0.156 eV, vibrational period of 26.5 fs). The calculated ground state and excited state frequencies differ by merely 0.6 % ($\tilde{\nu}_1$) and 1.9 % ($\tilde{\nu}_2$). These differences result in negligible changes of the calculated signals and are therefore neglected. The dimensionless horizontal displacements of the minimum of the excited state potential energy surface from the minimum of the electronic ground state surface are chosen as $\Delta_1 = 0.6$ and $\Delta_2 = 1.0$. These values yield the best fit of the experimental signals. The calculated signals are not sensitive to changes of the displacements within ± 10 %.

The electronic dephasing rate was retrieved by comparing the experimental results with the calculations. The best correspondence is obtained for an electronic dephasing time of 16.5 fs. The pump wavelength is 522.6 nm, which corresponds to the carrier frequency ω_p = 2.37 eV and the optical period 1.74 fs. The experimental pulse shapes are well described by Gaussian envelopes

$$E(t) = \exp\left\{-4\ln 2\left(\frac{t}{\tau_p}\right)^2 - i\beta t^2\right\}. \qquad (3.2.2)$$

Here τ_p is the pulse duration (full width at half maximum of the electric field amplitude), and β is the linear chirp. The pulse duration is τ_p = 18.4 fs for non-chirped pulses ($\beta = 0$). The full width at half maximum of the intensity envelope is 13 fs which was measured with the aid of an intensity autocorrelator. For chirped pulses, τ_p = 63.6 fs ($\beta = \pm 0.003$ fs^{-2}).

The master equation is converted into matrix form by an expansion in terms of the eigenstates of the system Hamiltonian and is solved by the fourth-order Runge-Kutta integrator. The field-matter interaction is treated numerically exactly (see Ref. [Ego08, Gel09] for computational details).

With the aid of a theoretical model the absorption spectrum as well as the emission spectrum can be calculated. The results obtained by the theoreticians are shown in Fig. 3.2.3 by dashed lines and are compared with the experimental absorption (black line) and emission (red line) spectra. The overall agreement is satisfactory. However, a closer comparison reveals two evident drawbacks of the model: (i) The shape of the experimental spectra is approximately Gaussian, while the calculated spectra exhibit Lorentzian line shapes. (ii) The maxima of the experimental absorption and fluorescence spectra are shifted (the so-called Stokes shift), while the calculated spectra do not exhibit this shift (the emission spectrum peaks at the same wavelength as the absorption spectrum). The theoreticians have tried to improve the model by introducing inhomogeneous broadening. This allowed us to significantly improve the fits of the absorption and emission spectra, but resulted in a deterioration of the fits of experimental and theoretical time-domain transients (not shown).

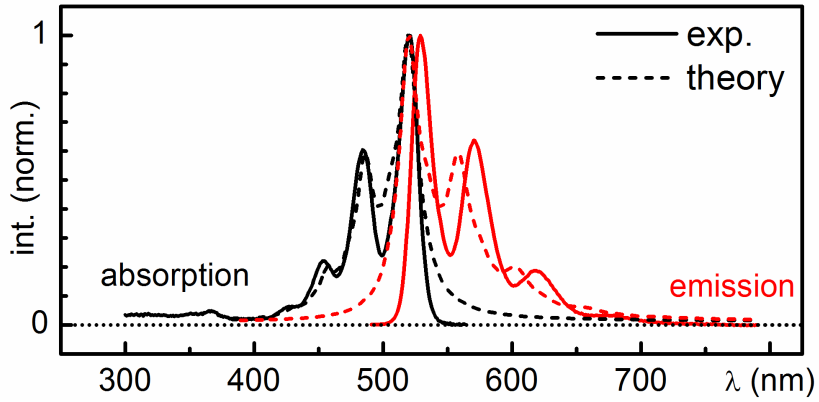

Fig. 3.2.3. Absorption (black lines) and emission (red lines) spectra of PO dissolved in ethylacetate. Experiment: Full lines. Simulation: Dashed lines.

The difference between the experimental and theoretical absorption and emission spectrum, being the missing Stokes shift, is a consequence of the simplification used in the theoretical formalism in the strong-field limit. By using the nonlinear response function formalism [Muk95] better results are possible. However, the response function formalism is based on perturbation theory in system-field interaction and becomes computationally expensive when higher-order terms become important. Its applicability in the strong-pulse regime is

questionable even from the fundamental point of view, leaving aside the issue of computational cost.

A potential extension of the equation-of-motion formalism applied in the present work would be its combination with the hierarchy approach, which yields a set of master equations which are valid for arbitrary system-bath coupling strength [Tan06b]. In this approach, which yet has to be developed, underdamped vibrational modes, overdamped vibrational modes, and nonperturbative system-fields interactions can be systematically treated.

Results for different pump pulse energies. At first, 2P1P measurements with low pump pulse energy were performed. To exclude that there are multiphoton processes contributing to the signal, separate measurements with only one pump pulse with variable pump pulse energy were performed beforehand. The result is shown in Fig. 3.2.4. The maximal achievable transient absorption amplitude, being the excited state absorption signal, is about 6 % for pulse energies of more than 200 nJ. For energies of less than 15 nJ, the excitation probability is in the linear regime. Therefore, for measurements with weak pump pulses (< 15 nJ) multiphoton processes can be neglected.

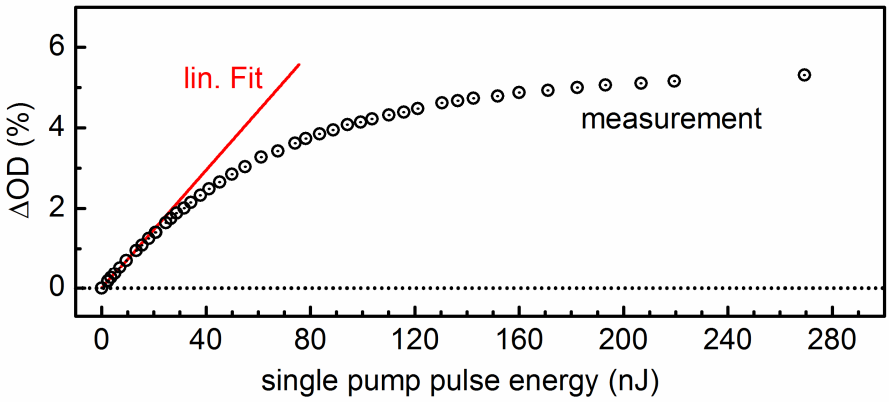

Fig. 3.2.4. Single-pump probe measurement of PO in ethylacetate for different pump pulse energies. The probe delay was set to 5 ps and monitors the excited state population which is proportional to ΔOD. The measurement shows the saturation of the amount of excited molecules for strong pump pulses. For pump pulse energies of less than 15 nJ one is still in the linear excitation regime.

The measured change in optical density (ΔOD) of the probe due to pumping with double pulses that have the same carrier envelope phase (for different interpulse delays Δt) is shown in Fig. 3.2.5a (red line). The measurement was done in the weak pump regime with about 2 nJ for each pump pulse.

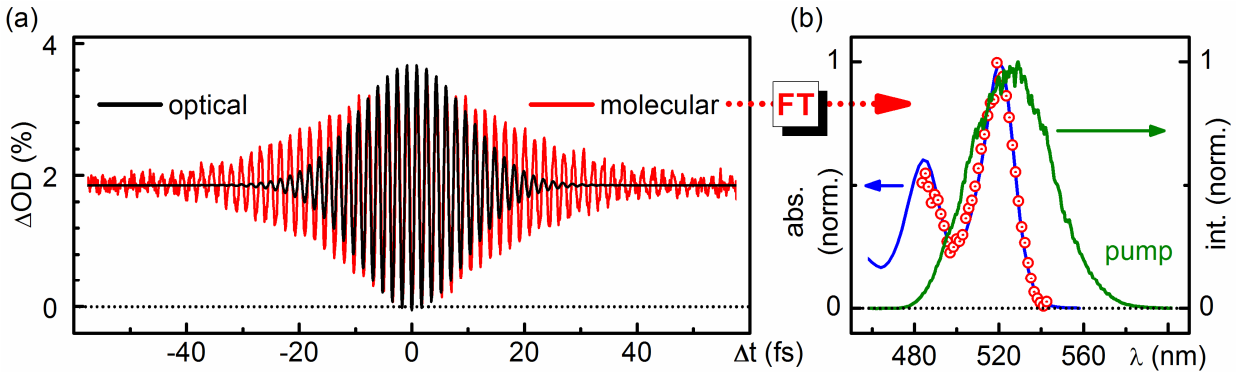

Fig. 3.2.5. Double-pump probe measurement of PO in ethylacetate in the weak pump regime (2 nJ). The probe delay was set to 5 ps and monitors the excited state population which is proportional to ΔOD. (a) The molecular response (red) shows a longer lasting coherence that the pure optical contribution (black). (b) The Fourier transform (FT) of the molecular response after deconvolution of the spectral intensity distribution of the pump (red circles) follows perfectly the molecular absorption.

The measured change in optical density is directly proportional to the number of molecules in the excited S_1 state. The double pulse scan shows fast oscillations with a period of $2\pi/\omega_p$ = 1.74 fs (522.6 nm). These fast oscillations are the consequence of the delay dependent amount of constructive or destructive interference of the electric field of the second pump pulse with the polarization induced in the molecule by the first pump pulse. The period of the oscillation corresponds to the central frequency of the absorbed part of the pump pulses, given by the convolution of the absorption and the pump spectra. The oscillating contribution vanishes for interpulse delays > 40 fs and the signal reaches a constant amplitude for longer delays. This decay is attributed to the molecular dephasing of the polarization induced by the first pump pulse. When the interpulse delay is larger than the dephasing time, the second pump pulse does not interfere any more with the induced polarization. Both pulses excite a constant amount of molecules to the S1 state independently. The molecular polarization lasts longer than the pure optical contribution.

This can be seen when calculating the first order autocorrelation function for the pump pulses which is shown as a black line in Fig. 3.2.5a. This contribution corresponds the pump intensity present at the sample for different interpulse delays, e.g., measured by a photodiode at the sample position. The pure optical signal contribution shows a faster decay of the oscillations than the molecular signal. From the difference of the decay times the electronic dephasing of

PO can be calculated to be 16.5 fs. This value will be verified later on by comparing theoretical simulations with the measured ones when using strong pump pulses.

The double-pump probe measurement in the linear excitation regime can be understood as a Fourier transform absorption spectrometer. The measured Δt scan is the time-domain representation of the absorbed part of the pump pulse spectrum in the frequency domain. Therefore, by dividing the Fourier transformed Δt scan by the pump spectral intensity distribution, the molecular absorption spectrum is retrieved (red dots in Fig. 3.2.5b). The perfect match of the retrieved and the separately measured absorption spectra illustrates the high quality of the measurements presented here.

Despite this "trivial" behavior in the weak pump regime, for strong pump pulses more complex signals arise, that allow retrieving more information about the molecular dynamics of PO. The 2P1P signals for different pump energies are shown in Fig. 3.2.6.

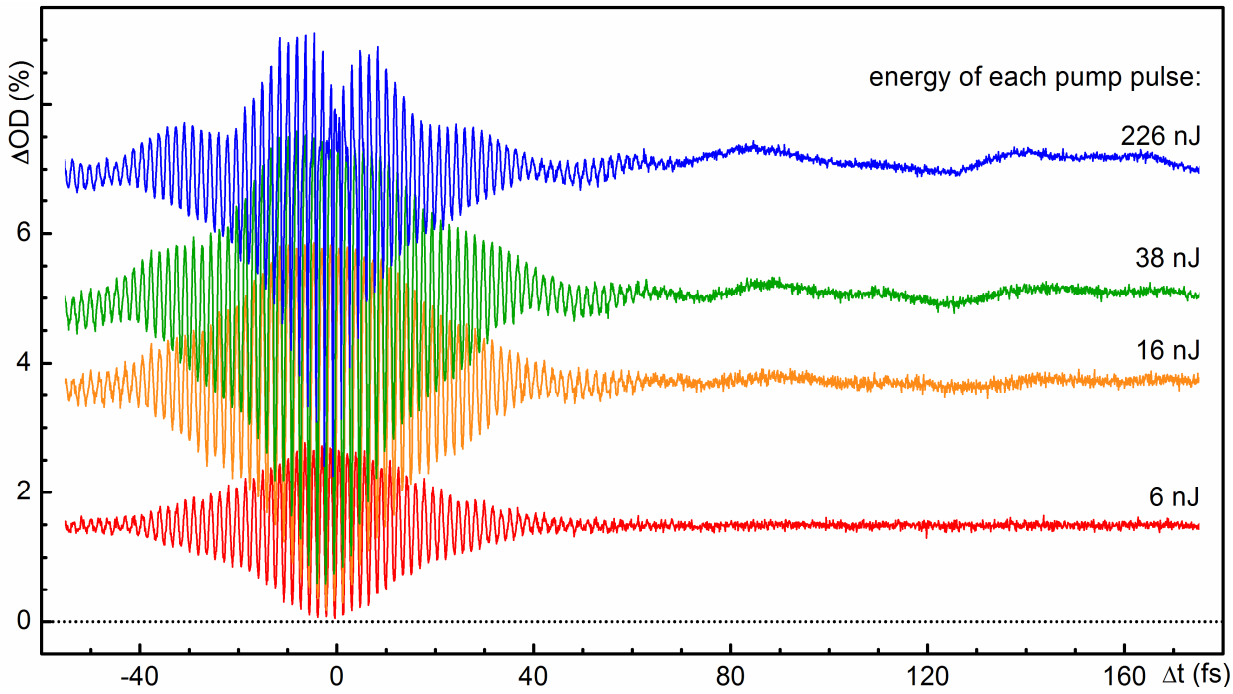

Fig. 3.2.6. Double-pump probe measurement of PO in ethylacetate for different pump energies. For increasing pump energies (individual pump pulse energy shown) the signal shows saturation effects for constructively interacting pulses (for 20 fs < Δt < 20 fs), an increasing amplitude for Δt > 40 fs and vibrational oscillations on the whole timescale.

For the analysis of the behavior of the 2P1P measurements one has to keep in mind that for a fixed pump pulse energy but decreasing Δt values, the overall pump energy impinging on the

sample increases for the delays when the electric fields interact constructively. The pulse energy values given here are the energy of a single pump pulse. The maximum pump energy is reached for $\Delta t = 0$ fs and is 4 times the single pump pulse energy and twice for $\Delta t \rightarrow \infty$. This is a consequence of the Michelson interferometer that transmits the full input pulse energy for constructively interfering arms ($\Delta t = 0$ fs) and half the input pulse energy split between the two temporally separated pulses for $\Delta t \rightarrow \infty$.

For the short-time perspective ($\Delta t < \pm 20$ fs) in Fig. 3.2.6, the maximum ΔOD amplitude for constructively interacting pump pulses is beginning to saturate for increasing pump energies. The signal amplitude does not reach twice the ΔOD value for non interacting pump pulses (e.g., $\Delta t > 100$ fs), as it is the case in the weak pump regime (Fig. 3.2.5). In this nonlinear pump energy regime parts of the excited molecules are dumped back to the ground state due to multiphoton processes and the population in the excited state decreases with higher pump intensities (when $\Delta t < 10$ fs, blue line, Fig. 3.2.6).

For the long-time perspective ($\Delta t > \pm 20$ fs) the signal shows modulations with periods of about 30 and 60 fs that match the frequencies of the vibrational modes in the excited state. Note that the vibrational oscillations are observed for changing the delay Δt rather than the pump-probe delay which is fixed to 5.5 ps where vibrational relaxation has occurred. Additionally, the probe pulse is long (150 fs) when compared to the period of the oscillations and thus does not resolve the wavepacket oscillations evolving on the pump-probe delay time. The observed modulations in the Δt-scan are a consequence of the interaction of the second pump pulse with the wavepacket generated by the first pump pulse that lead to amplitude modulations of the excited state population that is probed after 5.5 ps. For an interpulse delay in phase with the wavepacket oscillation, molecules can be effectively dumped back to the ground state, while for out of phase pulses de-excitation is less efficient and more molecules are in the excited state.

In the following sections the results will be discussed in detail from the long- and short-time perspective and are compared with the simulations.

Results for the short-time perspective. Qualitatively, the short-time behavior of $S(\Delta t)$ follows from Eq. 3.2.1.The short-time perspective of the excited state The population contribution is approximately constant on the short timescale, since the FC-active vibrations are essentially frozen for $\Delta t \sim 10$ fs. The time evolution of the 2P1P signal is thus determined by the coherent contributions $S^{(c)}(\Delta t)$.

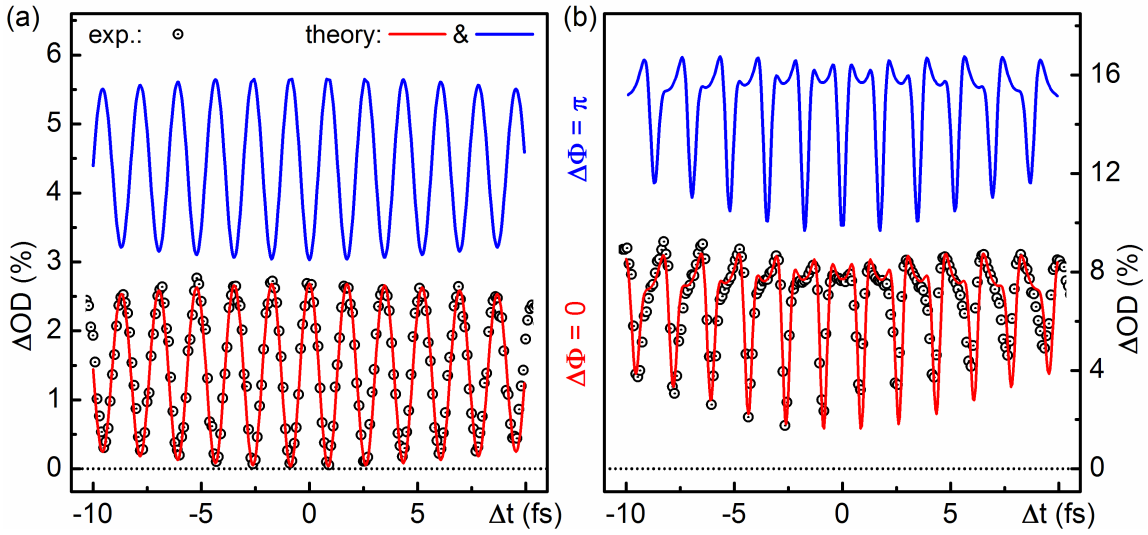

Fig. 3.2.7. Short-time behavior of the calculated (lines) and measured (dots) 2P1P signal for non-chirped pulses. Theoretical simulations of S(Δt) where performed for an interpulse phase ΔΦ = 0 (red) and ΔΦ = π (blue, up shifted for clarity). Weak (a) and strong pump pulses (b) with the respective single pump pulse energy 2 nJ (a) and 145 nJ (b).

Let us consider weak pulses first, for which the linear response description of the signal is correct. The experimental (black dots) and simulated (red & blue line) transients are presented in Fig. 3.2.7a. To understand their behavior, one can invoke the theoretical formalism. The formalism show that the signal exhibits damped (due to the optical dephasing) oscillations with a period of 1.74 fs. Mathematically the signal behavior is sufficiently described by the coherent signal contribution which can be written as

$$S^{(c)}(\Delta t) \sim \mathrm{Re}\exp\left\{-\left(i\omega_p - \Delta\Phi + \xi\right)\Delta t\right\}. \qquad (3.2.3)$$

ξ is the optical dephasing rate (1/ξ = 16.5 fs) and ΔΦ is the interpulse phase. ΔΦ can be understood as the difference in the carrier envelope phase of the two pulses.

One more aspect is instructive to discuss here. As has been pointed out in Ref. [Alb99], one can experimentally distinguish between the interpulse phase shift (ΔΦ) and the time delay (Δt) of optical pulses. In the present 2P1P experiment, the time delayed pulses are generated as identical replicas of the seeded pulse, hence the phase shift should be zero, ΔΦ = 0. It is thus interesting to check, if the phase shift can be extracted from the 2P1P signal. In the upper part of Fig. 3.2.7a, the simulated 2P1P signal S(Δt) for ΔΦ = π (blue line) while the experimental signal (black circles) is fitted with the simulated signal for ΔΦ = 0 (red line). The simulated

S(0) has maximum for $\Delta\Phi = 0$ and minimum for $\Delta\Phi = \pi$. On the other hand, the blue and red lines will coincide if we shift one of them by half of the optical period. The effect of the optical dephasing that follows the envelope of the decaying oscillations is negligible on this short timescale and can only give an approximate "zero time" with an accuracy of about 0.5 fs. Therefore the experimental "zero time" cannot be established precisely enough to extract information about the relative phase shift $\Delta\Phi$ of the pulses from the experimental weak-pulse 2P1P signal.

Let us now proceed beyond the linear response regime and consider the 2P1P signal induced by strong pulses (Fig. 3.2.7b). Again, the experimental and simulated $S(\Delta t)$ are shown by black circles and blue and red lines, respectively. The period of oscillations of $S^{(c)}(\Delta t)$ remains unchanged (1.74 fs) but the shape of the transients is no longer cosine-like. The reason is that the pulses overlap for $\Delta t < \pm 10$ fs, and the resulting Rabi cycling modifies the form of the transients. This behavior can best be seen for $\Delta t = 0$ fs, where the pulse energy is 4 times the given value. Then the amplitude of the signal is smaller than for $\Delta t \sim 1$ fs. A significant amount of molecules is dumped back to the ground state and do not contribute to the excited state population measured by the probe pulse.

The Rabi frequency Ω_0 can be calculated according to $\Omega_0 = \boldsymbol{\mu}\cdot\mathbf{E}/\hbar$ [Hil11], with $\boldsymbol{\mu}$ being the transition dipole moment (8 Debye, estimated from the absorption) and E being the laser field. For the total pump energy of 580 nJ (4 times 145 nJ) $\Omega_0 = 280$ THz. For a pulse length of 13.5 fs, the pulse area is about 5.3 rad. This is 1.7 times a π-pulse and corresponds to the nonlinear excitation regime where significant Rabi cycling back to the ground state is present. Therefore, the observed behavior is a combination of saturation effects due to the finite amount of molecules in the sample and the de-excitation due to Rabi cycling.

In Fig. 3.2.7b, we plot the simulated $S(\Delta t)$ for $\Delta\Phi = 0$ (blue line) while the experimental signal (black circles) is fitted with the simulated signal (red line) for $\Delta\Phi = 0$. As for weak pulses, the simulated S(0) has a maximum for $\Delta\Phi = 0$ and a minimum for $\Delta\Phi = \pi$. Now, however, the simulated $S(\Delta t)$ for $\Delta\Phi = 0$ and π are different and cannot be made coincident by a time shift of a half optical period. Therefore, the phase shift can be extracted from the 2P1P signal, but for strong pulses only. The comparison of the experimental and simulated signals reveals that the experimental pulses correspond to $\Delta\Phi = 0$. Since $\Delta\Phi = 0$, the pulses #1 and #2 are fully equivalent, hence the identity $S(\Delta t) = S(-\Delta t)$. Small violations of the symmetry in the measured transients are caused by experimental imperfections and have no physical significance.

Results for the long-time perspective. The long-time perspective allows retrieving information on the molecular dephasing and the vibrational dynamics. Fig. 3.2.8 shows a series of transients S(Δt) (experimental in black, simulated in red) for increasing pulse strengths. As has been mentioned above, the signal is symmetric with respect to the time origin, S(Δt) = S(-Δt). In all panels, the left side of the figure shows the experimental signal, while the right side shows the simulated signal superimposed on the experimental one. This presentation reveals most clearly the quality of the fit. The shape of the transients is seen to change significantly with the pulse strength. The weak pump signal (Fig. 3.2.8a, energy of 2 nJ) is determined by the linear response correlation function and contains, in principle, the same information as the linear absorption spectrum (see Fig. 3.2.5). Due to the strong optical dephasing, the signal can be fitted by the simple function $\mathrm{Re}\exp\{-(i\omega_p+\xi)\Delta t\}$. This situation is typical for polyatomic molecules in solutions [Muk95]: due to the strong (homogeneous and inhomogeneous) broadening, the linear response reveals the broadening rates.

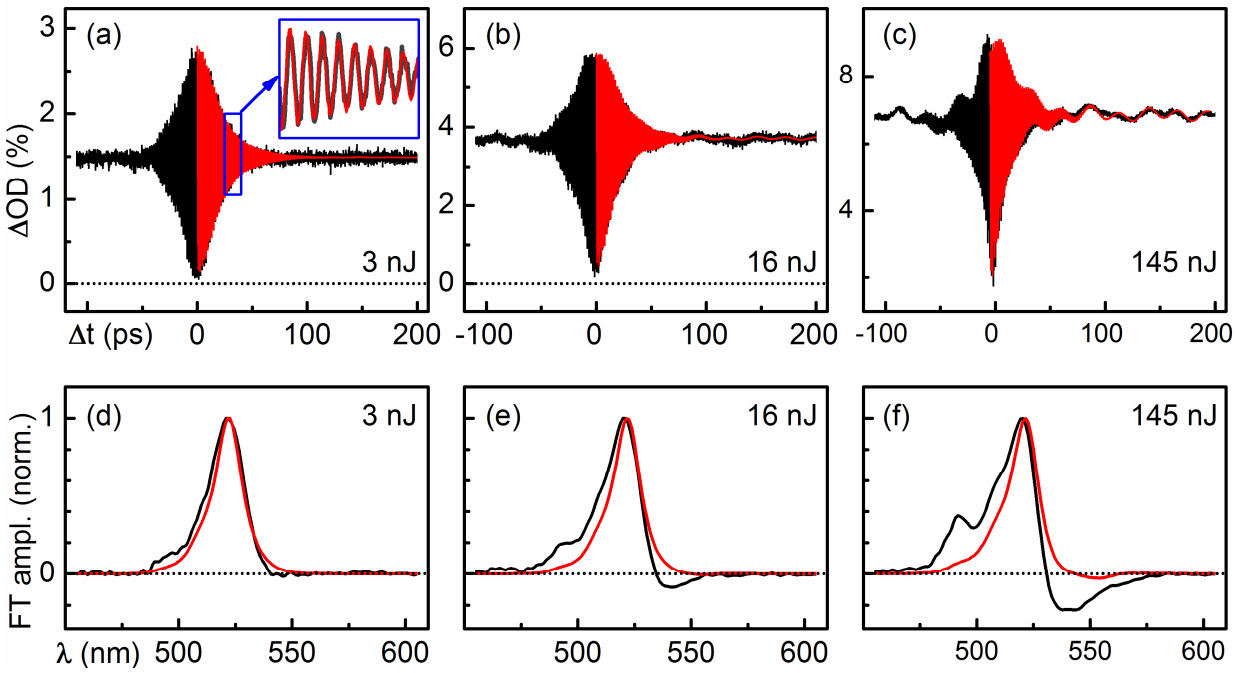

Fig. 3.2.8. Long-time behavior of the calculated (red) and measured (black) 2P1P signal for non-chirped pulses. (a-c) Measured and calculated signal amplitudes for different single pump pulse energies. (d-f) Normalized Fourier transform (FT) spectra of (a-c), respectively.

As the pulse energy increases, two qualitative changes appear (energy of 16 and 145 nJ): The central part of the signal narrows and the signal starts to exhibit vibrational beatings for $|\Delta t| > 50$ fs. Both FC-active vibrations manifest themselves in the beatings. The amplitude of the high frequency oscillations with the period $2\pi/\tilde{\nu}_2$ = 26.5 fs is modulated by the low-frequency beatings with the period $2\pi/\tilde{\nu}_1$ = 62.4 fs. This confirms that strong-pulse induced dynamics can compete with the relaxation and dephasing processes, amplifying the coherent vibronic responses. The phenomenon has been discussed in [Ego08, Gel09, Ban94] and references therein. To our knowledge, related strong-pulse effects were reported for the first time in Refs. [Ros89, Mat94]. In pump-probe experiments on NaI, an increase of the pump-pulse intensity resulted in pronounced oscillations of the signal, which were characteristic for the wavepacket motion of the excited NaI molecule.

The oscillatory vibrational responses in Fig. 3.2.8a (energy of 16 and 145 nJ) are not related to the electronic coherences of the system density matrix. Following the classification of W. H. Miller [Mil12], they can be considered as classical coherences. The electronic coherences decay on the timescale of the optical dephasing. Hence the signal resulting from the electronic ground and excited state populations dominates the 2P1P transients at times $\Delta t > 1/\xi$ = 16.5 fs. On this timescale the 2P1P signal is equivalent to the strong-pump strong-probe signal considered in Ref. [Gel11b].

For timescales shorter than the electronic coherence the strong pump pulses can induce multiphoton processes that manifest themselves as pump-dump-repump cycles. Note that the probe pulse does only measure the excited state population. Therefore, molecules that are dumped back to the ground state have to be excited again to be observable. The dumping of molecules back to the ground state is efficient for strong pump pulses here, because the pump spectral intensity distribution has a strong spectral overlap with the fluorescence spectrum (Fig. 3.2.1a), hence allowing for a significant dumping by stimulated emission. The influence of molecules that are dumped is best visible when looking at the real part of the Fourier transform spectrum of the measured 2P1P signal shown in Fig. 3.2.8b. The Fourier transform of the 2P1P signal represents the part of the pump pulse spectrum that is absorbed by the molecule. For increasing pump pulse energies the Fourier transformed spectra show negative amplitudes on the long wavelength edge. This contribution arises from the stimulated emission that is only present for the long wavelength edge where the fluorescence spectrum is present.

However, the Fourier transformed spectra of the **simulated** 2P1P signals only show weak negative amplitudes at the spectral position of the fluorescence. This is a consequence of the

simplifications used for the calculations. The absorption and fluorescence spectra used in the calculations (see Fig. 3.2.3) do not incorporate a Stokes shift. Additionally, the absorption spectrum has a significant contribution for the long wavelength part which is a consequence of the Lorentzian line shape. Therefore, the negative shoulder at the long wavelength part of the Fourier transform spectrum is reduced due to the incorrect absorption contribution when compared to the experiment. This indicates the limits of the theoretical formalism used so far.

Note that the absorption spectrum of PO (Fig. 3.2.1a) exhibits structures related to the high frequency mode $\tilde{\nu}_2$ only. The low-frequency mode $\tilde{\nu}_1$ has virtually no effect on the absorption spectrum. The strong-pulse 2P1P signal, on the other hand, clearly exhibits both frequencies (see Fig. 3.2.8c). The strong-pulse 2P1P spectroscopy thus amplifies the contribution of the mode with small FC factor.

Results for chirped pump pulses. Let us now consider the influence of the chirp on the 2P1P transients. In Fig. 3.2.9a-c (β = 0.003 fs^{-2}, positive chirp) and Fig. 3.2.9d-f (β = - 0.003 fs^{-2}, negative chirp) the long-time evolution of the signals is shown. The weak-pulse transients for both positively and negatively chirped pulses are virtually indistinguishable from each other and from the transients obtained without chirp (Fig. 3.2.8a, 2 nJ energy). The reason is that the shortest timescale governing the evolution of the signal is determined by the optical dephasing ($1/\xi$ = 16.5 fs) in this case.

Consideration of the signals obtained with stronger pulses reveals that positive and negative chirp influences the transients differently. Moderately-strong and positively-chirped pulses (Fig. 3.2.9a, left part) induce low-amplitude vibrational beatings, corresponding to the low-frequency mode ($2\pi/\tilde{\nu}_1$ = 62.4 fs). The simulations reproduce this effect fairly well. If the pulse strength is further increased, the vibrational beatings almost disappear. Moderately-strong and negatively-chirped pulses, on the other hand, result in the excitation of both the low- and high-frequency vibrational modes (Fig. 3.2.9b, left part). Simulations confirm this effect, which becomes more pronounced for stronger pulses. For both positive and negative chirps, the fits become progressively worse as the pulse strength increases (possibly due to the assumed harmonicity of the vibrational modes). The simulated S(Δt) in Fig. 3.2.9 (red lines) do not yield the best fit of the experimental results. However, they confirm the general trend, that is, the suppression (promotion) of vibrational beatings via positively (negatively) chirped strong pulses.

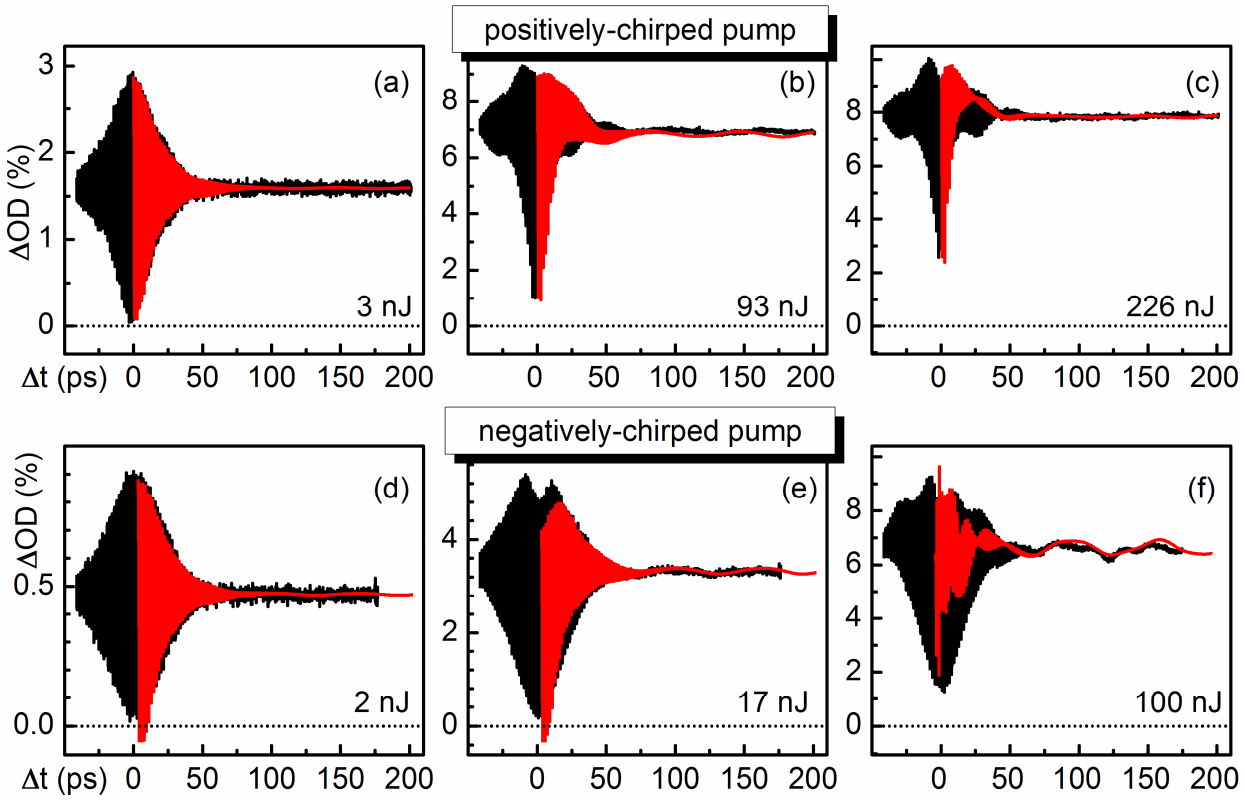

Fig. 3.2.9. Long-time behavior of the calculated (red) and measured (black) 2P1P signal for chirped pump pulses. (a) Positively-chirped pulses (β = 0.003 fs^{-2}) for weak (left) and strong (right) pump pulses. (b) Same as in (a) but for negatively-chirped pump pulses (β = - 0.003 fs^{-2}).

The chirped pulses used in the 2P1P experiments are approximately three times longer than those with non-chirped pulses. Their duration of τ_p = 63.6 fs measured with an autocorrelator is longer than the period of the high-frequency mode ($2\pi/\tilde{\nu}_2$ = 26.5 fs) but is comparable with that of the low-frequency mode ($2\pi/\tilde{\nu}_1$ = 62.4 fs). Therefore, only the low-frequency beating can be resolved with weak pulses. With strong pulses, on the other hand, both beatings become visible (see Ref. [Gel11b] for a general discussion of the related phenomena).

When using low energy excitation, it has been shown that chirping of the pump pulses does not have to influence the amount of population in the excited state but rather change the nature of the vibrational wavepacket prepared [Bar95]. However, for high excitation energy the amount of population in either the ground or excited state is influenced due to the interaction with more than one photon [Ger96]. After excitation, the non-equilibrium population in the potential energy surface of the excited state moves to lower energy due to the dynamic stokes shift and the vibrational motion. For a negative chirped pulse the incident frequencies follow that motion

and can resonantly lead to dumping via stimulated emission. Therefore the negative chirp facilitates the creation of wave packets in the ground electronic state [Ger96, Mis00, Mal05] accompanied by less excited molecules when compared to Fourier limited pulses. A positive chirp, on the other hand, can not resonantly follow the vibrational wavepacket motion and therefore favors the creation of wave packets in the excited electronic state accompanied by a high amount of population in the excited state. For strong pulses and multiple optically active modes, the situation depends on the interplay of the timescales of the system and the pulses [Sch11a, Wan10]. In addition, the FC factors play an essential role. Since the dimensionless displacements $\Delta_1 = 0.6$ and $\Delta_2 = 1.0$ of PO are not very large, the FC factors corresponding to the transitions between distant vibronic levels are small. This renders negatively-chirped pulses more efficient in exciting moving wave packets.

Conclusion. We have shown, both theoretically and experimentally, that strong-pulse spectroscopy with phase-locked double-pump pulses, 2P1P, allows us to retrieve more dynamical information from the system under study than can be obtained with traditional linear and third-order spectroscopies. By interrogating the molecular system via several Rabi cycles during the action of the pump pulses, highly nonequilibrium vibronic distributions in the chromophore can be purposefully prepared. These nonequilibrium distributions are less sensitive to bath-induced relaxation and dephasing processes than the distributions prepared in the weak-field limit. In this context, strong-pulse spectroscopies may be considered as realizations of two- (or multi-) dimensional correlation spectroscopies, where the strength (and the chirp) of the pulses can be regarded as additional correlation/control variables [Nod08].

The strong-pulse 2P1P signal can be considered as a superposition of a series of nonlinear N-WM (N = 2, 4, 6,…) spectroscopic signals (cf. Refs. [Wri11, Kue09, Kue11]) produced due to the (strong-pulse induced) wavepacket interference [Ohm09, Cin08]. The 2P1P signal can be split into population and coherence signals, $S(\Delta t) = S^{(p)}(\Delta t) + S^{(c)}(\Delta t)$. The former provides information on the relaxation and propagation of the wave packets in the ground and excited electronic states of the material system under study, while the latter contains information about the evolution of the electronic coherences of the system density matrix. 2P1P spectroscopy is a promising tool to unravel the condensed-phase dynamics of molecular chromophores possessing weak and damped FC-active modes and exhibiting strong electronic dephasing.

The robustness of the physical mechanisms governing the dissipative system dynamics in the strong-field regime indicates that coherent responses triggered by intensive phase-locked pulses are not specific for the particular chromophore PO, but are generic for sufficiently photostable

polyatomic molecules in solutions. It would be thus interesting to check, both experimentally and theoretically, if strong pulses can be applied to reveal even faster intramolecular electronic dynamics (due to, for example, conical intersections) in polyatomic species in the condensed phase. Feasibility of detection of photochemical processes by 2P1P spectroscopy also deserves to be studied.

The results of this chapter show that the strong field approach can identify molecular dynamics hidden in the low energy regime. In the context of this thesis, this approach is readily extendable to the field of 2D spectroscopy as the later technique also uses coherent double-pump pulses.

3.3 Quantum control spectroscopy of the proton transfer in HBT

Introduction. Accompanied by the growing availability of transient spectroscopy in the past decades the question arose whether the outcome of light-induced chemical reactions can be controlled by using tailored light [War83, War93]. Until now various successful coherent control experiments have been reported, e.g., the control the energy flow in light harvesting [Her02, Woh05], the optimization of nonlinear spectroscopy [Sil09] and the control of quantum phenomena in atoms and molecules [Rab00, Sha03, Nue07]. These control experiments are coherent in the sense, that the tailored light induces coherent electronic or vibrational wavepackets in the molecules that steer the outcome of the chemical reaction [Nue07]. Alternatively, the coherent excitations of multiple reaction pathways can lead to quantum interference that allows favoring one pathway over another [Sil09].

The tailored light pulses used in the first control experiments are chirped pulses [Bar95] and double pulses and pulse trains [Tan85, Tan86]. Multipulse excitation allows promoting or destroying vibrational or rotational wavepackets found in bound electronic states [Wei90, Buc08]. For many photoactive molecules the wavepacket motion plays a substantial role in the light-induced photoreaction. The selection of specific modes has been shown to influence the population transfer to different excited electronic states [Hau06, Buc08]. Quantum control spectroscopy (QCS) uses the control scheme to retrieve information about the molecular dynamics by using shaped pulses for excitation. In such an experiment, the molecular dynamics, e.g., measured by transient pump-probe spectroscopy, for transform-limited and shaped excitation are compared. This technique has proven to yield important results in the field of molecular vibrational dynamics and in photobiology [Buc06, Ter06, Rot09] but was demonstrated for the UV spectral domain only rarely [Möh12].

In this chapter, QCS is used to investigate the vibrational mode dependence of the UV light-induced proton transfer reaction in 2-(2'-hydroxyphenyl)benzothiazole (HBT). HBT is known to show an ultrafast intramolecular proton transfer in less than 40 fs after excitation of the enol form [Loc00, Loc03, Bar09] that is accompanied by a coherent skeletal deformation of the molecular structure [Wur00, Loc04, Sch08b]. The involved vibrational modes of the molecule are detectable in the transients of the stimulated emission of the keto product state [Wur00, Sch11b]. It has been suggested that a control of the vibrational modes in HBT should influence the proton transfer reaction, but an experimental investigation was still missing [Wur00].

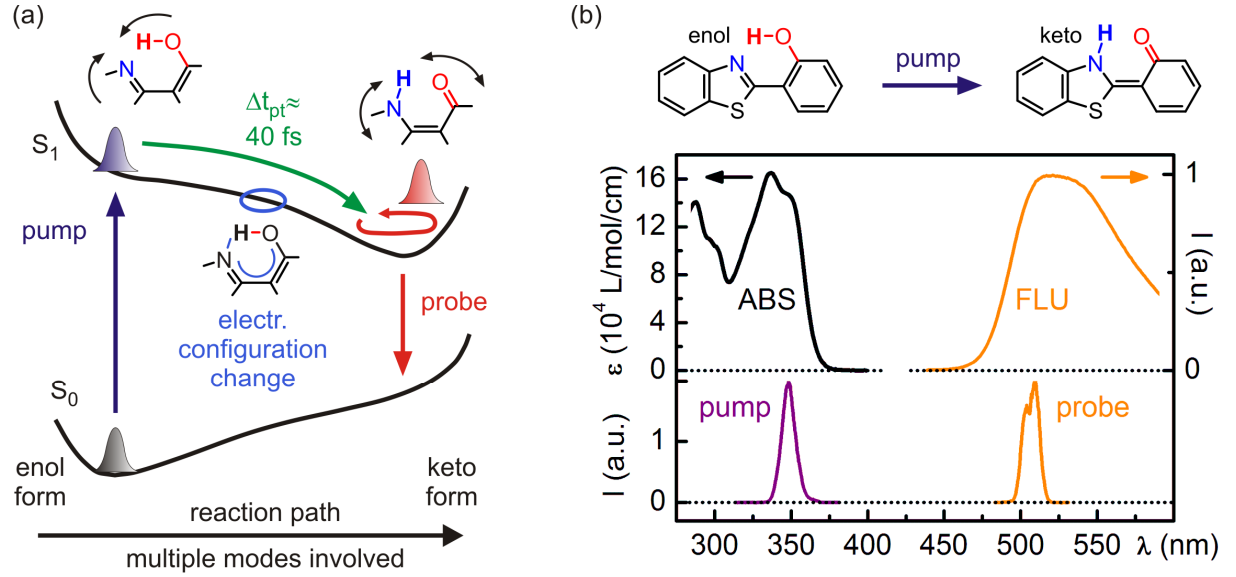

Fig. 3.3.1. Light-induced hydrogen transfer in 2-(2'-hydroxyphenyl)benzothiazole (HBT). (a) Reaction scheme describing the wavepacket motion leading to the time delayed (Δt_{pt}) product form after the proton transfer. (b) Chemical structure of the enol and keto form and the respective absorption and fluorescence spectra. The spectra of the pump and probe pulses used for the measurements is also shown.

The excited state intramolecular proton transfer after UV irradiation of HBT in solution was studied intensively by transient absorption measurement in the femtosecond domain. The retrieved understanding of the hydrogen dynamics are pictorially depicted in Fig. 3.3.1a.

After excitation, the excited state wavepacket evolves on the potential energy surface from the enol (educt) form to the keto (product) form in about 33 fs [Loc03]. This ballistic wavepacket motion is accompanied by a hydrogen transport from the oxygen atom to the nitrogen atom. The change of the bond of the hydrogen atom is accompanied by reaching the product potential energy surface which is adiabatically connected with the potential energy surface of the enol form. The product form shows a bathochromic shift of the fluorescence by roughly 200 nm with respect to ground state absorption of the educt. Theoretical calculations [Viv03] and experimental measurements [Wur00, Loc03] have shown that skeletal deformations of the molecule after excitation originate from vibrational modes of the molecule. The molecular dynamics are restricted to 4 main skeletal modes [Loc03]. After excitation, the H-chelate ring contracts due to an in-plane bending of the molecule which leads to a reduction of the hydrogen-nitrogen distance. For a certain progression of the excited state wavepacket, the electronic configuration is changed and the hydrogen-nitrogen bond is formed. In this new and displaced geometry (product) the molecule oscillates with the frequency of the vibrational

modes which have a large projection on the displacement [Loc03]. These modes are most prominent in the product stimulated emission contribution in transient absorption measurements. The lifetime of the product form is about 100 ps in cyclohexane which is long compared to the time scale investigated in this study (up to a few ps). From gas phase measurements, where the lifetime was measured to be about 2.6 ps, it was concluded that the internal conversion is mediated by an inter-ring torsional mode that is hindered strongly in solution [Bar09].

In summary, the excited state proton transfer in HBT after excitation with an ultrashort pulse is a strongly coherent process that is interlinked with the vibrational modes of the molecular structure. This makes HBT an ideal candidate for QCS by using double pulses to suppress or enhance certain vibrational modes by tuning the double pulse distance to match the period of the vibrational modes.

Experimental setup. The experimental setup to generate UV double pulses with defined interpulse delay is based on an UV Michelson interferometer. The setup is an UV adaptation of the Michelson interferometer based setup already described for the visible spectral domain in Chap. 3.2. Briefly, visible pulses with a Fourier limit of less than 15 fs and a central wavelength of about 700 nm are generated with a NOPA [Rie00]. Pulse compression of the visible pulses is done by a combination of Brewster angled chirped mirrors [Bau06] and a prism compressor. UV pulses are later on generated by frequency doubling the visible pulses with a typical energy of 2 µJ in a 50 µm thick BBO. The UV pulses with a central wavelength of about 350 nm and a pulse energy about 200 nJ have a Fourier limit in the order of 15 fs (Fig. 3.3.1b). To generate two phase stable UV pump pulses a Michelson interferometer with a dielectric coated fused silica beam splitter (1 mm thick) is used. An additional fused silica plate with the same thickness is placed in one arm of the Michelson interferometer to guarantee the same amount of dispersion for both arms. The end mirror of one arm of the Michelson interferometer is mounted on a computer controlled piezo to adjust the interpulse delay. The precise delay is measured by monitoring the interference of an additional continuous wave laser that is parallel but laterally shifted to the pump beam. The pulse length of the UV pulses was measured for both pulses with a ZAP-SPIDER [Bau04b] and the measured pulse length was minimized by optimizing the prism compressor in the visible. The pulse duration of the pump pulses was measured to be 20 fs (FWHM) and the typical pulse energy is in the order of 40 nJ at the sample. An aluminum coated spherical mirror was used to focus the pump beam to a focal diameter of about 150 µm. Typically 3 % of the molecules are excited by one pump pulse. This

guarantees that even for two pump pulses the excitation probability is still in linear regime.

The visible probe pulses are generated by a second NOPA. The central wavelength was tuned to 505 nm where the stimulated emission contribution of the keto product form of HBT is present (Fig. 3.3.1b). The probe pulses are compressed with a prism compressor and the pulse duration was measured with an autocorrelator [Koz04] to be 42 fs (FWHM). A delay stage in the probe beam allows changing the pump-probe delay. The spectrally integrated probe intensity was measured after the sample spectrally integrated by a photodiode. The change in optical density due to pumping was measured by chopping the pump. To increase the signal-to-noise ratio, the probe intensity fluctuations were measured additionally before transmission through the sample (details see Chap. 2.4 and [Sch08]). The temporal resolution of the experiment was about 55 fs, given by the cross-correlation between the pump and the probe pulse.

Measurement results. At first, the transient dynamics of the stimulated emission of HBT dissolved in cyclohexane were measured by using only one pump pulse for excitation. The polarization between the pump and the probe pulse was set parallel. For measurements done in the magic angle configuration, similar results were obtained. The result for the first few ps is shown in Fig. 3.3.2a together with the fit of the data based on a model that contains the signal contributions described in the following.

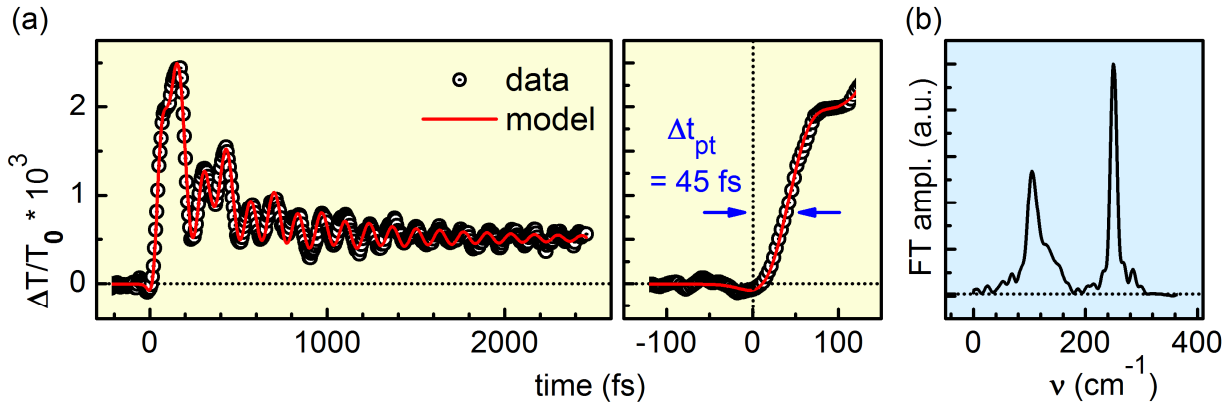

Fig. 3.3.2. Transient absorption measurement of HBT dissolved in cyclohexane with 55 fs temporal resolution. (a) Transient of the stimulated emission contribution at λ_{probe} = 505 nm. The delay (Δt_{pt}) of the appearance of the product (keto form) was determined to be about 45 fs. (b) Fourier transformed amplitudes of the vibrational oscillations visible in (a).

The zero time delay was calibrated by measuring a cross-correlation when both pump pulses are active beforehand with an uncertainty of about ± 10 fs. The transient dynamics of the stimulated

emission contribution shows a delayed rise (Δt_{pt}) of about 45 fs, which is in accordance with the 35 fs reported in the literature [Loc03], when considering the uncertainty of the measurement here. This time delay is assigned to the excited state wavepacket motion leading to the formation of the keto product form. The measured transient curve is composed of population dynamics as well as vibrational modes leading to the observed oscillations. The population dynamics appearing delayed with respect to Δt_{pt} are composed of a weak excited state component together with a stronger stimulated emission contribution which is constant on the timescale measured here [Loc03]. The fast decrease of the signal strength in the first hundreds of femtoseconds is due to vibrational cooling of the product that shifts the stimulated emission contribution to lower frequencies [Loc03]. The oscillatory components originate from vibrational wavepackets [Loc03]. The Fourier transform of the residual oscillatory components of the transient curve after subtraction of the population dynamics is shown in Fig. 3.3.2b. The two major components are about 113 cm^{-1} and 255 cm^{-1} which is in perfect agreement with earlier measurements and theoretical calculations [Loc03, Viv03]. There are also two other weak contributions at about 289 and 528 cm^{-1}, which are of lesser importance for the QCS here.

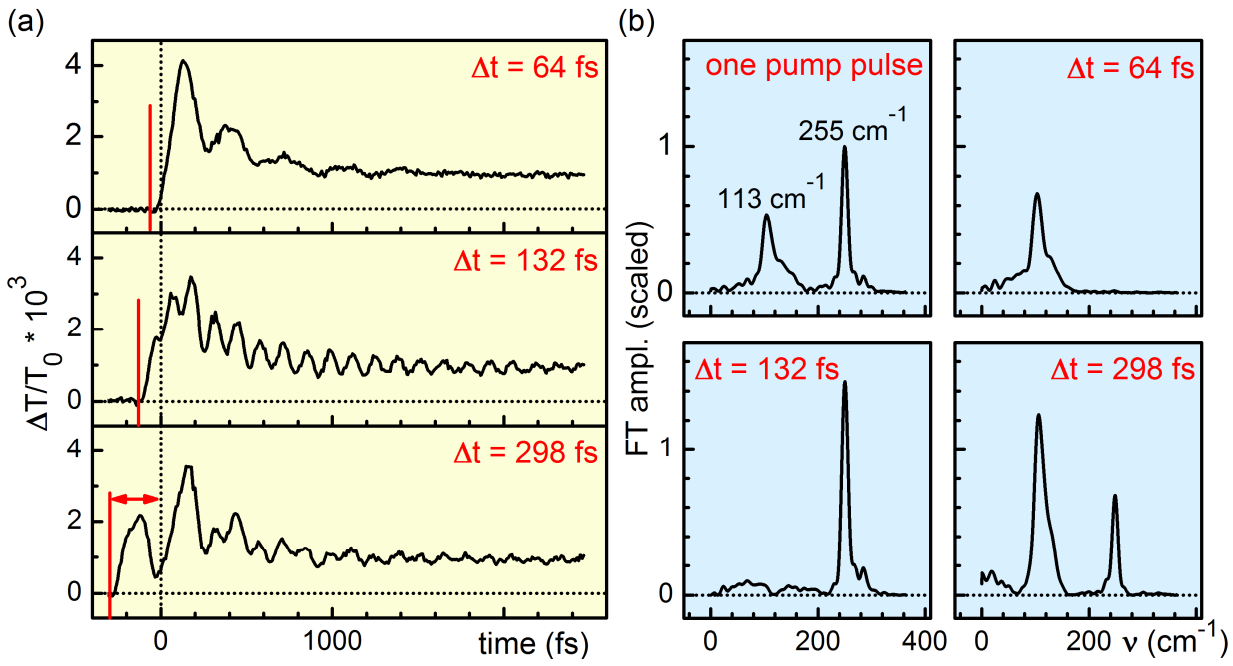

Fig. 3.3.3. Transient measurements of HBT with double pulse excitation. (a) Stimulated emission contribution (λ_{probe} = 505 nm) measured for different interpulse delays (Δt) of the two pump pulses. (b) Fourier transform of the vibrational oscillations contributions of (a). The amplitudes of the Fourier transform spectra are scaled with respect to the measurements done with only one pump pulse.

The transient measurements are in perfect agreement with previous results [Wur00, Loc03]. As mentioned earlier, the observed vibrational modes are of major importance for the proton transfer reaction because they mediate the proton transfer reaction by bending the molecular structure to reduce the hydrogen-nitrogen distance. The next step is to use two pump pulses with a defined interpulse delay. The interpulse delay is related to the period of the vibrational modes involved, thus allowing to enhance or to suppress the vibrational wavepackets. The measured transient curves done with double pulse excitation for different interpulse delays (Δt) are shown in Fig. 3.3.3a. After subtraction of the population dynamics the residual oscillatory contribution was Fourier transformed and the resulting spectra are shown in Fig. 3.3.3b.

To make the amplitudes of the Fourier transform spectra for double pulse excitation comparable with the amplitudes when only on pump pulse is present, the spectra for double pulse excitation were divided by a factor of 1.85. This value originates from the pulse energies of the two pump pulses which were measured to be (43 ± 1) nJ and (36 ± 1) nJ. The later energy value corresponds to the delayed pump pulse. This difference in the pump pulse energy originates from the beam splitter used in the Michelson interferometer which splits the pulses with an energy ratio of about 46:54. From the time traces and the frequency spectra of the oscillations it becomes obvious, that for the different interpulse delays the oscillation contributions could indeed be enhanced or suppressed. For $\Delta t = 64$ fs the high frequency contribution at 255 cm^{-1} could be suppressed completely. This is expected, as this delay corresponds to half of the oscillation period of this mode which is about 132 fs. The two pump pulses generate two wavepackets which are out of phase with each other and no vibrational oscillations are present any more. For $\Delta t = 132$ fs the amplitude of the 255 cm^{-1} contribution is enhanced, as the two wavepackets are now in phase with each other. The mode at 113 cm^{-1} is, on the other hand, strongly suppressed. This is due to the fact that the delay of 132 fs does roughly correspond to half of the time period of the 113 cm^{-1} mode, which is about 298 fs. Therefore, for an interpulse delay of 298 fs the amplitude of the 113 cm^{-1} contribution is enhanced. The contribution at 255 cm^{-1} is only slightly affected because this double pulse delay does not affect this mode as it is not a multiple integer of the time period of this mode.

Discussion. The measurements show that the amplitude of the vibrations in the transient measurements can indeed be controlled. From the point of view of the QCS approach the following question arises: Is the change in the vibrational amplitudes a coherent intramolecular process or is the observed behavior only a macroscopic effect. The latter can be understood as the overlay of multiple not-interacting molecules that are excited by either the first of the

second pump pulse. Hauer et al. showed that the use of multipulse excitation can coherently control not only the amplitudes of oscillations in the molecule Nile Blue but also the amount of population transfer [Hau06].

To check whether the double pulse excitation also coherently controls the population dynamics, the measured transient curves for single pulse and double pulse excitation were compared. To do that, the fit of the single pump pulse data (red line in Fig. 3.3.2) was taken and a time delayed version of this fit (scaled by 0.85 due to the lower intensity of the second pulse) was added to reproduce the double pulse measurements (data not shown). As a result, the double pulse measurements do perfectly match the summed curves for all individual interpulse delays. This means, that no coherent control of the population amount or dynamics by applying double pulse excitation was achieved.

At the first glace, this seems to be in contradiction to the expectations, namely, that a control of the vibrational modes that are interlinked with the proton transfer due to a bending of the molecule, should change the reaction process itself. However, the proton transfer reaction can be understood as a wavepacket motion that happens within 35 fs (45 fs measured here) after excitations. This time is roughly a quarter of the time period of the 255 cm^{-1} mode and even faster than the shortest interpulse delay measured (64 fs). The excited state wavepacket therefore leaves the Franck-Condon region in even less than 30 fs and the second pulse can not coherently interact with the excited molecules any more. Along the reaction path the potential energy surface of excited state reduces in energy [Viv03] thus the frequency of the second pump pulse is not in resonance any more. The change in vibrational oscillations of the product state can therefore be understood as a macroscopic effect rather than the coherent control of the vibrational modes of the educt after excitation to the first excited state.

This result is in agreement with previous coherent control measurements performed on a related UV absorbing molecule. Möhring et al. measured the double proton transfer molecule (2,2'-bipyridyl)-3-3'-diol by applying UV pulse trains and chirped pulses for excitation [Möh12]. Despite the observed change of vibrational oscillations in the transient spectra no change in the population dynamics could be observed.

In conclusion, the QCS approach used here could show that the control of the vibrational modes of the light-induced proton transfer reaction of HBT was a macroscopic effect rather than a coherent control of the vibrational wavepackets of individual molecules. Also the population dynamics of the reaction could not be controlled in any manner. This is a consequence of the

very fast (about 35 fs) coherent wavepacket dynamic of the product formation reaction itself. However, the experiment show that the temporal width of the control window, the time between the first interaction with the pump and the time after that there is no control possible by a second pulse, is less than ~ 50 fs. This shows that not only the control of the vibrational modes involved in the reaction are of importance but also the complete picture of the reaction has to be taken into account when trying to control and understand an ultrafast chemical reaction.

In principle the interpulse delay could be reduced to even less than 50 fs. However, the experimental setup described here did not allow fixing the interpulse phase of the respective electric field to a specific value for long time operation. As an example, having a delay of 32 fs and an interpulse phase of $\pi/2$ should destroy the wavepacket while it propagates on the excited state potential energy surface. Then the proton transfer reaction should be affected by stopping the ring bending mode that mediates the hydrogen transfer by reducing the hydrogen-nitrogen distance. With the acousto-optical pulse shaper introduced in Chap. 2.1 such an experiment is feasible. However, in accordance with the results in literature [Möh12], it is most probably necessary to have sub-10 fs UV pulses to achieve a measurable control effect in the transient spectra. 7 fs UV pulses were already demonstrated by using achromatic-frequency doubling of a broadband NOPA [Bau04a]. The combination of this technique with the shaping capabilities of the acousto-optical pulse shaper is on its way to completion at the time this thesis was written.

4. Collinear 2D spectroscopy in the UV

Similar to transient absorption (pump-probe) spectroscopy, two-dimensional (2D) spectroscopy aims at the determination of the third-order optical response function of a quantum-mechanical system [Bri04a, Bri04b]. The additional dimension in 2D spectroscopy, when compared to probe-frequency resolved transient absorption spectroscopy, is given by the excitation-frequency resolution. The real part of a 2D spectrum, in a simplified picture, can be understood as an excitation-frequency resolved pump-probe spectrum at one pump-probe delay [Fae99, Jon03]. Additionally to the excitation-frequency dimension the imaginary part of a 2D spectrum measures dispersive features of the system. The measured excitation-emission frequency correlation resolves congested spectra and provides ultrafast structural and dynamical information like intra- or interchromophoric couplings in the off-diagonal peaks of a 2D spectrum [Tia03, Hoc07, Hun09]. This allows direct visualizing vibrational and electronic energy transfer pathways or couplings [Bri05, Zig06, Gin09, Lew12], charge transfer processes [Bix12] and dynamics of chemical reactions [Muk00, Cho08, Ogi09]. The shape of diagonal peaks reveals the ratio between homogenous and inhomogeneous broadening [Fae99], which can be used to characterize the interaction with the surrounding.

2D spectroscopy has been implemented successfully in the IR and visible spectral range [Ham98, Bri04a]. The extension of this technique into the UV spectral range has alluring prospects [Can12, Wes12]. However it represents a major challenge because the available methods for the generation of broadband UV pulses are technically quite demanding. First 2D-UV experiments used the Fourier transform approach[1] either in the partial collinear geometry [Tse09, Tse12] or in the boxcar geometry [Sel10, Wes11]. In both cases the FWHM bandwidth of the pump pulses was limited to <10 nm (in the mid-UV). This is typically not broad enough to cover prominent absorptive features of most UV absorbing chromophores, e.g., biologically relevant DNA nucleotides or amino acids [Her04]. To cover a large part of the absorption bands of DNA nucleotides, a bandwidth of more than 20 nm is desirable.

An alternative approach to measure broadband 2D-UV spectra was recently proposed by Chergui and coworkers [Aub12]. Pump wavelength resolved transient spectra were measured by scanning the frequency of the narrowband pump pulse. However, this measurement is limited to retrieve only the absorptive part of the 2D spectrum. Additionally, a small bandwidth

[1] The Fourier transform approach refers to experimental techniques where the interpulse delay between two pump pulses is scanned and the excitation-frequency axis is afterwards retrieved by Fourier transformation.

of the pump of less than 1.5 nm is needed to achieve adequate spectral resolution. This inherently limits the achievable time resolution which was reported to be in the order of 300 fs.

4.1 Principles of collinear 2D spectroscopy

Femtosecond 2D spectroscopy can be realized experimentally by two most used types of geometrical layouts. The first one is a fully noncollinear design, where e.g., three noncollinear ultrashort pulses are used for excitation. This arrangement is referred to as the boxcar geometry [Bri04b]. The other layout which has gathered major attention in the last years is the (partially) collinear geometry, which is also called shaper-assisted geometry. This geometry has two main advantages. First, the phase stability between the electric fields of the two pump pulses is inherently given when a pulse shaper is used. Second, the probe pulses can easily be exchanged by another pulse with different frequency range compared to the pump pulse, e.g., a white light supercontinuum for broadband detection [Mye08].

In femtosecond collinear 2Dspectroscopy two collinear ultrashort pulses are used as pump and a noncollinear probe pulse measures the systems response (Fig. 4.1.1). Experimental realizations were first demonstrated in the IR [DeF07, Gru07], afterwards in the visible [Mye08] and UV [Tse09]. The first pump pulse generates a superposition between the ground and excited state which is accompanied by a macroscopic polarization in the system. For a two-level system where there are no higher lying optical-addressable states the second pulse (delayed by the coherence time τ) converts this superposition into a populative state (either the ground or excited state) [Cho06]. The third (probe) pulse arrives after the population time T and generates a superposition leading to a photon echo and a free induction decay signal. The emitted signal field contains the desired information of the system.

Due to the phase matching conditions $k_s=k_1-k_2+k_3$ (non-rephasing) and $k_s=k_2-k_1+k_3$ (rephasing) the emitted field is collinear with the wavevector of the probe beam (k_3) because $k_1 = k_2$. Consequently, due to the partially collinear geometry the probe pulse automatically heterodynes the emitted field for phase sensitive detection [Shi09]. Phase sensitive detection allows distinguishing between emissive (stimulated emission) and absorptive contributions (excited state absorption).

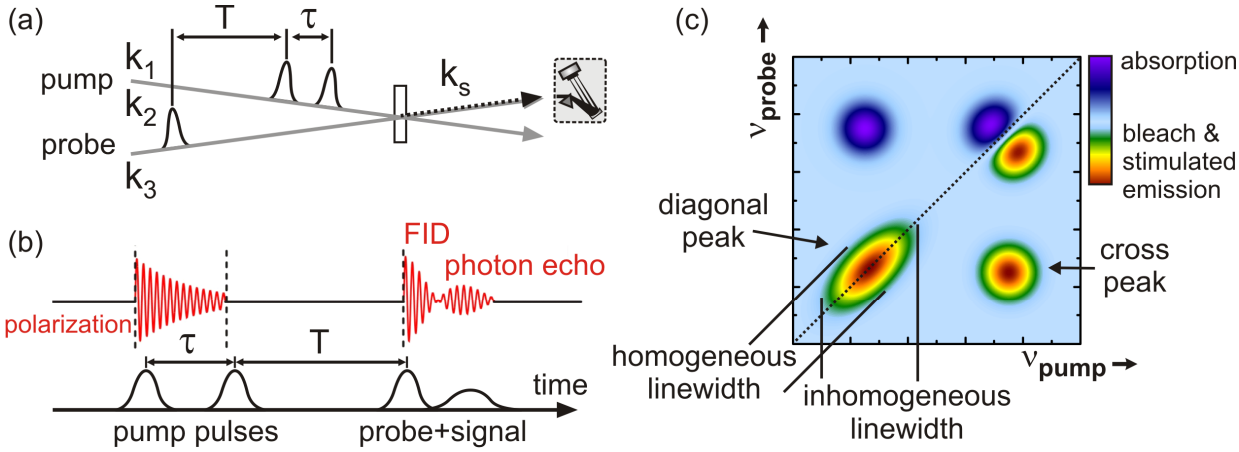

Fig. 4.1.1. Principle of collinear 2D spectroscopy. (a) Layout of the partially collinear geometry. The coherence time τ is scanned and the systems response is heterodyned with the probe and spectrally resolved in a spectrometer. Fourier transformation along τ retrieves the excitation-frequency axis. (b) Timing diagram of the three incident pulses. The polarization induced in the sample is shown in red. FID: free induction decay. (c) Nomenclature of the contributions in a fictive 2D spectrum, adapted from ref. [Cho06].

The idea of collinear 2D spectroscopy is to vary the timing of the incident electric fields in a systematic manner to retrieve the full third-order optical response function of the system: For a fixed population time T the delay τ is scanned and the resulting probe spectra are measured in the frequency domain by a spectrometer. Fourier transformation along the τ delays in 2D spectrum. The achievable time resolution with respect to the population delay T is given by the convolution of the pulse length of the pump and probe pulses. The spectral resolution is on the other side given by the inverse of the maximum coherence delay τ scanned. Therefore, the spectral and temporal resolution of a 2D experiment is automatically decoupled.

The real part of the complex valued 2D spectrum represents the absorptive part and the imaginary component is the dispersive part. Both parts contain the rephasing and non-rephasing contributions of the molecular response[2]. As mentioned earlier, these two contributions have different phase matching conditions with respect to the interaction with the wavevectors of the two pump pulses.

For the folded boxcar geometry where the two pump pulses are not collinear, the rephasing and

[2] Rephasing and non-rephasing contributions originate from different time-ordering of the interactions with the excitation pulses. The rephasing spectrum contains information of the rephasing of the induced dipoles in an inhomogeneous distribution of transition frequencies and is the photon echo signal. The non-rephasing spectrum contains contributions from free induction decay of the signals [Che08].

non-rephasing signals are emitted in different directions. However, when the time-ordering is reversed, e.g., the second pump pulse is now coming before the first one, the sign of k_1 and k_2 switch and the rephasing signal is emitted in the direction where the non-rephasing signal was before. This allows to measure the rephasing and non-rephasing signal separately which have to be phased and added correctly to retrieve the absorptive and dispersive 2D spectrum. Note, that separation of the 2D spectra into rephasing and non-rephasing components has been shown to provide dynamical information hidden in the purely absorptive or dispersive 2D spectra [Kha04, Che08, Tur11].

In collinear 2D spectroscopy, rephasing and non-rephasing signals are measured simultaneously as they are both collinear with the probe pulse because $k_1 = k_2$. Therefore the absorptive and dispersive 2D spectrum can readily be retrieved in this case. It is worth noting, that by phase cycling[3] the interpulse phase of the collinear pump pulses the rephasing and non-rephasing signals can be measured separately when desired [Gru07, Mye08, Zha12]. Double-quantum signals[4] are not discussed here, because for the partially collinear geometry they are only present when the last two pulses (the 2nd pump and the probe pulse) overlap in time which is typically not the case for the measurements presented in this work.

The absorptive 2D spectrum (Fig. 4.1.1c) has contributions which are usually referred to as ground state bleach, stimulated emission and excited state absorption [Gru07] similar to the contributions measured in transient absorption spectroscopy. However, due to the excitation-frequency resolution, the homogenous and inhomogeneous linewidth of the molecular absorption (e.g., in the ground state bleach) can be determined separately. The excitation-emission frequency correlation in the investigated system can be seen in the off-diagonal or cross peak contributions. When absorptive and emissive features spectrally overlap, complex signatures that change their sign along or in the vicinity of the diagonal can appear.

The following section describes the relevant theoretical formalism that illustrates the origin of the 2D signal and how it is retrieved in collinear 2D spectroscopy. It is not the aim to give a detailed description of the theory of nonlinear spectroscopy but to shortly review the formalism used further on in this chapter. A more detailed description of the theory of nonlinear spectroscopy can be found in the references [Muk95, Jon03, Cho08, Ogi09].

[3] The term phase cycling refers to a technique, where the interpulse electric field phase of the pump pulses is systematically modified to separate different signal contributions.

[4] Double-quantum signals originate from two quantum coherences generated by the interaction with the two pump pulses which evolve as a superposition state after the second pulse ($k_s=k_1+k_2-k_3$). They can be used to investigate excited state characteristics of the system [Kim09, Chr10].

Like pump-probe spectroscopy, two-dimensional spectroscopy is related to the third-order susceptibility χ^3. The signal detected in 2D spectroscopy is therefore related to the optically induced third-order polarization $P^{(3)}$ which contains the complete information of the third-order response of the system. This polarization is induced by three interactions with the incident electric fields, e.g., ultrashort laser pulses. In the time domain $P^{(3)}$ is a convolution of the third-order response function $R^{(3)}$ with the three incident electric fields $E_n(t)$. For the phase matched direction $k_s = k_3 = -k_1+k_2+k_3$ it reads as [Gru07, Tek10, Wes11, Tek12]:

$$P^{(3)}(\tau, T, t) = \\ = \int_0^\infty \int_0^\infty \int_0^\infty R^{(3)}(\tau_1, \tau_2, \tau_3) E_1^*(t - t_1 - \tau_1) E_2(t - t_2 - \tau_2) E_3(t - t_3 - \tau_3) d\tau_1 \, d\tau_2 \, d\tau_3 + \text{c.c.} \tag{4.1.1}$$

where $R^{(3)}(\tau_1, \tau_2, \tau_3)$ is molecular response function of the system that is zero for negative times, t_n are the arrival times of the pulse envelope maximums and τ_n are the positive valued times the system interacts with the electric fields (Fig. 4.1.2).

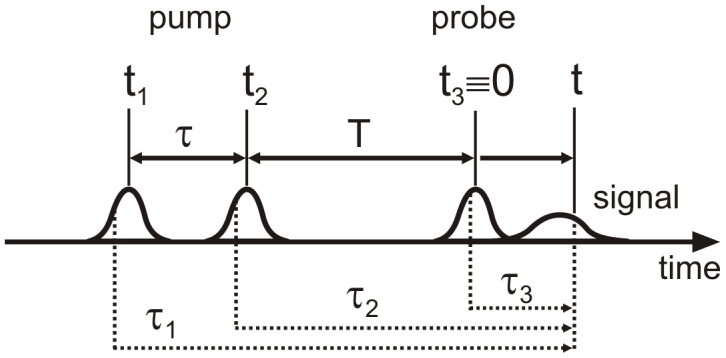

Fig. 4.1.2. Timing diagram for the three incident electric pulses adapted from ref. [Tek10]. τ: coherence time, T: population time; t_n: arrival times of the maximum pulse envelopes; τ_n: times at which the system interacts with the electric fields; t: signal time after the last interaction.

The molecular response function contains all possible molecular response pathways, which are often pictorially represented by double sided Feynman diagrams [Muk95]. The variables τ and T are the population time and coherences times which are given by $\tau \equiv t_2 - t_1$ and $T \equiv t_3 - \max(t_1, t_2)$. The need for the two timing variables t_n, τ_n accounts for the fact that each electric field interaction can occur at any time within the pulse duration of each pulse. When the pulses overlap in time, they can interact with the system in any time ordering which

is taken into account in Eq. 4.1.1. $R^{(3)}$ contains all relevant information of the system like dephasing characteristics or population dynamics.

For collinear 2D spectroscopy with two pump pulses and one non-collinear probe pulse, $P^{(3)}$ itself becomes the source of an electric field $E_s^{(3)}$ which is emitted collinear with the probe pulse (k_3). Under perfect phase matching conditions in the rotating-wave approximation this signal field is then directly proportional to the third-order polarization [Fae99, Hyb01, Bri04b, Wes11]:

$$E_S^{(3)}(\tau, T, t) \propto \frac{i\omega_t}{n(\omega_t)} P^{(3)}(\tau, T, t)\,. \tag{4.1.2}$$

In typical 2D spectroscopy, $E_s^{(3)}$ is measured in the experiment and by using Eq. 4.1.2, $P^{(3)}$ itself can be calculated. Furthermore, 2D spectroscopy aims at measuring $E_s^{(3)}$ in the frequency domain. This is done by first retrieving the time dependence of $E_s^{(3)}$ and then converting the result into the frequency domain with respect to τ and t as explained in detail in the following.

For collinear 2D measurement two phase stable pump pulses are needed and the delay between the two pulses (τ) is varied in an experiment. The electric field of two Fourier limited pump pulses (E_1, E_2) needed in a 2D experiment can be written as:

$$E_{pump}(t, \tau) = E_1(t) + E_2(t) = \sqrt{I_1(t)} \cdot e^{-i\omega t} + \sqrt{I_2(t+\tau)} \cdot e^{-i\omega(t+\tau) - i\Delta\Phi}\,. \tag{4.1.3}$$

with I_1, I_2 being the intensity envelope functions of the pulses, e.g., $I(t) = e^{-t^2/2\sigma^2}$ for Gaussian pulses with a FWHM pulse duration of $2\sqrt{2\ln 2}\sigma$. ω is the central frequency of the pulse spectrum which is identical for both pulses and $\Delta\Phi$ is an additional interpulse electric field phase. Note, that Eq. 4.1.3 means, that a change of τ does shift the complete electric fields of the two pulses rather than only the pulse envelopes (Fig. 4.1.3a). This is identical to the double pulses generated by a Michelson-Interferometer as it was described in Chap. 3.2. This means, that the carrier envelope phase of the two pulses is not affected when changing the interpulse delay.

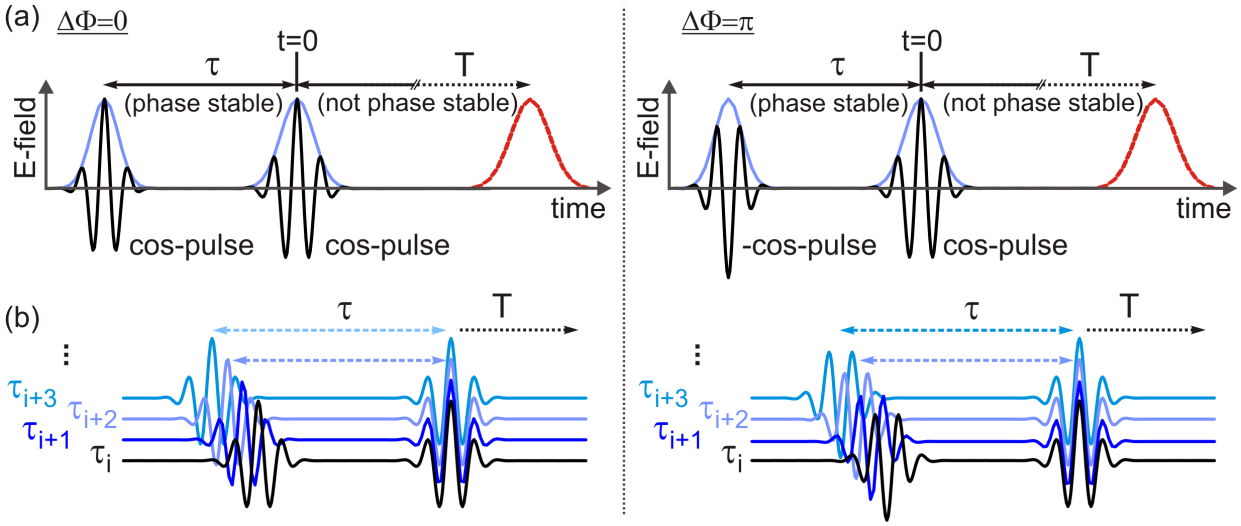

Fig. 4.1.3. Illustration of the electric field of the pump pulses. (a) Electric field of two Gaussian shaped cos-pulses with a phase stable interpulse electric field delay τ. On the right side, the interpulse phase ΔΦ was flipped by π leading to a -cos-pulse. The probe pulse comes after T. (b) Schematic of various τ delays. In a 2D experiment, τ is scanned.

The third electric field is delivered by an additional probe pulse, that can either be a replica of the pump pulse [Def07], a chirped supercontinuum [Tek09, Tek10] or a separately generated pulse, e.g., an additional NOPA [Mye08]. Due to the collinear geometry the probe pulse also acts as the local oscillator for the phase sensitive detection by heterodyning the emitted signal with a temporal delay between signal and local oscillator (i.e. the probe) which is known to be 0. When detected in the frequency domain by a spectrometer the resulting heterodyned signal is directly Fourier transformed with respect to the signal time t. The complete signal detected at the time integrating probe detector for $t > 0$ can then be written as [Gru07],

$$\mathrm{Sig}(\tau, T, \nu_{\mathrm{probe}}) \propto \left| \int \mathrm{d}t \left(E_S^{(3)}(\tau, T, t) + E_{\mathrm{probe}}(t) \right) e^{-2\pi i \nu_{\mathrm{probe}} t} \right|^2 . \qquad (4.1.4)$$

Note, that $E_S^{(3)}$ contains all possible molecular response pathways as given in Eq. 4.1.1. The measured signal already resolves the probe frequency dependence. To retrieve the pump frequency dependence of $P^{(3)}$ (respectively $E_S^{(3)}$) the τ delay between the pump pulses has to be scanned (Eq. 4.1.3 and Fig. 4.1.3b). Fourier transformation along the τ axis for each probe frequency then resolves the dimension of the pump frequency axis.

However, in collinear 2D spectroscopy the detected signal does not only contain the desired 2D information originating when each electric field interaction is happening with one of the three

different pulses (Eq. 4.1.1). Due to the collinearity of the pump pulses, there is also a transient absorption background. This contribution arises when the molecule interacts twice with the electric field of the same pump pulse (either E_1 or E_2) and is collinear with the 2D contribution. This is because such a phase-matched signal has the same wavevector as the 2D contribution, e.g., $k_s = k_3 = -k_1+k_1+k_3$. This contribution is given in equation 4.1.5, which can be obtained by inserting equation 4.1.2 into 4.1.4 when using equation 4.1.1:

$$\mathrm{Sig_{TA}}(\tau, T, \nu_{probe}) \propto \left| \int dt \left(R^{(3)}(\tau_1, \tau_2, \tau_3) \otimes E_n^* \otimes E_n \otimes E_{probe} + E_{probe} \right) e^{-2\pi i \nu_{probe} t} \right|^2, \tag{4.1.5}$$

where n is either 1 or 2. For clarity the convolution of the electric fields was abbreviated by $\otimes$ [5]. The transient absorption background does not show pump frequency dependence because it is independent of the interpulse delay τ. The 2D contribution arises when the molecule interacts once with the electric field E_1 and once with E_2 of the pair of pump pulses. This contribution is given in equation 4.1.6.

$$\mathrm{Sig_{2D}}(\tau, T, \nu_{probe}) \propto \left| \int dt \left(R^{(3)}(\tau_1, \tau_3, \tau_3) \otimes E_1^* \otimes E_2 \otimes E_{probe} + E_{probe} \right) e^{-2\pi i \nu_{probe} t} \right|^2. \tag{4.1.6}$$

The S_{TA} signal offsets the desired 2D signal. A separation of the 2D contribution from the S_{TA} contribution occurs already when the complete signal (Eq. 4.1.4) is Fourier transformed with respect to τ. However the S_{TA} background can cause ringing in the Fourier transform spectra [Shi09]. This is discussed with measured data in more detail in Chap. 4.2.2. To eliminate the transient absorption background the phase cycling scheme can be used. As can be seen from Eq. 4.1.5 and Eq. 4.1.6, the phase of the emitted electric field $E_S^{(3)}$ depends on the phase of the electric field of each pulse (E_1, E_2 and E_{probe}). However, from Eq. 4.1.5 one can conclude that the transient background does not depend on the interpulse phase of E_1 or E_2, while the 2D contribution is explicitly sensitive to this phase. Therefore, by flipping the interpulse phase $\Delta\Phi$ (Eq. 4.1.3) by an additional value of $+\pi$, the transient background signal does not change sign, while the 2D contribution changes sign. The transient background can therefore be effectively

[5] The convolution $\otimes$ is defined as $E_a(t) \otimes E_b(t) = \int_{-\infty}^{\infty} E_a(\tau) E_b(t-\tau) d\tau$ and is carried out for τ_1, τ_2, τ_3 for the individual pulses with arrival times t_i.

eliminated by measuring two different interpulse phases ($\Delta\Phi$=0 and $\Delta\Phi = \pi$) for each delay τ. The transient background free 2D signal $S_{2D}^{P(3)}(\tau, T, \nu_{probe})$ which is directly proportional to the third-order polarization (appendix A.II) can then be retrieved from the experiment by applying Eq. 4.1.7.

$$S_{2D}^{P(3)}(\tau, T, \nu_{probe}) = \frac{Sig(\Delta\Phi = 0) - Sig(\Delta\Phi = \pi)}{\omega_{probe}\, E_{probe}(\nu_{probe})} \qquad \boxed{\propto P^{(3)}} \qquad (4.1.7)$$

$E_{probe}(\nu_{probe})$ is the spectral electric field amplitude of the probe pulse which can be retrieved in the experiment by calculating the square-root of the probe spectral intensity distribution. Note that in collinear 2D spectroscopy due to heterodyning with the probe electric field, the measured signal is a multiplication with the probe spectral electric field amplitude which is taken into account by dividing through $\omega_{probe}E_{probe}$ [Jon03, Tek10]. The factor of $n(\omega_{probe})$ (Eq. 4.1.2) was neglected, as it has typically only a minor contribution [Bri04b].

To retrieve the frequency resolved 2D spectra $S_{2D}^{P(3)}(\nu_{pump}, T, \nu_{probe})$ the result of Eq. 4.1.7 has to be Fourier transformed along the coherence time τ according to Eq. 4.1.8. The real part of the Fourier transformation corresponds to the absorptive 2D spectrum:

$$S_{2D}^{P(3)}(\nu_{pump}, T, \nu_{probe}) = \mathrm{Re}\int S_{2D}^{P(3)}(\tau, T, \nu_{probe})\, e^{-2\pi i \nu_{pump}\tau} d\tau . \qquad (4.1.8)$$

It is crucial at this point to mention that there exist some inconsistency in the literature dealing with 2D spectroscopy, explicitly the proportionality of the reported 2D spectra when related to the third-order polarization: Some measurements done in the boxcar geometry show 2D spectra which are directly proportional to $P^{(3)}$ [Bri04b, Mil09]. For the collinear geometry, the measurements reported by Ogilvie and coworkers show 2D spectra which are heterodyned with the probe field and are proportional to $\mathrm{Re}(i\omega_{probe}P^{(3)}(\omega_{pump}, T, \omega_{probe})E^{*}_{probe}(\omega_{probe}))$ [Tek10, Tek12]. This proportionality is achieved when neglecting the $\omega_{probe}E_{probe}$ term in Eq. 4.1.7. The mentioned inconsistency is a consequence of the data acquisition and evaluation procedures used and can be avoided to make 2D measurements directly comparable independent of the measurement technique. However, both reported proportionalities of the 2D spectra are not directly comparable with transient absorption measurements that measure the change in optical density. When such a relation is desired it is necessary to retrieve the 2D spectra from the measured data in the correct way as will be described in the following.

It is important to keep in mind, that transient absorption spectroscopy is typically used to measure population dynamics of the investigated system rather than dephasing effects.

Comparing 2D spectroscopy with transient absorption is thus only possible when the 2D measurements are used to reveal excitation-frequency dependent population dynamics. When the population time T is larger than the dephasing of the molecular coherences (<100 – 500 fs in the UV [Zim97, Ajd08]), which is generally the case for the measurements presented in this work, the absorptive 2D spectra can directly be seen as a pump-wavelength resolved transient absorption measurement. Eq. 4.1.9 is used to calculate 2D signal amplitudes $S_{2D}^{\Delta OD}(\tau, T, \nu_{probe})$ which are directly proportional to transient pump-probe intensities ΔOD_{pp} (for details see Chap. 4.3.2 and appendix A.I&II).

$$S_{2D}^{\Delta OD}(\tau, T, \nu_{probe}) = \frac{Sig(\Delta\Phi = 0) - Sig(\Delta\Phi = \pi)}{\left| E_{probe}(\nu_{probe}) \right|^2} \qquad \boxed{\propto -\Delta OD_{pp}} \qquad (4.1.9)$$

Eq. 4.1.9 has to be Fourier transformed according to Eq. 4.1.8 and the real part is plotted to receive the absorptive 2D spectra $S_{2D}^{\Delta OD}(\nu_{pump}, T, \nu_{probe})$. The amplitude values of such a 2D spectrum are proportional to the amplitudes of conventional pump-probe spectroscopy but have the opposite sign. Note that the factor of ω_{probe} (Eq. 4.1.7) is not present in Eq. 4.1.9 to guarantee the desired proportionality with transient absorption spectroscopy (appendix A.I&II).

4.2 Experimental realization and data processing in collinear 2D-UV spectroscopy

A major advantage of 2D spectroscopy in the pump-probe geometry in comparison to the boxcar geometry is the simplicity of the experimental setup [Shi09]. By incorporating a pulse shaper to generate the phase coherent double pump pulses into a pump-probe setup, one gains the additional dimension of the spectrally resolved pump axis. Additionally, the advances and improvements made in pump-probe spectroscopy can directly be adapted for 2D measurements, e.g., the increase in signal-to-noise ratio by referencing for the probe intensity fluctuations.

4.2.1 Experimental setup

The setup for 2D ultraviolet spectroscopy is shown in Fig. 4.2.1. To generate tunable UV pump pulses over the whole UV spectral domain, the output of a visible NOPA is either frequency doubled (240 – 360 nm) or sum-frequency mixed with the CPA fundamental (300 – 370 nm) in a 50 μm thick BBO crystal [Koz03]. The prisms used in the prism compressor (PC) to temporally compress the chirped NOPA output pulses are made of fused silica and have an apex angle of 68.7°, so that the beam impinges in the Brewster angle configuration. The typical length of the prism compressor is about 60 cm. The polarization of the initially p-polarized (parallel to the surface of optical table) CPA fundamental and NOPA output leads to an s-polarized (perpendicular to the surface of the optical table) UV beam. The mirrors used for the UV beam are single-stack dielectric mirrors designed for the specific UV wavelength (bandwidth > 30 nm in the UV) to minimize reflective losses. A detailed description of all beam propagation distances and intermediate polarizations can be found in the appendix A.VI.

To further increase the bandwidth of the pump pulses they are spectrally broadened by SPM in a 1 mm thick CaF_2 crystal as described in detail in Chap. 2.2. Two dielectric coated Fused silica lenses (f=100 mm) are used to focus and recollimate the beam.

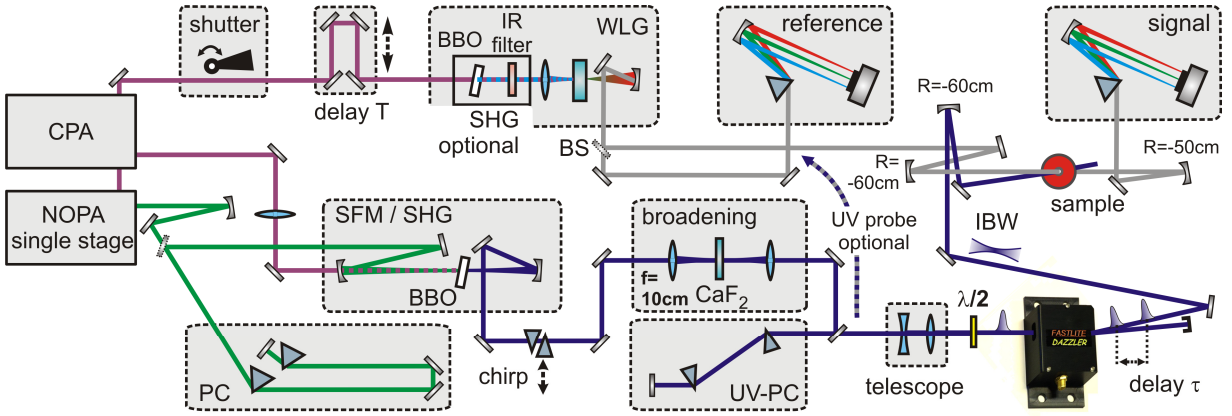

Fig. 4.2.1. Layout of the complete ultraviolet two-dimensional setup. BS: beam splitter, PC prism compressor, WLG: white light generation, IBW: intermediate beam waist.

The broadened pulses are compressed to nearly their Fourier limit with the combination of a UV-PC and the AOPDF (for details see Chap. 2.3). The UV-PC consists of two fused silica prism with an apex angle of 45° that have a dielectric anti-reflective coating (240 – 420 nm) to minimize reflective losses due to the s-polarization of the UV beam. The UV beam propagation distance between the two prisms is about 60 cm.

To achieve a clean spatial and temporal profile of the double pulses with the AOPDF, the geometric and Gaussian foci have to overlap at the sample position (for details see Chap. 2.1). This is achieved by the correct collimation of the beam entering the AOPDF with the aid of a telescope consisting of two fused silica lenses.

A λ/2-waveplate placed after the telescope is used to rotate the polarization to achieve the correct orientation for the AOPDF. Note, that instead of rotating the s-polarized UV beam to achieve p-polarization, the AOPDF can be rotates as well with adequate mechanical holders. The diffractive shaping process in the AOPDF itself rotates the polarization by 90°. The AOPDF generates the phase coherent double pulses with a variable delay. The double pump pulses with typical single pulse energies of 80 nJ are focused into the sample by a spherical mirror (R=-600 mm). The focal diameter is about 100 µm with a negligible astigmatism (< 5%) generated by the spherical mirrors. The excitation fluency was about $1.5 \cdot 10^{15}$ photons/cm^2 leading to a typical excitation probability of about 5 %.

For probing the molecular response one can either use a fraction of the UV pump pulse or a white light supercontinuum. The white light generated in a 4 mm thick CaF_2 crystal covers the spectral range of 290 -720 nm [Meg09] when generated with the CPA fundamental and 250 – 360 nm when generated by the second-harmonic of the CPA fundamental. The white light

continuum allows to probe the whole UV-visible spectral domain independent of the pump pulses used [Tek09]. Aluminum coated mirrors are used for steering the probe beam. The probe pulses transmitted through the sample are spectrally dispersed in a prism-based spectrometer. The prism spectrometer consists of a fused silica prism with an apex angle of 68.7° and the dispersed light is focused on the detection CCD array (Stresing Inc.) by a spherical mirror (R=-400 mm). The spectrally resolved intensity of each laser shot is measured at the full laser repetition rate of 1 kHz.

A fraction of the collimated probe beam before hitting the sample is separated by a beam splitter and measured in a second identical prism spectrograph. This allows using the single-shot referencing scheme of the probe by a second identical prism spectrograph (for details see Chap. 2.4). The beam splitter is a thin metal coated fused silica plate and the reflected part is used as probe in the sample. When using dielectric coated broadband beam splitters, the transmitted pulse should be used for probing the sample as it typically accumulated less higher-order chirp than the reflected beam. The probe beam is focused into the sample by a spherical mirror (R=-600 mm) to a focal diameter of about 50 μm in the sample.

For white light probing the wavelength calibration of the prism spectrograph is done by the procedure described in [Meg09]. In short, the spectral transmission characteristics of well known optical filters are used to evaluate the respective wavelength for each CCD pixel. However, in the case of probing with a fraction of the pump pulse the spectral features of such filters are spectrally not narrow enough to guarantee a precise calibration. In that case a narrow slit is placed directly in front of the CCD chip and the remaining spectral intensity for different positions of the slit along the spectrally dispersed light is measured. For the same positions of the slit, the transmitted spectra are measured with a fiber based spectrometer. This allows assigning each CCD pixel to a specific wavelength with a precision better than 0.1 nm.

It is instructive here to discuss the given experimental layout when using spectrally ultrabroad UV pulses generated by achromatic frequency doubling. This technique can generate UV pulses with Fourier limits well below 10 fs in the range between 270 – 380 nm [Bau04a]. When using such pulses, which can readily be shaped with the AOPDF, specially designed broadband dielectric coated UV mirrors should be used to minimize losses. The telescope has to be replaced by a telescope consisting of two spherical mirrors to avoid chirp and chromatic aberration. Astigmatism-free layouts for a spherical mirror based telescope are currently under development in the group.

The generation of double pulses by a pulse shaper has some advantages when compared to other techniques used for 2D spectroscopy. Other 2D spectroscopic techniques in the UV, visible or IR use diffractive optics [Mil09, Sel10], a Michelson-Interferometer [Vol05] or specially designed glass wedges [Bri12] to generate identical copies of the initial pump pulse. The first advantage of pulse shaper assisted 2D spectroscopy is that the two pump pulses are inherently phase stable (see next section) and there is no need for elaborate experimental techniques to guarantee the necessary phase stability, e.g., specially stabilized experimental setup [Zha05, Vol05]. The interpulse phase can be tuned independently from the delay, which is used for phase cycling. Another advantage is that the delay between these two pulses can be generated directly in the shaper without the need for additional optics. For double pump pulses which are generated by diffractive optics or collinearly with glass wedges [Bri12] the delay between the pulses is typically adjusted by the use of a variable amount of glass in one of the pump beams. This leads to a group delay between the two pulses but also introduces chirp in the delayed pump pulse. It has been shown for the visible that chirped pump pulses lead to distortions of the measured 2D spectra [Tek10], which makes this type of delay generation troublesome for the UV spectral domain as the dispersion is much more severe than in the visible or IR.

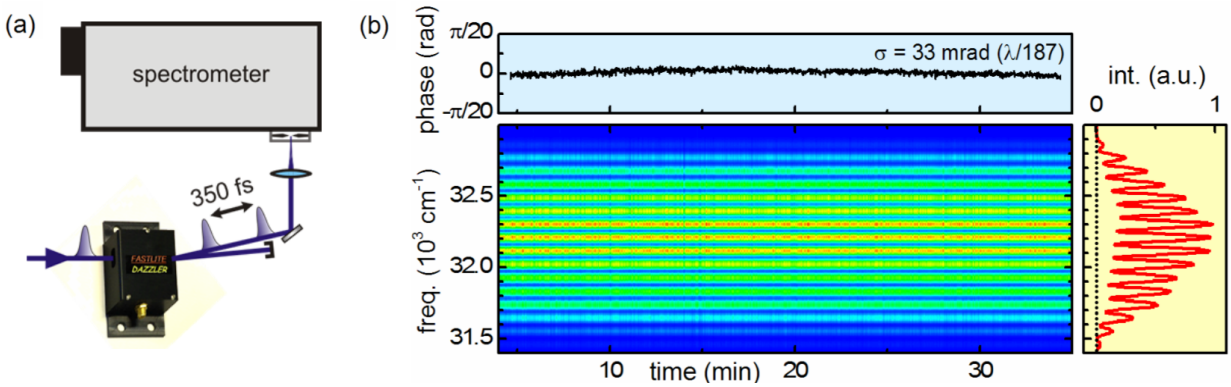

Fig. 4.2.2. Characterization of the interpulse phase stability of the pump pulses. (a) Schematic of the measurement layout. (b) Measured spectra and phase stability data with long-term standard deviation of λ/187.

To characterize the phase stability between the two pump pulses the spectral interference was measured in a spectrometer for an interpulse delay of 350 fs (Fig. 4.2.2). The phase deviation of an average of 75 laser shots was monitored over a period of half an hour. A slight systematic drift of the phase was observed on the long time scale which is attributed to a change of the beam pointing due to temperature deviations in the laboratory. The standard deviation of the

phase was calculated to be 33 mrad (< λ/190) over 30 minutes. For shorter time periods of 5 min this value even drops to 12 mrad (< λ/520) which is the typical measurement time of one 2D spectrum here. This indicates that the long time drifts are the main cause for the changes in the interpulse phase. Putting the relevant optical components into a separate compartment which is air conditioned can compensate for that. However, the phase stability reported is sufficient for 2D spectroscopy and is significantly better than the values reported in literature for 2D-UV spectroscopy in the boxcar geometry, where the phase stability between all three pulses is measured to be about λ/88 [Sel10].

It is worth noting that for most 2D spectroscopic applications, phase stability between the electric fields of the second pump pulse and the probe pulse is not always needed as the system evolves in a populative state in that time period. There are however two exceptions where such a phase stability is needed. First, for the measurement of double-quantum coherences (2Q-2D) where the population delay is scanned and subsequently Fourier transformed along this time delay [Sto09, Kim09, Chr10] and secondly a procedure to remove the undesired pump stray light [Shi09]. One source of the phase instability between the pump and probe pulses is due to the acoustic vibrations of the optics used in the experiment which can be minimized by optimizing the robustness of the experimental setup as it was done in ref. [Sel08]. The other source is the shaper itself, which has to guarantee phase stability between the undiffracted (or a fraction of the ingoing beam) and the shaped beam. This phase stability is now available with new electronics for the AOPDF which syncs directly with the master clock of the laser. The phase stability between the undiffracted and the shaped pulse after the AOPDF was measured to be better than 25 mrad (< λ/251).

4.2.2 Data acquisition and evaluation

The goal is to measure the intensity modulations on the probe spectral intensity induced by the two pump pulses for each coherence time τ (and a fixed population time T). Such a τ-scan is then Fourier transformed to retrieve the pump wavelength resolved 2D spectra. The details of the data acquisition and evaluation procedure are described in the following.

In Fig. 4.2.3 the schematic of a collinear 2D measurement is shown. For each laser shot, the probe spectral intensity is measured in the signal spectrometer (Sig) and in the reference spectrometer (Ref) simultaneously. For a fixed population time, the τ delay is scanned. When

the phase cycling scheme is used, for each coherence time τ, the probe spectral intensity is measured additionally for an additive interpulse electric field phase $\Delta\Phi = \pi$ (Sig^{π}, Ref^{π}). To relate the reference spectrometer intensity to the signal spectrometer intensity, prior to an actual τ-scan the detected probe signals have to be measured when the pump is blocked (Sig_{nopump} and Ref_{nopump}).

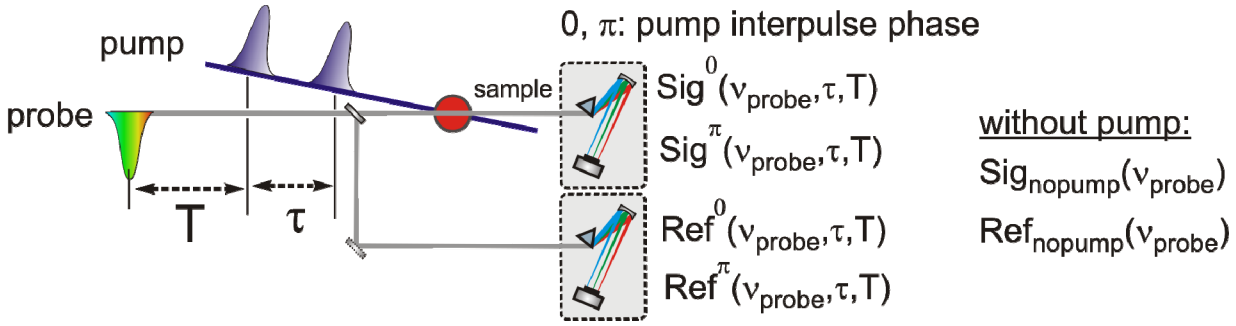

Fig. 4.2.3. Schematic of the measurement and definition of the measured values in a collinear 2D experiment. τ: coherence time; T: population time; 0 and π: phase cycled additional interpulse phase of the pump pulses. Sig_{nopump}, Ref_{nopump}: Before scanning the τ delay the probe spectral intensities were measured without pumping.

The phase stable pump pulses with an interpulse delay of τ are generated by the pulse shaper. As discussed in the last chapter, the complete electric field of the delayed pulse has to be temporally shifted by τ, meaning that both pulses have to have the same carrier envelope phase. However, the software of the AOPDF does not allow directly delaying the electric fields of the two pulses. The software does allow to delay the pulse envelopes of the two pulses and to change the additive interpulse phase ($\Delta\Phi_{AOPDF}$) of the electric fields. The electric field of the two pump pulses after the shaper can be mathematically expressed by Eq. 4.2.1.

$$E_{pump}(t,\tau) = E_1(t) + E_2(t) = \left(\sqrt{I_1(t)} + \sqrt{I_2(t+\tau)} e^{-i\Delta\Phi_{AOPDF}} \right) \cdot e^{-i\omega_{AOPDF} t}, \tag{4.2.1}$$

with I_1, I_2 being the intensity envelope functions of the pulses, e.g., $I(t) = e^{-t^2/2\sigma^2}$ for Gaussian pulses with a FWHM pulse duration of $2\sqrt{2\ln 2}\sigma$. ω_{AOPDF} is the central angular frequency of the pulse spectrum which is set in the AOPDF software. To generate two pump pulses where the electric field itself is delayed, it is necessary to use the $\Delta\Phi_{AOPDF}$ to shift the electric field accordingly. When comparing Eq. 4.2.1 with the desired pump electric field given in Eq. 4.1.3 the interpulse phase has to be changed for each τ delay according to Eq. 4.2.2.

$$\Delta\Phi_{AOPDF} = \omega_{AOPDF} \cdot \tau . \qquad (4.2.2)$$

Note, that when the phase cycling scheme is used, the phase cycling phase $\Delta\Phi$ (0 or π) is added to $\Delta\Phi_{AOPDF}$. Eq. 4.2.2 has an important implication for measuring 2D spectra. The central frequency value set in the AOPDF software has to match the real central frequency of the shaped pulse spectrum. If not, this leads to pump pulses that do not have the correct interpulse delay τ but there is a systematic error introduced by the incorrect phase calculated by Eq. 4.2.2. This leads finally to an incorrect pump frequency axis which is stretched or contracted (appendix A.III). Therefore it is necessary to measure the pump pulse spectrum of the shaped pulses and calculate the central frequency (intensity weighted barycenter) which is then refitted into the software. As a change of the central frequency in the AOPDF software may affect the shape of the diffracted pulse spectra, this procedure has to be repeated iteratively. It is worth noting, that the systematic error introduced by an incorrect frequency value in the AOPDF software can be corrected even after the measurement.

It is worth noting that the error introduced by an incorrect central frequency in the software is rather small. As an example, if the central wavelength set in the AOPDF software is off by 1 nm for a pulse central wavelength of 310 nm, this leads to a retrieved pump frequency axis which is modified by only 0.3 %. This value seems to be rather small, but has to be kept in mind when calculating absolute pump-frequency resolved product quantum yields (as will be discussed in Chap. 4.3).

In the following, the data acquisition and evaluation procedure is described when using the reference spectrometer, the phase cycling scheme and a procedure to remove the pump stray light subtraction. After that, each one of these techniques is discussed with the aid of experimental data.

Measurement procedure with phase cycling, pump stray light subtraction and single-shot referencing. To measure a 2D spectrum for one population delay T, the coherence time τ has to be scanned. For each τ delay the signal and reference spectrometer intensity is measured on a single laser shot basis. This is done by a self-written LabView software that communicates with the AOPDF and receives the data from the spectrometers. The data acquisition procedure for each laser shot is illustrated in Fig. 4.2.5.

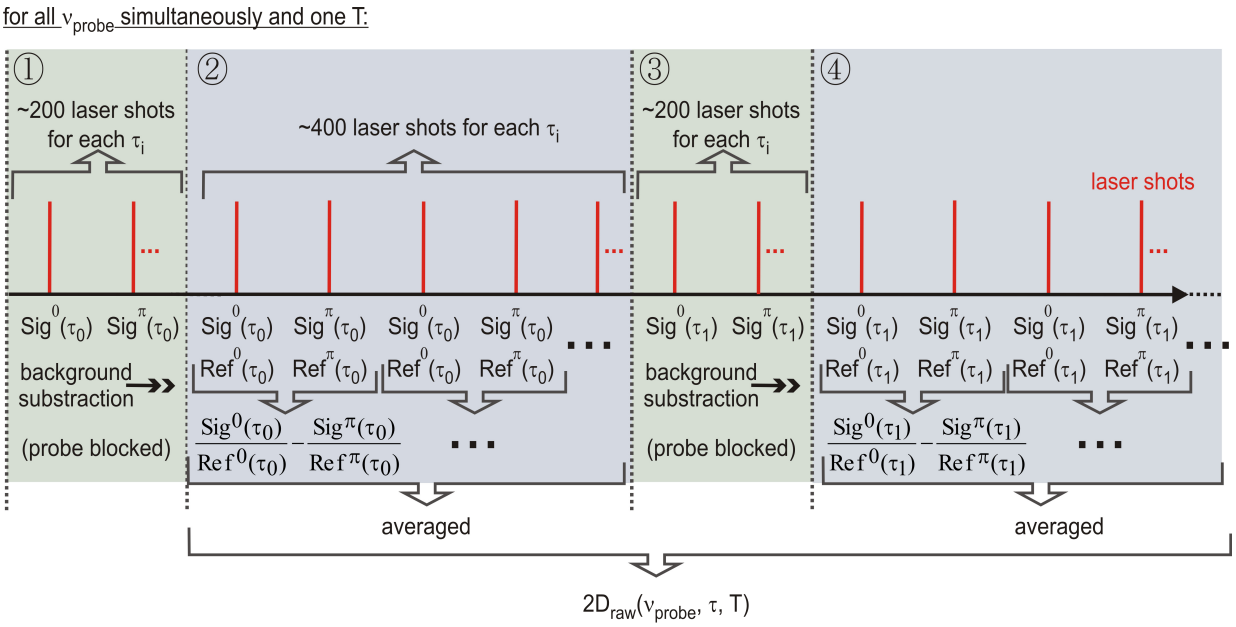

Fig. 4.2.4. Shot-to-shot measurement procedure: ① Background subtraction for the pump stray light subtraction when the pump is active but the probe is blocked (for τ_0). ② Measurement for one τ_0 delay, e.g., τ=0. ③ Background subtraction for τ_1. ④ Measurement for the next τ_1 delay. For each τ delay the averaged phase cycled probe spectra are calculated and combined in a matrix for further calculations.

Before measuring the 2D spectra for a specific τ delay, the pump-stray light is subtracted (Fig. 4.2.4 ①). This is done by generating the pump pulses with the desired τ value and closing an automated shutter in the probe beam. Then only the pump-stray light impinges on the signal spectrometer. The stray light is then measured for both interpulse phases of the pump pulses and is averaged for typically 200 laser shots. This measured stray light contributions are subtracted from the measurement of the 2D signal directly after the probe shutter is opened (Fig. 4.2.4 ②), selectively for each individual interpulse phase. Note, that this procedure has to be done for each τ delay again, as the pump spectral intensities of the double pulses differs for each delay. Pump-stray light subtraction is especially needed for weak probe pulses (e.g., white light supercontinuum). It also has the benefit of eliminating any systematic drifts in the measured intensities, e.g., due to changes of the background light in the laboratory.

As it was discussed in detail in Chap. 2.4, the intensity fluctuations of the probe pulses are the main source of noise in the experiment. Therefore the referencing technique in combination with a shot-to-shot phase cycling technique was applied. To reference the probe spectral intensity by the probe spectrometer, the signal intensity is divided by the reference intensity for each laser shot (Fig. 4.2.4 ②). To benefit additionally from the high shot-to-shot intensity

correlation of the probe pulse it is advisable to apply the phase cycling to consecutive laser shots: The probe spectral intensity is measured once with $\Delta\Phi = 0$ (Sig^0, Ref^0) and for the next laser shot with $\Delta\Phi = \pi$ (Sig^π, Ref^π). The AOPDF is capable of flipping the interpulse phase from one laser shot to the next one. As described in Chap. 4.1 (Eq. 4.1.7), to remove the transient pump-probe background from the 2D signal the phase cycled signals have to be subtracted for two consecutive laser shots according to Eq. 4.2.3.

$$\frac{Sig^0(\tau_i, \nu_{probe})}{Ref^0(\tau_i, \nu_{probe})} - \frac{Sig^\pi(\tau_i, \nu_{probe})}{Ref^\pi(\tau_i, \nu_{probe})}. \qquad (4.2.3)$$

The T dependence is not written in Eq. 4.2.3 for clarity as it is the same for all τ delays. To achieve sufficient signal-to-noise ratio the 2D signal is measured for typically 400 consecutive laser shots and the 200 spectra retrieved by applying Eq. 4.2.3 are averaged to retrieve the 2D spectra along the probe axis for one delay τ. The procedures ① and ② are then repeated for the next τ delays (τ_1: ③, ④) and the 2D probe spectra for all τ delays are combined in a matrix $2D_{raw}(\tau, T, \nu_{probe})$ for further processing.

Before describing the data analysis procedure, it is illustrative to look at the measured raw data. In Fig. 4.2.5 the measured $2D_{raw}(\tau, T, \nu_{probe})$ with phase cycling for pyrene dissolved in methanol is shown for T = 1 ps. For probing a fraction of the pump beam was used.

The step size of the τ delay in Fig. 4.2.5 was chosen to be 1/6 of one optical cycle of the electric field at 310 nm, corresponding to ~0.17 fs. This relatively narrow step size was chosen here for clarity of the data presented. However, we found that measuring only 2.321 time points per cycle didn't show any significant changes in the quality of the resulting 2D spectra. This is in accordance with the numbers reported in the literature for 2D spectroscopy in the visible or IR [Shi09, Tek09]. As this choice significantly reduces the measurement time it was used hereafter for all measurements.

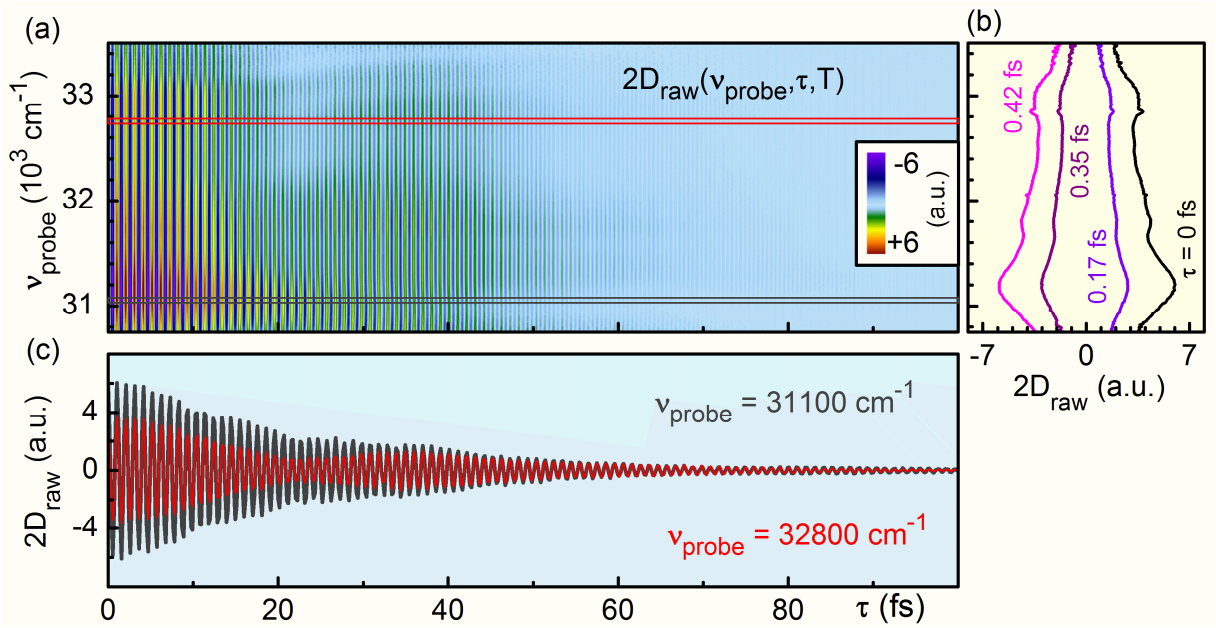

Fig. 4.2.5. Measured τ-scan of pyrene in methanol at T = 1 ps. (a) Intensity plot of $2D_{raw}(\tau, 1ps, \nu_{probe})$ where the probe frequency was already determined for each probe spectrometer CCD pixel. (b) Slices along the probe axis for the first 4 τ-delays. (c) Slice along the coherence time τ for two different probe frequencies which are highlighted by the red and black boxes in (a).

The high frequency modulations along the τ-axis (Fig. 4.2.5c) originate from the 2D contribution. The amplitude of these modulations vanishes over time due to the finite temporal width of the pulses and the dephasing of molecule for the increasing temporal spacing between the two pump pulses. The maximum delay for τ is chosen just long enough to guarantee that the electronic dephasing of the molecule is completed (~110 fs for pyrene). With the reduced 2.321 time points per optical cycle this leads to about 260 τ-points in a typical 2D measurement. Considering an average of about 600 laser shots (200 background, 400 signal) for each τ-point and the additional time the AOPDF needs to update to a new waveform (next τ-delay), this leads to a typical time of about 4 min for a complete 2D spectra for one population time T.

Data post processing procedure. Starting from the measured $2D_{raw}(\tau, T, \nu_{probe})$ matrix, the data evaluation procedure to retrieve a 2D spectrum for one T time is described in the following. The flow chart comprising all necessary calculations is given in Fig. 4.2.6.

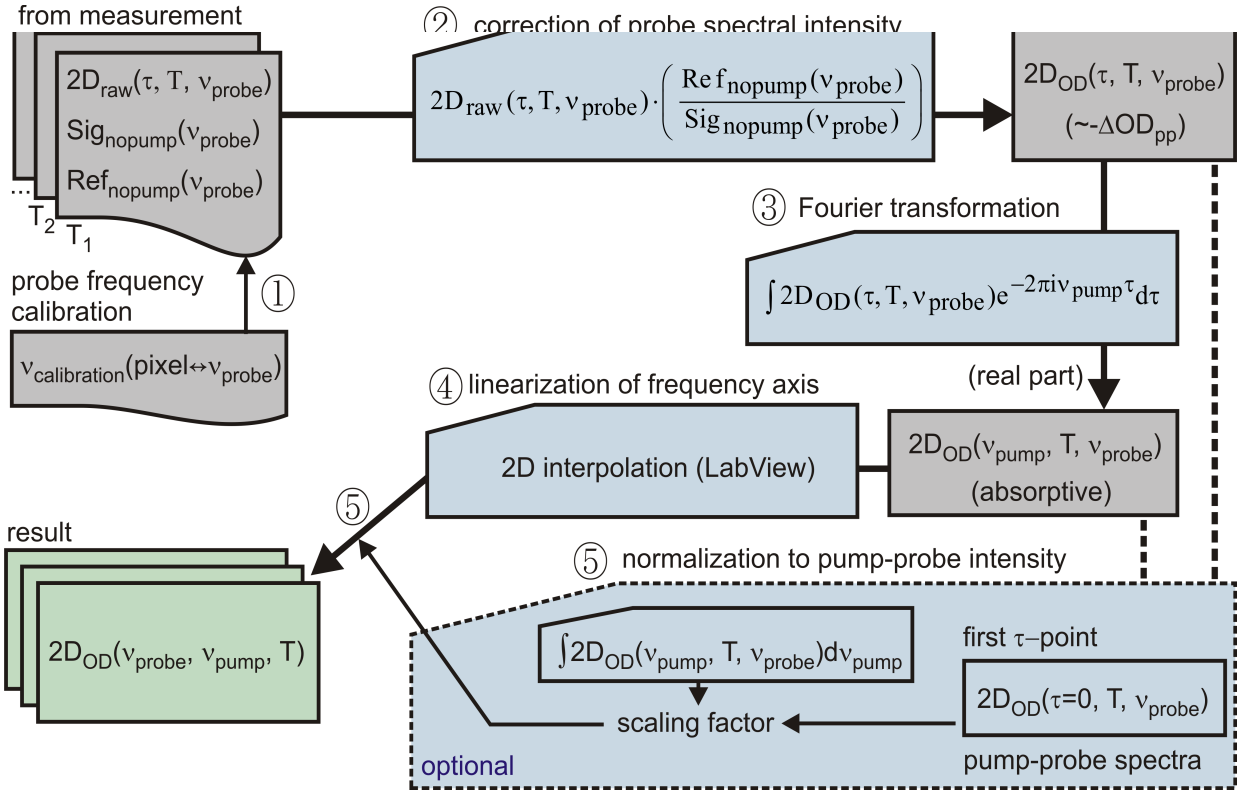

Fig. 4.2.6. Schematic of the post measurement data processing to retrieve an absorptive 2D spectrum. ① Probe frequency assignment. ② Correction of probe spectral intensity to retrieve 2D spectra which are related to transient pump-probe measurements. ③ Fourier transformation of the τ-axis. ④ Linearization of the probe frequency axis. ⑤ Normalization of the 2D spectral intensity to match the pump-probe intensity by using the projection slice theorem.

① Prior to further calculation the probe frequency axis calibration has to be done. In a measurement of the probe spectral intensity only the pixel number of the spectrometer CCD is known. To assign a probe frequency to each pixel number, the frequency calibration procedure described in Chap. 2.4 (see also in reference [Meg09]) is applied.

② The measured raw 2D spectra have to be corrected for the spectral intensity distribution of the probe pulses. Whether one is interested in retrieving 2D spectra which have an amplitude which is directly proportional to the third-order polarization $P^{(3)}$ (investigation of dephasing effects) or 2D spectra which are proportional to the change in optical density measured in conventional pump-probe spectroscopy (investigation of excitation-frequency resolved populative dynamics) two different procedures have to be applied. A detailed verification of the given relations is given later on in Chap. 4.4 due to the complexity of the theoretical formalism.

To retrieve a 2D spectrum which has amplitude values which are proportional to $P^{(3)}$ the measurement has to processed similar to Eq. 4.1.7 ($S_{2D}^{P^{(3)}}(\nu_{pump}, T, \nu_{probe})$). However, the single-shot referencing scheme with the additional reference spectrometer was done by dividing the signal spectrometer intensities by the probe spectral intensities for each τ_i delay and interpulse phase (Eq. 4.2.3). This is not included in Eq. 4.1.7. Therefore, to retrieve the pure $2D^{P(3)}$ signal, the measured raw data has to be corrected for each τ_i delay according to Eq. 4.2.4.

$$\left(\frac{Sig^{0}(\tau_i, \nu_{probe})}{Ref^{0}(\tau_i, \nu_{probe})} - \frac{Sig^{\pi}(\tau_i, \nu_{probe})}{Ref^{\pi}(\tau_i, \nu_{probe})} \right) \frac{Ref_{nopump}(\nu_{probe})}{2\pi\nu_{probe}\sqrt{Sig_{nopump}(\nu_{probe})}} \quad \boxed{\propto P^{(3)}} \tag{4.2.4}$$

Note, that $\sqrt{Sig_{nopump}(\nu_{probe})}$ is used for $E_{probe}(\nu_{probe})$ here.

To retrieve intensities which are proportional to the change in optical density (ΔOD) like they are measured in transient pump-probe spectroscopy ($S_{2D}^{\Delta OD}(\nu_{pump}, T, \nu_{probe})$), it is necessary to correct the measured 2D spectra for each τ delay with the probe spectral intensity as it was shown in Eq. 4.1.9. Therefore, the 2D spectra for each τ_i delay have to be calculated as given by Eq. 4.2.5.

$$\left(\frac{Sig^{0}(\tau_i, \nu_{probe})}{Ref^{0}(\tau_i, \nu_{probe})} - \frac{Sig^{\pi}(\tau_i, \nu_{probe})}{Ref^{\pi}(\tau_i, \nu_{probe})} \right) \frac{Ref_{nopump}(\nu_{probe})}{Sig_{nopump}(\nu_{probe})} \quad \boxed{\propto -\Delta OD_{pp}} \tag{4.2.5}$$

The latter ("nopump") term links the signal and reference spectrometer intensities. With that term the reference spectrometer intensity is scaled to the signal spectrometer intensity when there is no pump present. This means that the measured reference spectrometer intensity is virtually transmitted through the sample cell as does the probe beam impinging on the signal spectrometer. When applying Eq. 4.2.5, the retrieved $2D_{OD}(\tau,T,\nu_{probe})$ matrix has amplitude values that are mathematically proportional to the change in optical density ΔOD_{pp} measured in conventional pump-probe spectroscopy.

It is important to note here, that for some collinear 2D spectroscopy measurements reported in literature, the calculated 2D amplitudes are neither proportional to $P^{(3)}$ nor ΔOD_{pp} but to $P^{(3)} \cdot E_{probe}(\nu_{probe})$, e.g., see ref. [Tek10, Tek12]. To achieve this proportionality when using the single-shot referencing scheme, the measured raw data has to be corrected for each τ_i delay according to Eq. 4.2.6.

$$\left(\frac{Sig^{0}(\tau_i, \nu_{probe})}{Ref^{0}(\tau_i, \nu_{probe})} - \frac{Sig^{\pi}(\tau_i, \nu_{probe})}{Ref^{\pi}(\tau_i, \nu_{probe})} \right) Ref_{nopump}(\nu_{probe}). \qquad (4.2.6)$$

The influence of the former mentioned three different ways of correcting for the probe spectral intensity distribution (Eq. 4.2.4. to 4.2.6) will be discussed further in subitems ④.

③ The Fourier transformation of the measured data along the τ-axis is done (e.g., compare Eq. 4.1.8) for each probe frequency (probe pixel) individually to the retrieved pump frequency axis. To retrieve the absorptive part of the 2D spectrum, the real part of the Fourier transformation is used. The result is shown exemplarily for the data from Fig. 4.2.5c in Fig. 4.2.7.

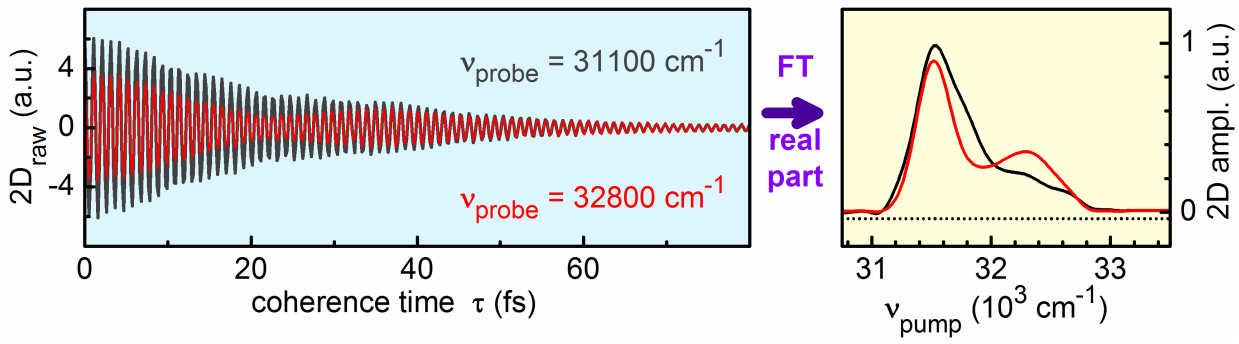

Fig. 4.2.7. Fourier transformation of the τ-scan for two selected probe frequencies of the data shown in Fig. 4.2.5.

The achievable spectral resolution after Fourier transformation is given by the inverse of the maximum delay τ scanned. As the desired 2D information is encoded in the high frequency modulations it is often sufficient to restrict the maximum τ delay to a value where the modulations have vanished completely and to use mathematical tricks to artificially increase digital spectral resolution within the Fourier transformation. This can be done by adding constant values to prolong the maximum delay (zero-padding). This procedure is used in 2D-IR spectroscopy and is called zero adding [Ham11].

When the Fourier transformation is applied to all probe frequencies individually, the 2D spectrum for one population time in the frequency domain is retrieved $2D_{OD}(\nu_{pump}, T, \nu_{probe})$. The real part of this matrix represents the absorptive 2D spectrum.

It is worth noting, that in collinear 2D spectroscopy the 2D spectra are automatically correctly *phased*. This term refers to the phase between the signal field and the pulse for heterodyne

detection. As for collinear 2D spectroscopy the probe pulse generates the signal field (third interaction) and also serves as the pulse for heterodyne detection, the phase is automatically correct. For noncollinear 2D spectroscopy the heterodyne detection is achieved by using a fourth pulse (referred to as the local oscillator) which is overlaid at the probe spectrometer with the signal field. Therefore, in noncollinear 2D spectroscopy a post processing technique called *phasing*[6] has to be applied for data analysis, which may introduce systematic errors when not done carefully.

④ As the probe frequency axis depends on the prism spectrometer design, it is advisable to linearize this axis to have equidistant frequency steps similar to the pump axis which is already linearized due to the Fourier transformation. This was done by using self-written LabView software that interpolates the 2D matrix by the aid of a spline algorithm at the desired equidistant probe frequencies.

The resulting pump and probe frequency resolved 2D spectrum represents the final result. When using different probe intensity corrections according to one of the Eq. 4.2.4, 4.2.5 or 4.2.6, the resulting 2D spectra have different shapes along the probe axis, while the qualitative behavior along the pump axis is identical. The resulting 2D spectra are shown in Fig. 4.2.8.

[6] *Phasing* is a procedure used in noncollinear 2D spectroscopy to manually correct the phase of a 2D spectra until the pump-integrated 2D spectra matches a separately measured transient pump-probe spectrum for the same population time [Bri04a].

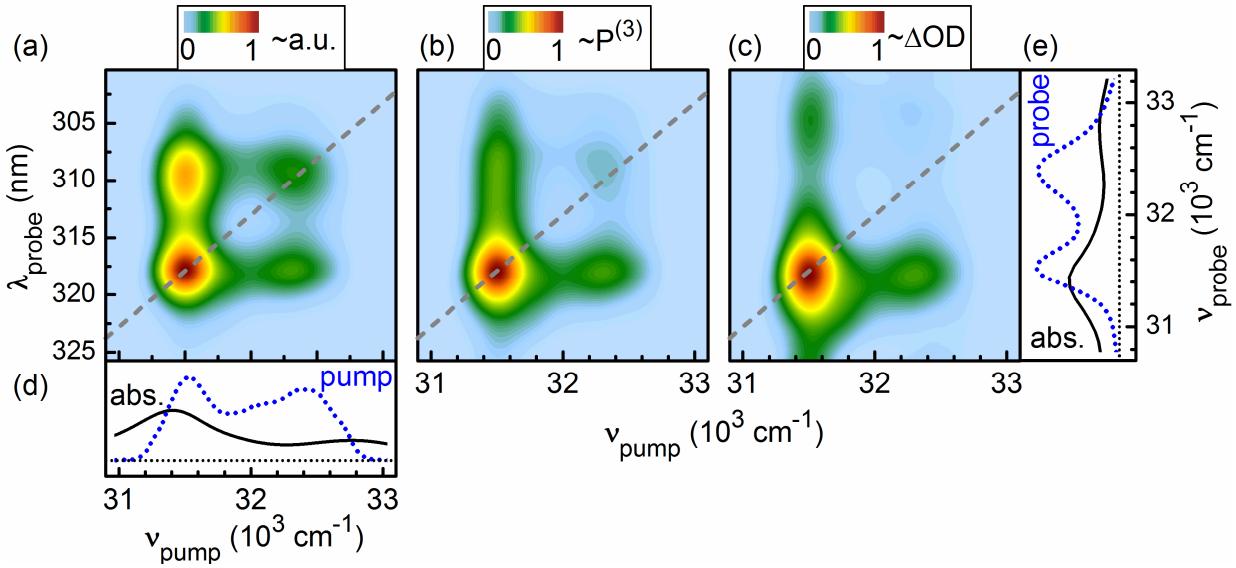

Fig. 4.2.8. Influence of the probe spectral intensity distribution on the absorptive 2D spectra of pyrene in methanol at T = 1 ps. Correction of the probe spectrum was done according to (a) Eq. 4.2.6, (b) Eq. 4.2.4 and (c) Eq. 4.2.5. For (a) the molecular signal along the probe axis is folded with I_{probe}, for (b) it is folded with E_{probe} and for (c) it is independent of the probe spectrum. The absorption of pyrene (black) and the spectral intensity of the pump and probe pulse are shown in (d) and (e), respectively.

When using Eq. 4.2.6 (Fig. 4.2.8a) the 2D spectra clearly resolves the diagonal and off diagonal (cross) peaks of the ground state bleach of pyrene for the two vibrational bands which were pumped. However, the position of the 2D peaks along the probe axis, e.g., for ν_{pump} = 31500 cm^{-1} (ν_{probe} = 31500 cm^{-1} (309.2 nm) and 32340 cm^{-1} (317.5 nm)) do not match the respective absorptive peaks of the vibrational bands of pyrene (ν_{probe} = 31400 cm^{-1} (318.5 nm) and 32790 cm^{-1} (305 nm)). This is due to the fact that for this type of probe spectral correction, the 2D signal is a convolution of the molecular signal (ground state bleach) and the probe spectral intensity (I_{probe}) which modulates the shape of the 2D spectrum.

When using Eq. 4.2.4 (Fig. 4.2.8b) the 2D spectrum is elongated along the probe axis and is a convolution of the molecular signal (ground state bleach) and the probe electric field amplitude (E_{probe}). The amplitudes are proportional to the third-order polarization $P^{(3)}$ and are typically used to investigate coherent effects like homogeneous and inhomogeneous broadening effects arising from the interaction with the surrounding [Bri04a].

When using Eq. 4.2.5 (Fig. 4.2.8c) the peaks of the ground state bleach signal along the probe

axis closely match the peak positions of the absorption spectrum of pyrene. The 2D amplitude is proportional to ΔOD (as measured in conventional pump-probe spectroscopy) and is independent of the probe spectral intensity distribution. This type of probe correction allows retrieving information about the molecular dynamics (e.g., population dynamics) from a 2D measurement. However, the retrieved 2D amplitudes are only proportional to ΔOD and are not yet absolutely linked to, e.g., the amount of excited molecules. The necessary post processing procedure to pave the way for quantitative analysis is described in the following. In Chap. 4.3. the full quantitative analysis procedure is described.

⑤ To achieve a quantitative relation to a physical quantity (like the population of excited molecules) the correction of the 2D spectra is done according to Eq. 4.2.5. All the additional information necessary to achieve absolute amplitudes as would be measured in a conventional pump-probe experiment are already inherent in the measured data and there is no need for separate measurements.

To do so, one needs a transient pump-probe spectrum which is measured for the pump intensity of the constructively interfering pump pulses for the specific population delay T. This transient spectra is indeed measured for the first τ delay where τ = 0. For this delay, the two pump pulses interact constructively for ΔΦ = 0, generating one single pump pulse ($Sig^0(\tau=0) = Sig^* = I^*$) and interact completely destructively for ΔΦ = π, meaning that there is no pump pulse present ($Sig^\pi(\tau=0) = Sig_0 = I_0$). Therefore, for τ = 0 a conventional transient pump-probe spectrum is automatically measured. This can be seen best when looking at the calculation of 2D spectra according to Eq. 4.2.5 when neglecting the intensity fluctuations of the probe beam, meaning that $Ref^0 = Ref^\pi = Ref_{nopump}$. Then Eq. 4.2.5. simplifies to Eq. 4.2.7.

$$\frac{Sig^* - Sig_0}{Sig_0} \approx +\log\left(\frac{Sig^*}{Sig_0}\right) = -\Delta OD_{pp}^{\tau=0}. \qquad (4.2.7)$$

Note that the abbreviation used to describe conventional pump-probe measurements (Sig_0 and Sig^*) are used here. The first equal sign is a consequence of a Taylor expansion of the second term and is valid for small pump induced signal changes that are in the range of less than a few percent [Sch08]. The Taylor expansion is described in detail in appendix A.I. Therefore, the 2D probe spectrum for τ = 0 is the pump-probe spectrum needed for the respective population time T. Note that the negative sign of ΔOD in Eq. 4.2.7 becomes important when the sign of the pump-probe measurement is compared with the sign of the signals retrieved in 2D spectroscopy, which have the opposite sign.

With the retrieved transient absorption spectrum the 2D measurement has to be scaled correctly. The projection slice theorem used in 2D spectroscopy states, that the projection of a 2D spectrum onto the probe axis equals the pump-probe spectrum for the specific population time T [Jon03, Bri04b]. This projection can be understood as the integration along the pump axis for each probe frequency. Therefore this projected probe spectrum should equal the pump-probe spectrum retrieved from the $\tau = 0$ measurement (Eq. 4.2.7). Mathematically, this can be expressed as given in Eq. 4.2.8 (using the terminology given in Fig. 4.2.6).

$$\int 2D_{OD}(\nu_{pump}, T, \nu_{probe}) d\nu_{pump} = \Delta OD_{2D}(T, \nu_{probe}) . \qquad (4.2.8)$$

By comparing the results of Eq. 4.2.7 and Eq. 4.2.8 a scaling factor can be retrieved which has to be multiplied to all elements of $2D_{OD}(\nu_{pump}, T, \nu_{probe})$. Then the retrieved 2D spectrum has amplitude values which are quantitatively related to conventional pump-probe measurements. The dimension of the 2D amplitude is $\Delta OD/\Delta\nu$ [$1/cm^{-1}$] and allows calculating pump-frequency resolved product quantum yield from a 2D measurement (see Chap. 4.3).

4.2.3 Benefit of phase cycling, probe referencing and pump stray light subtraction

2D spectroscopy allows gaining a deeper insight into the molecular dynamics due to the pump-probe frequency correlation. The measurement of the population dynamics is time consuming as one has to measure multiple population times T and for each one of them a complete scan of the coherence time τ. To keep the overall measurement time in reasonable limits it is necessary to reduce the averaging time used in the experiment. To achieve that without any loss in signal quality, it is necessary to increase the signal-to-noise ratio. This can be done by: 1) phase cycling of the interpulse phase of the pump pulses 2) referencing of the probe intensity fluctuations by an additional probe spectrometer 3) elimination of the pump-stray light subtraction by chopping the probe beam. With (without) pump-stray light subtraction the time needed for one population time T is about 4 min (2 min). This is comparable to the values reported in literature for collinear spectroscopy in the IR of ~1 min [Shi09] and is very short compared to 2D-UV spectroscopy in the noncollinear geometry of about 50 min [Sel10].

Phase cycling scheme: Elimination of transient pump-probe background. To demonstrate the benefit of the phase cycling scheme in collinear 2D measurements, the measurement without using the phase cycling scheme is presented first and then compared to the same

measurement with phase cycling.

In principle it would be enough to measure the probe spectral intensity detected at the signal spectrometer Sig(τ, T, ν_{probe}) for each τ delay of the pump pulses. However, the change in intensity induced by the pump pulses is typically small compared to the intensity fluctuations of the probe pulse itself (typically 0.1 % compared to 1 % fluctuations, respectively). It is therefore necessary to look at the transmission change induced by the pump as it is done in conventional pump-probe spectroscopy. This is done by additionally measuring the probe spectral intensity $Sig_{nopump}(\tau, T, \nu_{probe})$ (for each τ delay) when the pump pulses are blocked for the laser shot directly after the one with pumping. This technique profits from the high shot-to-shot correlation and is capable of measuring transmission changes smaller than 10^{-4} with the laser system used in this work (see Chap. 2.4 or [Meg09]). The change in optical density induced by the pump pulses is calculated as discussed in Chap. 2.4 (Eq. 2.4.4, being the negative logarithm of the transmission change). A τ-scan for a single probe wavelength of 305 nm measured for pyrene dissolved in methanol is shown in Fig. 4.2.9a, red line.

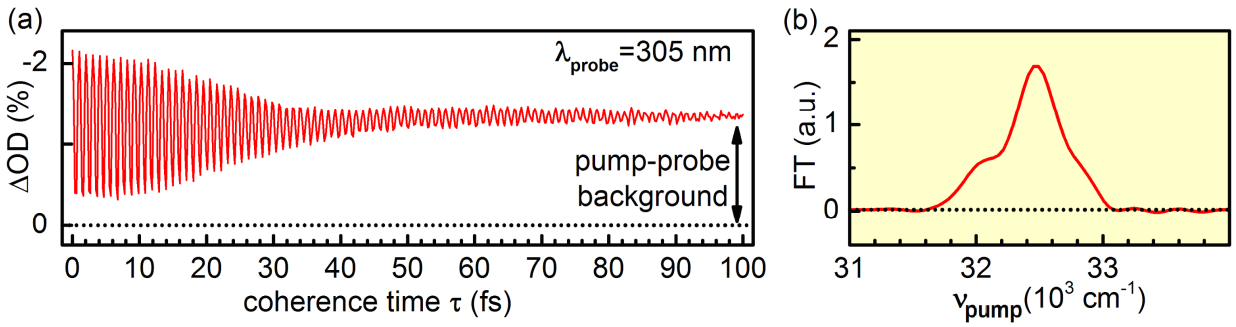

Fig. 4.2.9. 2D measurement without phase cycling for pyrene in methanol. (a) τ-scan for λ_{probe}=305 nm. (b) Real part of the Fourier transformed data of (a).

The high frequency modulations originate from the 2D contribution. The amplitude of these modulations vanishes over time due to the decay of the coherence in the molecule for the increasing temporal spacing between the two pump pulses. The slowly varying offset (~13 mOD) of the τ-scan comprises the transient pump-probe background generated by the two pump pulses individually. When the τ-scan is Fourier transformed these two contributions can be separated as they appear at different frequencies. The high frequency component is the 2D contribution and represents a slice of a complete 2D spectrum for the specific probe frequency (Fig. 4.2.9b, red line).

The transient background typically does not disturb the 2D measurement as it appears on a

different frequency range. However, if the molecule shows fast population dynamics comparable to the modulation frequency (e.g., as in 2D-IR) or the dephasing is not complete within the measured population dynamics then it may disturb the retrieved 2D spectra [Shi09]. Additionally, the transient background cannot be used to retrieve transient population dynamics because it is "nonlinear" in intensity. The signal is not just the sum of the two separate pump pulses but the contribution of the second pulse depends on the percentage of molecules already excited by the first pulse. It is therefore convenient to apply the phase cycling scheme to remove the transient background which is shown in Fig. 4.2.10 for the same measurement as in Fig. 4.2.9.

To illustrate the phase cycling scheme a τ-scan for a single probe wavelength of 305 nm is shown in Fig. 4.2.10a for $\Delta\Phi = 0$ (red line), $\Delta\Phi = \pi$ (blue) and when the two signals are subtracted (green). Note that the data shown was calculated by chopping the pump and plotting the transmission change for clarity. In a real 2D measurement chopping the pump is not needed due to the phase cycling of consecutive laser shots. The phase cycled curve has no pump-probe background contribution anymore. This allows using zero-padding to artificially increase the spectral resolution within the Fourier transform. Due to subtraction of the two phase-cycled measurements the Fourier transformed signal (Fig. 4.2.10b) has double the amplitude accompanied in an increased signal-to-noise ratio.

Another advantage of phase cycling is that the overall measurement time is the same as when the phase cycling scheme is not applied. This is because for the not phase cycled measurement the pump has to be chopped to receive sufficient signal quality to benefit from the high shot-to-shot correlations. This doubles the laser shots needed for averaging at one τ delay the same way as the phase cycling does.

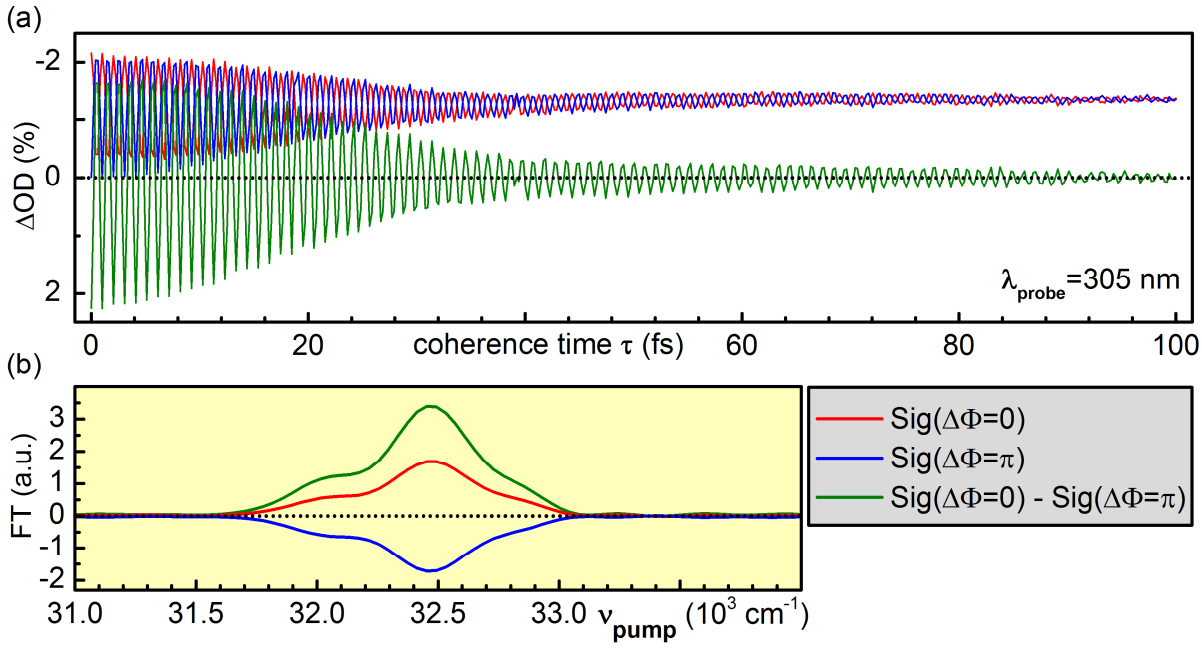

Fig. 4.2.10. Measured 2D data illustrating the removal of the pump-probe background using the phase cycling scheme. For clarity the transmission change was measured, which is not necessary (see text). (a) τ-scan for λ_{probe}=305 nm. (b) Real part of the Fourier transform of the data in (a).

Single-shot referencing: Reduction of noise. The signal-to-noise ratio can moreover be increased by using the referencing scheme using a second identical probe spectrometer as discussed in detail in Chap. 2.4. Elimination of the probe intensity fluctuations is achieved by division of the signals of the two spectrometers as given in Eq. 4.2.4. or Eq. 4.2.5.

In Fig. 4.2.11 the τ-trace for a probe frequency of 32650 cm^{-1} measured for pyrene dissolved in methanol fro a population time of 1 ps. The τ-trace is shown with and without referencing the probe spectral intensity fluctuations. To calculate the increase in signal-to-noise ratio due to referencing, the standard deviation of the base line for τ-delays larger than 80 fs was calculated. The signal-to-noise ratio shows an increase by a factor of up to 10 which allows using shorter averaging times for each τ delay.

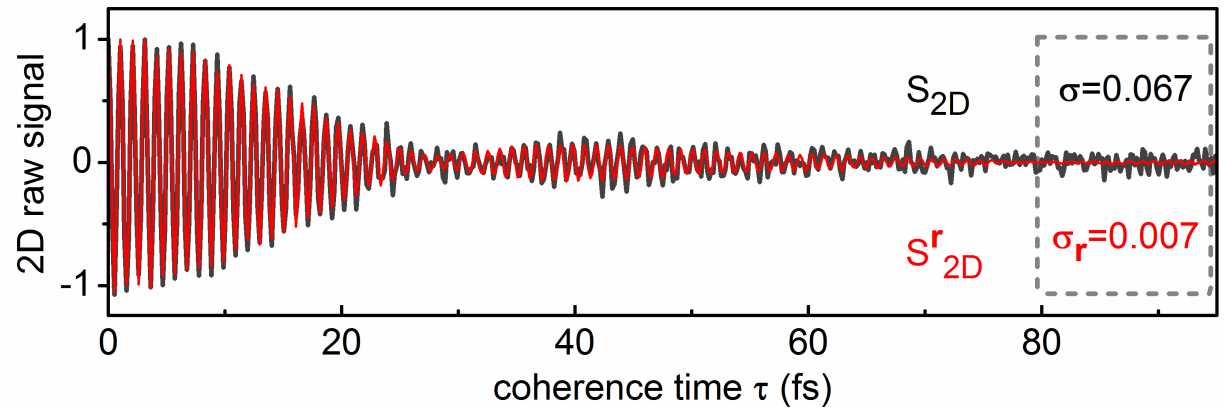

Fig. 4.2.11. Benefit of single-shot referencing for 2D spectroscopy when using phase cycling. Exemplary measured coherence time traces with (black) and without single-shot referencing (red) for a selected probe frequency where the ground state bleach is present. A clear reduction of the noise level due to referencing is present. The standard deviations σ of the baselines (τ > 80 fs) are also given.

Additional remarks to the shape of the coherence time trace. The τ-trace in Fig. 4.2.11 shows modulations at the pump carrier frequency along the τ-axis. These modulations originate from the polarization created by the pump pulses. The amplitude of these modulations vanish over time due to the finite temporal width of the pulses and the electronic dephasing of the molecule. A revival of the modulations peaking around the coherence time τ = 40 fs. The revival of the coherence is associated with a π phase shift in the high frequency component at τ = 30 fs.

To interpret this finding one has to look at what is actually monitored in the 2D experiment. The first pulse creates a polarization in the sample. This polarization is a Hertzian coherence between the ground state and the electronically excited state. It oscillates with the main transition energy that is equal to the carrier frequency of the pump pulse if it is tuned into resonance. Since our pump pulse is shorter than the typical electronic dephasing time of some ten femtoseconds [Big91, Nib91], the second phase-locked pump pulse encounters this freely oscillating polarization prior to significant dephasing. Depending on whether the electric field of the second pulse is in phase or out of phase, the additional polarization generated by the second pulse adds or subtracts to the one from the first pulse. For a static two-level system the frequency of the polarization does not evolve in time and the decrease in 2D signal is solely due to a stochastic decay of the polarization. In this simplified picture it is hard to explain why the sample polarization recurs after a complete disappearance and changes its phase by π.

One explanation of the observed behavior of the τ-trace uses the intrinsic signature of the molecular energy structure and the ultrafast molecular dynamics following the optical excitation. The experimental findings can be explained by two contributing transitions with distinct central frequencies and broad spectral bands. The nature of these transitions is not a priori known but they could be two vibronic side bands of the $S_2 \leftarrow S_0$ electronic transition. In this picture, the broadband pulse creates two polarizations with different oscillatory frequencies. These two polarizations can then beat and lead to the observed experimental behavior, including the phase shift between the oscillations before and after the revival shown in Fig. 4.2.11 (red line).

An alternative explanation builds on the concept of a τ-dependent modulation of the electronic polarization due to structural motion. The first laser pulse induces a nuclear motion that can be associated with the time evolution of a vibronic wavepacket created in the excited and also the ground state. This motion is the consequence of the differing equilibrium geometry in the excited state as compared to the ground state, also seen in the Franck-Condon structure of the absorption band. The wavepacket propagates with time and the second pump pulse encounters a changed molecular configuration. Note that the modulations along τ are not a result of vibrational modulation directly, rather the effect of structural motion on the electronic polarization.

Formally the two pictures, i.e. the τ-dependent modulation of the electronic polarization due to structural motion and the polarization beating are closely related and can both explain the experimental observations. An intensity dependent study should be able to elucidate and differentiate the suggested mechanisms in greater detail.

Pump-stray light subtraction: Weak probe intensities feasible. When the probe pulse has relatively low intensities when compared to the pump pulses, e.g., when a white light supercontinuum is used for probing (Chap. 4.2.4), even weak contributions of pump stray light can distort the 2D spectra in the spectral region of the pump pulse spectrum (left part of Fig. 4.2.12).

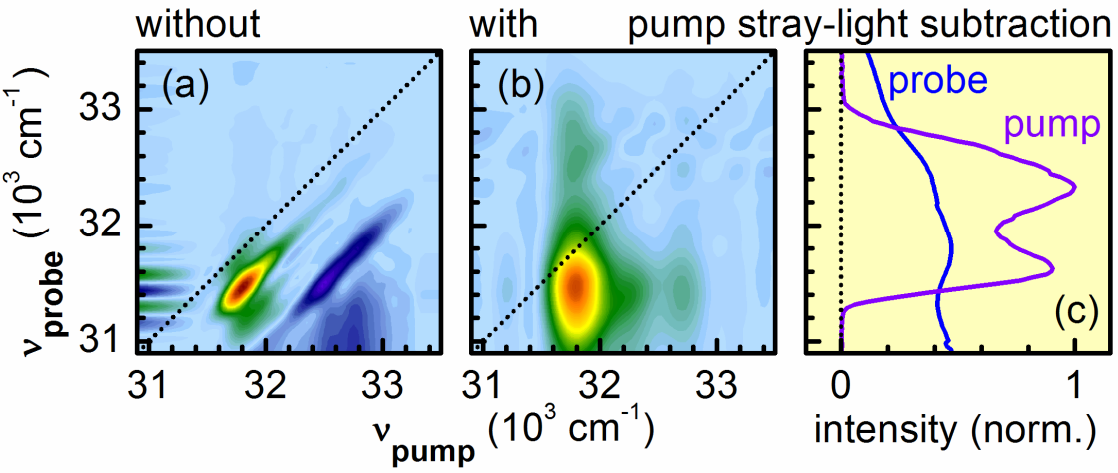

Fig. 4.2.12. Demonstration of the benefit of pump-stray light subtraction for weak probe pulses. Visible white light supercontinuum was used as probe. (a) Measured 2D spectra without pump-stray light subtraction shows severe distortions in the spectral overlap region. (b) Measured 2D spectra with pump stray light subtraction clearly resolves the overlap region.

Various procedures to minimize the influence of stray light have been proposed in literature. Using well chosen polarization between the incident pulses has shown good results but needs precise adjustment and additional optical components [Mye08]. Using an additional phase cycling scheme were the carrier envelope phase of the pump pulses is systematically changed was used successfully in the UV [Tse09]. However, this technique needs phase stability between the pump and the probe pulses which is not always the case if the laser itself is not carrier envelope stable (e.g., when using the frequency doubled CPA and white light generated by the fundamental of the laser as the probe). To achieve applicability for all pump and probe combinations we developed a new technique. As already described in the data acquisition procedure (Chap. 4.2.2) the pump stray light is measured for each coherence delay τ when the probe beam is blocked with an automatically controlled shutter. This background is subtracted from the 2D measurement when the shutter is opened again. The overall measurement time is typically increased by 90 %. With this procedure the distortions in the spectral region of the pump can effectively be eliminated when the visible white light is used as probe. This procedure also accounts for eventual drift in the background count rates of the spectrometers allowing longer lasting measurements. For measurements that are not interested in measuring the pump-probe spectral overlap region this technique can be avoided and the overall measurement time is reduced.

4.2.4 White light continuum probe in 2D spectroscopy

When using a fraction of the pump pulse for probing the investigated system, the spectral window of the probe is limited to the bandwidth of the pump pulse. For the noncollinear (boxcar) geometry of 2D spectroscopy this is typically the case. The advantage of partially collinear 2D spectroscopy is that the probe pulse can easily be generated independently from the pump pulses. This allows probing spectral regions independently of the UV pump pulse spectrum. In femtosecond transient absorption spectroscopy, the ultimate broadband probe pulse represents a white light supercontinuum [Meg09]. Is has been shown in the visible domain, that collinear 2D spectroscopy allows to use such a white light pulse for probing [Tek09, Tek10, Tek12, Ogi09]. Here supercontinuum probing is adapted for the 2D-UV setup which allows probing the complete UV-visible spectral domain.

The two types of white light supercontinuum used in this study are on the one side a UV-visible white light that is generated by focusing the CPA fundamental into a CaF_2 crystal. The resulting spectrum spans the spectral domain between 290 – 720 nm [Meg09]. The other UV white light is generated by focusing the 2^{nd} harmonic of the CPA fundamental into a CaF_2 crystal and spans the spectral domain between 250 – 360 nm. Due to the overlap region between 290 – 360 nm the measurements with the two white light types can be concatenated which allows probing more than an octave spanning spectral domain. The only drawback for supercontinuum probing is that the white light is strongly chirped (typical pulse length 0.6 – 1 ps [Meg09]). This complicates 2D measurements because each probe frequency interacts with the system at different delays, meaning that the probe frequencies have different population delays T. When a chirp free 2D spectrum is desired, an elaborate correction procedure by measuring multiple population times can be applied [Tek12]. However, when one is interested in pump frequency dependent dynamics only, most of the time it is sufficient to characterize the precise frequency delay of different probe frequencies which can readily be done in the same setup by measuring a transient pump-probe spectrum.

In Fig. 4.2.13 a 2D measurement of pyrene in methanol (T = 1ps) is shown together with the spectral intensity distribution of the UV and UV-visible white light supercontinuum. For this measurement, the probe spectral intensity distribution was corrected for according to the transient pump-probe equivalence procedure (Eq. 4.1.9). This means, that the amplitudes of the 2D spectra are proportional to the change of optical density measured in transient pump-probe measurements. To verify that experimentally, transient pump-probe measurements were done separately for the same population time of 1 ps and overlaid with the projection of the 2D

spectra onto the probe frequency axis (Fig. 4.2.13b). Note, that the amplitude of the pump-probe spectra has an opposite sign when compared to the projection of the 2D spectra, which is a consequence of the subtraction procedure applied in the phase cycling scheme (appendix A.II). A very good agreement between pump-probe and 2D is observed which also proves the high quality of the 2D-UV setup.

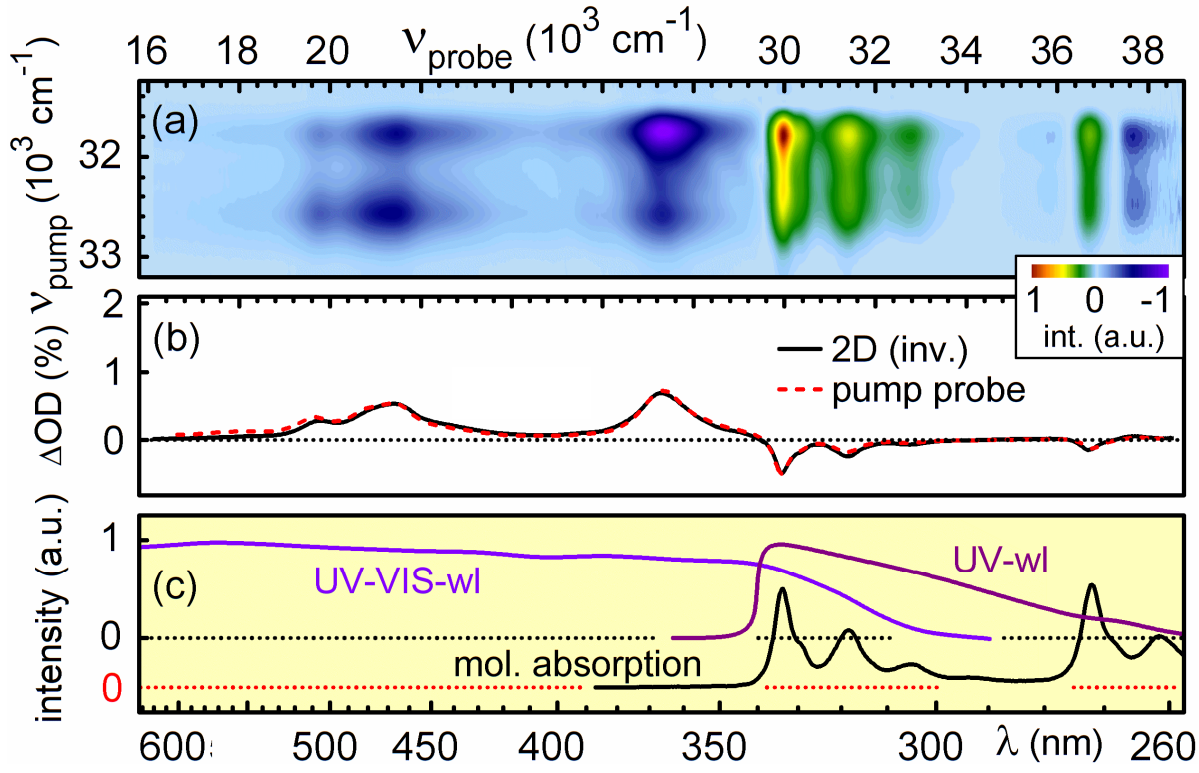

Fig. 4.2.13. 2D spectrum (T = 1ps) of pyrene when using white light continua as probe. The pump and probe axes have been turned around. The pump was centered at 310 nm. (a) Concatenated 2D spectra probing the whole UV-visible spectral domain. (b) Comparison between projected 2D spectra (black, inverted) and pump-probe (red dashed). (c) Spectral intensity of the probe pulses and absorption spectrum of pyrene in methanol (black).

The 2D setup presented is fast, compact and can be used for long time operation. Due to the tunability of the pump pulses and a detection scheme for the whole UV-visible spectral domain it can be applied to a large variety of UV absorbing molecules. The setup was used to investigate the vibrational progression in pyrene and the excitation energy dependent dynamics of the photoswitch chromene (Chap. 5).

4.3 Quantitative analysis of 2D measurements

2D spectroscopy contains additional information compared to conventional pump-probe spectroscopy as it resolves the excitation frequency. From the experimental point of view it would be beneficial for the interpretation of 2D measurements when a quantitative relation between the measured signals and the properties of the system can be retrieved, e.g., the population of molecules in a specific product state. The 2D measurements reported in literature seem to avoid such a quantitative discussion. An indication for that is the fact, that the most frequently used term to describe 2D signal amplitudes is still “arbitrary units”.

The quantitative amplitudes retrieved in conventional pump-probe spectroscopy, namely the change in optical density ΔOD, are directly proportional to the population of molecules probed. In 2D spectroscopy such a relation is not always possible, as the measured signal is a convolution of all electric fields involved. However, for collinear 2D spectroscopy a direct relation with transient pump-probe spectroscopy can easily be found under the restriction that one is only interested in pump-frequency resolved population dynamics rather than dephasing dynamics. In this chapter the amplitudes measured in 2D spectroscopy are analyzed quantitatively, e.g. to retrieve the amount of molecules in a given excited or product state directly from the measured data. To the best of my knowledge, such a quantitative analysis of 2D measurements has not been done so far.

4.3.1 Motivation for this thesis

The idea to analyze the 2D measurements quantitatively was initiated by the observation that the measurements on pyrene and 5,6DPBC (photoswitch chromene) showed a non-trivial excitation-frequency dependence. Explicitly, the measured 2D spectra had a qualitatively different spectral shape along the pump frequency axis when analyzed for different probe frequencies. This indicates that the molecular dynamics observed at different transient signals (probe) are influenced by the excitation frequency.

Such qualitative comparisons of the 2D spectral shape along the pump frequency axis are shown in Fig. 4.3.1. The measurements were performed with visible whitelight probing and the pump was centered at 32200 cm^{-1} (311 nm).

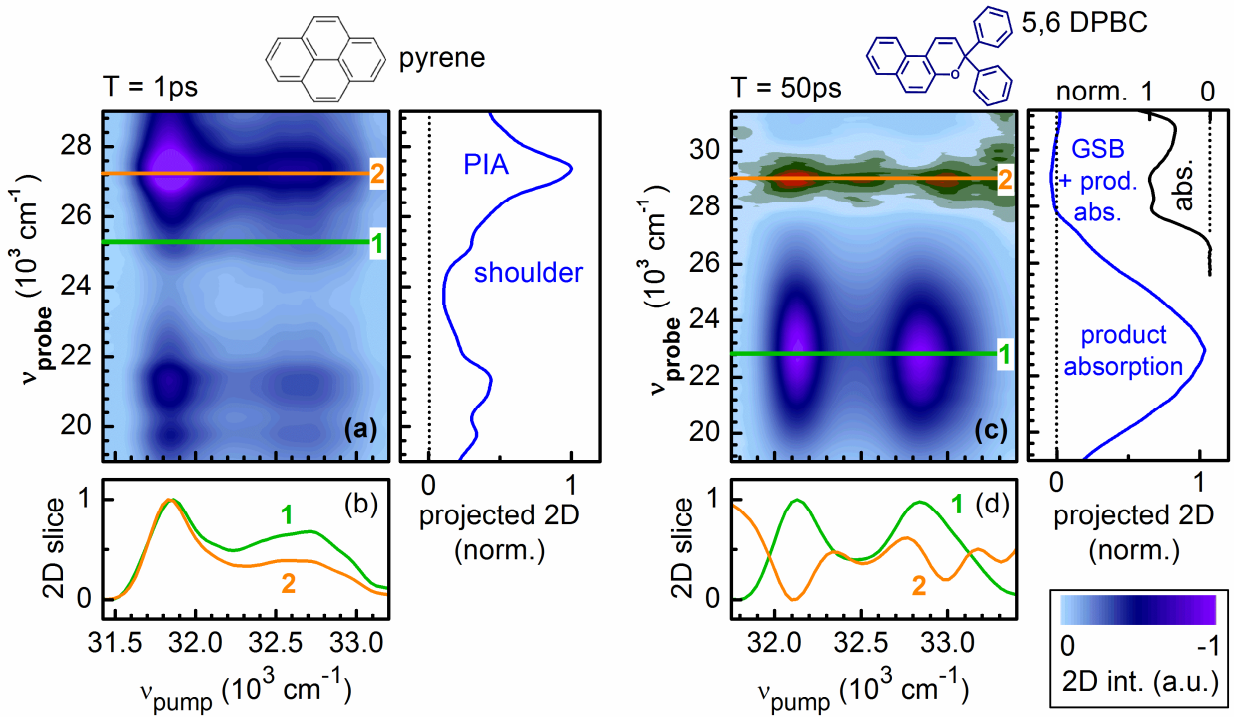

Fig. 4.3.1. Excitation-frequency dependent transient 2D spectra observed for (a, b) pyrene dissolved in methanol and (c, d) 5,6DPBC (chromene) dissolved in acetonitrile. (b) Comparison of the normalized 2D slice of the photo-induced absorption (PIA) for ν_{probe} = 25300 cm^{-1} and 27200 cm^{-1}. (d) Comparison of the normalized 2D slice for ν_{probe} = 22800 cm^{-1} (product absorption) and 29100 cm^{-1} (ground state bleach + product absorption). The qualitative differently shaped 2D slices (b, d) indicate excitation-frequency dependent molecular photoreactions. In both measurements the pump spectra had a central frequency of ν_{pump} = 32200 cm^{-1} (311 nm).

After excitation of the S_2 state, the transient signal of pyrene shows a photo-induced absorption (PIA) all over the visible spectral domain (Fig. 4.3.1a). The PIA is formed in about 85 fs after excitation. This time constant is assigned to an ultrafast internal conversion from the S_2 to the S_1 state (details see Chap. 5.1). However, the shoulder of the PIA band at ν_{probe} = 25300 cm^{-1} shows a qualitatively different spectral shape along the pump frequency axis when compared to the PIA amplitude at ν_{probe} = 27200 cm^{-1} (Fig. 4.3.1b). The molecules excited at about 32500 cm^{-1} give rise to a relatively stronger contribution at the PIA shoulder when compared to the molecules excited at lower pump frequencies. This indicates that the molecular dynamics of pyrene depends on the excitation frequency.

After excitation of the S_2 state, the photoswitch 5,6DPBC (chromene) undergoes a light-induced ring-opening reaction. The ring-open product shows a spectrally broad transient

absorption signal between ν_{probe} = 20000 and 26000 cm^{-1} (Fig. 4.3.1c). At ν_{probe} = 29000 cm^{-1} this product band overlays with the ground state bleach contribution of the S_1 state that has an opposite sign. When comparing the spectral shape of the 2D spectrum along the pump frequency axis for the pure product band (ν_{probe} = 22800 cm^{-1}) and the combination of ground state bleach and product absorption (ν_{probe} = 32200 cm^{-1}), they show a qualitatively different spectral shape (Fig. 4.3.1d). This shows that the amplitude ratio between the ground state bleach contribution and the product absorption depends explicitly on the excitation frequency, indicating that the photo-induced molecular dynamics of 5,6DPBC depends on the excitation frequency.

To elucidate the meaning of the correlation between the excitation-frequency observed at different probe frequencies, a quantitative description of the origin of the 2D amplitudes is derived in the following. The investigation of the light-induced molecular dynamics of pyrene and 5,6DPBC are described in Chap. 5.

4.3.2 Relation between pump-probe and 2D measurement

2D spectroscopy and transient pump-probe spectroscopy measure signals that are related to the light-induced third-order polarization $P^{(3)}$ of the investigated system. Nevertheless it is necessary to keep in mind, that both signals are of different nature when quantitatively related to $P^{(3)}$. As already mentioned in Chap. 4.1, there are different ways to process the measured data. The procedure to retrieve 2D spectral amplitudes which are directly proportional to the change in optical density (ΔOD) is used here. The 2D-UV measurement can then be understood as pump-frequency resolved pump-probe spectroscopy and the measured amplitudes are directly proportional to the population of the (electronic or vibrational) states of the investigated system and when dephasing processes have finished. In the following, the theoretical relation between pump-probe and 2D amplitudes is shortly reviewed.

The change of optical density ΔOD_{pp} measured in transient pump-probe spectroscopy can be calculated from the measured transmission of the probe pulse spectral intensity by [Kov99]

$$\Delta OD_{pp} = -\log\left(\frac{I^*}{I_0}\right), \tag{4.3.1}$$

with I* (and I_0) being the transmitted intensity of the probe with (and without) pump. Note, that

this calculation is done for a given population delay T (delay between pump and probe pulse) and for all individual probe angular frequencies $\omega_{pr} = 2\pi\nu_{pr}$ when the probe is spectrally resolved. For small pump induced transmission changes in the order of 10^{-3}, Eq. 4.3.1 can be written as described in appendix A.I and in Ref. [Kov99, Sch08] as:

$$\Delta OD_{pp} = -\frac{I^* - I_0}{I_0}\frac{1}{\ln 10}. \tag{4.3.2}$$

$(I^*-I^0)/I^0$ can be approximated in terms of the third-order polarization $P^{(3)}$ induced by the pump and probe pulse with the electric field spectral amplitudes $E(\omega)$ in the system as given in Eq. 4.3.3 [Kov99] (appendix A.II).

$$\Delta OD_{pp}(T,\omega_{pr}) = -2\omega_{pr}\,\mathrm{Im}\left[\,E^*_{pr}(\omega_{pr})P^{(3)}(T,\omega_{pr})\,\right] / \left|E_{pr}(\omega_{pr})\right|^2 \tag{4.3.3}$$

The pump-probe measurement is then related to $P^{(3)}$ as given in Eq. 4.3.4.

$$\Delta OD_{pp}(T,\omega_{pr}) \propto \frac{\omega_{pr}\,\mathrm{Re}\left(\,iP^{(3)}(T,\omega_{pr})\,\right)}{E_{pr}(\omega_{pr})}. \tag{4.3.4}$$

The imaginary factor i allows to write the real part component instead of the imaginary component of $P^{(3)}$. Note that this means that the change in optical density measured in pump-probe spectroscopy ΔOD_{pp} is not depending on the probe field but is proportional to only the pump intensity and the "complete" absorption coefficient α_{comp} [Muk00]. α_{comp} contains all the necessary components like the extinction coefficient of the initial system as well as the extinction coefficients of the excited state. This is only valid in the Markov approximation, where there are no coherent effects [Muk95]. Then the electric field can be factored out from the polarization $P^{(3)}$ (i.e. $P^{(3)} \propto \alpha_{comp}\left|E_{pump}\right|^2 E_{pr}$) leading to $\Delta OD_{pp} \propto \alpha_{comp}\left|E_{pump}\right|^2$, which is independent of the probe.

The 2D signal impinging on the probe detector in 2D spectroscopy can be written as given in Eq. 4.3.5 [Tek10, Tek12] (appendix A.II):

$$Sig_{2D}(\omega_{pu},T,\omega_{pr}) \propto \mathrm{Re}\left(\,i\omega_{pr}P^{(3)}(\omega_{pu},T,\omega_{pr})E^*_{pr}(\omega_{pr})\,\right) \tag{4.3.5}$$

with T being the population time and ω_{pu} being the pump frequency. Note, that the pump frequency is already retrieved by Fourier transformation of the coherence time τ which is the delay between the two pump pulses. To get from the 2D signal impinging on the detector (Eq. 4.3.5) to the final 2D spectrum, the evaluation procedure described in Chap. 4.2 has to be

theoretically applied. The first part of this procedure does involve phase cycling but does not change the proportionalities, as Eq. 4.3.5 only contains the 2D signal components. The second part of the evaluation procedure is the elimination of the probe spectral intensity distribution. It was mentioned in Chap. 4.1&2 that a division of the 2D signal after phase cycling by the spectral intensity distribution of the probe pulse retrieves 2D spectral amplitudes which are proportional to the change in optical density (ΔOD) as measured in transient pump-probe spectroscopy. This can now easily be seen by dividing Eq. 4.3.5 by the probe spectral intensity given by $\left|E_{pr}(\omega_{pr})\right|^2$. This leads to Eq. 4.3.6.

$$\begin{aligned} 2D_{OD}(\omega_{pu},T,\omega_{pr}) &\propto \frac{\mathrm{Re}\left(i\omega_{pr}P^{(3)}(\omega_{pu},T,\omega_{pr})E^{*}_{pr}(\omega_{pr})\right)}{\left|E_{pr}(\omega_{pr})\right|^2} \\ &\propto \frac{\omega_{pr}\,\mathrm{Re}\left(iP^{(3)}(\omega_{pu},T,\omega_{pr})\right)}{E_{pr}(\omega_{pr})}. \end{aligned} \tag{4.3.6}$$

When comparing Eq. 4.3.6 with Eq. 4.3.4, one can see that the amplitude of the 2D signal has the same proportionality to $P^{(3)}$ as the transient pump-probe amplitude. This fact is also stated by the projection slice theorem which says that the pump-integrated 2D spectrum equals the pump-probe measurement [Jon03]. It is worth noting, that one has to take special care how the 2D spectra are measured and calculated to guarantee such a relationship. The projection slice theorem now enables one to retrieve a quantitative relationship by using Eq. 4.3.7.

$$\int 2D_{pp}(\omega_{pu},T,\omega_{pr})d\omega_{pu} \overset{!}{=} \Delta OD_{pp}(T,\omega_{pr}). \tag{4.3.7}$$

Eq. 4.3.7 allows one to normalize the final 2D spectrum onto a pump-probe spectrum measured with only one pump pulse which has the intensity of the sum of the two pulses used in the 2D measurement. As already mentioned in Chap. 4.2, fortunately such a measurement is automatically done for the interpulse delay of zero ($\tau = 0$). Normalization of the 2D spectrum on this pump-probe spectrum results in a pump-wavelength resolved pump-probe (2D) spectrum with an amplitude value given as $\Delta OD/\nu_{pu}$. The measurement units are (cm^{-1}), which is a consequence of Eq. 4.3.7, because integration of the pump frequency axis of the 2D spectrum represents a transient spectrum which has amplitudes proportional to ΔOD.

Now that the amplitude of a 2D spectrum along the probe axis is quantitatively described it remains to clarify how the 2D spectral amplitudes along the pump-frequency axis emerge in a 2D measurement.

4.3.3 Influence of the pump spectral intensity distribution

The shape of the pump spectral intensity distribution directly modifies the shape of a 2D spectrum when a slice along the pump frequency (ν) axis is analyzed. To experimentally determine whether the electric field amplitude $\sqrt{I(\nu)}$, the spectral intensity I(ν) or the square of the spectral intensity $I^2(\nu)$ is contained in the 2D slice, an experiment with differently shaped pump pulse spectra was performed.

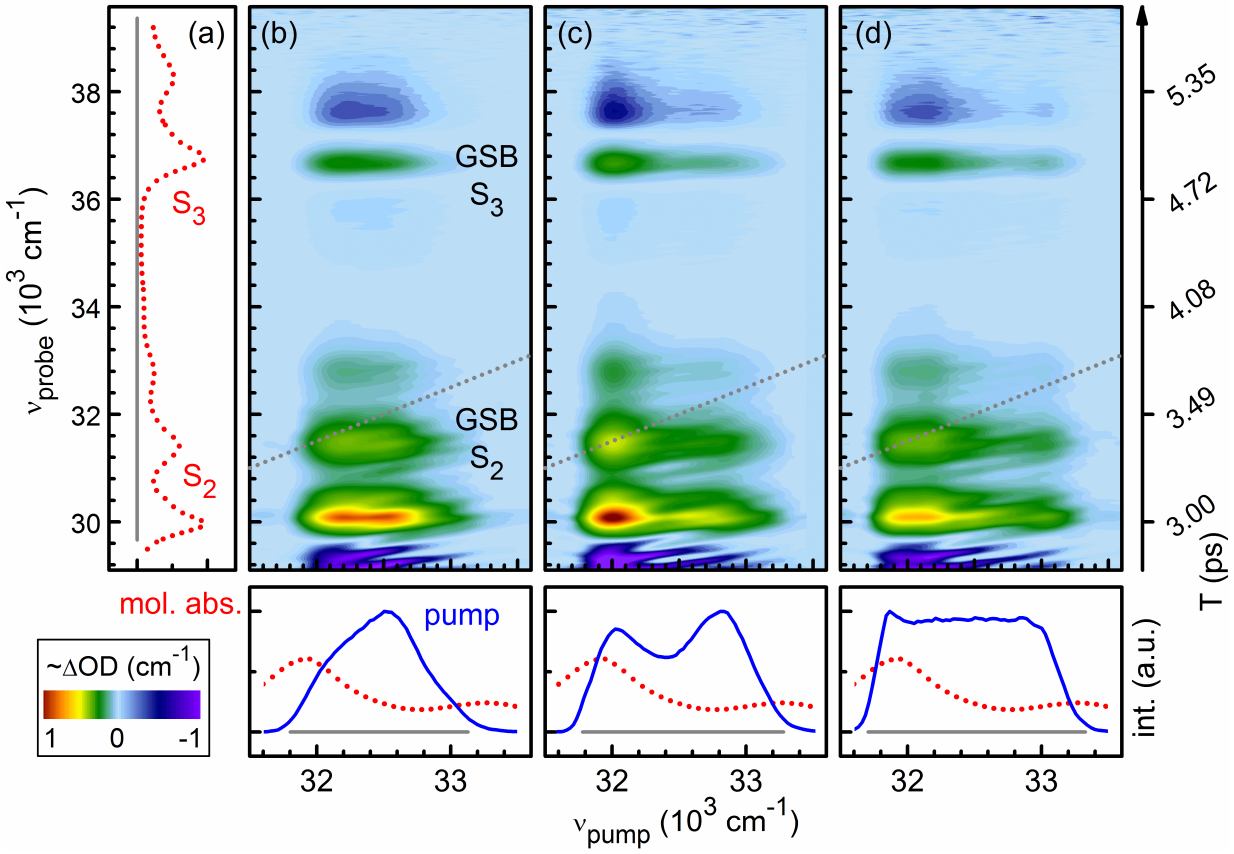

Fig. 4.3.2. 2D measurements of pyrene dissolved in methanol with UV whitelight probing. (a) Steady-state absorption spectrum (red dotted line). The 2D spectra show the ground state bleach contribution of the S_2 and S_3 state (color code: green to red) and the photo-induced absorption signal (color code: pink to violet). In each 2D measurement (b-d) only the pump pulse spectral shape (blue lines) was changed. Due to the chirp of the whitelight probe, each probe frequency has a different population time T (axis at the right part).

As an example pyrene solved in methanol was measured. In the 2D experiments an UV only supercontinuum white light was used for probing. The pump pulse spectra were centered at

310 nm, where the absorption of the S_2 state is present. The result is shown in Fig. 4.3.2 for population delays larger than 3 ps, which individually depend on the probe frequency due to the chirp of the probe pulse. For population delays larger than 3 ps, the ultrafast internal conversion from the S_2 to the S_1 state is finished. The transient signature is then comprised of strong ground state contributions of the S_2 state (ν_{probe} = 30000 to 34000 cm^{-1}) and the S_3 state (ν_{probe} ~ 37000 cm^{-1}) and the PIA signal after reaching the S_1 state (ν_{probe} = 29000 and 38000 cm^{-1}). When looking at the shape of the 2D spectra along the probe frequency axis, the transient signatures are identical for each pump pulse spectrum.

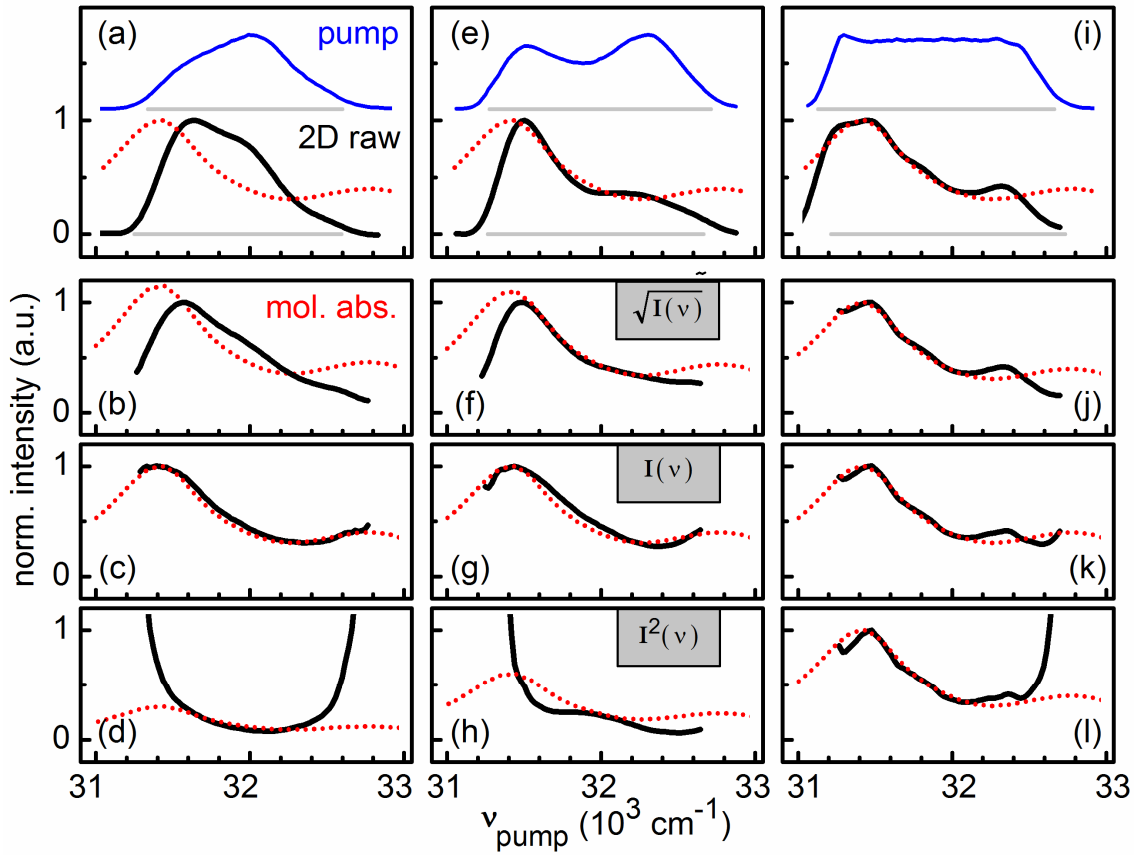

Fig. 4.3.3. Demonstration of the influence of the pump spectral intensity distribution in 2D spectroscopy. (a, e, i) Spectral intensity I(ν) of the pump pulses (blue line), 2D slice along the transient ground state bleach signal of pyrene (ν_{probe} = 36700 cm^{-1}, black line) and absorption spectrum of pyrene (red dotted line). When dividing the 2D slices with $\sqrt{I(\nu)}$ (b, f, j) or with $I^2(\nu)$ (d, h, l), the retrieved curves are differently shaped and the pump pulse spectral shape is not erased by the division. For division with I(ν), the retrieved curves are very similar and follow the shape of the absorption spectrum. This demonstrates that the shape of a 2D measurement along the pump axis is proportional to I(ν).

To analyze the shape along the pump frequency axis, 2D slices along the pump axis were taken at the probe frequency of about 36700 cm^{-1} where the ground state bleach of the S_3 state is dominant. Due to the chirp of the UV whitelight probe each probe frequency has a different population delay. The population time for the selected probe frequency is about 5 ps. As the ground state bleach signal of pyrene does not show significant pump-frequency dependence here, the 2D amplitudes are directly proportional to the amount of excited molecules. The results for dividing the 2D slices with the differently scaled pump pulse spectra are shown in Fig. 4.3.3.

When comparing the scaled 2D slices for different spectral pump pulse shapes (Fig. 4.3.3(a, e, i)) it becomes obvious that only for scaling with $I(\nu)$ the retrieved curves have similar spectral shapes (Fig. 4.3.3(c, g, k). When scaling with $\sqrt{I(\nu)}$ (Fig. 4.3.3(b, f, j)) and $I^2(\nu)$ (Fig. 4.3.3(b, f, j)), strong deviations of the retrieved curves for different pump pulse spectra are observed. This shows that the shape of a 2D spectrum along the pump frequency axis is linearly depending on the pump pulse spectral intensity distribution. The shape of the retrieved curves for scaling with $I(\nu)$ follows nearly perfectly the shape of the absorption spectrum of the molecule (red dotted line in Fig. 4.3.3).

The result of Fig. 4.3.3 show that for pyrene the pump-frequency dependent amount of excited molecules behaves qualitatively as the multiplication of the absorption spectrum with the pump spectral intensity distribution. To use this understanding quantitatively to calculate absolute product yields, e.g., of a light-induced photoreaction, the pump-frequency dependent excitation probability has to be considered theoretically.

For molecules which are initially in the ground state, the excitation probability P_{exc} at the pump frequency ν is given by the excitation photon density $n_{ph}(\nu)$ and the absorption cross-section $\sigma(\nu)$ of the system according to Eq. 4.3.8 [Meg09].

$$P_{exc}(\nu) = n_{ph}(\nu)\,\sigma(\nu)\,. \qquad (4.3.8)$$

Note that Eq. 4.3.8 is linearly depending on the photon density and is only valid for weak excitation intensities. For higher intensities the influence of saturation effects and multi-photon absorption has to be taken into account. However, for $P_{exc} < 10$ % those effects can be neglected, which is always the case for all the spectroscopic experiments done in this work. For a Gaussian spatial intensity distribution the photon density in the sample can be written as given in Eq. 4.3.9 [Meg09].

$$n_{ph}(\nu) = \frac{N_{h\nu}(\nu)\ln 2}{\pi D_{pu}{}^2/4}. \tag{4.3.9}$$

With D_{pu} being the FWHM of the spatial intensity distribution of the pump beam. $N_{h\nu}(\nu)$ is the frequency dependent photon number. $N_{h\nu}(\nu)$ is defined by the photons per frequency range $\Delta\nu$. For $\Delta\nu \rightarrow 0$ the frequency dependent photon number resembles the shape of the spectral intensity distribution $I_{pump}(\nu)$ of the pump pulses.

Using only the pump beam size in Eq. 4.3.9 is an approximation valid only if the probe beam size is small compared to the pump beam size. When the probe spot size is in the order of the pump spot size, $D_{pu}{}^2$ has to be replaced by ($D_{pu}{}^2 + D_{probe}{}^2$), with D_{probe} being the FWHM of the spatial intensity distribution of the probe beam in the sample (details see appendix A.IV).

The absorption cross-section can be written in terms of the molar extinction coefficient $\varepsilon(\nu)$ according to Eq. 4.3.10 [Meg09].

$$\sigma(\nu) = \varepsilon(\nu)\frac{\ln 10}{N_A}, \tag{4.3.10}$$

with $N_A = 6.0221 \cdot 10^{23}$ mol^{-1} being the Avogadro constant. The pump-frequency dependent excitation probability can now be written as given in Eq. 4.3.11.

$$P_{exc}(\nu) = \frac{N_{h\nu}(\nu)\ln 2}{\pi D_{pu}{}^2/4}\varepsilon(\nu)\frac{\ln 10}{N_A}. \tag{4.3.11}$$

The excitation probability, which is proportional to the amount of excited molecules, is therefore linear proportional to the $\varepsilon(\nu)$ and $N_{h\nu}(\nu)$.

It is necessary to retrieve $N_{h\nu}(\nu)$ from the experiment. For that, the spectral intensity distribution of the pump pulses is measured separately for each 2D measurement with a spectrometer. The spectrometer used here was a grating based spectrometer (HR2000+, OceanOptics) with a CCD as the detector. Due to the grating, the spectrometer has a linear wavelength scale with constant bin widths $\Delta\lambda$ at each wavelength points. Due to the CCD the spectrometer is automatically a photon counting device; therefore the measured signal is directly proportional to the number of photons in each $\Delta\lambda$. The wavelength dependence of the CCD sensitivity was neglected because the pump pulse spectrum is fairly narrow and this is only a minor effect. To get from the wavelength scale of the spectrometer to a frequency scale (e.g., wavenumbers), the measured photon counts $N_{h\nu}(\lambda)$ at each measured wavelength λ have to be corrected as given in Eq. 4.3.12.

$$N_{h\nu}(\nu) \propto \frac{N_{h\nu}(\lambda)}{\lambda^2}. \tag{4.3.12}$$

Eq. 4.3.12 is a consequence of the nonlinear relationship between the bin width of the frequency and wavelength scales.

In principle the spectrometer can be calibrated to give absolute photon counts but this is quite elaborate. Therefore it is better to use a power meter and measure the complete pulse energy PE_{pump} which can then be used to calculate the complete amount of photons in the pulse $N_{h\nu}^{total} = PE_{pump}/h\nu_{central}$, with $\nu_{central}$ being the *central* frequency of the pulse. The *central* frequency can be retrieved as the intensity weighted barycenter of the measured spectrum. $N_{h\nu}(\nu)$ can now be scaled to retrieve the real amount of photons at different frequencies by fulfilling Eq. 4.3.13.

$$\int N_{h\nu}(\nu)d\nu = N_{h\nu}^{total}. \tag{4.3.13}$$

The calculation of $N_{h\nu}(\nu)$ requires the precise determination of the pump pulse energy PE_{pump}. However, due to the optical density of the sample, the pump pulse energy is attenuated within the sample along the propagation distance x according to [Sail12]

$$PE_{pump}(x) = PE_{pump} \cdot 10^{-OD\, x/d}. \tag{4.3.14}$$

d is the thickness of the sample (d = 110 μm). The effective pump pulse energy is therefore given by [Sail12]

$$PE_{pump}^{ave} = \frac{1}{d}\int_0^d PE_{pump}(x)dx = PE_{pump}\frac{1-10^{-OD}}{OD\ln 10}. \tag{4.3.15}$$

This leads to a correction factor of typically 20 % for optical densities used in the 2D experiments of about 0.2.

When all parameters of P_{exc} (Eq. 4.3.11) are known, the pump-frequency dependent absolute excitation probability can be calculated in a 2D experiment. Note, that $P_{exc}(\nu)$ is only valid for calculating the amount of excited molecules. Pump-frequency dependent processes or dynamics can change the spectral shape of a 2D slice along the pump axis. Then the 2D slice does not have to resemble the amount of excited molecules anymore.

4.3.4 Extraction of quantum yields from 2D measurements

To extract the pump-frequency dependent yield of a photoreaction, the amount of initially excited molecules has to be compared with the absolute amount of molecules in a specific state after the photoreaction. For 2D spectroscopy this relation can be resolved spectrally for different excitation frequencies.

For transient absorption spectroscopy, the photo-induced product quantum yield of a product state (Q_{prod}) after excitation is given by the ratio of the concentration of the molecules in the product state (c_{prod}) and the concentration of excited molecules (c_{exc}) as given in Eq. 4.3.16 [Sai13].

$$Q_{prod} = \frac{c_{prod}}{c_{exc}}. \tag{4.3.16}$$

The concentration of excited molecules is described by the multiplication of the concentration of the educt molecules (in solution) before excitation (c_{educt}) with the excitation probability $P_{exc}(\nu_{pump})$. The excitation probability of a 2D measurement depends on the excitation frequency ν_{pump}.

The concentration of molecules in the product state can be calculated from the measured change in optical density ΔOD_{prod} that is induced by this form when the molar extinction coefficient of this form ε_{prod} is known. Depending on the system investigated, the transient signal can be the ground state bleach, excited state absorption or stimulated emission contribution at a specific probe frequency ν_{probe}. Compared to conventional transient absorption spectroscopy, for 2D spectroscopy ΔOD depends additionally on the excitation (pump) frequency.

The excitation frequency dependent 2D quantum yield then reads as given in Eq. 4.3.17.

$$Q_{prod}(\nu_{pump}) = \frac{\Delta OD(\nu_{pump}, \nu_{probe}) / (d \cdot \varepsilon_{prod}(\nu_{probe}))}{c_{educt} \cdot P_{exc}(\nu_{pump})}. \tag{4.3.17}$$

d is the thickness of the sample, e.g., the thickness of a flow cell. As discussed in Chap. 4.3.1, a 2D measurement can be performed in such a way that the amplitude of the 2D spectrum is given in absolute units of ΔOD. Then Eq. 4.3.17 allows calculating absolute reaction quantum yields with 2D spectroscopy.

The error in the product yield calculation is originating from the uncertainties of the individually measured parameters used in Eq. 4.3.17 and can directly be calculated by using the uncertainties of the individual parameters. As an estimate, such an uncertainty in the

experiments performed here is about 11 %.

Additionally to the uncertainties originating from the uncertainty of the parameters used in the calculations there is yet another aspect that has to be kept in mind. The uncertainty also originates from an incorrect frequency calibration of the individually measured spectra, e.g., the pump spectrum and the absorption spectrum which are typically measured with different types of spectrometers. As for the quantum yield calculations one is multiplying or dividing these frequency resolved spectra, an incorrect frequency calibration means an unphysical shift of the individual spectra with respect to each other.

However, a way to circumvent this problem is to use the same spectrometer for all measured spectra. While for the wavelength calibration of the pulse shaper one is generally using the same spectrometer as for the pump pulse measurement this is typically not the case for the absorption spectrometer. This can be achieved by building a fiber coupled absorption spectrometer with the same spectrometer.

The error due to the frequency calibration is typically smaller than the overall uncertainty originating from the uncertainty of the individual parameters used in Eq. 3.1.17. An analysis of influence of an incorrect frequency calibration on the retrieved product yields is given in appendix A.V.

The application of the product yield calculation of 2D measurements is done for pyrene and 5,6DPBC (photoswitch chromene) in Chap. 5.1 and Chap. 5.2, respectively.

5. 2D-UV measurements of excitation-frequency dependent molecular dynamics

Due to the quantum nature of light the energy deposited in a molecule when a photon is absorbed depends only on the energy, and thus the frequency, of the absorbed photon itself. For visible or UV photons the optically active transitions in a molecule are typically the excitation of an energetically higher lying electronic state with the respective vibrational substructure. It has been discovered in photochemistry that the outcome of a light-induced photoreaction can depend on the specific electronic or vibrational state addressed [Les91, Nak98, Led98, Gen02, Kim03]. Such excitation-frequency dependent molecular dynamics are ideally suited to be investigated by 2D spectroscopy. Due to the excitation-frequency resolution, 2D spectroscopy reveals directly the correlation between the energy of the absorbed photon (excitation) and the outcome of the photoreaction.

In this chapter, the capability of broadband 2D-UV spectroscopy to investigate excitation-frequency dependent molecular dynamics is demonstrated for molecules that have their absorption in the UV spectral domain. The two molecules selected in this study have distinct absorption bands of different vibrational modes in the spectral region that overlaps with the large but still limited spectral bandwidth of the pump pulses used (~ 25 nm).

5.1 Ultrafast internal conversion in pyrene

Pyrene is a rigid, compact and versatile molecule that is used in various applications in biophysics, e.g., as a sensor incorporated in membranes and for monitoring protein structures and conformations [Pen02, Bai11]. Pyrene is also used to probe the solvent polarity [Rei94] due to a change of its fluorescence characteristics for different polarities of the surrounding. Furthermore it comprises the building block for many larger photoactive molecules, e.g., antenna systems [Tal00].

Despite this versatility and the simplicity of the molecular structure, pyrene shows a complex inter- and intramolecular photophysic: 1) The S_1 state shows very weak absorption strength yet after excitation into higher electronic states the literature reports suggest that the emission originates mainly from the S_1 state. Typical S_1 fluorescence quantum yields of pure pyrene dissolved in solution (< 1µM concentration) are in the order of 70 % [Kar95]. 2) The intermolecular energy redistribution after excitation of higher electronic states involves strong vibronic couplings of the electronics states [Dei71] leading to a fast $S_n - S_1$ internal conversion that has been measured to be faster than 150 fs [Fog95, Neu99] (85 fs measured here). 3) The vibrational coupling depends explicitly on the solvent polarity [Dei74, Kar95]. 4) All these processes are excitation energy dependent, leading ultimately to a fluorescence contribution originating from the S_2 state in a supersonic jet or gas phase [Dei71, Num12]. 5) For high concentrations of pyrene (>1 mM) in solutions a temporally delayed red shifted fluorescence is observed which is attributed to an excimer. An excimer is a dimer that is only bound in the excited state. However, the literature reports interpret the mechanism leading to the delayed florescence rather differently: Due to the formation of the excimers, by diffusion controlled collision of one ground state and one excited molecule [Mar87, Rut93] or from dimers that are already bound in the ground state [And92, Kha01]. The delayed fluorescence was also interpreted as a result of triplet-triplet annihilation processes, via the interaction of two triplet-state molecules [Gre73, Boh90].

Over the past decades the molecule has been subject to intensive studies [Bir75, Win93, Par06] both theoretically and experimentally in gas phase as well as in condensed phase. However, the mechanism of the ultrafast internal conversion process in the first hundreds of femtoseconds after excitation is not yet fully understood. To decipher this process, it is of major importance to resolve the question whether the excimer formation is diffusion controlled or if there are ground state dimers present. The study done here focuses on the investigation of the internal conversion and the excimer formation and how these processes are influenced by the excitation energy.

5.1.1 Introduction to the photophysics of pyrene

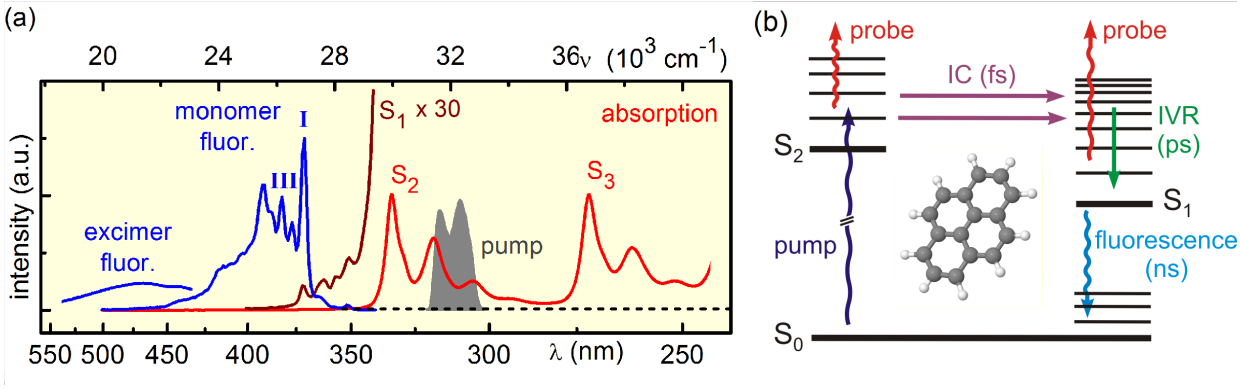

Fig. 5.1.1. (a) Absorption and emission spectra (with the bands I and II marked) of pyrene in methanol. The S_1 absorption region is scaled up for clarity. The pump spectra used in all upcoming experiments is shown in grey. (b) Scheme showing the relaxation processes of pyrene after excitation of the S_2 state [adapted from Num12]. IC: internal conversion, IVR: internal vibrational relaxation.

Pyrene has its absorption in the UV spectral domain and shows distinct electronic absorption bands. Each electronic absorption band consists of a variety of vibrational modes that give rise to the structure in the absorption spectra (Fig. 5.1.1a) [Bab09]. The S_1 $^1B_{3u}$ ← S_0 ^1A_g absorption is weak compared to the absorption into higher lying electronic states (e.g., S_2 $^1B_{2u}$ ← S_0 ^1A_g) because this transition is forbidden due to the symmetry of the states [Bab09]. When pyrene is excited to higher electronic states (S_n, n>2) a fast (85 fs for the S_2 state) internal conversion to the S_1 state occurs mediated by vibronic coupling of the electronic states [Fog95, Neu99] (Fig. 5.1.1b).

Starting from the excited electronic S_1 state multiple processes happen. They give rise to signals detected in ultrafast spectroscopy and they are therefore shortly discussed in the following. From the S_1 state, intersystem crossing to the triplet state, internal conversion and fluorescence as well as excimer formation can occur.

Intersystem crossing, internal conversion and fluorescence. The S_1 excited state lifetime of pyrene dissolved in methanol for a concentration of about 10^{-2} mM was measured to 339 ns and the fluorescence quantum yield to 0.75 [Kar95]. These values are observed to be concentration dependent. This means that the nonradiative relaxation processes or intersystem crossing to the T_1 state are slow compared to the fluorescence. All these processes are fairly slow compared to internal conversion from the S_2 state or vibrational relaxation in the S_1 state and only give rise

to negligible constant contributions on the ps time scale of the measurements presented here.

The fluorescence spectrum (Fig. 4.4.1a) shows individual peaks that are attributed to vibrational bands of the ground state [Kar95]. The relative band intensities of the I band (S_1 $^{\nu=0} \rightarrow S_0$ $^{\nu=0}$) and the III band (S_1 $^{\nu=0} \rightarrow S_0$ $^{\nu=1}$) depend linearly on the solvent polarity [Kar95]. This behavior was explained by dipole – induced dipole interactions between the solvent and the molecule affecting the vibrational coupling between S_1 and S_2 [Kar95]. It is a consequence of the vibronic coupling perturbations arising from the Herzberg-Teller effect and non-Born-Oppenheimer vibronic coupling. This coupling influences the two bands of the fluorescence differently because the I band is modulated by the coupling to the S_2 state.

Foggi et. al [Fog95, Neu99] directly observed that the S_2 to S_1 internal conversion occurs within 150 fs measured by femtosecond transient spectroscopy in solution. They found that the rate of formation of the S_1 state is a function of the electronic state excited. For excitation of higher electronic states, the formation of the S_1 state had a longer time constant (about 400 fs when excitation of the S_4 state). The time constant of the internal vibrational excess energy redistribution after formation of the S_1 state was found to be about 4 ps for all measurements exciting different electronic states.

Excimers. Because the existence of excited dimeric complexes may be relevant when retrieving results from the 2D measurements, this topic will be discussed in detail in the following. The excimers give rise to fluorescence which is red shifted compared to the monomeric S_1 fluorescence by roughly 5500 cm^{-1} and is found for concentrations even below 1 mM. (Fig. 5.1.1a). The ratio of monomer to dimer fluorescence is shifted nearly completely to the favor of dimer fluorescence for higher concentrations. The red shift is a consequence of the potential energy curves of the excimers [Win93, Bar93, Kha01].

According to the literature, excimers are formed either from one singlet-excited molecule and one ground state molecule [Bir75, Win93] or by triplet-triplet annihilation of two triplet-state molecules [Gre73, Boh90]. However, the literature reports seem to be inconclusive regarding the interpretation of the formation of an excimer. Either by diffusion controlled collisions of one excited molecule with one ground state molecules [Mar92, Bar93, Rut93, Win93, Dyk98, Akb05, Sab10] or by excitation of two molecules that are already bound in their ground state [And92, Kha01].

The diffusion controlled generation of excimers of pure pyrene dissolved in solution was concluded from ns-fluorescence measurements that showed that the dimer fluorescence is

delayed compared to the instantaneous appearing S_1 fluorescence. The temporal behavior of the transient excimer formation dynamics depends on the solvent [Bir63, Dyk98], the concentration [Mar87, Mar92] and the temperature [Mar92]. This dependence is explained by formation of excimers by a diffusion controlled collision of an excited monomer with a ground state monomer. A typical value of the rise time of the excimer fluorescence after excitation at room temperature is about 58 ns in tetradecane (10^{-3} M) [Dyk98]. Martinho et al. could show that the experimental findings for different concentrations and temperatures of pyrene dissolved in cyclohexanol can be well described by a model which incorporates the diffusion controlled excimer formation [Mar92]. Furthermore, newer studies of pure pyrene in o-dichlorobenzene could exclude the formation of ground state dimers [Akb05].

Despite the findings favoring the excimer formation after excitation of monomers, there are also reports in the literature proposing pyrene dimers bound in their ground state. These findings are nearly exclusively limited to substituted pyrene compounds [Win93, Rut93, Akb05] or for pyrene not freely dissolved in solution, e.g., pyrene bound to solid surfaces [Fuj88], pyrene crystals [Bir75, Win93] or incorporated in amorphous silica glass [Yam91]. However, Anderiessen et al. suggested the existence of ground state dimers of pure pyrene dissolved in cyclohexane at room temperature [And92]. The authors came to the conclusion that there should be ground state dimers by using quenching experiments and by observing a difference in the fluorescence excitation spectra monitoring the monomer respectively dimer fluorescence. Additionally, previous reports indicate remaining excimer fluorescence when a solution of pyrene in cyclohexane is frozen down to 77 K even for low concentrations (10^{-5} M) [Fer65]. Because in the frozen state the pyrene molecules can not collide due to diffusion, the existence of ground state dimers seems feasible. Also the binding energy of pyrene molecules in the ground state was calculated for the gas phase to be in the order of 12 kcal/mol [Gri04] which is significant higher than the room temperature energy which is in the order of 0.6 kcal/mol. When concurring with the solvation energy for free pyrene molecules in solution, ground state association should be present to some extent.

In summary, the former mentioned results indicate that the existence of ground state dimers is most probably mainly a question of the solvent and the surrounding rather than a general property of pyrene. Therefore, the amount of possible ground state dimers has to be checked for the experiments done in this work. To do this, the absorption spectra and fluorescence excitation spectra for the monomer and excimer fluorescence were measured for pyrene dissolved in methanol at room temperature (1 mM). The experiments showed that there is no

concentration dependent change in the shape of both absorption and fluorescence excitation spectra (data not shown). This indicates that any possible ground state dimers do not strongly interact electronically. However, due to the hydrophobic character of pyrene and the hydrophilic solvent like methanol, the existence of loosely bound pyrene molecules pushed together by the repulsive solvent cage seems feasible. Then the formation of a bound excimer can happen very fast after the excitation of one of the monomers without the time delay introduced by the diffusion controlled mechanism. When taking into account that the two molecules still have to move and rotate to the correct orientation with respect to each other, the formation of excimers could then happen within some ps after excitation.

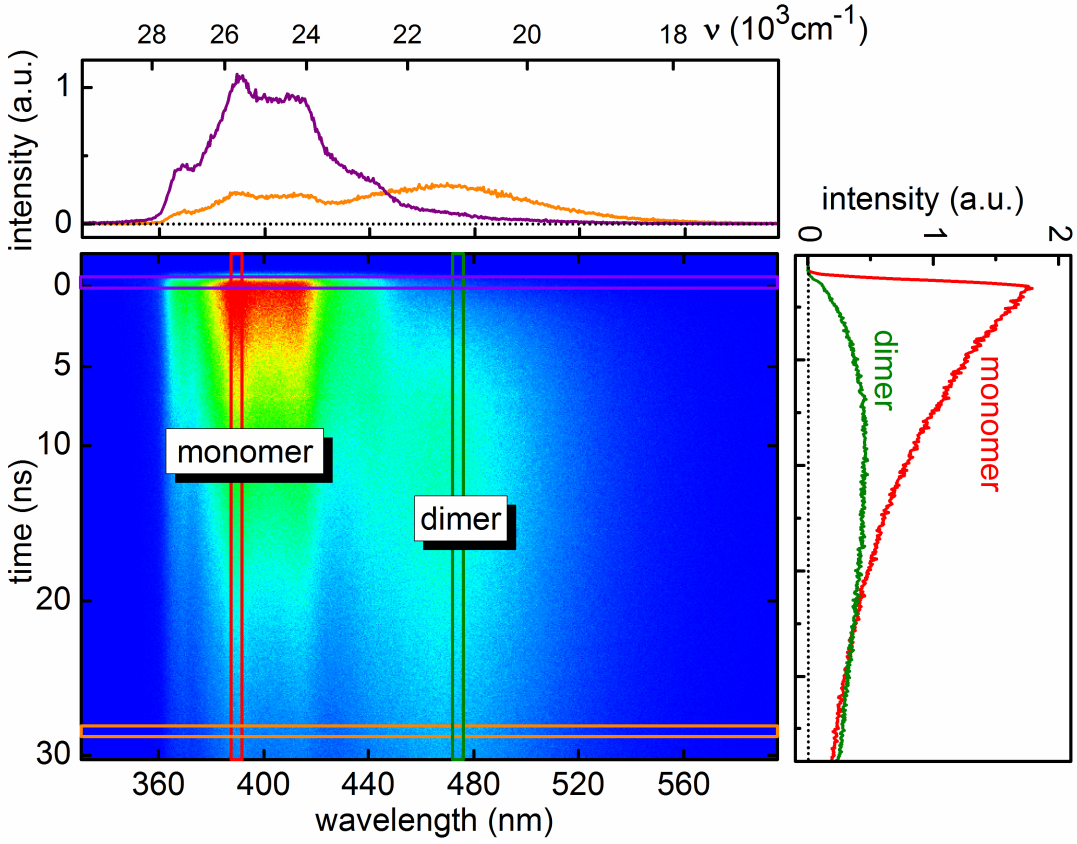

Fig. 5.1.2. Time-resolved fluorescence measurement of pyrene dissolved in methanol. The measurement shows the formation of the dimers fluorescence at 465 nm after excitation of the monomers that have a S_1 fluorescence spectrum at around 400 nm.

To further investigate the formation process of excimers, we measured the time resolved ns fluorescence of pyrene dissolved in methanol after excitation at 308 nm. The result for a 1 mM solution of pyrene dissolved in methanol is shown in Fig. 5.1.2. The monomer fluorescence shows a strong contribution around 390 nm and occurs instantaneous after excitation. The

monoexponential decay of this fluorescence contribution has a time constant of 13.8 ns. The dimer fluorescence at about 475 nm shows a rise after excitation and a decay for longer time. The excimer fluorescence can be fitted with 2 exponential functions with a rise time of 11 ns and a decay time of 14 ns. As there is no significant amount of dimer fluorescence present in the sub-ns time scale, the existence of a majority of stable ground state dimers that form fluorescing excimers in the ps regime is unlikely.

However, the delayed fluorescence can also originate from the formation of a fluorescing excimers state, e.g., a charge separated state, from a non-fluorescing intermediate monomer like excimer state within the 10 ns rise time. Diffusion controlled collisions can then lead to quenching processes that lead to the concentration dependent fluorescence dynamics as observed in the literature [Mar87, Mar92], despite that these findings were solely interpreted as diffusion controlled excimer formation by collision of one excited and one ground state monomer.

In pyrene crystals a two-step excimer formation process was indeed postulated [Sey92]. The metastable intermediate B-state shows a blue-shifted fluorescence relative to the excimer fluorescence that is less structured than the dissolved pyrene monomer fluorescence. The monomer like fluorescence in Fig. 5.1.2 is indeed less structured than the steady-state fluorescence spectrum (Fig. 5.1.1a). This makes the existence of an intermediate state that is formed from loosely bound ground state dimers plausible. Then a fraction of the pyrene molecules in solution are loosely bound while another fraction is monomeric. This result is in conclusion with ongoing spectroscopic and chemical investigations that are in progress when this thesis was finished. Nuclear magnetic resonance measurements of pyrene dissolved in methanol indicate the existence of a fraction bound ground state molecules that is so far only sure to be much less than 50 % [Fel13].

5.1.2 Molecular dynamics revealed by transient spectroscopy

In Fig. 5.1.3 the first 15 ps of the transient absorption measurement of pyrene in methanol (1 mM) are shown. Note, that the pyrene solution measured are not free of dissolved oxygen, which is however expected to influence only the ns long time behavior of the photodynamics. As pump pulse, a spectrally broadened pulse with a central wavelength of 310 nm and a pulse length of about 40 fs was used. This pulse covers a substantial part of the second and third

vibrational band of the $S_2\ ^1B_{2u} \leftarrow S_0\ ^1A_g$ absorption. As probe a visible white light continuum in the magical angle polarization configuration was used [Meg09]. Note, that additional transient absorption measurements performed with longer pump-probe delays showed, that the transient spectrum in the magic-angle configuration does reach a stable form after 15 ps and does not change significantly within the 150 ps maximum delay measured (data not shown).

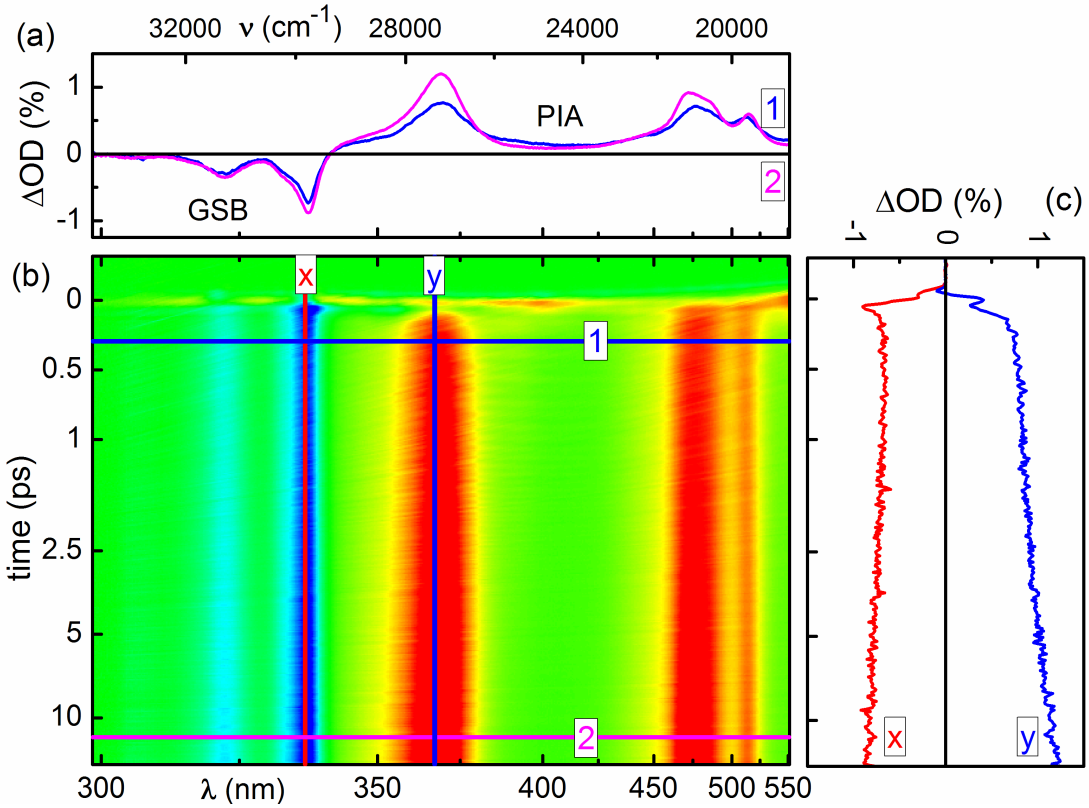

Fig. 5.1.3. Transient pump-probe measurement of pyrene in methanol. (a) Transient spectra at 300 fs [1] and 13 ps [2] showing the photo-included (PIA) and the ground state bleach (GSB) contributions. (b) Complete transient scan with a maximum pump-probe delay of 15 ps. (c) Selected time traces at 325 nm ([x], GSB) and 365 nm ([y], PIA).

The transient spectrum shows contribution of the ground state bleach between 290 - 330 nm and distinguishable photo-induced absorption signatures around 360 and 470 nm (Fig. 5.1.3a). Additional transient absorption features visible at 400 and 550 nm decay in about 85 fs. These signals can be attributed to the ESA of the S_2 state that vanishes due to the ultrafast internal conversion into the lower lying electronic S_1 state. Reports in the literature assigned the transient absorption band at 550 nm to the $S_{14} \leftarrow S_2$ absorption [Neu99]. The long lasting PIA signals between 350 and 525 nm show an ultrafast rise in about 85 fs. They are therefore

assigned to the ESA of the S_1 state. On the ps time scale, the time traces (Fig. 5.1.3c) show a weak increase in the GSB contribution at 335 nm and a significant increase of the S_1 ESA amplitude at 365 nm happening with a time constant of 4.7 ps.

These transient dynamics with a time constant of 4.7 ps can have two origins. On the one side, it can be a result of internal vibrational energy redistribution (IVR) and vibrational relaxation of the excess energy in the S_1 state after IC from the initially excited S_2 state. The weak increase of the GSB contribution can then be understood as a change in an ESA contribution that spectrally overlaps with the GSB. This interpretation is in accordance with the results reported in Ref. [Fog95, Neu99] who found a very similar time constant of about 4 ps for the vibrational cooling processes.

Alternatively, the dynamics can result from the formation of a non-fluorescence excimer like structure from loosely bound ground state dimers present in solution. When excimers are formed in a few ps after excitation, the GSB and ESA signal should increase due to the interaction of a second molecule with the excited one which then should induce an increase in the signal amplitudes. The increase of the ground state bleach is in the order of 20 % (Fig. 5.1.3c) and suggests that the relative amount of loosely bound ground state dimers present in solution is less than 20 %.

When the ps dynamics originate from IVR and vibrational relaxation in the monomeric S_1 state, a transient ESA signal should present in the GSB region. To see that there is indeed an underlying ESA contribution between 300 – 340 nm, the steady-state absorption spectrum was decomposed from the transient spectrum for a pump-probe delay of 120 ps. The result is shown in Fig. 5.1.4.

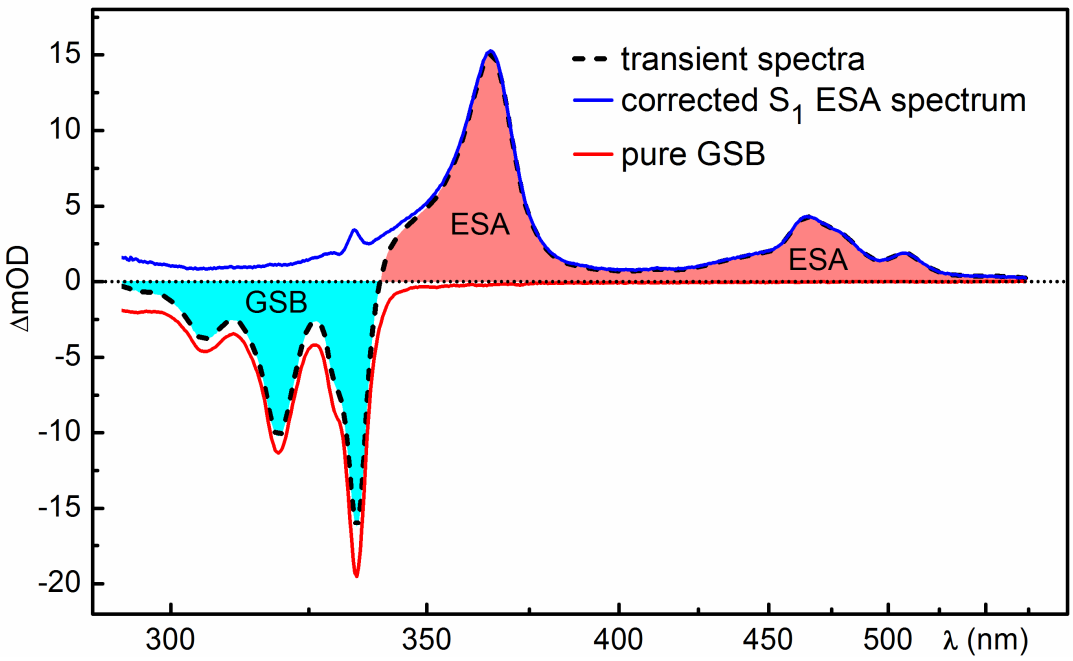

Fig. 5.1.4. Transient absorption measurement of pyrene for a pump-probe delay of 120 ps to retrieve the extinction coefficient ε_{prod} of the product state. The scaled absorption spectrum (red line) was subtracted from the measured transient spectrum (black dashed line) to retrieve the pure S_1 ESA spectrum (blue line).

For the measured delay of 120 ps, vibrational relaxation processes have finished and the molecules have reached the vibrational ground state of the S_1 state. The scaled subtraction of the absorption spectrum from the ESA spectrum results in smooth corrected ESA spectrum. The narrowband modulation of the corrected ESA spectrum at 365 nm is an evaluation error due to the limited spectral resolution and has no physical meaning. The corrected S_1 ESA spectrum shows a significant amount of transient absorption present in the spectral region of the GSB.

The weak increase of the GSB with a time constant of 4.7 ps observed in the transient measurement (Fig. 5.1.3c, red line) can then be understood as an amplitude change of the underlying ESA. As will be show in the next chapter for the spectral region of 385 - 410 nm, it is most plausible that an additional ESA band originating from higher vibrational levels of the S_1 state is present also at the GSB region. Due to IVR and vibrational relaxation in the electronic S_1 state, this additional ESA contribution then vanishes with 4.7 ps, accompanied by the increase of the ESA band at 365 nm (Fig. 5.1.3c, blue line).

To deduce the influence of vibrational progression in the molecular dynamics, a high-temporal resolution transient pump-probe experiment was performed. The result is shown in Fig. 5.1.5.

The temporal resolution of the experiment was in the order of 60 fs. The measurements were performed with a parallel polarization between the pump and the probe pulse to achieve a higher sensitivity.

In Fig. 5.1.5 the S_2 ESA is clearly resolved at 580 nm and decays with 85 fs as discussed before. The GSB peak at 334 nm shows a decrease in amplitude that can be fitted with a monoexponential decay time of about 6 - 7 ps. This decay is most likely due to the rotation of the molecules as the measurements were performed with parallel polarization between pump and probe.

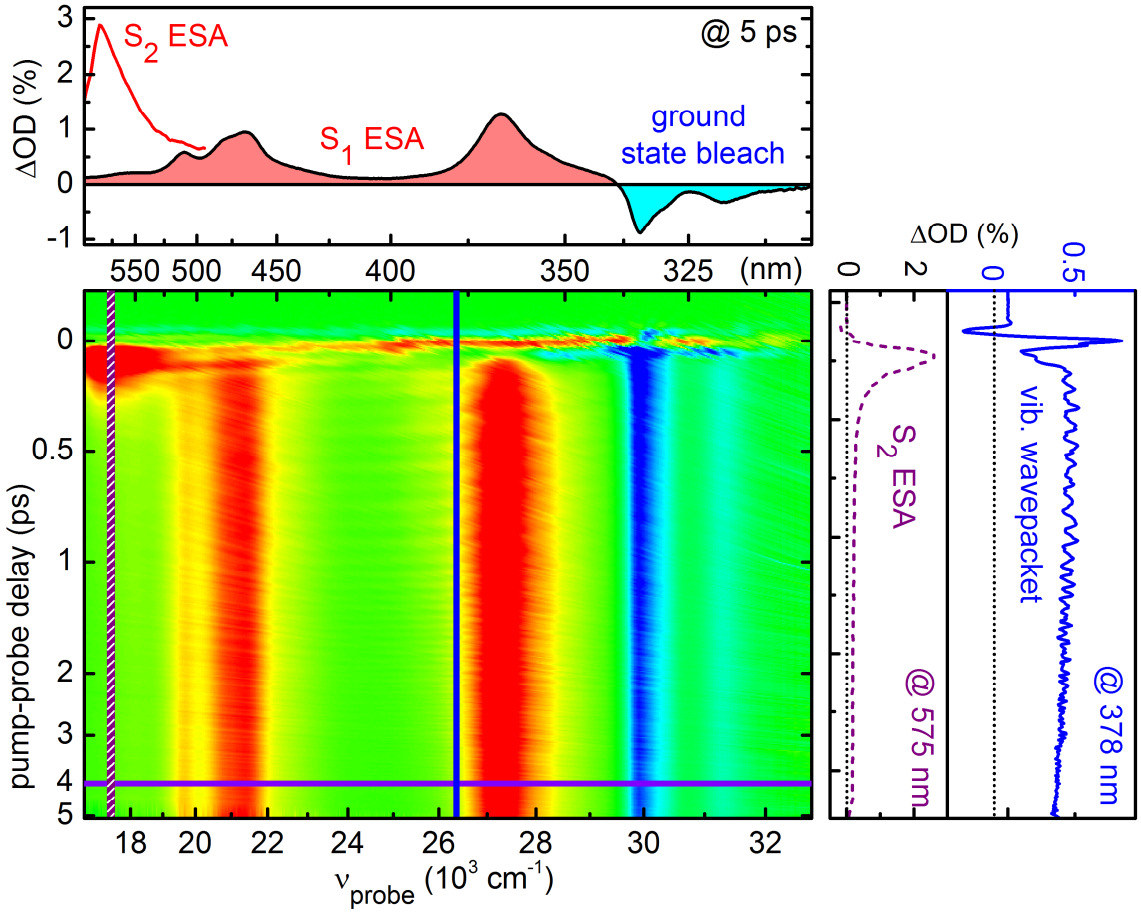

Fig. 5.1.5. (a) High temporal resolution transient pump-probe measurement of pyrene in methanol. (b) Transient spectra at 5 ps with excited state absorption (ESA) and ground state bleach contributions. (c) The time trace detected at 378 nm shows high frequency oscillations from vibrational wavepacket dynamics. At 575 nm the rapid decay in 85 fs of the S_2 ESA is visible.

The transient spectrum shows fast oscillations of the time traces disappearing in the first few ps. They do not originate from Raman active modes of the solvent as there are no contributing

modes of methanol in the respective frequency range between 150 – 1000 cm^{-1}. The oscillations can therefore be assigned to coherent vibrational wave packet motion in the S_1 state. The ground state bleach shows oscillations with a frequency of 409 cm^{-1} while the oscillations visible at the S_1 ESA around 360 nm has a frequency of about 393 cm^{-1}. These values correspond well with the values reported in literature for the S_0 ground state mode of 408 cm^{-1} and the excited state S_1 mode of 393 cm^{-1} in gas phase [Bor95, Shi98, Zha10].

The S_1 wavepacket dephases with a decay constant of about 3 ps. This decay of the oscillation is attributed to the vibrational dephasing and relaxation in the S_1 state. The observation of the vibrational wave packets in the first excited electronic state is somewhat surprising, as the molecule was initially excited to the S_2 state.

This observation suggests that the internal conversion happens as a ballistic vibrational wavepacket motion through the S_2 – S_1 conical intersection and the wavepacket finally oscillates in the S_1 state. The IC process conserves the impulse of the nucleic motion excited in the S_2 and leads to nucleic motion in the S_1 state with the respective vibrational modes.

Additionally to the observed modes around 400 cm^{-1}, in the spectral region of 350 – 420 nm an oscillatory component with a frequency of 183 cm^{-1} and a decay time of about 0.9 ps is detected. However, there was no literature found that reported the observation of a vibrational mode with a frequency alike. Theoretical calculations predict vibrational energies in the energy range of 150 and 200 cm^{-1}, however they are strongly suppressed due to symmetry reasons [Bab09].

The oscillatory component of 183 cm^{-1} is most probably originating from vibrational beating of two vibrational modes. If the oscillations originate from a beating with the dominant mode around 393 cm^{-1}, the other frequency should appear at about 576 cm^{-1}. A vibrational mode of the S_1 state with a frequency of 573 cm^{-1} was indeed observed in the literature [Zha10]. This mode could not be resolved in the intensity dependent transient dynamics of the S_1 ESA band due to the noise present in the experiment. However, by analyzing the temporal and spectral behavior of the peak of the ESA band at 360 nm this frequency can be resolved. A band shift analysis (for technical details see [Sail13]) can reveal the vibrational wave-packet motion [Pol90]. The temporal behavior of the band shift is shown in Fig. 5.1.6. Two additional vibrational modes are observed at 570 and 784 cm^{-1} comprising the oscillatory component. Note, that the S_1 mode with a frequency of 783 cm^{-1} is also reported in literature [Zha10].

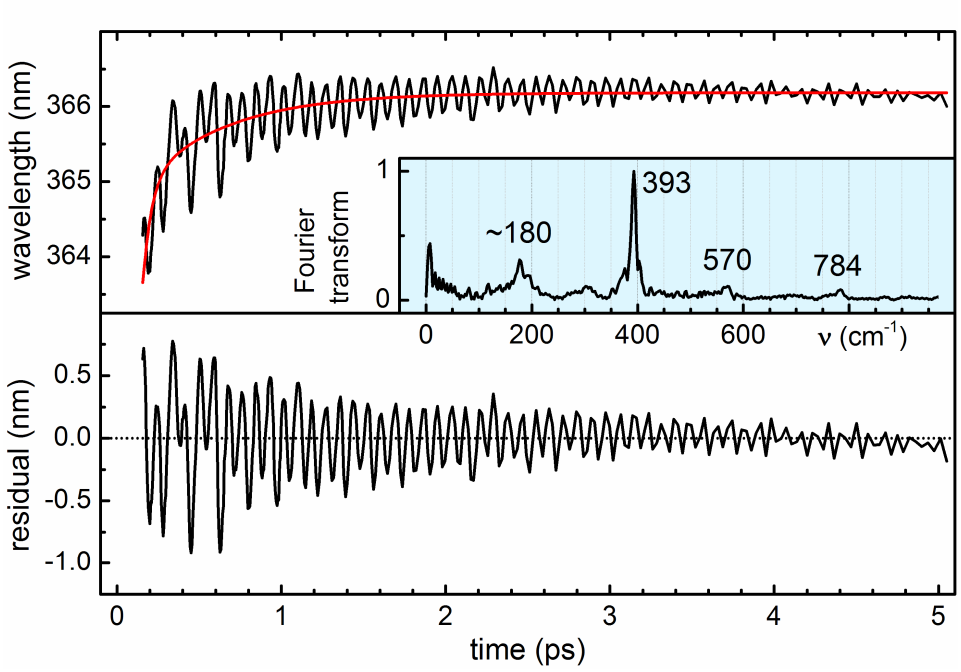

Fig. 5.1.6. Temporal behavior of the spectral peak position of the S_1 ESA peak at 360 nm. The Fourier transformation of the residual oscillations after subtraction of the slow dynamics (lower part) is shown in the inset. The observed vibrational modes are identical to the ones reported in the literature [Bor95, Shi98, Zha10].

Because the IC process happens as a ballistic wavepacket motion through the $S_2 - S_1$ conical intersection, the amplitude of the S_2 wavepacket should influence the amplitude of the S_1 wavepacket motion. Because the amplitude of the wavepacket motion is hardly measurable, an indirect approach can be applied: By exciting higher levels of a vibrational mode, higher vibrational levels of the final S_1 mode should then be populated. Therefore the transient signals of the S_1 state should reflect the vibrational excess energy in the S_2 state after excitation. We therefore performed 2D-UV measurements exciting the second and third vibrational band of the S_2 state (Chap. 5.1.3).

The clear observation of vibrational progression in the S_1 state after excitation of the S_2 state suggests that the vibrational progression plays a crucial role in the molecular dynamics on the ps time scale. This makes the interpretation of the amplitude change of the GSB and ESA signal with 4.7 ps originating from IVR and vibrational relaxation most likely. Excimers formed from loosely-bound ground-state dimers, on the other hand, seem to play a minor role. A quantitative analysis of the amount of molecules inducing a GSB signal can resolve this issue and is performed on the 2D-UV measurements presented in the following.

5.1.3 Excitation-frequency resolved dynamics revealed by 2D spectroscopy

To investigate the existence of loosely ground state dimers the 2D-UV measurements were analyzed quantitatively. As mentioned earlier, loosely-bound ground state dimers that form excimers with some ps after excitation should lead to an increase of the GSB contribution. As the extinction coefficient of the molecules that induce the GSB contribution equals the molar extinction coefficient, the amount of molecules inducing the GSB signal can be calculated. The amount of excited molecules can be calculated with the aid of the pump pulse intensity and concentration of the molecules. The comparison of the initially excited molecules and the amount of molecules inducing the GSB signal, the question whether there is an additional excimer GSB contribution can be resolved. This procedure equals the procedure to calculate the product quantum yield of a 2D measurement as described in Chap. 4.3.

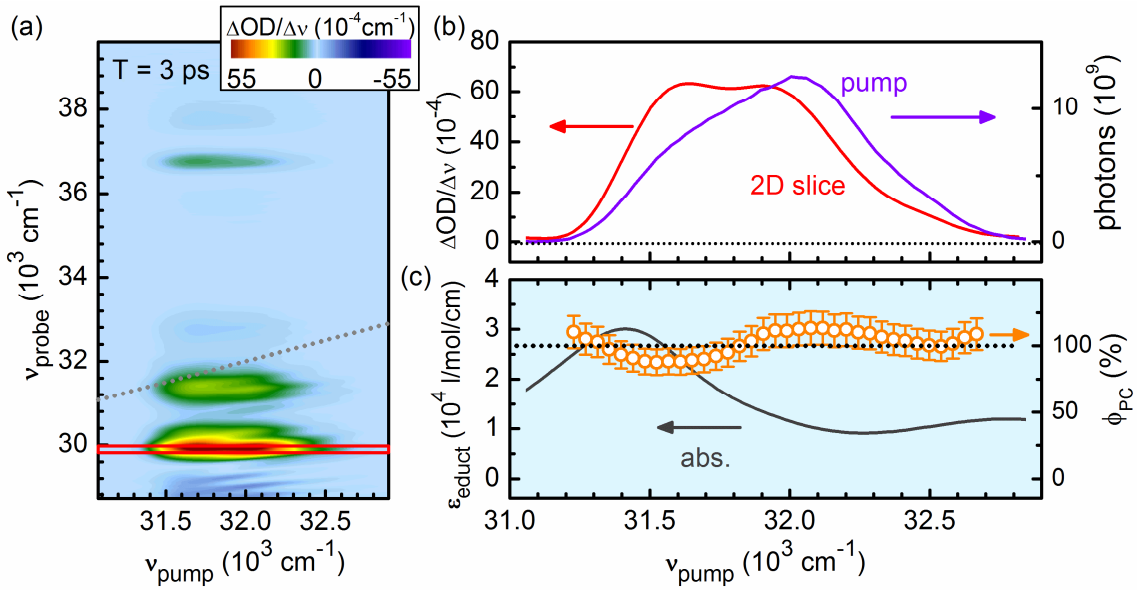

Fig. 5.1.7. Calculation of the ratio between initially excited molecules and molecules inducing the GSB contribution ϕ_{rel}. (a) 2D measurement of pyrene for a population delay of 3 ps. (b) Overlay of the 2D slice along the pump axis for ν_{probe} = 29940 cm^{-1} (red line) and the spectral photon number distribution of the pump pulses (violet). (c) Absorption spectra of pyrene (black line) and the calculated ratio of the S_1 state formation after excitation into the S_2 state. Note, that the product quantum yield is 100 % as expected when there is no excimer formation within 3 ps.

The relative quantum yield ϕ_{rel} is then defined as the ratio between initially excited molecules and molecules inducing the GSB contribution. It should be 100 % if there are no excimer formed in the ps domain and should be larger than 100 % if there are excimers present. The

result for a 2D-UV measurement with a pump pulse that is centered at 312.5 nm (32000 cm^{-1}) is shown in Fig. 5.1.7.

The resulting ϕ_{rel} is about 100 % for the whole UV pump pulse spectrum. Systematic deviation of about 20 % are attributed to the influence of the S_1 ESA contribution that overlaps with the GSB peak at 334 nm (29940 cm^{-1}) which is expected to have an explicit excitation-frequency dependence. The average value of the ϕ_{rel} is about 100 % and indicates that there is no strong additional GSB contribution that may originate from the excimer formation. Therefore, the existence of a large extend of loosely bound ground state dimers seems unlikely. However, due to the noise present in the experiment and the overlapping S_1 ESA contribution, the existence of a fraction of ground state dimers (< 20 %), seems feasible. In this manner, the spectroscopic and chemical investigations heavily in progress at the point this thesis was finished, will help to retrieve quantitative results.

To measure the excitation-frequency dependence of the S_1 ESA contribution, additional 2D-UV measurements were performed with visible super continuum probing. The absorptive 2D spectra of pyrene for a delay of 1 and 5 ps are shown in Fig. 5.1.8a. In Fig. 5.1.8b slices along the probe axis for low and high frequency excitation corresponding to the excitation of the second and third vibronic band (2^{nd}: 31400 cm^{-1} and 3^{rd}: 32800 cm^{-1}) of the S_2 state are plotted for the first 5 ps after excitation. The delay of the probe frequencies due to the chirp of the white light probe are given above the graph. Just as in the pump-probe experiments, the ESA signal between 29400 – 24000 cm^{-1} (340 - 420 nm) originates from the S_1 state after internal conversion from S_2. The shoulder at 25350 cm^{-1} (395 nm) is only prominent in the spectra when the higher vibrational mode of the S_2 state is excited. When the lower vibrational mode is excited the amplitude of the shoulder is weak. The temporal behavior of the shoulder shows a decrease with a time constant of about 2-3 ps. This correspond well with the dephasing of the 393 cm^{-1} ESA vibrational oscillations seen in the pump-probe measurements and is therefore assigned to the vibrational progression in the S_1 state.

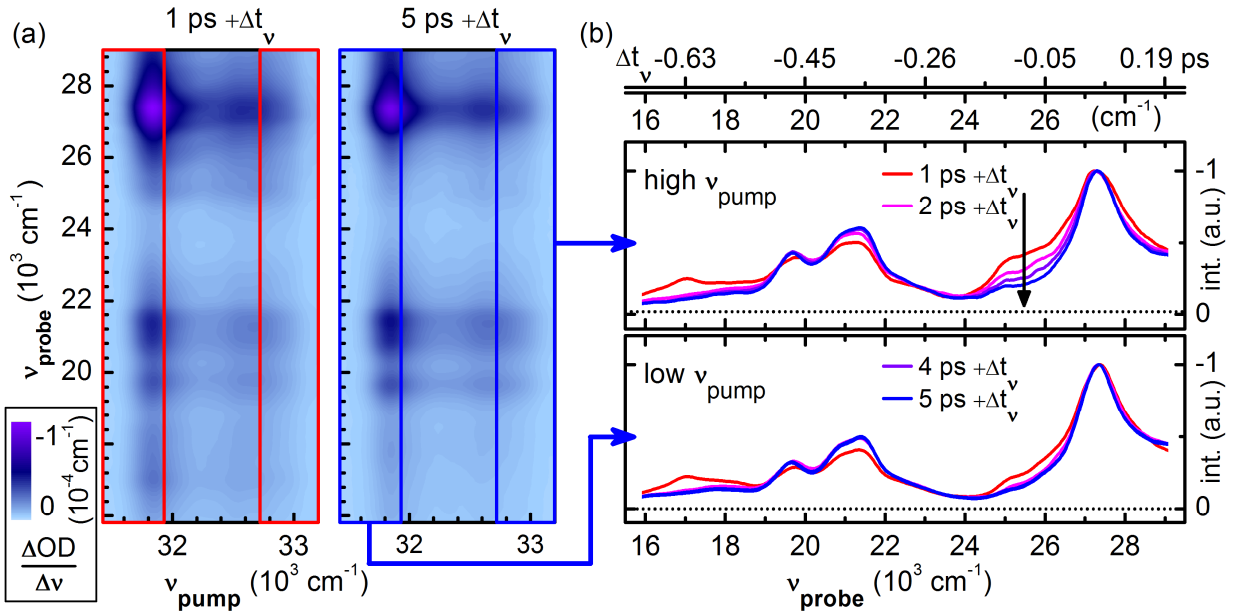

Fig. 5.1.8. (a) 2D spectra of pyrene in methanol after 1 ps and 5 ps. (b) Averaged slices along the probe axis for pump frequencies centered at 32990 cm^{-1} (303 nm, high) and 31670 cm^{-1} (315.7 nm, low) representing transient spectra. The absolute delay of the probe frequencies due to the chirp of the probe pulse are given by the additive value on top.

The excitation-frequency dependence of the amplitude of the ESA contribution at 25350 cm^{-1} can be understood in terms of the vibrational modes populated in the S_1 state after excitation of the S_2 state. Higher vibrational levels of the S_1 state can be populated after the IC when the high frequency components of the pump pulse excite the molecule. These higher lying vibrational levels of the S_1 state have an additional ESA contribution at 25350 cm^{-1} to higher lying electronic states. As the vibrational relaxation into the vibronic ground state of the S_1 state happens, the Franck-Condon overlap to the higher electronic states vanishes.

Internal vibrational relaxation of the hot S_1 state after excitation to higher electronic states was also observed by Foggi et al. [Fog95]. They measured the transient spectra of pyrene in n-octane and found that the S_1 ESA bands around 22000 cm^{-1} (460 nm) showed internal vibrational relaxation of the hot S_1 bands with a time constant of 4 ps which is similar to the one observed here.

To investigate the correlation between the relative amplitude of the ESA shoulder and the excitation frequency, 2D slices along the pump axis for a probe frequency of 25350 cm^{-1} are shown in Fig. 5.1.9 for different population times. Note, that the 2D spectra where normalized

to the peak intensity of the S_1 ESA peak at ν_{probe} = 27200 cm^{-1}. The curves plotted in Fig. 5.1.9b therefore show the relative amplitude of the shoulder when compared to the S_1 ESA peak.

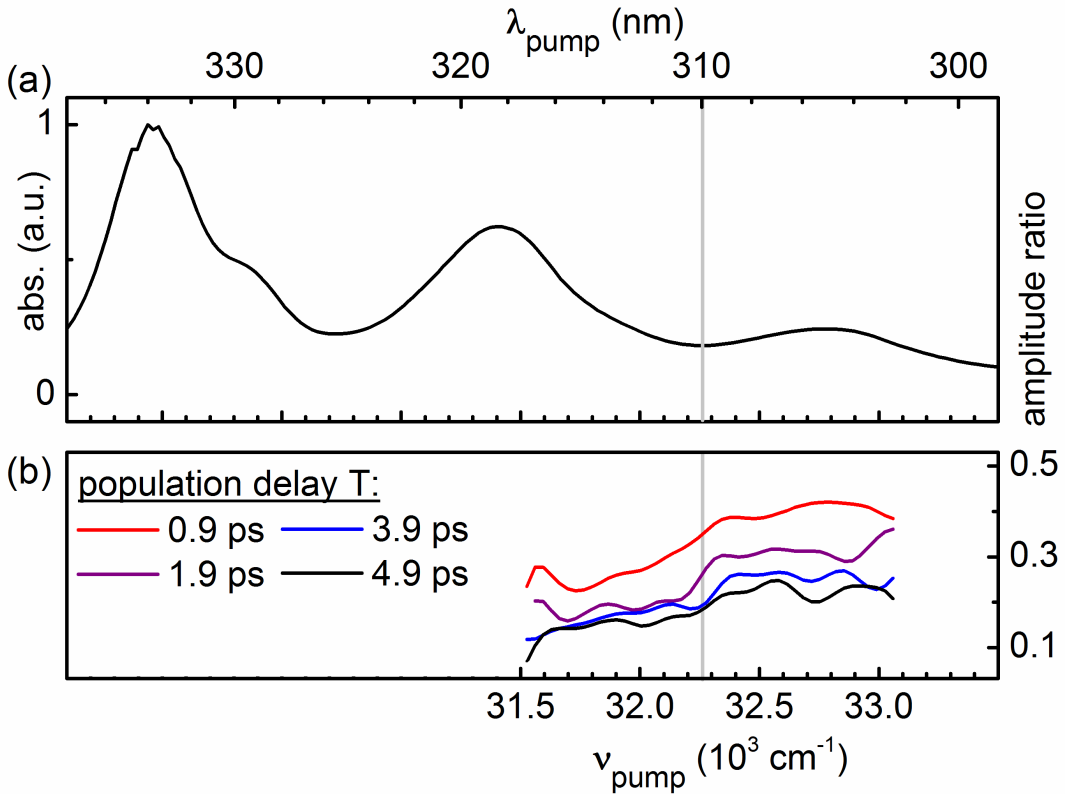

Fig. 5.1.9. Excitation-frequency dependence of the ESA contribution at the shoulder of the S_1 ESA at ν_{probe} = 25350 cm^{-1} of pyrene (Fig. 5.1.5). The pump pulses are centered at 311 nm. (a) S_0 - S_2 absorption spectrum of pyrene. (b) Ratio of the 2D amplitudes at ν_{probe} = 25350 cm^{-1} (S_1 ESA shoulder) and ν_{probe} = 27200 cm^{-1} (S_1 ESA peak) for different pump frequencies. For higher pump frequencies (> 32300 cm^{-1}) the amplitude of the ESA shoulder is stronger than for lower pump frequencies. This behavior correlates with the excitation of the two different vibrational bands of the S_2 absorption.

The 2D slices clearly show that the amplitude of the ESA shoulder is stronger for higher excitation frequencies and drops for longer delays. The 2D slices show a stepwise jump from lower values to higher values at about 32250 cm^{-1} (310 nm). The position of the jump corresponds well with the minimum in the absorption spectrum between the two neighboring dominant vibrational bands. This can be understood in terms of the vibrational coupling between the excited S_2 and the detected ESA of the S_1 state: The vibrational levels of the S_1

state that contribute to the ESA shoulder can only be significantly populated when the S_2 absorption band at 305 nm is excited. However, the vibrational excess energy in the S_1 state after internal conversion from the excited S_2 state is about 4500 cm^{-1} (energy gab between the excited vibrational modes of the S_2 state and the S_1 state). It remains puzzling why the energy difference between the two addressed vibrational modes of the S_2 state (at 31400 and 32800 cm^{-1}) can generate such a difference in the amplitude of the S_1 ESA shoulder.

In that sense, a detailed theoretical and experimental study, e.g., in gas phase experiments, of the vibrational structure of pyrene may unambiguously help to understand which modes of the S_2 state serve as donator modes and which modes of the S_1 state are the accepting modes.

The transient measurements described in this chapter support the following overall picture of the ultrafast internal conversion process of pyrene: After excitation of the S_2 state, the initially excited vibrational wavepacket moves on the potential energy surface towards the $S_2 - S_1$ conical intersection which in trespassed within 85 fs. The impulse of the initial wavepacket is conserved when the S_1 potential energy surface is reached. After the IC, the vibration excess energy in the S_1 state is redistributed along the vibrational S_1 modes in about 2 ps. The vibration relaxation to the S_1 vibration ground state happens within 4.7 ps.

2D spectroscopy was shown to be an ideal tool to gain a deeper insight into the energy dependence of the photophysics of pyrene. The tunability of the central wavelength of the pump allows to investigate these dependencies for other electronic and vibrational states, e.g., when exciting the S_3 state. Of special interest would be to investigate the fast perishing S_2 ESA in the first 85 fs after excitation. This could help unveiling the influence of the solvent and the vibrational modes on a time scale shorter than the dephasing of the molecule.

5.2 Photochromicity of the photoswitch chromene

To demonstrate the capability of 2D-UV spectroscopy to retrieve the excitation-frequency dependent reaction yields and dynamics of a light-induced photoreaction, the molecule 2,2-diphenyl-5,6-benzo(2H)chromene (**5,6DPBC**) was selected as an example.

5,6DPBC belongs to the family of photochromic molecules undergoing a UV-light-induced transition between two states that show distinguishable absorption spectra which can be thermo- or photoreversible [Bou01]. The light-induced absorption change is accompanied by a pericyclic ring-opening reaction [Len86, Ott98] and subsequently by a conformational change two different isomers [Del98, Joc02, Arn03] (Fig. 5.2.1).

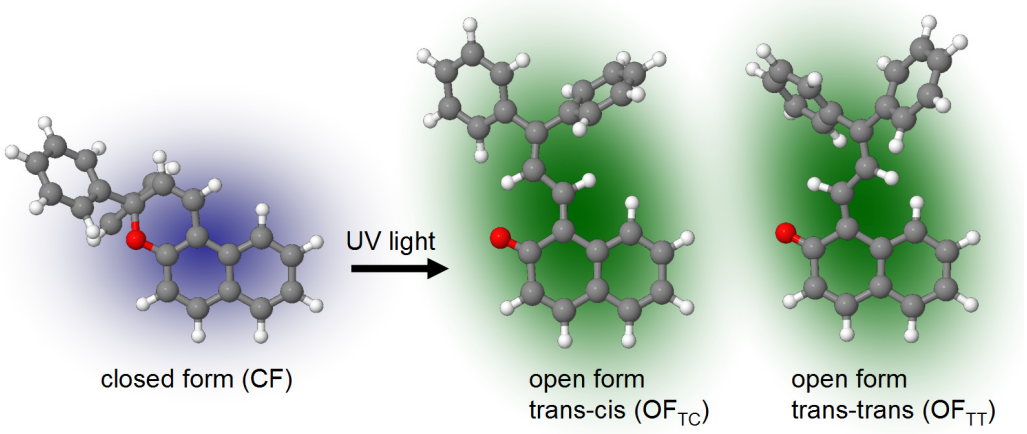

Fig. 5.2.1. Scheme of the UV-light-induced pericyclic ring-opening reaction of 5,6DPBC. After bond-cleavage at the oxygen (red) the ring open form (OF) has two isomers, a trans-cis (OF_{TC}) and a trans-trans configuration (OF_{TT}). Both product isomers show nearly identical absorption spectra in the visible. Equilibrium geometries retrieved by ab initio optimization.

First spectroscopic measurements for the strongly related molecule 5,6-benzo(2H)chromene (5,6DMBC), where only the two phenyl moieties of 5,6DPBC are replaced with two methyl groups, showed that the ring-open product quantum yield depends on the excitation frequency [Bec05, Bec11]. For 5,6DPBC it was found that the ring-opening reaction happens on the few-ps time scale [Moi07, Moi08] and the speed of the ring-opening reaction change when the excitation frequency was varied [Her13, Gen04].

The excitation-frequency dependence of the ring-opening reaction makes 5,6DPBC an ideal candidate to be studied by 2D-UV spectroscopy. The excitation-frequency resolution of 2D-UV

spectroscopy for excitation of the S_2 electronic state of 5,6DPBC dissolved in acetonitrile (ACN) at room temperature can reveal in which way the product quantum yield and the speed of the ring-opening reaction depend on the excitation frequency.

5.2.1 Vibrational modes influencing the molecular dynamics

The photochromic behavior of chromenes was driven by the observation that the fluorescence excitation spectra showed vast differences from the absorption spectra [Bec66, Bec69]. The closed form of 5,6DPBC, which is thermally stable when solved in ACN at room temperature, shows absorption in the UV spectral domain with a vibrational substructure visible both in the S_1 and S_2 state (Fig. 5.2.2). When irradiated with UV light, the absorption spectrum changes and the most prominent feature is the rise of a strong visible absorption contribution. This absorption is attributed to the ring-open form as the conjugation of the π-electron system now elongates over a larger fraction of the molecule leading to a bathochromic shift of the absorption [Len86, Del98].

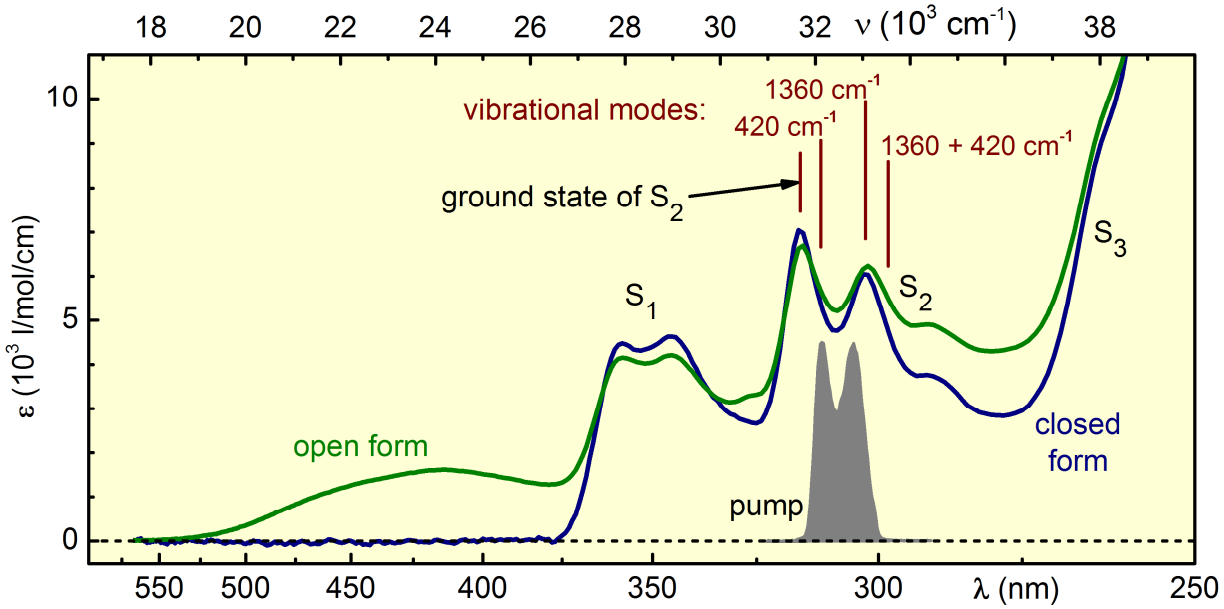

Fig. 5.2.2. Absorption spectra of 5,6DPBC measured in ACN at room temperature before (blue) and after (green) UV irradiation. The absorption band at 425 nm (23530 cm^{-1}) corresponds to the absorption of two isomers after the polycyclic ring-opening reaction. The vibrational frequencies (wine) of the S_2 state were estimated by deconvolution of the absorption spectrum.

The visible absorption originates from two stable isomeric photoproducts, trans-cis (OF_{TC}) and trans-trans (OF_{TT}) of the ring-open form which have similar absorption but different extinction coefficients [Ott98, Del98]. The OF_{TC} thermally relaxes back to the closed form in about 10 s when solved in ACN, while the OF_{TT} form is thermally more stable [Gör02]. The back reaction can be induced by visible light. The reports in the literature state, that at room temperature in solution there is no continuous-wave fluorescence detectable [Len86, Gör02, Joc02, Moi07]. 5,6DPBC has no observable triplet transition and phosphorescence [Gen04].

The race to unravel the details of the light-induced reaction dynamics of chromenes started with the investigation of the dependence of the fluorescence quantum yields Φ_{Fl} and the photochemical yield Φ_{PC} on the excitation frequency of 5,6DMBC [Bec69, Bec11]. In these experiments in a 3-methylpentane matrix at 77 K, fluorescence with a Φ_{Fl} of a few percent was observed. Both Φ_{PC} and Φ_{Fl} were found to vary as a function of the electronic state, the vibrational mode and the vibrational level that was excited. Short-termed, the higher the vibrational mode and level excited in the optically addressed electronic state, the lower Φ_{Fl} was. For Φ_{PC} the opposite behavior was measured. This excitation-frequency dependence of Φ_{PC} was also found at room temperature [Len86, Bec05].

To explain the behavior of the photochemistry of chromenes, Becker and co-workers [Bec05, Bec11] proposed a kinetic model that explains the excitation-frequency dependence of Φ_{PC}. The key statement is that Φ_{PC} depends on the type and level of the vibrational modes excited in the addressed electronic state. In this model, the behavior of Φ_{PC} was explained by a competition between vibrational relaxation to the electronic ground state, where the fluorescence originates from, and the product formation, while both processes happen directly from each vibrational level populated [Bec99, Bec05].

For the S_2 state of 5,6DMBC at 77 K two vibrational modes could be distinguished. One high frequency mode of 1360 cm^{-1} and a low vibrational mode of about 400 cm^{-1}. Measurements of Φ_{PC} for different excitation frequencies showed that excitation of the 400 cm^{-1} mode has a significantly higher product yield as the excitation of the high frequency mode. This was later on explained by using ab inito calculations for a related molecule (2,2-diethyl-2H-chromene) [Mig05]. In this molecule, a high-frequency in plane π-system skeletal stretching mode together with a low-frequency out-of-plane ring-puckering mode was found. The low-frequency mode is preparatory to activate the bond-breaking mode required for the ring-opening of the molecule. Therefore, when exciting the 400 cm^{-1} mode, a higher overall product yield results compared to the excitation of the 1360 cm^{-1} frequency mode.

For increasing excitation frequency, Φ_{PC} increases as higher lying vibrational levels in a specific electronic state are excited [Bec05, Bec11]. This behavior was explained by a cascaded product formation process: At each vibrational level, a fraction of the molecules undergo relaxation and the other fraction undergoes product formation. When the fraction of molecules undergoing relaxation to lower vibrational levels reach these lower levels, an additional fraction of the molecules can form products. Therefore, for higher vibrational levels, more and more molecules undergo product formation and only a minor fraction reaches the vibrational ground state, and thus do not form a product.

However, the model proposed by the authors is in contradiction with the common understanding of the vibrational relaxation processes in molecules [Els91, Nak98]. The model states [Bec11]: 1) There is no crossing between different vibrational modes, vibrational relaxation occurs only within the levels of the same mode. 2) Relaxation from the 0 level of an upper electronic state S_x ($x > 2$) does not proceed via vibrational/vibronic levels of any of the electronic states below.

In contrast, a more common understanding states that: (1) After excitation of the Franck-Condon active vibrational modes the internal vibrational redistribution process is considered to distribute the excess energy to other vibrational modes within the molecule [Els91] and does not happen exclusively within the same mode. (2) The internal conversion from a higher electronic state does typically happen via vibrational coupling with the modes of the lower lying electronic state and the relaxation process does involve the vibrational levels of the state below (see e.g., pyrene; Chap. 5.1). (3) After excitation with ultrashort pulses, the molecular dynamics are described by a vibrational wavepacket motion on the multidimensional potential energy surface rather than a pure statistical rate model for different electronic and vibrational states excited.

Because the limited amount of measurements on 5,6DPBC described in this chapter do not unambiguously allow to clarify the contradictious interpretation we restrict ourselves to demonstrate the capability of 2D-UV spectroscopy to investigate such excitation-frequency dependent photochemical questions. This is done by investigating the product quantum yield and the ultrafast reaction dynamics when photoexciting different vibrational modes in the S_2 state of 5,6DPBC. So far, reports in literature suggest that the measured ultrafast time constants showed a significant dependence on the excitation frequency. However, an opposite tendency was found in the literature [Her13 vs. Gen04]. This discrepancy is most likely a consequence of the chosen excitation frequencies: In the experiments not only different vibrational modes but

also different electronic states, namely S_3 and S_1, were excited.

Addressing different vibrational levels of only one excited electronic state can reveal the influence of vibrational effect on the ultrafast photochemical reaction of 5,6DPBC. This can readily be done by using 2D-UV spectroscopy as it will be described in the following.

5.2.2 Absorptive 2D-UV spectra: Measurement details and results

To illustrate the capability of 2D-UV spectroscopy to quantitatively measure the influence of the excitation frequency on a photochemical reaction, 5,6DPBC solved in ACN at room temperature was used as a model system. 5,6DPBC was purchased from TCI Europe and used without further purification (>98 %). To verify, that the possible 2 % impurity does not affect the 2D-UV measurements, at first a chemical and spectroscopic analysis of the sample was performed. The chemical analysis comprised a gas chromatography and a melting point determination. Both measurements did not show a detectable amount of impurity. Subsequently the sample was investigated by fluorescence spectroscopy. Despite the observations in literature that there is no detectable fluorescence [Len86, Gör02, Joc02, Moi07] a very weak fluorescence (quantum yield < 1‰) was observed here. The fluorescence excitation spectrum does not resemble the absorption spectrum, which indicates that the fluorescence can originate from an impurity. The result is shown in Fig. 5.2.3 together with the absorption spectrum.

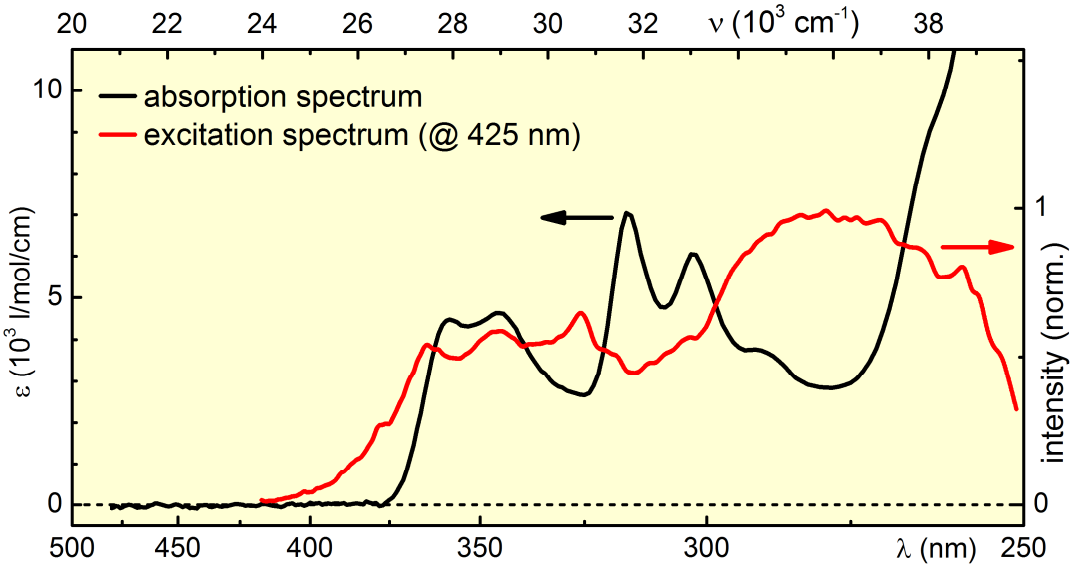

Fig. 5.2.3. Absorption (black line) and fluorescence excitation (red line) spectra of 5,6DPBC dissolved in ACN. The fluorescence was detected at 425 nm.

A rather similar difference between the absorption and the fluorescence excitation spectra was observed for 5,6DPMC [Bec66]. However, due to the extremely low amount of fluorescence detected, we conclude that the suspected impurity does not affect the 2D-UV measurements because the induced absorption of the ring-open product, that is used to investigate the photochemical reaction, is comparable in strength with the strength of the absorption spectrum. Therefore any contribution of the suspected impurity is still a factor of more that 1000 weaker than the photoproduct signal.

The concentration of 5,6DPBC dissolved in ACN used in the experiment was 8 mM. A 100 μm thick flow cell of our own design was used as the sample holder. The central wavelength of the pump pulses was tuned to 308.5 nm, just in the middle of the two main vibrational signatures of the S_2 state. This choice, in combination with the large spectral bandwidth of up to 1600 cm^{-1} (boarders where the intensity drops to < 5 %), allows the investigation of the excitation of 4 different vibrational levels of the S_2 state (Fig. 5.2.2): 1) The vibrational ground state. 2) The first level of the 420 cm^{-1} mode. 3) The first level the of 1360 cm^{-1} mode. 4) The combination of both modes (1360 + 420 cm^{-1}).

For probing a visible white light continuum (290 – 720 nm) was used which covers well the spectral region where the product absorption appears (425 nm). The pump had a focal diameter at the sample position of 87 μm and each pump pulse had typical pulse energies of 97 nJ. The magic angle polarization between the pump pulses and the probe pulse was used to eliminate contributions from molecular rotation. The chirp of the probe pulse was not corrected for the 2D-UV measurements but was determined in a separate measurement. The group delay between the probe wavelengths of 300 and 650 nm was about 1 ps. The chirp is explicitly taken into account when needed for the analysis of the 2D results. The spot size of the probe beam had a diameter of 63 μm.

The coherence time τ was scanned in steps of 0.436 fs and a complete scan was comprised of 253 delay points leading to a maximum scanning range of 110.4 fs. The phase cycling scheme was applied for consecutive laser shots. For every τ delay 400 laser shots were averaged, namely 200 laser shots for each interpulse phase. 2D-UV spectra were recorded for pump-probe delays (population time T) between ~0.2 and 100 ps automatically. The measured data was corrected for the probe spectral intensity distribution, to receive 2D signal amplitudes ($\Delta OD/\Delta\nu$) which are directly proportional to conventional pump-probe signals (ΔOD) and thus to the population of the states investigated.

Measured 2D spectra of 5,6DPBC for selected T times are shown in Fig. 5.2.4. For the probe axis the region between 15500 cm^{-1} (645 nm) and 31500 cm^{-1} (318 nm) is shown. The part of the probe axis (> 31500 cm^{-1}) which is in the frequency range of the pump pulse spectrum is not shown, as it does not contain relevant information for the upcoming analysis. Note that the probe pulse is chirped, leading to an additional delay for each probe frequency that is taken into account for the later analysis. The 2D spectra for all population times show an induced transient absorption signal, which is an off-diagonal contribution. The 2D spectrum at T = 0 ps shows 4 peaks that correspond to a double peak structure when viewed along the probe axis (maximums at 19100 cm^{-1} and 26000 cm^{-1}) or when viewed along the pump axis (maximums at 32130 cm^{-1} and 32840 cm^{-1}).

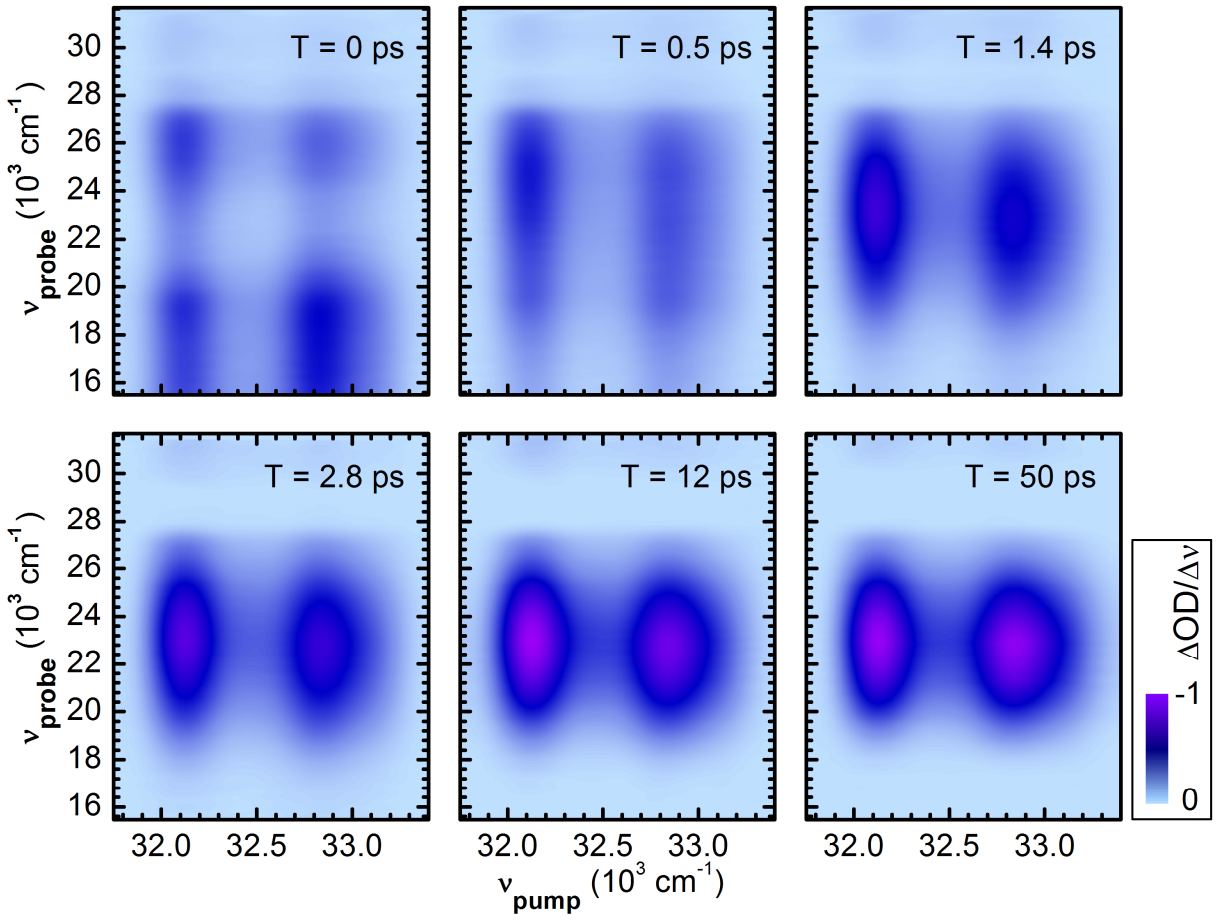

Fig. 5.2.4. 2D-UV measurements of 5,6DPBC in ACN for selected population times T measured with visible white light for probing. The 2D intensity was normalized to the maximum of the T = 50 ps spectra. The spectra show the formation of the rise of the absorption of the light-induced photoproduct.

The double peaked structure along the probe axis (T = 0 ps) vanishes in the first 500 fs after excitation and forms a broad induced absorption with a maximum at about 23000 cm^{-1} (435 nm). This structure corresponds to the absorption of the photoproduct which is formed on the ps timescale [Aub00, Gör02, Gen04, Moi07, Moi08, Her13]. For later times, the intensity of the product absorption increases until after roughly 20 ps the signal stays constant and no more product is formed.

The double peaked structure along the pump axis is a consequence of the pump spectral intensity, the absorption spectra of the molecules and the efficiency of product formation at each individual pump frequency. The number of excited molecules when considered along the pump axis is a convolution of the pump spectral intensity with the absorption strength of the molecule. The detected signal itself is proportional to the number of molecules that are in the respective state which is detected. In the case of 5,6DPBC, the states corresponding to the induced absorption visible in the 2D spectra at ν_{probe} = 23000 cm^{-1} (435 nm) are the ring open forms of the light-induced photoproduct (OF_{TC} and OF_{TT}). By comparing the number of excited molecules with the number of molecules that are in the open form, the photochemical quantum yield Q_{PC} can be calculated for different excitation frequencies ν_{pump}. The results are described in the following.

5.2.3 Excitation-frequency dependent quantum product yields

To calculate the product quantum yield in the 2D-UV experiment the procedure described in Chap. 4.3 is applied. At first, the extinction coefficient of the photoproduct ε_{prod} has to be determined. This value can not be retrieved from the transient measurements by decomposing the GSB contribution from the transient spectrum because the ground state bleach contribution is not sufficiently distinguishable to be separated from the transient absorption spectra (as done for pyrene in appendix A.V). Therefore, the literature value of 16000 ± 1000 L/mol/cm [Ott98] for the trans-cis ring-open form (OF_{TC}) is used for further analysis. It was shown in literature that after excitation this form is the predominant one [Ott98, Gör02]. The pump beam had a focal diameter of 87 µm and an average pump energy of 111 nJ. This value includes the attenuation of the pulse energy due to the absorption by the molecules when propagating in the sample holder.

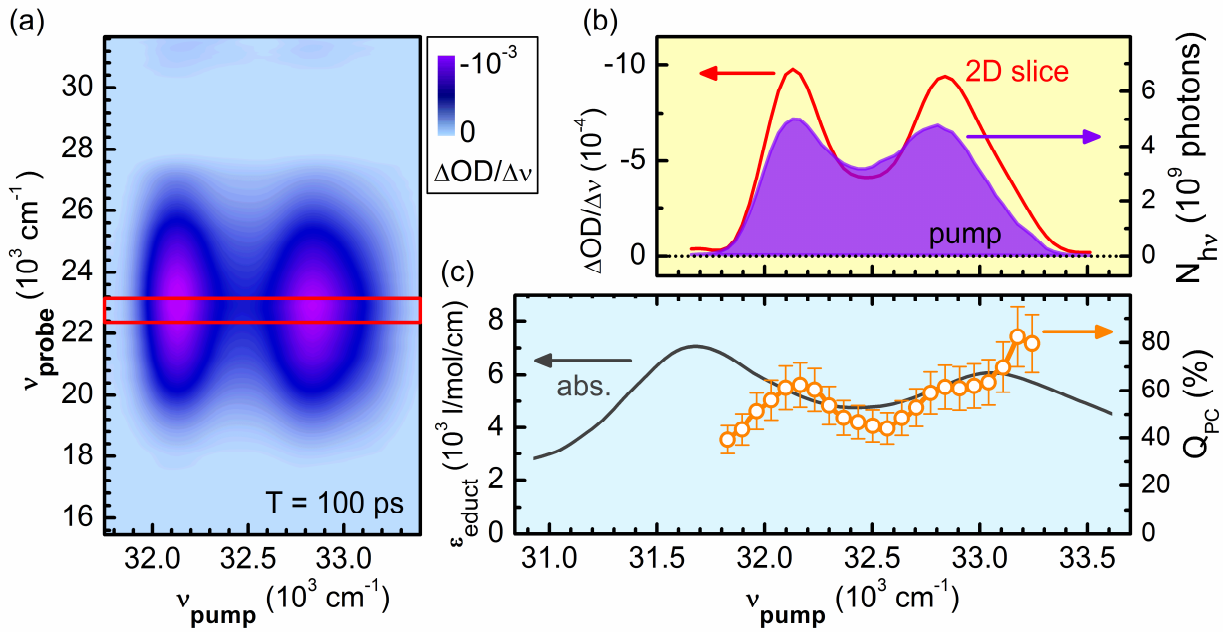

Fig. 5.2.5. Calculation of the pump frequency resolved Q_{PC} of 5,6DPBC from the pump wavelength resolved 2D measurement. (a) 2D-UV spectra at T = 100 ps. The 2D slice along ν_{pump} which is averaged along ν_{probe} is marked in red. (b) Overlay of the pump spectra with the retrieved 2D slice (c) Calculated Q_{PC} overlaid with the absorption spectra of the educt. The relative uncertainty is about 10 %.

At first, the product quantum yield is calculated from the 2D spectra measured for a population time of 100 ps. At this pump-probe delay, the photoreaction is finished and the photoproduct absorption is stable on the ns time scale. The result together with the relevant calibration spectra are shown in Fig. 5.2.5. The slice of the 2D spectra along the pump frequency axis is an average of the probe frequencies between 22350 cm^{-1} and 23160 cm^{-1}. The pump spectral photon density and the extinction coefficient of the educt were measured separately. Shown in Fig. 5.2.5c is the absorption spectrum of 5,6DPBC for the region of the two vibrational bands of S_2 absorption and the $Q_{PC}(\nu_{pump})$ retrieved. Q_{PC} is in the range of 40 - 80 % which is in very good agreement with the values reported in literature (Q_{PC} = 0.7 - 0.9 [Gör02]).

As a general trend one can see that the higher the pump frequency is the higher Q_{PC} becomes. This indicates that there exists a barrier on the potential energy surface of the excited state that has to be trespassed to reach the conical intersection to the product state. A barrier is indeed observed for 5,6DPMC [Zer84, Day95, Mig05].

Additionally, substructures showing amplitude modulations of up to 30 % are observable over the whole detection window. This indicates that the vibrational substructure underneath the two

main peaks of the absorption into the S_2 state is relevant for the molecular dynamics. This is in accordance with observations reported in the literature for the molecule 5,6DPMC measured in a rigid matrix at 77 K [Bec05, Bec11]. In those studies, Becker et al. measured the product quantum yields when exciting different vibrational and electronic bands. Their results are shown in Fig. 5.2.6 together with the 2D-UV measurement of 5,6DPBC for the vibrational bands of the S_2 state.

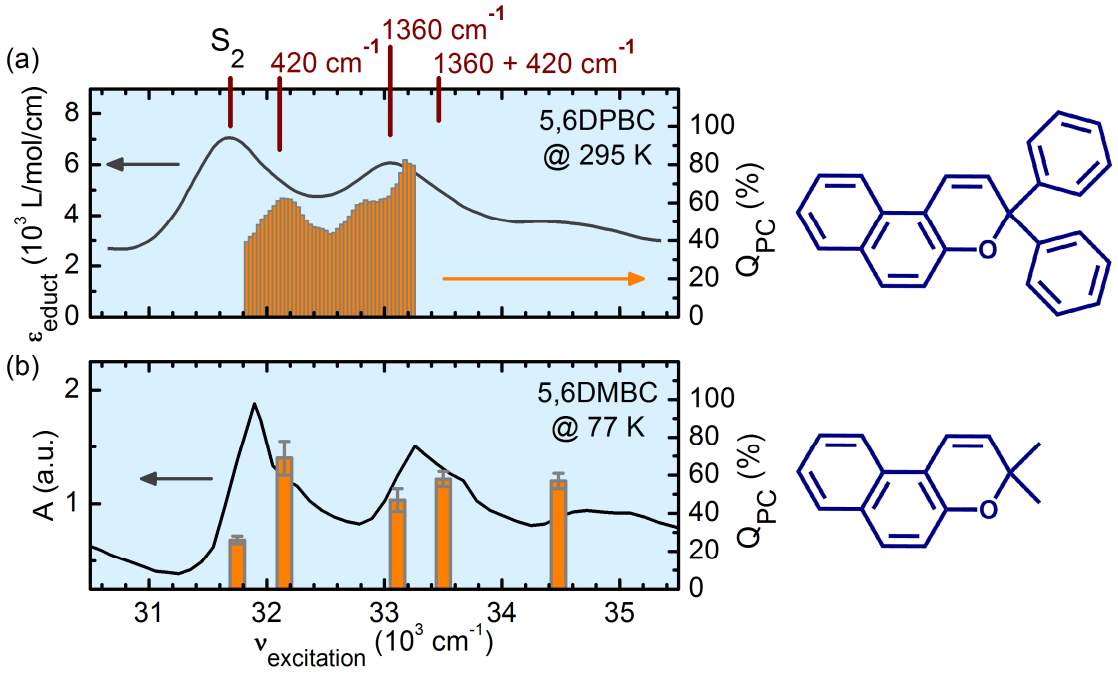

Fig. 5.2.6. Comparison of the measured product quantum yield of 5,6DPBC (a) with that one of a related chromene molecule 5,6DMBC (b). The absorption spectra of both molecules as well as the frequency dependence of Q_{PC} show strong similarities. Data for 5,6DPMC adapted from references [Bec05] and [Bec11].

These two photochromic molecules have nearly identical chemical structure. The only differences are the two phenyl rings which are linked with two single bonds. The benzo-2H-chromene moiety is responsible for the absorption bands in the near UV spectral domain as it has a conjugated π-electronic system. This leads to nearly identical absorption spectra for the two molecules. The only difference is that the vibrational bands of 5,6DPMC have a smaller spectral bandwidth. This can readily be understood, because the absorption of 5,6DPMC was measured at 77 K and homogeneous broadening is suppressed. Becker et al. found that for 5,6DPMC the Q_{PC} depends on the vibrational mode excited and found that for the S_2 state the low frequency mode is more efficient than the high frequency mode.

When looking at the measurements of 5,6DPBC the spectral changes in the Q_{PC} can then be interpreted in a similar way. The vibrational ground state of the S_2 state has a low Q_{PC} which increases when the first level of the 420 cm^{-1} mode is excited. For higher frequencies, at 32700 cm^{-1}, the dominant 1360 cm^{-1} mode is more efficiently excited and fewer products are formed, as this mode is less efficient for the product formation (see [Mig05] for 2,2-diethyl-2H-chromene). For frequencies with an excess energy of more than 1400 cm^{-1} above the S_2 ground state, a high Q_{PC} is a consequence of the excitation of higher vibrational levels thus having a higher vibrational excess energy after excitation.

This result indicates that the barrier on the potential energy surface, that partially hinders the excited molecular wavepacket to reach the product conical intersection, has a significant multidimensional character. Depending on the vibrational mode excited, the excited wavepacket sees a differently shaped barrier on its pathway. Simply speaking, when dominantly exciting the 420 cm^{-1} mode, the height of the barrier seen by the wavepacket is smaller as compared to the excitation of the 1360 cm^{-1} mode, as different multidimensional pathways on the potential energy surface result. This description is in accordance with the proposed shape of the potential energy surface proposed in the literature [Moi05, Her13], however the multidimensionality was not stressed there explicitly.

These processes happen on the fs to ps timescale and it is therefore most instructive to analyze the temporal behavior (population time T) of the 2D measurements. The time resolved results are described in the following chapter.

5.2.4 Excitation-frequency dependent dynamics

In addition to the pump-frequency resolved static information retrieved in the last chapter, the measurement of multiple population times in a 2D experiment allows to investigate the transient dynamics directly. By investigating the temporal development of the amplitude and/or shape of the 2D spectra for different excitation frequencies the mechanism underlying the photo-induced reaction can be unraveled.

It is instructive to look at the temporal development of the 2D measurement of 5,6DPMC at first from the point of view of conventional pump-probe spectroscopy. Transient pump-probe spectra are retrieved by projecting the 2D spectra onto the probe axis which is done by integration along the pump axis for each probe frequency individually. The result for selected pump-probe delays (population time T) is shown in Fig. 5.2.7.

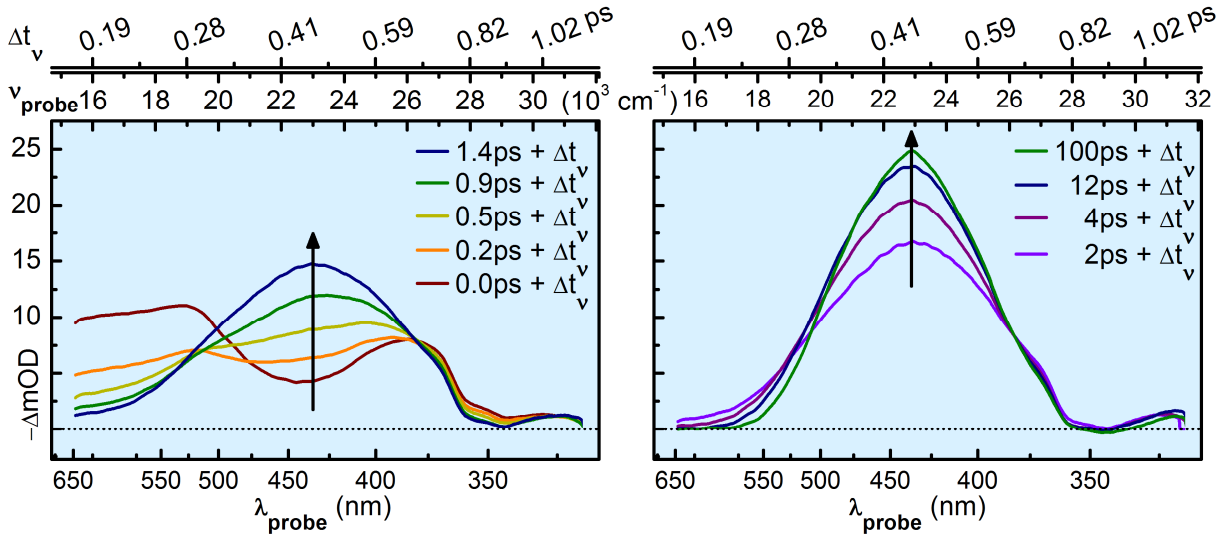

Fig. 5.2.7. Transient spectra of chromene in ACN, retrieved from the 2D-UV measurement by integrating the pump axis. The absolute delay of the probe frequencies due to the chirp of the probe pulse is given by adding the value Δt_ν on top.

The transient spectra show an unstructured transient absorption all over the visible, present directly after excitation ($T = 0 + \Delta t_\nu$). Subsequently, a prominent absorption in the spectral region of the ring-open forms (at about 435 nm) arises in about a few ps. The shape of this absorption signature, which corresponds to the shape of the absorption of the ring-open forms, changes slightly on a timescale of about 10 ps, until it reaches a saturation both in intensity and shape at about 20 - 50 ps. These observations are in perfect agreement with other measurements reported in literature for different excitation frequencies and also various solvent polarities [Aub00, Gör02, Gen04, Moi07, Moi08, Her13]. In the literature reports, three time constants were found which are responsible for all spectral transformations observed in the experiment: 1) The decay of the broad unstructured transient absorption all over the visible happens with the shortest time constant (τ_1) of less than 400 fs. 2) Subsequently, the prominent absorption of the ring-open forms arises with the second time constant (τ_2) in the order of a few ps. 3) The shape of this induced absorption changes slightly with a time constant (τ_3) greater than 10 ps. Despite some inconsistencies in the assignments of the shortest time constant to a specific molecular process in the literature, the transient dynamics on the longer time scale were consistently attributed to the generation of the photoproduct.

The upcoming time dependent analysis of the 2D spectra therefore concentrates on the development of the absorption band around 435 nm, to evaluate the temporal dynamics of the photoproduct generation. The 2D spectral intensity for ν_{probe} = 23000 cm^{-1} (435 nm) at

different population times T is the best measure for a value which is directly related to the number of product molecules. It is not appropriate to calculate a value like Q_{PC} for the sub-20 ps population times, because it was shown in the transient 2D spectra (Fig. 5.2.7) that other transient signals spectrally overlap with the photoproduct absorption. As it is not clear how the other contributions behave exactly, the values retrieved for Q_{PC} would therefore not be the correct ones. Only for long time delays were all photo-induced processes are finished Q_{PC} is retrieved correctly, as it was done in the last chapter. It is therefore most practical to look directly at the 2D signal intensity ($\Delta OD/\Delta\nu$) at ν_{probe} = 23000 cm^{-1} for delays >500 fs to analyze the temporal dynamics of the photoproduct formation solely.

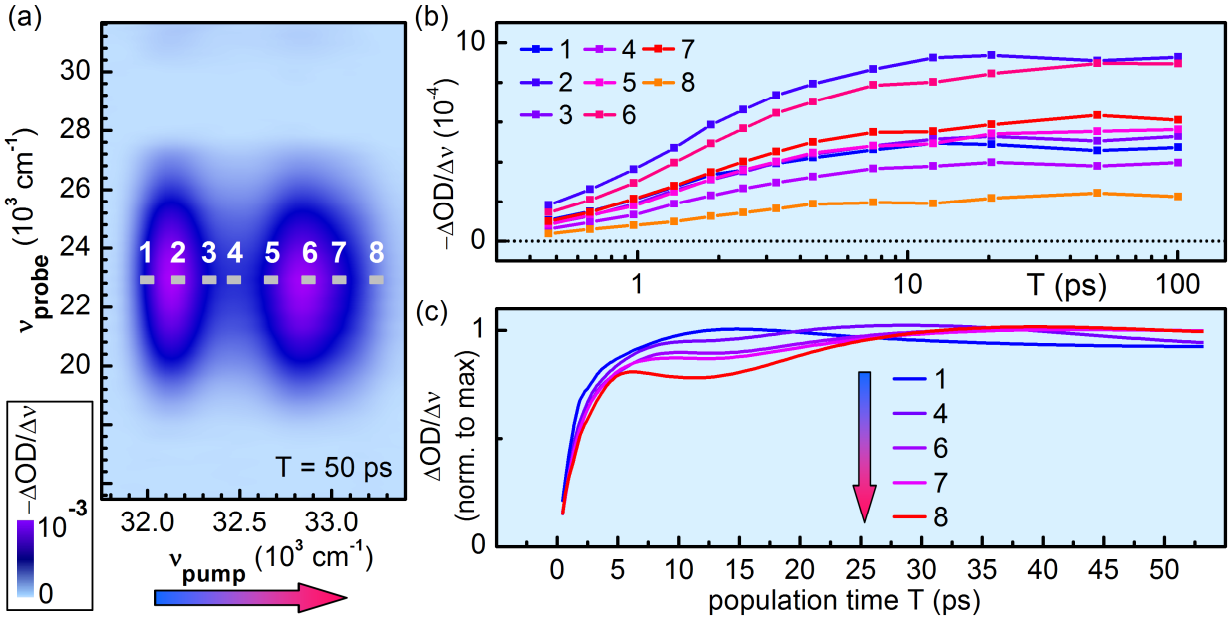

Fig. 5.2.8. Analysis of the excitation-frequency dependence of the product formation of 5,6DPBC from the 2D spectra for different delays T. (a) 2D spectra measured at 50 ps delay. The average value of the areas 1 – 8 (grey) are analyzed in (b) and (c). (b) Time evolution of the 2D signal intensities of the areas marked in (a). (c) Time curves of (b) normalized to the maximum values of each time trace.

To retrieve the pump-frequency resolved dynamics of the photoproduct formation, 8 different pump frequency regions are selected at the peak of the product absorption band (Fig. 5.2.8a). For better signal quality an area of ν_{probe} between 22800 cm^{-1} and 23040 cm^{-1} was averaged. The spectral width along the pump axis for each area was 65 cm^{-1} at the respective central pump frequencies given in Tab. 5.2.1. As all areas have the same probe frequency, they all have the same additional population delay of Δt_ν = 460 fs, due to the chirp of the white light probe.

This is also the shortest delay measured for that probe frequency and guarantees that the unstructured transient absorption all over the visible has decayed. In Fig. 5.2.8b the 2D intensities of the 8 areas are given for the measured population delays $T + \Delta t_v$. The retrieved time traces show an increase of the product absorption in the first 10 ps after excitation and stay constant for longer delay times. The maximum amplitude of the time traces for the selected pump frequencies are different because the pump intensity and the product quantum yield changes along the pump axis. To see the difference in the temporal behavior of the time traces, they where normalized to their maximum saturation level (Fig. 5.2.8c). The normalized time traces indicate qualitatively, that the product formation in the first few ps after excitation is slower when higher pump frequencies excite the molecule.

A quantitative analysis of the time traces shown in Fig. 5.2.8b was done by determining the rise time of the product absorption for the different pump frequencies. This was done by individually fitting the time traces with an exponential rise in combination with a constant offset value for long time delays. This is the minimal set of contributions necessary to match the experimental time traces. Fitting with two or more time constants does introduce too many free parameters for the fitting routine to unambiguously retrieve the observed changes in the temporal behavior of the time traces. As mentioned earlier, transient pump-probe measurements reported in the literature revealed three time constants [Aub00, Gör02, Gen04, Moi07, Moi08, Her13]. Note that the transient signals decaying with the shortest time constant are not visible here, because the minimal delay is larger than 460 fs. The longer time constants were attributed to the product formation. By using only one time constant here, an average time constant for the product formation is obtained.

Tab. 5.2.1 Regions of the 2D spectra used for the analysis of the product formation and retrieved fitting parameters. Area averaged for ν_{probe}: 22800 - 23040 cm^{-1} and for $\nu_{pump} = \nu_{pump,central} \pm 32.5$ cm^{-1}.

Label number	**1**	**2**	**3**	**4**	**5**	**6**	**7**	**8**
$\nu_{pump,central}$ [cm^{-1}]	32000	32160	32330	32470	32670	32870	33040	33240
a_o (offset) [a.u.]	47	91	51	38	53	85	59	22
a_r (exp. rise) [a.u.]	-47	-91	-52	-39	-53	-85	-59	-21
$1/\tau_r$ (exp. rise) [ps^{-1}]	0,60	0,51	0,48	0,48	0,44	0,43	0,45	0,42

The zero-time delay is determined from the chirp of the white light probe and was held constant for all time traces. At zero time delay the amplitude of the fit is set to zero amplitude, as there is no photo product formed. The fitting routine had three free parameters that were optimized to match the experimental results. These parameters are the amplitude and time constant (τ_r) of the exponential rise and the amplitude of the offset. Two representative fits are shown in Fig. 5.2.9a and the fitting results are summarized in Tab. 5.2.1.

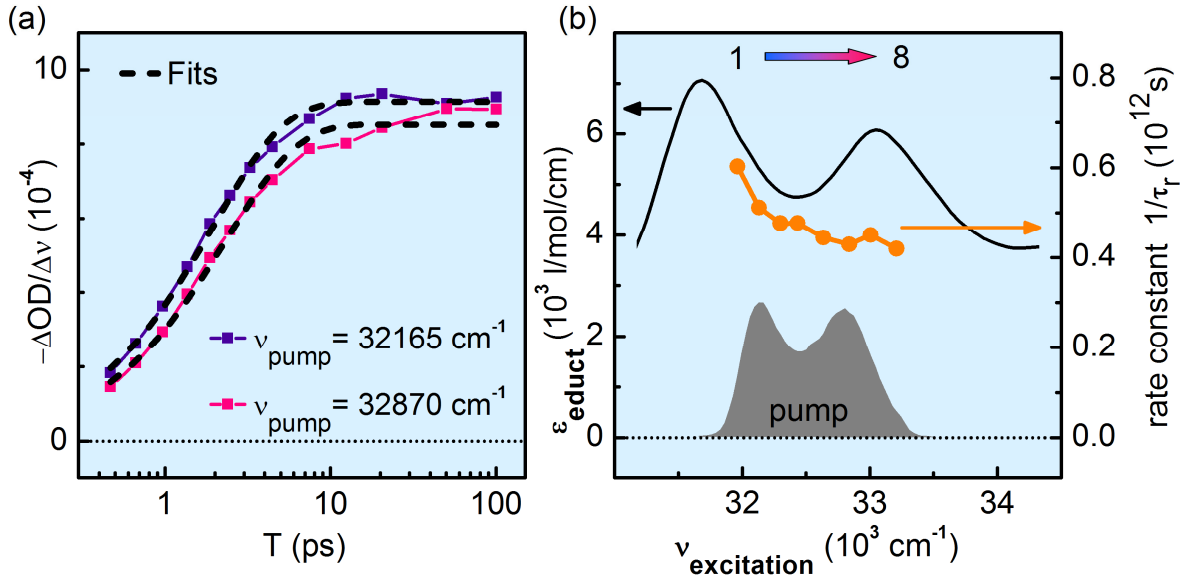

Fig. 5.2.9. Excitation-frequency dependent rate constants of the photo product formation. (a) Measured time traces of the product absorption with the respective fits. (b) Rate constants of the exponential rise retrieved from the fits for different pump frequencies overlaid with the pump intensity spectrum and the molecular absorption.

The fitting function combines the positive amplitude of the offset with a negative contribution from the exponential function which decays until only the offset amplitude remains. Therefore the amplitude of both functions have an equal value but opposite sign. Small deviations of the two amplitude values are due to the fact that the contribution from the exponential function did not decay completely for all fits.

The decay times retrieved (1.7 – 2.4 ps) do agree well with the values reported in literature (1.8 – 2 ps in [Her13, Moi07, Moi08]), in spite of the fact, that these measurements were done when exciting other electronic states than the S_2 state. The retrieved rate constants show a systematic decrease when the excitation frequency is increased (Fig. 5.2.9b). This means that the speed of the product formation is slower when higher vibrational modes are excited in the

S_2 state. As both, the amount of products as well as the product formation rate in the ps regime, depend on the excitation energy, the ps time constant observed in the transients can now univocally be assigned to the product formation process.

When increasing the excitation frequency, an increase in product yield is accompanied by a decrease of the product formation rate. This behavior seems to be counterintuitive at the first glance. For example, when assuming a simple rate model with product and relaxation pathways, a decreasing product formation rate would lead to lesser product. Therefore, the molecular dynamics cannot be described appropriately by a static rate model but rather by considering the wavepacket propagation on the multidimensional potential energy surface.

The excited state wavepacket has to trespass a conical intersection to the product state that is located on a local minimum of the multidimensional excited state surface. The propagating excited state wavepacket cannot directly reach the conical intersection (it moves past its position) and is therefore partially trapped for some time until the vibrational relaxation has occurred and the conical intersection at the minimum is finally reached. The higher the excitation energy, the stronger is the impulse of the wavepacket and a longer trapping time occurs. The partially delayed product formation then leads to the observed slower product formation rate, independent of the actual product yield.

In conclusion, the photochromic effect of 5,6DPBC at room temperature is not a competition between vibrational relaxation and the ring-opening reaction but rather a combination of both effects. I propose the following overall picture of the photo-induced reaction in 5,6DPBC: After UV excitation the excited state wavepacket has to pass a barrier in the potential energy surface that is more efficiently done for higher vibrational excess energy and depends on the type of vibrational mode excited, due to the multidimensionality of the potential energy surface. After the barrier, the wavepacket propagates towards the conical intersection into the product state. Depending on the multidimensional impulse of the wavepacket, the conical intersection can be trespassed directly or temporally delayed after vibrational relaxation.

The results of this chapter show that it is necessary to explicitly consider the excitation conditions when describing light-induced molecular dynamics, which is expected to be true for a vast amount of photochemical reactions. The vibrational mode dependence of the photophysics of 5,6DPBC offers the opportunity for coherent control which can improve the applicability of chromenes for applications like optical switching [Ire02, Eva05] and optoelectronic devices [Dol03].

6. Summary and outlook

In this thesis, I presented new developments in ultrafast spectroscopy and their application to open questions in molecular photophysics. The extension of 2-dimensional spectroscopy into the UV spectral domain was realized for the first time in collinear geometry with tunable sub-20 fs pulses. An innovative data evaluation procedure for 2D spectroscopy was established that retrieves excitation-frequency resolved quantum yields of chemical reactions and molecular processes in an all optical experiment. Finally, newly developed measurement techniques have been used to clarify coherent photo-induced molecular processes like photodissociation, intermolecular energy migration and conformational rearrangements in small molecules.

Experimental and analytical developments

In order to investigate photo-induced molecular processes on a sub-100 fs time scale, transient spectroscopy with high temporal resolution and absolute time-zero calibration is needed. Therefore, a pump-probe setup with sub-40 fs temporal resolution was developed for the investigation of the bond cleavage of benzhydryl chlorides. For UV pump and UV probe pulses, the tunable outputs of non-collinear optical parametric amplifiers (NOPA) were frequency doubled in thin (~30 μm) BBO crystals. The use of a 50 μm thick free flowing liquid jet allows to reduce spurious effects and dispersion of the UV beams, e.g., in the windows of a cuvette. Absolute time-zero calibration was achieved by simultaneous measurement of the pump-probe cross-correlation in a second pump-probe branch that is a mirror image of the sample branch. The two-color transient experiment allows to measure UV light-induced transient signatures with sub-40 fs time resolution and < 5 fs absolute time-zero determination.

When using intense pump pulses in transient absorption measurements, the molecular dynamics might be affected by multiphoton processes, as evident in perylene orange. The measured signals contain additional information about electronic and vibrational coherences that last for about 20 – 100 fs. To investigate these coherences a double-pump-single-probe setup was built that uses two visible pump pulses and a visible probe pulse. The variable interpulse delay of the two pump pulses generated in a Michelson interferometer allows monitoring the coherence dynamics for increasing pump pulse energies. Ultrashort, 13-fs pump pulses were generated with a broadband NOPA and compressed with a prism compressor and Brewster-angled chirped mirrors. The absolute interpulse delay is monitored with a continuous wave laser that is incorporated additionally into the Michelson interferometer and thus guarantees precise

knowledge of the interpulse electric-field phase. The setup allows investigating the development of the light-induced polarization in the strong-field limit with sub-13 fs temporal resolution and resolves the excitation frequency, similar to 2D spectroscopy.

For the investigation of vibrational coherences in 2-(2'-hydroxyphenyl)benzothiazole, two phase-stable ultrashort UV pulses are needed for excitation. Therefore, the Michelson interferometer based setup described above was transferred into the UV spectral domain. Only the 40 fs long probe pulse is in the visible regime. Sub-20 fs UV pulses centered at 350 nm were generated by frequency doubling of the NOPA output that was compressed with a visible prism compressor. The variable interpulse delay between the pump pulses allows using this setup for quantum control spectroscopy with the shortest pulses described in the UV so far.

To develop collinear 2D spectroscopy in the UV spectral domain, double pulses with a variable interpulse delay and phase are needed. Those pulses are generated best by using a pulse shaper device that works directly in the UV. Shaped tunable UV pulses with sub-20 fs substructures have been demonstrated for the first time with the aid of a commercially available acousto-optical dispersive filter (AOPDF; Dazzler^{TM}, Fastlite). In order to generate nearly Fourier limited pulses with a clean spatial beam profile in the interaction region, it is of major importance to explicitly consider the spatio-temporal coupling of the shaper device. The diffracted (shaped) output pulse shows a lateral shift of the individual diffracted components that depends on the induced temporal delay introduced. Considering the geometrical and Gaussian description of the shaped beam simultaneously allows one to find a simple experimental layout that guarantees coherent superposition of all diffracted components after focusing, e.g., into the interaction region. With the aid of the UV pulse shaper, Fourier limited sub-20 fs or arbitrarily shaped pulses tunable between 250 – 400 nm are now available.

The source to generate UV pulses also limits the shortest available pulse duration. However, it is often desirable to have even shorter pulses. A convenient approach to reduce the pulse length of few-µJ UV pulses after their generation was introduced. Pulse shortening of 20-fs UV pulses by a factor of up to 1.5 was achieved using spectral broadening by self-phase modulation in few-mm thick UV transparent crystals. Even higher factors were obtained for longer pulses. This was achieved by determining the correct experimental conditions to avoid beam distortions or beam breakup due to self-focusing inside the crystal. Pulse shortening of UV pulses can be easily incorporated in any existing spectroscopic experiment by using just 2 lenses and, e.g., a 1 mm thick CaF_2 crystal.

Before generating shaped UV pulses the correct phase function for optimal pulse compression

has to be found. This can be achieved by minimizing the pulse length which has to be measured on a day-to-day basis. Therefore an UV-autocorrelator was developed that allows to measure sub-20 fs pulses all over the UV spectral domain by using two-photon absorption in thin crystals (e.g., < 100 μm).

In a time consuming experiment, the additional technical effort to increase the signal-to-noise ratio can be highly beneficial, e.g., to reduce the overall measurement time. In transient absorption and collinear 2D spectroscopy the main source of noise is given by the intensity fluctuations of the probe. The concept of single-shot-referencing was therefore realized for spectrally resolved broadband detection. By simultaneously measuring a fraction of the probe with an additional spectrometer for every laser shot, an increase of the confidence interval from about $\pm 6 \cdot 10^{-5}$ OD (only one CCD, [Meg09]) to $\pm 2 \cdot 10^{-5}$ OD was achieved in a pump-probe experiment when using a super-continuum white light probe. The measurement time is typically reduced by a factor of 5 or even 10 in a 2D-UV experiment.

To measure the excitation-detection frequency correlations in an UV light-induced process 2D spectroscopy is needed. A novel collinear 2D setup comprising UV pulses tunable between 240 – 370 nm with a useable spectral coverage of 2000 cm^{-1} (25 nm at 316 nm) was built. Other experimental realizations in the UV are at best 1500 cm^{-1} (FWHM) at a fixed wavelength of 267 nm or 400 cm^{-1} (FWHM) for tunable pulses. For probing either a replica of the pump pulses or a super-continuum probe covering 250 - 720 nm were used. High signal-to-noise ratios and fast acquisition times of about 4 minutes (for one population time) were achieved by using single-shot-referencing and phase cycling. The latter one benefits from the high shot-to-shot correlation of the laser pulses and does not increase the measurement time. A measurement procedure that uses pump stray light subtraction was introduced for weak probe pulses (a few pJ/nm for a white light supercontinuum [Bra09]). Data acquisition and evaluation procedures were described in detail. The developed (Fourier transform) 2D-UV setup compares well with other experiments reported only recently in the literature. The large spectral bandwidth of the pump pulses allows investigating congested and broad (> 20 nm) absorption spectra typically found in proteins and DNA strands.

Despite the great benefits of a quantitative analysis of 2D measurements for the investigation of excitation-frequency dependent molecular processes, this type of analysis has not yet been addressed in the related literature. To do so, a careful analysis of the origin and proportionality of 2D signals was given. It was found that signal amplitudes which are proportional to the population of molecules in a specific state can be retrieved. However, this is only possible when

measuring population times that are larger than the electronic dephasing in the molecule. The excitation-frequency dependent amount of excited molecules is a convolution of the absorption spectrum with the spectral photon density of the pump pulses. This knowledge allows extending the calculation of product quantum yields used in conventional transient absorption spectroscopy by the dimension of the excitation frequency. The 2D product yield approach can be applied to a variety of photo-induced chemical reactions for all spectral domains without the need of elaborately tuning the frequency of a narrowband pump pulse step-by-step.

Coherent molecular dynamics

In the course of this thesis, the initial dynamics of the photo-induced bond cleavage of benzhydryl chloride was investigated within the first hundreds of femtoseconds. After UV excitation of the precursor two different products are spectroscopically distinguishable. Either an ion pair (benzhydryl cation / chlorine anion) is formed heterolytically or a radical pair (benzhydryl radical / chlorine radical) is formed homolytically. Measurements in conjunction with theoretical calculations show that the molecular dynamics can be considered as ballistic wavepacket propagation on the excited state potential energy surfaces. The wavepacket can cross either one of the two conical intersections leading to the different products. The first conical intersection is reached at about 76 fs after excitation into the Franck-Condon region and leads to radical pairs (~ 40 %). The fraction of excited molecules that did not cross the first one can reach a second distinct conical intersection at about 124 fs leading to ion pairs (~ 2 %). The remaining ~ 57 % do not dissociate and go back to the ground state. The results show that a classical kinetic description (rate model) of the depopulation of the excited state is not correct as the measured rise times would not reproduce the observed quantum yields. The correct picture is a dynamic description as a coherent wavepacket motion on the excited state potential energy surfaces.

The influence of high intensity excitation on the photo-induced molecular dynamics was studied exemplarily on the dye perylene orange. A combined theoretical and experimental study was done. In the transient measurements I used two pump pulses with a variable interpulse delay, to study vibrational and electronic coherences for different excitation intensities. The results can be divided into a weak pump regime (linear regime of excitation) and a strong pump regime (nonlinear regime of excitation) containing additional information about the system studied. In the linear excitation regime a dependence on the observed dynamics is found that can be described by its steady state absorption spectrum. From the technical point of view, the

nonlinear excitation regime allows to determine the absolute inter-pump pulse phase, which may avoid the need for *phasing* in 2D spectroscopy. For increasing pump energies the induced coherence oscillates between the excited state and the ground state for interpulse delays within the electronic dephasing time (16.5 fs). In addition, a pronounced vibrational wavepacket motion was observed that showed a dependence on the pump pulse chirp. A change in the line shape of the retrieved absorption spectra (band narrowing) was observed in the nonlinear excitation regime that can be helpful to decipher overlapping vibronic bands of the absorption spectra and to unravel wavepacket-related phenomena in photochemical reactions or resolve congested spectra with 2D spectroscopy in the strong-field limit. The increasing vibrational signal contributions can be seen as a virtual increase in temporal resolution as already observed in theory for strong-pump-probe spectroscopy [Gel11b].

The light-induced proton transfer in 2-(2'-hydroxyphenyl)benzothiazole takes place within 35 fs after excitation. The reaction happens as a vibrational wavepacket motion on the excited state potential energy surface that is accompanied by a change of the electronic configuration. In order to elucidate the importance of the vibrational modes to the population dynamics, two delayed pump pulses are used to manipulate the vibrational wavepacket contribution in a quantum control spectroscopy approach. It was found that the population dynamics of the proton transfer could not be controlled coherently for inter-pump pulse delays > 60 fs. The result shows that control is, if at all, only possible for times < 50 fs after excitation and before the molecule has propagated away from the Franck-Condon point. The result is a guide for the investigation of a variety of ultrafast photoreactions as it allows limiting the time period in which the electronic coherence is optically addressable within the ultrafast wavepacket motion.

Excitation-frequency dependent photochemistry

When a photoactive molecule absorbs a photon, the excess energy steers molecular processes like conformational rearrangement. Explicitly, the excitation of different electronic or vibrational levels can have a severe influence on the molecular dynamics. This is observable as an excitation-frequency dependent outcome of the process. 2D spectroscopy is ideally suited to reveal those dependencies.

As an example, the intramolecular energy dissipation in pyrene was investigated with 2D-UV and transient absorption spectroscopy. When exciting the S_2 electronic state, an ultrafast internal conversion most probably to the S_1 state mediated by vibrational coupling occurs within 85 fs. The observation of vibrational oscillations in the transient dynamics of the excited

state absorption bands of the S_1 state clearly shows that the process is highly coherent. This is due to the fact that internal conversion proceeds fast enough for an impulsive excitation of the S_1 vibrational modes to occur. In the 2D-UV measurements the pump pulse spectrum overlaps with the second and third vibronic band of the S_2 state absorption. For probing, a white light supercontinuum was used that allows monitoring all the S_1 excited state absorption contributions observed in the visible spectral domain. The measurements show that for high and low frequency excitation there is a severe difference in the shape of the S_1 excited state absorption bands. This difference decays with a time constant of about 4 ps and is assigned to vibrational relaxation in the S_1 state. Therefore, the specific vibrational bands populated in the S_1 state (acceptor modes) depend on the vibrational modes excited in the S_2 state (donor modes). The results indicate that the specific mode structures of both S_2 and S_1 have to be considered to derive a complete picture of the intramolecular processes. The excitation-frequency dependent properties of pyrene have not been measured before and with the aid of theoretical simulations there is a good chance to unravel the mode dependencies.

The photo-cyclic ring-opening reaction of chromenes is known to depend on the excitation frequency which is observed in the ring-opening product yield as well as in the temporal dynamics of the reaction. 2D-UV measurements using pump pulses that span over two vibronic bands in the S_2 electronic absorption were employed for the first time on 2,2-diphenyl-5,6-benzo(2H)chromene in solution. The results show that the product quantum yield increases when higher vibrational levels are excited (from 40 to 80 %). Furthermore, the 2D-UV measurements reveal that for increasing excitation frequency, slower dynamics were observed in the product formation (from 1.6 to 2.5 ps). The following picture for the light-induced molecular dynamics arises: After UV irradiation the excited state wavepacket has to pass a barrier in the potential energy surface that is more efficiently done for higher vibrational excess energy and depends on the type of vibrational mode excited, due to the multidimensionality of the potential energy surface. After the barrier, the wavepacket propagates towards the conical intersection into the product state. Depending on the multidimensional impulse, the wavepacket can pass through the conical intersection directly or temporally delayed after vibrational relaxation. The results demonstrate that 2D-UV spectroscopy can be used to solve ambiguities in the interpretation of the photochemistry of chromenes and other photoswitches.

The 2D-UV measurements presented in this thesis have proven that, despite the large but still limited spectral range of the UV pump pulses, 2D spectroscopy in the UV has great potential to unravel photophysical processes on the microscopic level.

Outlook

I propose the following technical modifications for the 2D-UV:

- Implementation of the newly available shaper software to switch the interpulse delay and phase on the 1 kHz repetition rate of the laser. The *rapid-scan* increases the signal-to-noise ratio and drops the measurement time for one population time to < 1 minute.
- Combining achromatic frequency doubling [Bau04a] with the UV pulse shaper to measure 2D spectra covering the most of the UV spectral domain. Preliminary experiments have shown that the pulse shaper can diffract pulses with a Fourier limit of 3.7 fs.

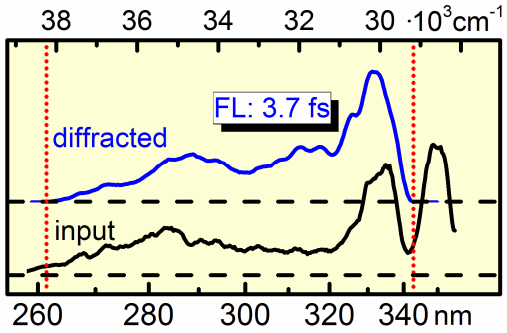

- Application of sophisticated phase cycling schemes (without optical modifications) to measure two-quantum signals or realize 3D spectroscopy [Zhe12] to measure high lying excited states [Din07, Gar09] and uncover hidden couplings [Fid10]. However, the interpretation of the results is cumbersome and the additional effort not automatically pays off.

I propose the following experiments to address open questions in photo-induced molecular processes:

- Investigation of the molecular processes in DNA and nucleotides. It is known, that the UV light-induced production of harmful photoproducts in DNA (such as the thymine dimer) is not very efficient (< 1%) due to ultrafast nonreactive decay pathways (in ps). However, fully mapping the decay pathways is still ongoing research [Tak08, Mil09]. 2D-UV spectroscopy allows measuring the energy and charge transfer processes, couplings between nucleobases and can unravel the role of electronic excitons in the efficient energy redistribution within DNA strands. The excitation frequency resolution allows addressing different absorptive features and their influence on the molecular dynamics.
- Indole, which is a common chromophore of many nitrogen heterocyclic biomolecules (such as the essential amino acid Tryptophan), can serve as a model system for nucleotides. The molecule shows overlapping UV absorption features of the L_a and L_b state, a reversal of the energy of these states after excitation in strongly polar solvents due to solvation, an excitation-frequency dependent fluorescence quantum yield (also depending on the pH

value of the solvent), and solvated electrons that can be generated for excitation energies even below the classical photoinization threshold. Preliminary transient measurements (Fig. 6.1a) show, that the state-reversal process (Fig. 6.1b) can be detected as a bathochromic shift (~ 3400 cm^{-1}) of the L_a ESA. Despite the fact that the observed time constant (630 fs) corresponds well with the *long* time behavior of solvation in water reported in literature [Jim94], the authors mention that there is also a *short* time behavior (reorientation of water molecules) in less than 50 fs, not observable due to the lack of temporal resolution. Therefore it is most interesting to use the 2D-UV setup with the high time resolution. To achieve sub-30 fs resolution, a compressed broadband UV pulse (320 – 390 nm bandwidth) generated by up-conversion of a visible NOPA [Cer12] can be used as probe. The solvated electron signature (at around 650 nm) can be measured with visible white light probing allowing for a complete picture of the transient signatures. Selective excitation of L_a and L_b in a 2D-UV experiment can answer the following questions: (1) Clarify how the absorption bands of L_a and L_b overlap and how the entangled excitation is linked with the photo-induced processes. (2) Identify their transient signatures which are simultaneously present in conventional measurements, especially if it is possible to resolve a L_b signature (e.g. in the NIR) at a wavelength where this state is predominantly addressed. (3) Identify the fluorescing state (most probably the L_a state) and investigate nonfluorescent pathways. (4) Resolve the sub-50 fs time-behavior of the solvation process for each state individually. (5) Decipher from which state the solvated electrons originate and how the temporal dynamics depend on the respective excited state.

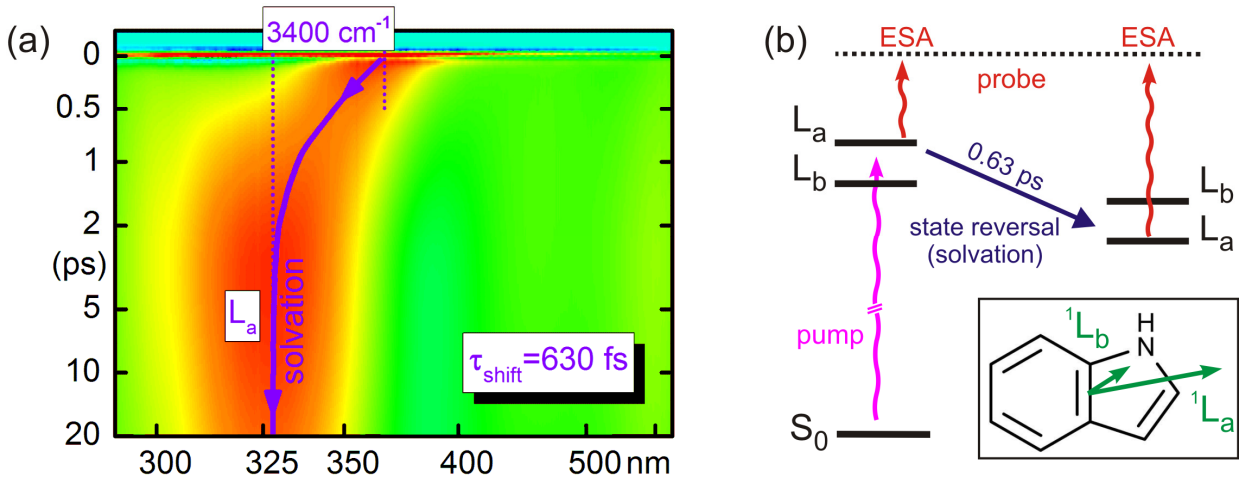

Fig. 6.1. (a) Transient measurement of indole in water reveals the dynamics of the state-reversal process due to solvation. (b) Reaction model.

7. Literature

[Ahl89] R. Ahlrichs, M. Bär, M. Häser, H. Horn, and C. Kölmel, *Chem. Phys. Lett.* **162**, 165 (1989).

[Ajd08] A.A. Oskouei, O. Bräm, A. Cannizzo, F. van Mourik, A. Tortschanoff, M. Chergui, *Chem. Phys.* **350**, 104 (2008).

[Akb05] K. Akbarzadeh, D.C. Bressler, J. Wang, K.L. Gawrys, M.R. Gray, P.K. Kilpatrick, H.W. Yarranton, *Energy & Fuels* **19**, 1268 (2005).

[Alb99] A.W. Albrecht, J.D. Hybl, S.M.G Faeder, D.M. Jonas, *J. Chem. Phys.* **111**, 10934 (1999).

[Ald07] A. Aldongarov, N.N. Barashkov, I.S. Irgibaeva, *I. J. Quant. Chem.* **107**, 2331 (2007).

[All12] T. K. Allison, H. Tao, W. J. Glover, T. W. Wright, A. M. Stooke, C. Khurmi, J. van Tilborg, Y. Liu, R. W. Falcone, T. J. Martínez, and A. Belkacem*, J. Chem. Phys.* **136**, 124317 (2012).

[And08] M.E. Anderson, A. Monmayrant, S.-P. Gorza, P. Wasylczyk, I.A. Wamsley, *Laser Phys. Lett.* **5**, 259 (2008).

[And92] R. Andriessen, M. Ameloot, N. Boens, F.C. De Schryver, *J. Phys. Chem.* **96**, 314 (1992).

[Arn03] J.C. Arnall-Culliford, Y. Teral, P. Sgarabotto, M. Campredon, G. Giusti, *J. Photochem. Photobiol. A: Chem.* **159**, 7 (2003).

[Aub00] J. Aubard, F. Maurel, G. Buntinx, O. poizat, G. Levi, G. Guglielmetti, A. Samat, *Mol. Cryst. Liq. Cryst.* **345**, 215 (2000).

[Aub12] G. Auböck, C. Consani, F. van Mourik, M. Chergui, *Opt. Lett.* **37**, 2337 (2012).

[Bab09] M. Baba, M. Saitoh, Y. Kowaka, K. Taguma, K. Yoshida, Y. Semba, S. Kasahara, T. Yamanaka, Y. Ohshima, Y.-C. Hsu, S.H. Lin, *J. Chem. Phys.* **131**, 224318 (2009).

[Bac96] S. Backus, J. Peatross, Z. Zeek, A. Rundquist, G. Taft, M.M. Murnane, H.C. Kapteyn, *Opt. Lett.* **21**, 665 (1996).

[Bai11] G. Bains, A.B. Patel, V. Narayanaswami, *Molecules* **16**, 7909 (2011).

[Ban94] U. Banin, A. Bartana, S. Ruhman, R. Kosloff, *J. Chem. Phys.* **101**, 8461 (1994).

[Bar07] M. Barbatti, G. Granucci, M. Persico, M. Ruckenbauer, M. Vazdar, M. Eckert-Maksić, and H. Lischka, *J. Photochem. Photobiol. A* **190**, 228 (2007).

[Bar09] M. Barbetti, A.J.A. Aquino, H. Lischka, C. Schriever, S. Lochbrunner, E. Riedle, *Phys. Chem. Chem. Phys.* **11**, 1406 (2009).

[Bar93] N.N. Barashkov, T.V. Sakhno, R.N. Nurmukhametov, O.A. Khakhel, *Russ. Chem. Rev.* **62**, 539 (1993).

[Bar95] C.J. Bardeen, Q. Wang, C.V. Shank, *Phys. Rev. Lett.* **75**, 3410 (1995).

[Bar97] C.J. Bardeen, V.V. Yakovlev, K.R. Wilson, S.D. Carpenter, P.M. Weber, W.S. Warren, *Chem. Phys. Lett.* **280**, 151 (1997).

[Bau04a] P. Baum, S. Lochbrunner, E. Riedle, *Opt. Lett.* **29**, 1686 (2004).

[Bau04b] P. Baum, S. Lochbrunner, E. Riedle, *Opt. Lett.* **29**, 210 (2004).

[Bau06] P. Baum, M. Breuer, E. Riedle, G. Steinmeyer, *Opt. Lett.* **31**, 2220 (2006).

[Bau97] T. Baumert, T. Brixner, V. Seyfried, M. Strehle, G. Gerber, *Appl. Phys. B* **65**, 779 (1997).

[Bec05] R.S. Becker, G. Favaro, A. Romani, P.L. Gentili, F.M.B. Dias, *Chem. Phys.* **316**, 108 (2005).

[Bec11] R.S. Becker, G. Favaro, *J. Photochem. Photobiol. C: Photochem. Rev.* **12**, 167 (2011).

[Bec66] R.S. Becker, J. Michl, J. *Am. Chem. Soc.* **88**, 5931 (1966).

[Bec69] R.S. Becker, E. Dolan, D.E. Balke, *J. Chem. Phys.* **50**, 239 (1969).

[Bec99] R.S. Becker, A.P. Pelliccioli, A. Romani, G. Favaro, *J. Am. Chem. Soc.* **121**, 2104 (1999).

[Bit94] T. Bittner, K.-D. Irrgang, G. Renger, M.R. Wasielewski, *J. Phys. Chem.* **98**, 11821 (1994).

[Big91] J.-Y. Bigot, M. T. Portella, R. W. Schoenlein, C. J. Bardeen, A. Migus, and C. V. Shank, *Phys. Rev. Lett.* **66**, 1138 (1991).

[Bir75] J.B. Birks, *Rep. Prog. Phys.* **38**, 903 (1975).

[Bix12] O. Bixner, V. Lukeš, T. Mančal, J. Hauer, F. Milota, M. Fischer, I. Pugliesi, M. Bradler, W. Schmid, E. Riedle, H.F. Kauffmann, N. Christensson, *J. Chem. Phys.* **136**, 204503 (2012).

[Boh90] C. Bohne, E.A. Albuin, J.C. Scaiano, *J. Am. Chem. Soc.* **112**, 4226 (1990).

[Bor95] N.A. Borisevich, L.B. Vodovatov, G.G. D'yachenko, V.A. Petukhov, M.A. Semyonov, *J. Appl. Spectrosc.* **62**, 482 (1995).

[Bou01] H. Bouas-Laurent, H. Dürr, *Pure Appl. Chem.* **73**, 639 (2001).

[Bra09] M. Bradler, P. Baum, E. Riedle, *Appl. Phys. B* **97**, 561 (2009).

[Bri04a] T. Brixner, I.V. Stiopkin, G.R. Fleming, *Opt. Lett.* **8**, 884 (2004).

[Bri04b] T. Brixner, T. Mančal, I.V. Stiopkin, G.R. Fleming, *J. Chem. Phys.* **121**, 4221 (2004).

[Bri05] T. Brixner, J. Stengerm H.M. Vaswani, M. Cho, R.E. Blankenship, G.R. Fleming, *Nature* **434**, 625 (2005).

[Bri11] D. Brinks, R. Hildner, F.D. Stefani, N.F. van Hulst, *Opt. Express* **19**, 26486 (2011).

[Bri12] D. Brida, C. Manzoni, G. Cerullo*, Opt. Lett.* **37**, 3027 (2012).

[Bri63] J.B. Birks, D.J. Dyson, I.H. Munro, *Proc. Roy. Soc. Lond. A* **275**, 575 (1963).

[Buc06] T. Buckup, T. Lebold, A. Weigel, W. Wohlleben, M. Motzkus, *J. Photochem. Photobiol. A: Chem.* **180**, 314 (2006).

[Buc08] T. Buckup, J. Hauer, C. Serrat, M. Motzkus, *J. Phys. B: At. Mol. Opt. Phys.* **41**, 074024 (2008).

[Can12] A. Cannizzo, *Phys. Chem. Chem. Phys.* **14**, 11205 (2012).

[Cel00] P. Celani, and H.-J. Werner, *J. Chem. Phys.* **112**, 5546 (2000).

[Ger96] G. Gerullo, C.J. Bardeen, Q. Wang, C.V. Shank, *Chem. Phys. Lett.* **262**, 362 (1996).

[Cer12] G. Cerullo, *Personal communication* (2012).

[Che08] Y.-C. Cheng, G.R. Fleming, *J. Phys. Chem. A* **112**, 4254 (2008).

[Cho06] M. Cho, T. Brixner, I. Stiopkin, H. Vaswani, G.R. Fleming, *J. Chin. Chem. Soc.* **53**, 15 (2006).

[Cho08] M. Cho, *Chem. Rev.* **108**, 1331 (2008).

[Chr10] N. Christensson, F. Milota, A. Nemeth, I. Pugleisi, E. Riedle, J. Sperling, T. Pullerits, H.F. Kauffmann, J. Hauer, *J. Phys. Chem. Lett.* **1**, 3366 (2010).

[Cin08] J.A. Cina, *Annu. Rev. Phys. Chem.* **59**, 319 (2008).

[Cou06] S. Coudreau, D. Kaplan, P. Tournois, *Opt. Lett.* **31**, 1889 (2006).

[Dad91] J.I. Dadap, G.B. Rocht, D.H. Reitze, M.C. Downer, *Opt. Lett.* **16**, 499 (1991).

[Dan87] M. Dantus, M.J. Rosker, A.H. Zewail, *J. Chem. Phys.* **87**, 2395 (1987).

[Day95] P.N. Day, Z. Wang, R. Pachter, *J. Phys. Chem.* **99**, 9730 (1995).

[DeF07] L.P. DeFlores, R.A. Nicodemus, A. Tokmakoff, *Opt. Letters* **32**, 2966 (2997).

[Dei71] T. Deinum, C.J. Werkhoven, J. Langelaar, R.P.H. Rettschnick, J.D.W. Voorst, *Chem. Phys. Lett.* **12**, 189 (1971).

[Dei74] T. Deinum, C.J. Werkhoven, J. Langelaar, R.P.H. Rettschnick, J.D.W. Voorst, *Chem. Phys. Lett.* **27**, 552 (1974).

[DeL94] K.W. DeLong, R. Trebino, D.J. Kane*, J. Opt. Soc. Am B* **11**, 1595 (1994).

[Del98] S. Delbaere, B. Luccioni-Houze, C. Bochu, Y. Teral, M. Campredon, G. Vermeersch, *J. Chem. Soc. Perk. Trans. 2*, 1153 (1998).

[DeM66] A. J. DeMaria, D. A. Stetser, H. Heynau, *Appl. Phys. Lett* **8**, 174 (1996).

[Den06] B. Denegri, A. Streiter, S. Jurić, A. R. Ofial, O. Kronja, and H. Mayr*, Chem. Eur. J.* **12**, 1648 (2006).

[Din07] F. Ding, M.T. Zanni, *Chem. Phys.* **341**, 95 (2007).

[Dob10] A.L. Dobryakov, S.A. Kovalenko, A. Weigel, J.L. Pérez-Lustres, J. Lange, A. Müller, N.P. Ernsting*, Rev. Sci. Instrum.* **81**, 113106 (2010).

[Dol03] D. Dulić, S.J. van der Molen, T. Kudernac, H.T. Jonkman, J.J.D. de Jong, T.N. Bowden, J. van Esch, B.L. Feringa, B.J. van Wees, *Phys. Rev. Lett.* **91**, 207402 (2003).

[Dom04] W. Domcke, D. R. Yarkony, H. Köppel, *Conical Intersections: Electronic Structure, Dynamics and Spectroscopy* (World Scientific Publishing, Singapore, 2004).

[Dur99] C.G. Durfee III, S. Backus, H.C. Kapteyn, M.M. Murnane, *Opt. Lett.* **24**, 697 (1999).

[Dyk98] D.A. Van Dyke, B.A. Pryor, P.G. Smith, M.R. Topp, *J. Chem. Ed.* **75**, 615 (1998).

[Ede88] D.C. Edelstein, E.S. Wachman, L.K. Cheng, W.R. Bosenberg, C.L. Tang, *Appl. Phys. Lett.* **52**, 2211 (1988).

[Ego08] D. Egorova, M.F. Gelin, M. Thoss, H. Wang, W. Domcke, *J. Chem. Phys.* **129**, 214303 (2008).

[Els91] T. Elsaesser, W. Kaiser, *Annu. Rev. Phys. Chem.* **42**, 83 (1991).

[Ern01] N. P. Ernsting, S. A. Kovalenko, T. Senyushkina, J. Saam, V. Farztdinov, *J. Phys. Chem. A* **105**, 3443 (2001).

[Eva05] R.A. Evans, T.L. Hanley, M.A. Skidmore, T.P. Davis, G.K. Such, L.H. Yee, G.E. Ball, D.A. Lewis, *Nature* **4**, 240 (2005).

[Fae99] S.M.G. Faeder, D.M. Jonas, *J. Phys. Chem. A* **103**, 10489 (1999).

[Fel13] Personal communication: Christian Feldmeier, University of Regensburg, Germany (2013.07.11).

[Fer65] J. Ferguson, *J. Chem. Phys.* **43**, 306 (1965).

[Fid10] A.E. Fidler, E. Harel, G.S. Engel, *J Phys. Chem. Lett.* **1**, 2876 (2010).

[Fin08] B. P. Fingerhut, D. Geppert, and R. de Vivie-Riedle, *Chem. Phys.* **343**, 329 (2008).

[Fin12] B. P. Fingerhut, C. F. Sailer, J. Ammer, E. Riedle, and R. de Vivie-Riedle, *J. Phys. Chem. A* **116**, 11064 (2012).

[Fin12b] B. P. Fingerhut, S. Oesterling, K. Haiser, K. Heil, A. Glas, W. J. Schreier, W. Zinth, T. Carell, and R. de Vivie-Riedle, *J. Chem. Phys.* **136**, 204307 (2012).

[Fog95] P. Foggi, L. Pettini, I. Sànta, R. Righini, S. Califano, *J. Phys. Chem.* **99**, 7439 (1995).

[Fre10] F. Frei, R. Bloch, T. Feurer, *Opt. Lett.* **35**, 4072 (2010).

[Fuj88] T. Fujii, E. Shimizu, S. Suzuki, *J. Chem. Soc. Faraday Trans. 1* **84**, 4387 (1988).

[Gar09] S. Garrett-Roe, P. Hamm, *J. Chem. Phys.* **130**, 164510 (2009).

[Gei10] D. Geisler, T. Rozgonyi, J. González-Vázquez, L. González, S. Nichols, T. Weinacht, *Phys. Rev. A* **82**, 011402(R) (2010).

[Gel02] M.F. Gelin, A.V. Pisliakov, W. Domcke, *Phys. Rev. A* **65** ,062507 (2002).

[Gel09] M.F. Gelin, D. Egorova, W. Domcke, *J. Chem. Phys.* **131**, 124505 (2009).

[Gel11a] M. F. Gelin, D. Egorova, W. Domcke, *J. Phys. Chem. B* **115**, 5648 (2011).

[Gel11b] M.F. Gelin, D. Egorova, W. Domcke, *J. Phys. Chem. Lett.* **2**, 114 (2011).

[Gen02] T. Gensch, C.C. Gradinaru, I.H.M. van Stokkum, J. Hendriks, K.J. Hellingwerf, R. van Grondelle, *Chem. Phys. Lett.* **356**, 347 (2002).

[Gen04] P.L. Gentili, E. Danilov, F. Ortica, M.A.J. Rodgers, G. Favaro, *Photochem. Photobiol. Sci.* **3**, 886 (2004).

[Gho11] M. Ghotbi, P. Trabs, M. Beutler, *Opt. Lett.* **36**, 463 (2011).

[Gie99] S. Linden, J. Kuhl, H. Giessen, *Opt. Lett.* **24**, 569 (1999).

[Gin09] N.S. Ginsberg, Y.-C. Cheng, G.R. Fleming, *Acc. Chem. Res.* **42**. 1352 (2009).

[Gör02] H. Görner, A.K. Chibisov, *J. Photochem. Photobiol. A: Chem.* **149**, 83 (2002).

[Gra08] M.W. Graham, Y.-Z. Ma, G.R. Fleming, *Nano Letters* **8**, 3936 (2008).

[Gre73] K.H. Grellmann, A.R. Watkins, *J. Am. Chem. Soc.* **95**, 983 (1973).

[Gri04] S. Grimme, *J. Comp. Chem.* **25**, 1463 (2004).

[Gru07] E.M. Grumstrup, S.-H. Shim, M.A. Montgomery, N.H. Damrauer, M.T. Zanni, *Opt. Express* **15**, 16681 (2007).

[Hac03] M. Hacker, G. Stobrawa, R. Sauerbrey, T. Buckup, M. Motzkus, M. Wildenhain, A. Gehner, *Appl. Phys. B* **76**, 711 (2003).

[Ham11] P. Hamm, M. Zanni, *Concepts and Methods of 2D Infrared Spectroscopy* (Oxford University Press, Cambridge, 2011).

[Ham98] P. Hamm, M. Lim, R.M. Hochstrasser, *J. Phys. Chem. B* **102**, 6123 (1998).

[Har01] S. A. Harich, X. Yang, X. Yang, R. N. Dixon, *Phys. Rev. Lett.* **87**, 253201 (2001).

[Hau06] J. Hauer, H. Skenderovic, K.-L. Kompa, M. Motzkus, *Chem. Phys. Lett.* **421**, 523 (2006).

[Hen01] M. Hentschel, R. Kienberger, Ch. Spielmann, G.A. Reider, N. Milosevic, T. Brabec, P. Corkum, U. Heinzmann, M. Drescher, F. Krausz, *Nature* **414**, 509 (2001).

[Her02] J.L. Herek, W. Wohlleben, R.J. Cogdell, D. Zeidler, M. Motzkus, *Nature* **417**, 533 (2002).

[Her04] C.E. Crespo-Hernández, B. Cohen, P.M. Hare, B. Kohler, *Chem. Rev.* **104**, 1997 (2004).

[Her13] T.T.H. Herzog, G. Ryseck, E. Ploetz, T. Cordes, *Photochem. Photobiol. Sci.* **12**, 1202 (2013).

[Hil11] R. Hildner, D. Brinks, F.D. Stefani, N.F. van Hulst, *Phys. Chem. Chem. Phys.* **13**, 1888 (2011).

[Hoc07] R.M. Hochstrasser, *Proc. Natl. Acad. Sci. USA* **104**, 14190 (2007).

[Hom12] C. Homann, P. Lang, E. Riedle, *J. Opt. Soc. Am. B* **29**, 2765 (2012).

[Hun09] N.T. Hunt, *Chem. Soc. Rev.* **38**, 1837 (2009).

[Hyb01] J.D. Hybl, Y. Christophe, D.M. Jonas, *Chem. Phys.* **266**, 295 (2001).

[Iac98] C. Iaconis, I.A. Walmsley, *Opt. Lett.* **23**, 792 (1998).

[Ire02] M. Irie, T. Fukaminato, T. Sasaki, N. Tamai, T. Kawai, *Nature* **420**, 759 (2002).

[Jan00] A.K. Jana, *J. Photochem. Photobiol. A: Chem.* **132**, 1 (2000).

[Jim94] R. Jimenez, G.R. Fleming, P.V. Kumar, M. Maroncelli, *Nature* **369**, 471 (1994).

[Joc02] S. Jockusch, N.J. Turro, F.R. Blackburn, *J. Phys. Chem. A* **106**, 9236 (2002).

[Jon03] D.M. Jonas, *Annu. Rev. Phys. Chem.* **54**, 425 (2003).

[Kal01] S. Kalinin, M. Speckbacher, H. Langhals, L.B.-Â. Johansson, *Phys. Chem. Chem. Phys.* **3**, 172 (2001).

[Kar95] D.S. Karpovich, G.J. Blanchard, *J. Phys. Chem.* **99**, 3951 (1995).

[Kha01] O.A. Khakhel, *J. Appl. Spec.* **68**, 280 (2001).

[Kha04] M. Khalil, N. Demirdöven, T. Tokmakoff, *J. Chem. Phys.* **121**, 362 (2004).

[Kid11] Y. Kida, J. Liu, T. Kobayashi, *Appl. Phys. B* **105**, 675 (2011).

[Kim03] J.E. Kim, M.J. Taubner, R.A. Mathies, *Biophys. J.* **84**, 2492 (2003).

[Kim09] J. Kim, S. Mukamel, G.D. Scholes, *Acc. Chem. Res.* **42**, 1375 (2009).

[Kle86] M. V. Klein, and T. E. Furtak, *Optics* (John Wiley & Sons, New York, USA, 1986), Chap. 7, p. 477.

[Kli08] M. Kling, F. Krausz, *Nature Phys.* **4**, 515 (2008).

[Koz03] I.Z. Kozma, P. Baum, S. Lochbrunner, E. Riedle, *Opt. Express* **11**, 3110 (2003).

[Koz04] I.Z. Kozma, P. Baum, U. Schmidhammer, S. Lochbrunner, E. Riedle, *Rev. Sci. Instrum.* **75**, 2323 (2004).

[Kre10] N. Krebs, R.A. Probst, E. Riedle, *Opt. Express* **18**, 6164 (2010).

[Kue09] W. Kuehn, K. Reimann, M. Woerner, T. Elsaesser, *J. Chem. Phys.* **130**, 164503 (2009).

[Kue11] W. Kuehn, K. Reimann, M. Woerner, T. Elsaesser, R. Hey, *J. Phys. Chem. B* **115**, 5448 (2011).

[Lai06] S. Laimgruber, H. Schachenmayr, B. Schmidt, W. Zinth, and P. Gilch, *Appl. Phys. B* **85**, 557 (2006).

[Led98] I.K. Lednev, T.-Q. Ye, P. Matousek, M. Towrie, P. Foggi, F.V.R. Neuwahl, S. Umapathy, R.E. Hester, J.N. Moore, *Chem. Phys. Lett.* **290**, 68 (1998).

[Len86] C. Lenoble, R.S. Becker, *J. Photochem.* **33**, 187 (1986).

[Les91] D.E. Lessen, R.L. Asher, P.J. Brucat, *J. Chem. Phys.* **95**, 1414 (1991).

[Lev94] A. M. Levine, E. Özizmir, R. Trebino, C.C. Hayden, A.M. Johnson, K.L. Tokuda, *J. Opt. Soc. Am B* **11**, 1609 (1994).

[Lew12] K.L.M. Lewis, J.P. Ogilvie, *J. Phys. Chem. Lett.* **3**, 503 (2012).

[Lin99] S. Linden, J. Kuhl, H. Giessen, *Opt. Lett.* **24**, 569 (1999).

[Loc00] S. Lochbrunner, A.J. Wurzer, E. Riedle, *J. Chem. Phys.* **112**, 10699 (2000).

[Loc03] S. Lochbrunner, A.J. Wurzer, E. Riedle, *J. Phys. Chem. A* **107**, 10580 (2003).

[Loc04] S. Lochbrunner, K. Stock, E. Riedle, *J. Mol. Struct.* **700**, 13 (2004).

[Lor02] M. Lorenc, M. Ziolek, R. Naskrecki, J. Karolczak, J. Kubicki, and A. Maciejewski, *Appl. Phys. B* **74**, 19 (2002).

[Mad11] M. El-Amine Madjet, O. Vendrell, and R. Santra, *Phys. Rev. Lett.* **107**, 263002 (2011).

[Mai60] T.H. Maiman, *Nature* **187**, 493 (1960).

[Mal05] S. Malkmus, R. Dürr, C. Sobotta, H. Pulvermacher, W. Zinth, M. Braun, *J. Phys. Chem. A* **109**, 10488 (2005).

[Mar87] J.M.G. Martinho, M.A. Winnik, *J. Phys. Chem.* **91**, 3640 (1987).

[Mar92] J.M.G. Martinho, J.P. Farinha, M.N. Berberan-Santos, J. Duhamel, M.A. Winnik, *J. Chem. Phys.* **96**, 8143 (1992).

[Mat03] V.V. Matylitsky, C. Riehn, M.F. Gelin, B. Brutschy, *J. Chem. Phys.* **119**, 10553 (2003).

[Mat94] A. Materny, J.L. Herek, P. Cong, A.H. Zewail, *J. Phys. Chem.* **98**, 3352 (1994).

[McC11] D.J. McCabe, D.R. Austin, A. Tajalli, S. Weber, I.A. Wamsley, B. Chatel, *J. Opt. Soc. Am. B* **28**, 58 (2011).

[Meg09] U. Megerle, I. Pugliesi, C. Schriever, C. F. Sailer, and E. Riedle, *Appl. Phys. B* **96**, 215 (2009).

[Mes99] D. Meschede, *Optik, Licht und Laser* (B. G. Teubner, Stuttgart/Leipzig, Germany, 1999), Chap. 2, p. 54.

[Mid09] C.T. Middleton, K. de La Harpe, C. Su, Y.K. Law, C.E. Crespo-Hernández, B. Kohler, *Annu. Rev. Phys. Chem.* **60**, 217 (2009).

[Mig05] A. Migani, P.L. Gentili, F. Negri, M. Olivucci, A. Romani, G. Favaro, R.S. Becker, *J. Phys. Chem. A* **109**, 8684 (2005).

[Mil09] F. Milota, J. Sperling, A. Nemeth, T. Mančal, H.F. Kauffmann, *Acc. Chem. Res.* **42**, 1364 (2009).

[Mil12] W.H. Miller, *J. Chem. Phys.* **136**, 210901 (2012).

[Mis00] K. Misawa, T. Kobayashi, *J. Chem. Phys.* **113**, 7546 (2000).

[Möh09] J. Möhring, T. Buckup, C.S. Lehmann, M. Motzkus, *J. Opt. Soc. Am. B* **26**, 1538 (2009).

[Möh10] J. Möhring, T. Buckup, M. Motzkus, *Opt. Lett.* **35**, 3916 (2010).

[Möh12] J. Möhring, T. Buckup, M. Motzkus, *IEEE J. Sel. Topics Quantum Electron.* **18**, 449 (2012).

[Moi07] B. Moine, G. Buntinx, O. Poizat, J. Rehault, C. Moustrou, A. Samat, *J. Phys. Org. Chem*. **20**, 936 (2007).

[Moi08] B. Moine, J. Réhault, S. Aloïse, J.-C. Micheau, C. Moustrou, A. Samat, O. Poizat, G. Buntinx, *J. Phys. Chem. A* **112**, 4719 (2008).

[Muk00] S. Mukamel, *Annu. Rev. Phys. Chem.* **51**, 691 (2000).

[Muk90] S. Mukamel, *Annu. Rev. Phys. Chem.* **41**, 647 (1990).

[Muk95] S. Mukamel, *Principles of Nonlinear Optical Spectroscopy* (Oxford University Press, New York, 1995).

[Mye08] J.A. Meyers, K.L.M. Lewis, P.F. Tekavec, J.P. Ogilvie, *Opt. Express* **16**, 17420 (2008).

[Nag09] T. Nagy, P. Simon, *Opt. Lett.* **34**, 2300 (2009).

[Nak98] T. Nakabayashi, H. Okamoto, M. Tasumi, *J. Phys. Chem. A* **102**, 9686 (1998).

[Nen10] A. Nenov, T. Cordes, T. T. Herzog, W. Zinth, and R. de Vivie-Riedle, *J. Phys. Chem. A* **114**, 13016 (2010).

[Neu99] F.V.R. Neuwahl, P. Foggi, *Laser Chem.* **19**, 375 (1999).

[Nib91] E. T. J. Nibbering, D. A. Wiersma, K. Duppen, *Phys. Rev. Lett.* **66**, 2464 (1991).

[Nig89] W.L. Nighan, T. Gong, L. Liou, P.M. Fauchet, *Opt. Comm.* **69**, 339 (1989).

[Noa05] F. Noack, O. Steinkellner, P. Tzankov, H.-H. Ritze, J. Herrmann, Y. Kida, *Opt. Express* **13**, 2467 (2005).

[Nod08] I. Noda, *J. Mol. Struct.* **883**, 2 (2008).

[Nue07] P. Nuernberger, G. Vogt, T. Brixner, G. Gerber, *Phys. Chem. Chem. Phys.* **9**, 2470 (2007).

[Num12] Y. Numata, Y. Suzuki, I. Suzuka, *J. Photochem. Photobiol. A* **237**, 49 (2012).

[Ogi09] J.P. Ogilvie, K.J. Kubarych, *Adv. Atom. Mol. Opt. Phys.* **57**, 249 (2009).

[Ohm09] K. Ohmori, *Annu. Rev. Phys. Chem.* **60**, 487 (2009).

[Oli00] M. Olivucci, M. A. Robb, and F. Bernardi, *Conformational Analysis of Excited States* (Wiley-VCH, New York, 2000).

[Osk08] A.A. Oskouei, O. Bräm, A. Cannizzo, F. van Mourik, A. Tortschanoff, M. Chergui, *Chem. Phys.* **350**, 104 (2008).

[Ott98] G. Ottavi, G. Favaro, V. Malatesta, *J. Photochem. Photobiol. A: Chem.* **115**, 123

(1998).

[Par06] Y.H. Park, B.-S. Cheong, *Cur. Appl. Phys.* **6**, 700 (2006).

[Par09] D.S.N. Parker, A.D.G. Nunn, R.S. Minns, H.H. Fielding, *Appl. Phys. B* **84**, 181 (2009).

[Pea07] B.J. Pearson, T.C. Weinacht, *Opt. Express* **15**, 4385 (2007).

[Pen02] P. Somerharju, *Chem. Phys. Lipids* **116**, 57 (2002).

[Pet89] V. Petrov, W. Rudolph, B. Wilhelmi, *J. Mod. Opt.* **36**, 587 (1989).

[Pol10] D. Polli, P. Altoè, O. Weingart, K. M. Spillane, C. Manzoni, D. Brida, G. Tomasello, G. Orlandi, P. Kukura, R. A. Mathies, M. Garavelli, and G. Cerullo, *Nature* **467**, 440 (2010).

[Pol90] W.T. Pollard, S.-Y. Lee, R.A. Mathies, *J. Chem. Phys.* **92**, 4012 (1990).

[Pro11] V.I. Prokhorenko, A. Halpin, P.J.M. Johnson, R.J.D. Miller, L.S. Brown, *J. Chem. Phys.* **134**, 085105 (2011).

[Rab00] H. Rabitz, R. de Vivie-Riedle, M. Motzkus, K. Kompa, *Science* **288**, 824 (2000).

[Rah97] M.D. Rahn, T.A. King, A.A. Gorman, I. Hamblett, *Appl. Opt.* **35**, 5862 (1997).

[Rei01] R. Reisfeld, *Opt. Mat.* **16**, 1 (2001).

[Rei10] F. Reiter, U. Graf, M. Schultze, W. Schweinberger, H. Schröder, N. Karpowicz, A.M. Azzeer, R. Kienberger, F. Krausz, E. Goulielmakis, *Opt. Lett.* **35**, 2248 (2010).

[Rei10] F. Reiter, U. Graf, M. Schultze, W. Schweinberger, H. Schröder, N. Karpowicz, A.M. Azzeer, R. Kienberger, F. Krausz, E. Goulielmakis, *Opt. Lett.* **35**, 2248 (2010).

[Rei94] C. Reichardt, *Chem. Rev.* **94**, 2319 (1994).

[Ren01] T. Renger, V. May, O. Kühn, *Phys. Rep.* **343**, 137 (2001).

[Reu97] A. Reuther, A. Laubereau, D.N. Nikogosyan, *Opt. Comm.* **141**, 180 (1997).

[Ric07] M. Richter, Th. Renger, G. Renger, A. Knorr, *J. Chem. Phys.* **127**, 075105 (2007).

[Ric08] M. Richter, T. Renger, A. Knorr, *Photosynth. Res.* **95**, 119 (2008).

[Rie00] E. Riedle, M. Beutter, S. Lochbrunner, J. Piel, S. Schenkl, S. Spörlein, W. Zinth, *Appl. Phys. B* **71**, 457 (2000).

[Rol88] C. Rolland, P.B. Corkum, *J. Opt. Soc. Am. B* **5**, 641 (1988).

[Ron09] A. Rondi, J. Extermann, L. Bonacina, S.M. Weber, J.-P. Wolf, *Appl. Phys. B* **96**,

757 (2009).

[Ros89] T.S. Rose, M.J. Rosker, A.H. Zewail, *J. Chem. Phys.* **91**, 7415 (1989).

[Rot05] M. Roth, M. Mehendale, A. Bartelt, H. Rabitz, *Appl. Phys. B* **80**, 441 (2005).

[Rot09] M. Roth, L. Guyon, J. Roslund, V. Boutou, F. Courvoisier, J.-P. Wolf, H. Rabitz, *Phys. Rev. Lett.* **102**, 253001 (2009).

[Rut93] S.C. Rutan, J.M. Harris, *J. Chrom. A* **656**, 197 (1993).

[Sai13] C. F. Sailer, S. Thallmair, B.P. Fingerhut, C. Nolte, J. Ammer, H. Mayr, I. Pugliesi, R. de Vivie-Riedle, E. Riedle, accepted by Chem. Phys. Chem. (2013).

[Sch05] S. Schenkl, F. can Mourik, G. van der Zwan, S. Haacke, M. Chergui, *Science* **309**, 917 (2005).

[Sch06] C. Schriever, S. Lochbrunner, M. Optiz, E. Riedle, *Opt. Lett.* **31**, 543 (2006).

[Sch08] C. Schriever, S. Lochbrunner, E. Riedle, and D. J. Nesbitt, *Rev. Sci. Instrum.* **79**, 013107 (2008).

[Sch08b] C. Schriever, M. Barbatti, K. Stock, A.J.A. Aquino, D. Tunega, S. Lochbrunner, E. Riedle, R. de Vivie-Riedle, H. Lischka, *Chem. Phys.* **347**, 446 (2008).

[Sch11a] J. Schneider, M. Wollenhaupt, A. Winzenburg, T. Bayer, J. Köhler, R. Faust, T. Baumert, *Phys. Chem. Chem. Phys.* **13**, 8773 (2011).

[Sch11b] C. Schriever, S. Lochbrunner, A.R. Ofial, E. Riedle, *Chem. Phys. Lett.* **503**, 61 (2011).

[Sch91] N.F. Scherer, R.J. Carlson, A. Matro, M. Du, A.J. Ruggiero, V. Romero-Rochin, J.A. Cina, G.R. Fleming, S.A. Rice, *J. Chem. Phys.* **95**, 1487 (1991).

[Sch92] N.F. Scherer, A. Matro, L.D. Ziegler, M. Du, R.J. Carlson, J.A. Cina, G.R. Fleming, *J. Chem. Phys.* **96**, 4180 (1992).

[Sch96] R. Schödel, F. Hillmann,T. Schrötter, J. Voigt, K.-D. Irrgang, G. Renger, *Biophys. J.* **71**, 3370 (1996).

[Sel10] U. Selig, C.-F. Schleussner, M. Foerster, F. Langhojer, P. Nuernberger, T. Brixner, *Opt. Lett.* **35**, 4178 (2010).

[Sey92] R. Seyfang, H. Port, P. Fischer, H.C. Wolf, *J. Luminescence* **51**, 197 (1992).

[Sha74] C. V. Shank, E. P. Ippen, *Appl. Phys. Lett.* **24**, 373 (1974).

[Sha03] M. Shapiro, P. Brumer, *Rep. Prog. Phys.* **66**, 859 (2003).

[Shi09] S.-H. Shim, M.T. Zanni, *Phys. Chem. Chem. Phys.* **11**, 748 (2009).

[Shi98] H. Shinohara, Y. Yamakita, K. Ohno, *J. Mol. Struct.* **442**, 221 (1998).

[Sib12] W. Sibbett, A.A. Lagatsky, C.T.A. Brown, *Opt. Express* **20**, 6989 (2012).

[Sil09] Y. Silberberg, *Annu. Rev. Phys. Chem.* **60**, 277 (2009).

[Sto09] K.W. Stone, K. Gundogdu, D.B. Turner, X. Li, S.T. Cundiff, K.A. Nelson, *Science* **324**, 1169 (2009).

[Syt11] O.A. Sytina, V.I. Novoderezhkin, R. van Grondelle, M.L. Groot, *J. Phys. Chem. A* **115**, 11944 (2011).

[Tak08] T. Takaya, C. Su, K. de La Harpe, C.E. Crespo-Hernández, B. Kohler, *Proc. Natl. Acad. Sci. USA* **105**, 10285 (2008).

[Tal00] E.M. Talavera, M. Afkir, R. Salto, A.M. Vargas, J.M. Alvarez-Pez, *J. Photochem. Photobiol. B* **59**, 9 (2000).

[Tan05] T. Tanabe, F. Kannari, F. Korte, J. Koch, B. Chichkov, *Appl. Optics* **44**, 1092 (2005).

[Tan06a] N. Tanaka, N. Barashkov, J. Heath, W.N. Sisk, *Appl. Opt.* **45**, 3846 (2006).

[Tan06b] Y. Tanimura, *J. Phys. Soc. Jpn.* **75**, 082001 (2006).

[Tan85] D.J. Tannor, S.A. Rice, *J. Chem. Phys.* **83**, 5013 (1985).

[Tan86] D.J. Tannor, R. Kosloff, S.A. Rice, *J. Chem. Phys.* **85**, 5805 (1986).

[Tek09] P.F. Tekavec, J.A. Myers, K.L.M. Lewis, J.P. Ogilvie, *Opt. Lett.* **34**, 1390 (2009).

[Tek10] P.F. Tekavec, J.A. Myers, K.L.M. Lewis, F.D. Fuller, J.P. Ogilvie, *Opt. Express* **18**, 11015 (2010).

[Tek12] P.A. Tekavec, K.L.M. Lewis, F.D. Fuller, J.A. Myers, J.P. Ogilvie, *IEEE J. Select. Top. Quant. Electron.* **18**, 210 (2012).

[Ter06] Y. Teranishi, *Phys. Rev. Lett.* **97**, 053001 (2006).

[Tia03] P. Tian, D. Keusters, Y. Suzaki, W.S. Warren, *Science* **300**, 1553 (2003).

[Tre00] R. Trebino, *Frequency-Resolved Optical Gating: The Measurement of Ultrashort Laser Pulses* (Kluwer Academic Publishers, Norwell, USA, 2000).

[Tse09] C.-H. Tseng, T.C. Weinacht, *Opt. Express* **17**, 18788 (2009).

[Tse12] C.-H. Tseng, P. Sándor, M. Kotur, T.C. Weinacht, S. Matsika, *J. Phys. Chem. A* **116**, 2654 (2012).

[Tul90] J. C. Tully, *J. Chem. Phys.* **93**, 1061 (1990).

[Tur10] D.B. Turner, K.A. Nelson, *Nature* **466**, 1089 (2010).

[Tur11] D.B. Turner, K.E. Wilk, P.M.G. Curmi, G.D. Scholes, *J. Phys. Chem. Lett.* **2**, 1904 (2011).

[Vau06] J.C. Vaughan, T. Feurer, K.W. Stone, K.A. Nelson, *Opt. Express* **14**, 1314 (2006).

[Viv03] R. de Vivie-Riedle, V. De Waele, L. Kurtz, E. Riedle, *J. Phys. Chem. A* **107**, 10591 (2003).

[Vol05] V. Volkov, R. Schanz, P. Hamm, *Opt. Lett.* **30**, 2010 (2005).

[Wan10] A. Wand, S. Kallush, O. Shoshanim, O. Bismuth, R. Kosloff, S. Ruhman, *Phys. Chem. Chem. Phys.* **12**, 2149 (2010).

[War83] W.S. Warren, A.H. Zewail, *J. Chem. Phys.* **78**, 2279 (1983).

[War93] W.S. Warren, H. Rabitz, M. Dahleh, *Science* **259**, 1581 (1993).

[Web10] S. Weber, M. Barthélemy, B. Chatel, *Appl. Phys. B* **98**, 323 (2010).

[Wei00] A.M. Weiner, *Rev. Sci. Instrum.* **71**, 1929 (2000).

[Wei90] A.M. Weiner, D.E. Leaird, G.P. Wiederrecht, K.A. Nelson, *Science* **247**, 1317 (1990).

[Wes11] B.A. West, J.M. Womick, A.M. Moran, *J. Phys. Chem. A* **115**, 8630 (2011).

[Wes12] B.A. West, A.M. Moran, *J. Phys. Chem. Lett.* **3**, 2575 (2012).

[Win93] F.M. Winnik, *Chem. Rev.* **93**, 587 (1993).

[Woh05] W. Wohlleben, T. Buckup, J.L. Herek, M. Motzkus, *Chem. Phys. Chem.* **6**, 850 (2005).

[Wol11] M. Wollenhaupt and T. Baumert, *Faraday Discuss.* **153**, 9 (2011).

[Wri11] J.C. Wright, *Annu. Rev. Phys. Chem.* **62**, 209 (2011).

[Wur00] A.J. Wurzer, S. Lochbrunner, E. Riedle, *Appl. Phys. B* **71**, 405 (2000).

[Yam91] T. Yamanaka, Y. Takahasi, T. Kitamura, K. Uchida, *J. Lumin.* **48 & 49**, 265 (1991).

[Yar01] D. R. Yarkony, *J. Phys. Chem. A* **105**, 6277 (2001).

[Zer84] F. Zerbetto, S. Monti, G. Orlandi, *J. Chem. Soc. Farad. Trans. 2* **80**, 1513 (1984).

[Zew99] "Ahmed Zewail - Nobel Lecture: Femtochemistry: Atomic-Scale Dynamics of the Chemical Bond Using Ultrafast Lasers". Nobelprize.org. 10 Aug 2012 http://www.nobelprize.org/nobel_prizes/chemistry/laureates/1999/zewail-lecture.html

[Zha09] B. Zhao, Y. Jiang, K. Sueda, N. Miyanaga, T. Kobayashi, *Opt. Express* **17**, 17711 (2009).

[Zha10] J. Zhang, F. Han, W. Kong, *J. Phys, Chem. A* **114**, 11117 (2010).

[Zha12] Z. Zhang, K.L. Wells, E.W.J. Hyland, H.-S. Tan, *Chem. Phys. Lett.* **550**, 156 (2012).

[Zhe12] Z. Zhang, K.L. Wells, H.-S. Tan, *Opt. Lett.* **37**, 5058 (2012).

[Zig06] D. Zigmantas, E.L. Read, T. Mančal, T. Brixner, A.T. Gardiner, R.J. Cogdell, G.R. Fleming, *Proc. Natl. Acad. Sci. USA* **103**, 12672 (2006).

[Zim97] D. Zimdars, R.S. Francis, C. Ferrante, M.D. Fayer, *J. Chem. Phys.* **106**, 7498 (1997).

8. Appendix A: Mathematical derivations and supplemental informations

Appendix A.I: Two ways to calculate ΔOD

In pump-probe spectroscopy one is interested in the change in optical density after pumping (ΔOD_{pp}). This signal can be calculated by measuring the probe intensity (e.g., spectrally resolved by a spectrometer) with pumping (I*, Sig*) and without pumping (I_0, Sig_0) and subsequently calculating

$$\Delta OD_{pp}(\nu_{probe}) = -\log\left(\frac{Sig^*(\nu_{probe})}{Sig_0(\nu_{probe})}\right) = -\log\left(\frac{I^*}{I_0}\right). \qquad (I.1)$$

Using the Taylor series for the natural logarithm given by Eq. I.2., Eq. I.1 can be expanded in a Taylor series centered at 1 ($I^*/I_0 \approx 1$) leading to Eq. I.2.

$$\ln(1+x) = \sum_{n=1}^{\infty} (-1)^{n+1} \frac{x^n}{n} \qquad \text{for } -1 < x \leq 1 \qquad . \qquad (I.2)$$

This equation can be expanded into a Taylor series as given in Eq. I.2.

$$\Delta OD_{pp} = \left[-\left(\frac{I^*}{I_0} - 1\right) + \frac{1}{2}\left(\frac{I^*}{I_0} - 1\right)^2 + \ldots \right] / \ln 10 . \qquad (I.2)$$

Neglecting the higher order terms due to $I^*/I_0 \approx 1$, Eq. I.2 can be written as [Sch08]

$$\Delta OD_{pp} \approx -\frac{I^* - I_0}{I_0} \frac{1}{\ln 10} . \qquad (I.3)$$

Note that the negative sign in Eq. I.3 becomes important when the sign of the pump-probe measurement is compared with the sign of the signals retrieved in 2D spectroscopy. Eq. I.3 is a reasonable approximation for pump induced signal changes in the order of 10^{-3} [Sch08] and is often used in the theoretical framework for the description of pump-probe spectroscopy [Yan89].

This leads to the conclusion, that

$$-\log\left(\frac{I^*}{I_0}\right) = \Delta OD_{pp} \approx -\frac{I^* - I_0}{I_0}\frac{1}{\ln 10}. \qquad (I.4)$$

Eq. I.4 shows that ΔOD can be calculated in two ways. The left part of Eq. I.4 is used in transient absorption spectroscopy while the right part is used in 2D spectroscopy (when one is interested in 2D amplitudes which are proportional to ΔOD). Note, that in 2D spectroscopy the amplitude is retrieved by calculations that resemble a form like $+(I^*-I_0)/I_0$. This means that the sign of the 2D spectra retrieved is opposite to the sign of ΔOD_{pp}.

Appendix A.II: Mathematical description of the third-order polarization $P^{(3)}$ dependence of transient pump-probe and 2D spectroscopy

To relate the measured intensities in a 2D experiment with the intensities measured in conventional pump-probe spectroscopy it is in principle required to write down the detailed mathematical formalism developed for nonlinear spectroscopy. Note that it is not the aim of this section is to repeat the complete theoretical framework of nonlinear spectroscopy but only to give a short overview of the relevant proportionalities.

In the beginning, the dependence of pump-probe spectroscopy on the induced third-order polarization is developed. The third-order polarization induced in the system $P^{(3)}$ is generated by three interactions with the incident electric fields. Two interactions happen with the electric field of the pump pulse and one interaction happens with the probe electric field. For the following discussion it is assumed that the pulses are temporal δ-shaped pulses, meaning that any interaction within one pulse is happening at the same time, e.g., the two interactions with the pump pulse. This is called the *impulsive limit*. The $P^{(3)}$ itself becomes the source of the emitted electric field which can be written under perfect phase matching conditions and in the rotating-wave approximation as:

$$E_S^{(3)}(T,t) \propto \frac{i\omega_t}{n(\omega_t)} P^{(3)}(T,t). \qquad (II.1)$$

Where T is the delay between the pump and probe pulses. Note, that there is no coherence time τ dependence, as the first two interactions happen within the temporal presence of the single pump electric field. ω_t is the angular frequency of the emitted signal field and t is the time after

the third interaction within the duration of the probe pulse. This expression for the signal field is similar to the one for 2D spectroscopy, as these are both processes related to $P^{(3)}$.

For clearness of the equations derived later on, a fixed pump-probe delay T time is selected and the emitted field is simply denoted as $E^{(3)}(t)$ here. Depending on the phase of the emitted field, it interferes constructively (stimulated emission of ground state bleach) or destructively (excited state absorption) with the probe electric field. Starting from Eq. 4.3, the frequency resolved signal field intensity Sig(ω) detected at the time integrating probe detector can be written as [Shi09]

$$\mathrm{Sig}(\omega_{pr}) = \left| \int dt \left(E_{pr}(t) + E^{(3)}(t) \right) e^{-i\omega_{pr} t} \right|^2 , \tag{II.2}$$

while E_{pr} is the probe pulse after transmission through the sample and ω_{pr} is the probe angular frequency. Note, that the incident electric field of the probe is given by $E_0(t)$. The probe field is absorbed in the system according to the linear polarization $P^{(1)}(t)$ leading to the emitted field $E^{(1)}(t)$. The signal contributions are assumed to be small, so that there are no propagation effect of $P^{(1)}$ affecting $P^{(3)}$ or vice versa. Then the probe field can be written as

$$E_{pr}(t) = E_0(t) + E^{(1)}(t) . \tag{II.3}$$

Eq. II.2 leads to the spectrally resolved signal at the probe detector ($\omega = \omega_{pr}$) as given in Eq. II.4.

$$\mathrm{Sig}(\omega) = \left| E_{pr}(\omega) + E^{(3)}(\omega) \right|^2 . \tag{II.4}$$

In pump-probe spectroscopy one is interested in the change in optical density after pumping (ΔOD_{pp}). This signal can be calculated by measuring the probe intensity (e.g., spectrally resolved by a spectrometer) with (Sig*=I*) and without pumping ($Sig_0=I_0$) and subsequently calculating

$$-\log\left(\frac{\mathrm{Sig}^*(\omega)}{\mathrm{Sig}_0(\omega)} \right) \approx \frac{\mathrm{Sig}^*(\omega) - \mathrm{Sig}_0(\omega)}{\mathrm{Sig}_0(\omega)} . \tag{II.5}$$

For details of the transformation in Eq. II.5, see appendix A.I. Inserting Eq. II.4 into the later part of Eq. II.5 and using $\mathrm{Sig}_0(\omega) = \left| E_{pr}(\omega) \right|^2$ this leads to

$$\frac{\left|E_{pr}(\omega)+E^{(3)}(\omega)\right|^2-\left|E_{pr}(\omega)\right|^2}{\left|E_{pr}(\omega)\right|^2}=\frac{2E_{pr}(\omega)E^{(3)}(\omega)+\left|E^{(3)}(\omega)\right|^2}{\left|E_{pr}(\omega)\right|^2}\approx\frac{2E_{pr}(\omega)E^{(3)}(\omega)}{\left|E_{pr}(\omega)\right|^2}. \quad \text{(II.6)}$$

In the later step, $\left|E^{(3)}(\omega)\right|^2$ was neglected, because $E^{(3)}$ is very small. By using the Fourier transformation of Eq. II.1 the pump-probe signal, for $\sqrt{\left|E_{pr}(\omega)\right|^2}=E_{pr}(\omega)$, can be written as

$$\Delta OD_{pp}(\omega)\propto\frac{\omega P^{(3)}(\omega)}{E_{pr}(\omega)}. \quad \text{(II.7)}$$

The constant of i was neglected when comparing to Eq. II.1 as it only accounts for the fact that the absorptive part of $P^{(3)}$ is imaginary and has to be multiplied with i to represent the real valued signal field. It is not needed when the proportionalities are investigated. The factor of $n(\omega_{probe})$ (Eq. II.1) was neglected, as it has only a minor contribution [Bri04b].

Now, the dependence of 2D spectroscopy on the induced third-order polarization is developed. When one is interested in measuring 2D spectra which have amplitude values that are directly proportional to $P^{(3)}$, Eq. 4.1.7 has to be applied, which was a priory given without yet proving its validity. This prove is now given by using this equation and then looking at the resulting proportionality. Then the 2D signal is calculated by phase cycling of the additional interpulse phase $\Delta\Phi$ of the two pump pulses according to Eq. II.8.

$$S_{2D}^{P^{(3)}}(\tau,\omega)=\frac{Sig(\Delta\Phi=0)-Sig(\Delta\Phi=\pi)}{\omega E_{pr}(\omega)}, \quad \text{(II.8)}$$

where Sig(…) are the signals detected at the probe spectrometer for a given coherence time τ (and population time T). With $Sig(\Delta\Phi=0)=Sig^0$ and $Sig(\Delta\Phi=\pi)=Sig^\pi$.

Sig(…) can be written similar to Eq. II.4 but now the signal electric field $E^{(3)}(\omega)$ has contributions from the 2D signal $E_{2D}{}^{(3)}(\omega)$ and from the transient pump-probe background $E_{pp}{}^{(3)}(\omega)$. Inserting Eq. II.4 into Eq. II.8 lead to Eq. II.9.

$$\frac{\left|E_{pr}(\omega)+E_{pp}{}^{(3)}(\omega)+E_{2D}{}^{(3)}(\omega)\right|^2-\left|E_{pr}(\omega)+E_{pp}{}^{(3)}(\omega)-E_{2D}{}^{(3)}(\omega)\right|^2}{\omega E_{pr}(\omega)}. \quad \text{(II.9)}$$

Note, that the sign of the 2D signal field in the right part of Eq. II.9 is negative due to the shift of the interpulse phase by π. The term $\left(E_{2D}{}^{(3)}(\omega)\right)^2$ is rather small and is further on neglected when explicitly calculate the squares in Eq. II.9. This calculation leads to Eq. II.10.

$$\frac{4E_{pr}(\omega)E_{2D}^{(3)}(\omega)+4E_{pp}^{(3)}(\omega)E_{2D}^{(3)}(\omega)}{\omega E_{pr}(\omega)}. \qquad \text{(II.10)}$$

The term $4E_{pp}^{(3)}(\omega)E_{2D}^{(3)}(\omega)$ is rather small and can be neglected. By using Eq. II.1 for the emitted electric 2D field, the 2D signal of Eq. II.8 is directly proportional to $P^{(3)}$ as given in Eq. II.11.

$$S_{2D}^{P^{(3)}}(\tau,T,\omega)=\frac{4\omega P^{(3)}E_{pr}(\omega)}{\omega E_{pr}(\omega)} \propto P^{(3)}. \qquad \text{(II.11)}$$

When one is interested in measuring 2D spectra which have amplitude values that are directly proportional to the change in optical density ΔOD_{pp} of transient pump-probe spectroscopy, Eq. 4.1.9 has to be applied. Then the 2D signal is calculated by phase cycling of the interpulse phase of the two pump pulses according to Eq. II.12.

$$S_{2D}^{\Delta OD}(\tau,T,\omega)=\frac{Sig(\Delta\Phi=0)-Sig(\Delta\Phi=\pi)}{\left|E_{pr}(\omega)\right|^2}. \qquad \text{(II.12)}$$

With similar calculations as it was done before, the 2D signal now reads as given in Eq. II.13.

$$S_{2D}^{\Delta OD}(\tau,T,\omega)=\frac{4\omega P^{(3)}E_{pr}(\omega)}{\left|E_{pr}(\omega)\right|^2}\cdot\frac{4\omega P^{(3)}}{E_{pr}(\omega)} \propto \Delta OD_{pp}(\omega). \qquad \text{(II.13)}$$

Appendix A.III: Double pulses generated by the pulse shaper

It was mentioned in Chap. 4.2.2, that the pulse shaper can not directly delay the electric field of the double pump pulses used in 2D spectroscopy but can only control the pulse envelope delay and the interpulse phase. A method was described that can indeed change the interpulse delay of the respective electric fields of the pulses by incrementally change the interpulse phase parallel to the envelope delay. However, it was already mentioned that a systematic error in the delay time axis can occur, if the central angular frequency defined in the shaper software (ω_{AOPDF}) does not match the central angular frequency (e.g., the barycenter frequency) of the optical pulse itself (ω_{pulse}). It is the aim of this section to describe this phenomenon quantitatively and name a procedure to correct the measured data even after the measurement.

The desired electric field of the two pump pulses for a interpulse electric field delay of τ was given in Eq. 4.1.3:

$$E_{pump}(t,\tau) = E_1(t) + E_2(t) = \sqrt{I(t)} \cdot e^{-i\omega_{pulse}t} + \sqrt{I(t+\tau)} \cdot e^{-i\omega_{pulse}(t+\tau)}, \qquad \text{(III.1)}$$

with ω_{pulse} being the central angular frequency of the optical pulse itself. It can be determined by calculating the spectral intensity weighted barycenter of the spectral intensity distribution. I(t) are the intensity envelope functions of the pulses, e.g., I(t) = $e^{-t^2/2\sigma^2}$ for Gaussian pulses with a FWHM pulse duration of $2\sqrt{2\ln 2}\sigma$. Note, that there is no interpulse phase ΔΦ implemented in Eq. III.1, as it is not necessary for the analysis in this section and is only necessary for the phase cycling scheme.

The electric field that the pulse shaper generates reads as:

$$E_{pump}(t,\tau) = E_1(t) + E_2(t) = \left(\sqrt{I(t)} + \sqrt{I(t+\tau)} e^{-i\Delta\Phi_{AOPDF}} \right) \cdot e^{-i\omega_{AOPDF}t}. \qquad \text{(III.2)}$$

$\Delta\Phi_{AOPDF}$ is the interpulse phase and ω_{AOPDF} is the central frequency set in the shaper software. This equation only holds, if the $\omega_{pulse} = \omega_{AOPDF}$. For that condition, a double pulse delay for the electric fields of the two pulses according to Eq. III.1 can be generated by the AOPDF when the interpulse phase is flipped incrementally as it is given in Eq. III.3:

$$\Delta\Phi_{AOPDF} = \omega_{AOPDF} \cdot \tau. \qquad \text{(II.3)}$$

However, if the central frequencies differ, meaning $\omega_{pulse} \neq \omega_{AOPDF}$, Eq. 4.2.1 has to be written as

$$E_{pump}(t,\tau) = \left(\sqrt{I(t)} + \sqrt{I(t+\tau)} e^{-i\Delta\Phi_{AOPDF}} \right) \cdot e^{-i\omega_{pulse}t}, \qquad \text{(III.4)}$$

with $\Delta\Phi_{AOPDF}=\omega_{AOPDF}\cdot\tau$. The last term in Eq. III.4 accounts for the fact that the electric field of the pulses is given by the pulse central frequency and not by the central frequency set in the shaper software. Eq. III.4 means, that the delay of the electric field does not match the delay of the electric field envelope.

Note, that the pulse envelope function I(t+τ) is written in a way that does not account for any incorrectness of the delay of the envelope function. This is a reasonable simplification, as the error in the generated delay is in the order of less than 1 %. For a maximum τ delay of about 100 fs, an error of about 1 fs is not significant when compared to the pulse length of about 20 fs, while for a pulse with a central wavelength of about 300 nm, this corresponds to nearly on optical cycle of the electric field. Therefore, the phase of the electric field is important here.

When comparing the desired electric field (Eq. III.1) with the field generated by the shaper (Eq. III.4) the true delay τ_{true} can be calculated from Eq. III.5.

$$\begin{aligned}&\sqrt{I(t)}\cdot e^{-i\omega_{pulse}t}+\sqrt{I(t+\tau)}\cdot e^{-i\omega_{pulse}(t+\tau_{true})}\\&\equiv\left(\sqrt{I(t)}+\sqrt{I(t+\tau)}e^{-i\omega_{AOPDF}\tau_{AOPDF}}\right)\cdot e^{-i\omega_{pulse}t}.\end{aligned}\tag{III.5}$$

Note, that for the envelope functions only a general τ delay was used, because the error in the delay of the envelope functions is neglected. Eq. III.5 leads to a true delay according to Eq. III.6.

$$\tau_{true}=\frac{\omega_{AOPDF}}{\omega_{pulse}}\cdot\tau_{AOPDF}.\tag{III.6}$$

Eq. III.6 shows, that an incorrect central frequency defined in the shaper software does lead to a stretched or compressed coherence delay τ-axis. In 2D spectroscopy, this τ-axis is Fourier transformed and the pump-frequency axis is retrieved. When the error in the τ-axis is given by Eq. III.6, this leads then to an error in the retrieved frequency axis which can be corrected even after the measurement and data evaluation process: The frequency steps of the retrieved pump axis have to be simply multiplied with

$$\frac{\omega_{pulse}}{\omega_{AOPDF}}.\tag{II.7}$$

Appendix A.IV: Excitation probability in transient absorption measurements for finite pump and probe beam spot sizes

To calculate the excitation probability P_{exc} in a transient absorption measurement, the pump photon density n_{pu} is needed. The excitation probability, when neglecting the influence of the probe beam, is then given by Eq. IV.1 (Meg09).

$$P_{exc}=n_{pu}\varepsilon\frac{\ln 10}{N_A}.\tag{IV.1}$$

Where ε is the molar extinction coefficient at the pump frequency and N_A is the Avogadro constant. In a real experiment, the photon density of the bum beam is not a constant along the special beam profile. For a Gaussian shaped beam (e.g., at the focus in the sample) the spatial

dependence of the photon density can be written as given in Eq. IV.2.

$$n_{pu}(r) = \text{const.} \cdot \exp\left(-\frac{4 \ln 2 \cdot r^2}{D_{pu}{}^2} \right). \tag{IV.2}$$

D_{pu} is the FWHM of the Gaussian shaped spatial intensity distribution of the pump beam and r is the distance to the center (to the propagation axis). The spatial integral of Eq. IV.2 over the complete beam area A has to be equal to the complete amount of pump photons $N_{pu}{}^{total}$ which allows to determine the missing constant:

$$\int_A n_{pu}(r) dA = N_{pu}^{total}. \tag{IV.3}$$

This leads to the photon density of the pump pulse as given in Eq. IV.4.

$$n_{pu}(r) = \frac{\ln 2 \cdot N_{pu}^{total}}{\pi \left(D_{pu}/2 \right)^2} \cdot \exp\left(-\frac{4 \ln 2 \cdot r^2}{D_{pu}{}^2} \right). \tag{IV.4}$$

When the probe beam is significantly smaller than the pump beam ($D_{pr} << D_{pu}$) the relevant photon density that is probed is given at the peak of the Gaussian shaped spatial profile, meaning r = 0. Then n_{pu} is given by Eq. IV.5 which was already used in Chap. 4.3, Eq. 4.3.8.

$$n_{pu} = n_{pu}(0) = \frac{4 \ln 2}{\pi} \frac{N_{pu}^{total}}{D_{pu}{}^2}. \tag{IV.5}$$

However, when the probe beam has a size in the sample that is comparable to the pump beam, the spatial beam profile of the probe beam has to be taken into account. At first, the probe beam itself does not see a homogeneous distribution of excited molecules due to the spatial beam profile of the pump. Additionally, the spatial intensity distribution of the probe leads to different contributions of the measured pump induced transmission change at different probe beam areas: The absolute photon numbers of the probe beam are the highest in the middle of the beam and this part will contribute the most to the overall transmission change. Therefore both, pump and probe, spatial intensity distributions affect the measurement.

Assuming a Gaussian shaped probe beam the spatial photon density of the probe can be written similar to Eq. IV.4 as given in Eq. IV.6.

$$n_{pr}(r) = \frac{\ln 2 \cdot N_{pr}^{total}}{\pi \left(D_{pr}/2 \right)^2} \cdot \exp\left(-\frac{4 \ln 2 \cdot r^2}{D_{pr}{}^2} \right). \tag{IV.6}$$

For the probe beam one is interested in measuring the pump induced intensity change of the probe rather than the change in absolute photon numbers. It is therefore convenient to set the total probe photon number $N_{pr}^{total} = 1$, which is equal to the statement, that an integration of Eq. IV.6 gives a value of 1. Note, that this means, that Eq. IV.6 can be seen as a statistical weight function that takes the spatial beam profile of the probe into account. To calculate the probe weighted spatial pump photon density (n_{pu}^{pr}) the pump photon density has to be multiplied with the probe photon density and integrated over the beam area A as given in Eq. IV.7. Both beams have the same center which means that r is the same for both beams.

$$n_{pu}^{pr} = \int_A n_{pr}(r) \cdot n_{pu}(r) dA = \int_0^{2\pi} d\varphi \int_0^{\infty} dr \cdot r \cdot n_{pr}(r) \cdot n_{pu}(r) = \frac{4 \ln 2}{\pi} \frac{N_{pu}^{total}}{D_{pu}^2 + D_{pr}^2} \quad . \qquad \text{(IV.7)}$$

For a fixed pump beam size and a relatively small probe beam with $D_{pr} << D_{pu}$ Eq. IV.7 simplifies to Eq. IV.5. When the probe beam is large compared to the pump beam ($D_{pr} >> D_{pu}$) the effective pump photon density inducing the transmission change goes to zero, as one would expect in an experiment.

The correction that is implied by Eq. IV.7 compared to Eq. IV.5 for the calculation of the photon excitation probability measured in a transient absorption experiment depends on the ratio between the spot sizes of the probe and pump beam. For a typical 2D experiment, D_{pu} = 90 µm and D_{pr} = 40 µm. Then the correction by introducing Eq. IV.7 is in the order of 20 % which can not be neglected when the product quantum yields are determined.

Appendix A.V: Additional error analysis of the product quantum yield calculations in 2D spectroscopy

It has been pointed out in Chap. 4.3, that the calculation of the excitation-frequency resolved product yield from a 2D measurement has two main contributions to the uncertainty of the retrieved quantum yield values. The first one is originating from the uncertainty of the parameters used in the calculation, e.g., the uncertainty of the pulse power measurement.

The other one, which is discussed in this chapter, originates from an incorrect frequency

calibration of the individually measured spectra, e.g., the pump spectrum and the absorption spectrum which are typically measured with different types of spectrometers. As for the product yield calculations one is multiplying or dividing these pump-frequency resolved spectra, an incorrect frequency calibration means an unphysical shift of the individual spectra with respect to each other which leads to an error in the retrieved product yield values.

To demonstrate the influence of an incorrect frequency calibration of the individual spectra used in the calculation, a 2D-UV measurement on pyrene is used. The 2D measurement of pyrene dissolved in methanol for a population time of 10 ps is shown in Fig. V.1. A supercontinnum white light was used for probing. The pump pulse spectrum was tuned to 311 nm which overlaps with the absorption into the S_2 state.

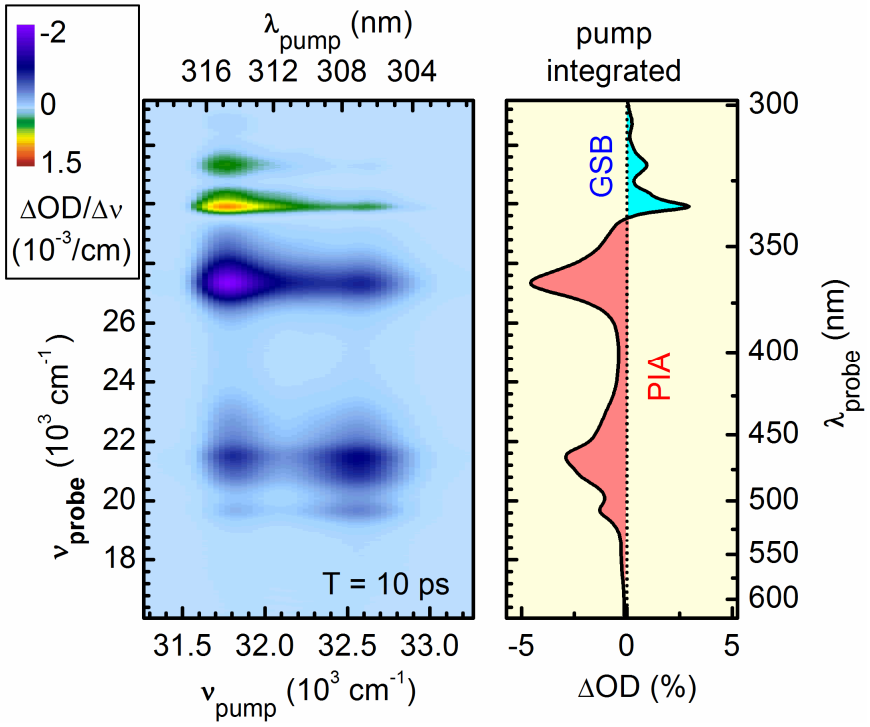

Fig. V.1. 2D measurement of pyrene dissolved in methanol for a population delay of 10 ps when using a visible white light supercontinuum for probing. The integration of the 2D measurement along the pump axis retrieves the transient absorption spectrum (right part) which shows the ground state bleach (GSB) of the S_2 state and the photo-induced absorption (PIA, having an opposite sign). The 2D spectra were calculated in a way to retrieve amplitude values which are proportional to the change in optical density ($\sim$-ΔOD_{pp}) as it is measured in conventional transient absorption spectroscopy.

After excitation of the S_2 state, pyrene undergoes a fast (85 fs) internal conversion into the S_1 state. This internal conversion is expected to have an efficiency of 100 % (details see Chap. 5.1). The photo-induced absorption (PIA) at a population delay of 100 ps shows a strong peak at $\nu_{probe} = 27500\ cm^{-1}$ (363 nm) (Fig. V.1).

The excitation frequency dependent 2D product yield then reads as given in Eq. V.1 (equals Eq. 4.3.17 of Chap. 4.3).

$$Q_{prod}(\nu_{pump}) = \frac{\Delta OD(\nu_{pump}, \nu_{probe}) / (d \cdot \varepsilon_{prod}(\nu_{probe}))}{c_{educt} \cdot P_{exc}(\nu_{pump})}. \qquad \textbf{(V.1)}$$

The PIA signal at $\nu_{probe} = 27500\ cm^{-1}$ (363 nm) (Fig. V.1) is used to retrieve the amount of molecules in the S_1 state, which is called product state in the following, by calculating the numerator of Eq. V.1. The amount of initially excited molecules can be separately calculated with the aid of the denominator of Eq. V.1.

In the following all terms of Q_{prod} (Eq. V.1) are derived step-by-step and the product quantum yield is then calculated. The product state chosen here is the state of pyrene that shows the PIA signal. This state is most probably the S_1 state after excitation into the S_2 state, when there are no ground state dimers present.

Determination of ε_{prod}. At first, the molar absorption coefficient ε_{prod} of the molecules that induce the PIA signal at $\nu_{probe} = 27500\ cm^{-1}$ (363 nm) has to be determined. ε_{prod} has to be determined with the aid of transient absorption spectroscopy. It can be retrieved by decomposing the steady-state absorption spectrum from the transient absorption spectrum measured separately by transient absorption spectroscopy. The procedure is described in the following.

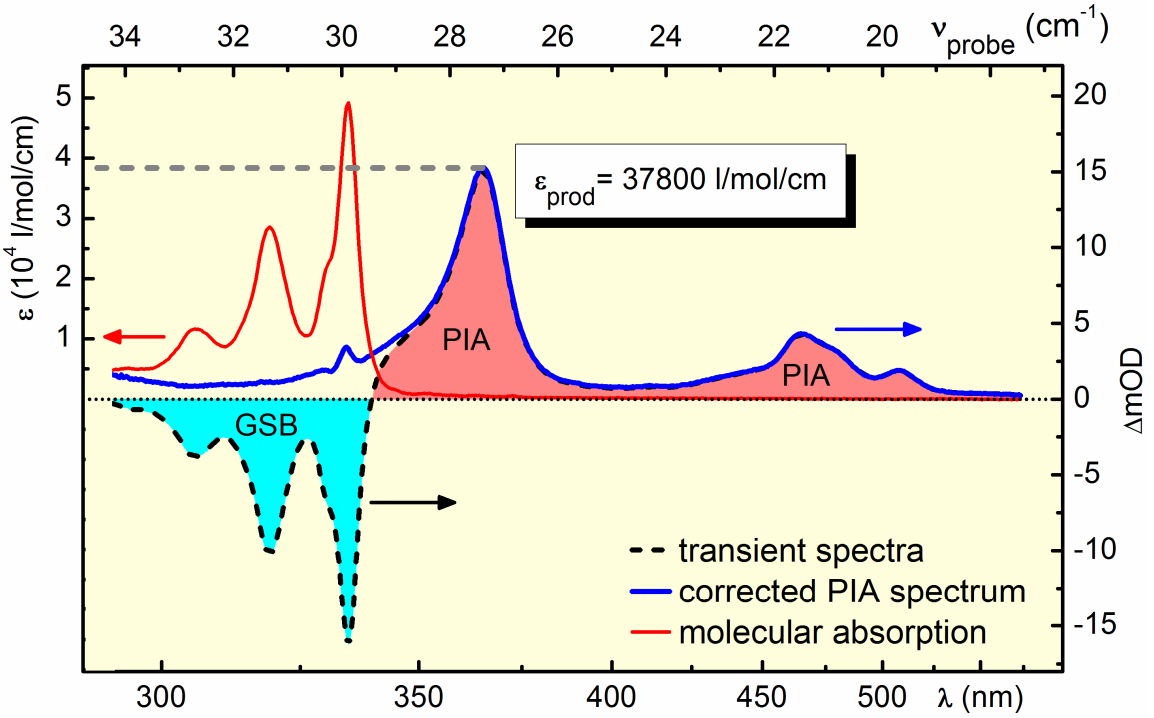

Fig. V.2. Transient absorption measurement of pyrene for a pump-probe delay of 120 ps to retrieve the extinction coefficient ε_{prod} of the product state. The scaled absorption spectrum (red line) was subtracted from the measured transient spectrum (black dashed line) to retrieve the pure PIA spectrum (blue line). As the molar extinction coefficient (red line) is known, the extinction coefficient of the PIA band at 363 nm can be determined quantitatively (378000 l/mol/cm at ν_{probe} = 27500 cm^{-1}).

In Fig. V.2 the transient absorption spectrum of pyrene for a pump-probe delay (or population delay T) of 120 ps is shown. The transient spectrum shows a pronounced ground state bleach contribution between 300 and 350 nm and a strong PIA for longer wavelength. To determine the extinction coefficient of the PIA band at 363 nm, the steady-state absorption spectrum was subtracted from the transient spectrum. The absorption spectrum was scaled in such a way, that the clearly visible vibrational substructure of the ground state bleach contribution are flattened out. Note, that the transient spectrum is in units of ΔOD which is directly proportional to the molar extinction coefficient. Because the molar extinction coefficient of the steady-state absorption spectrum is known, ε_{prod} can thus be retrieved by comparing the peak height of the PIA band with the peak height of the absorption. However, this procedure strongly relies on how good one can estimate the amount of GSB contribution. Therefore, a fairly high error estimate of about 5 % seems adequate. The retrieved value for ε_{prod} is 37800 ± 2000 l/mol/cm.

It is worth noting that this procedure does assume that there are no ground state dimers present and there is no excimer formation within 100 ps (details see Chap. 5.1). If there is an excimer formation happening, the ground state bleach signal would not have a 1:1 relation to the PIA peak height and the retrieved ε_{prod} would not be correct. However, for a pure error analysis, this is not relevant directly.

Determination of the excitation probability P_{exc}. In the experiment, the pump pulse energy in the sample was 176 ± 5 nJ. The effective optical density for the pump pulses which was calculated by convolution of the spectral intensity of the pump pulse with the spectrally resolved optical density of the sample was about 0.20. This leads to an average pump pulse energy of 137 ± 5 nJ. The central frequency of the pump pulses (barycenter) was 312.2 nm leading to a total photon number per pulse ($N_{h\nu}^{total}$) of (2.19 ± 0.08) $\cdot 10^{11}$ photons. The maximum value of the excitation-frequency dependent P_{exc} is in order of about 9 %, which is still in the linear excitation regime.

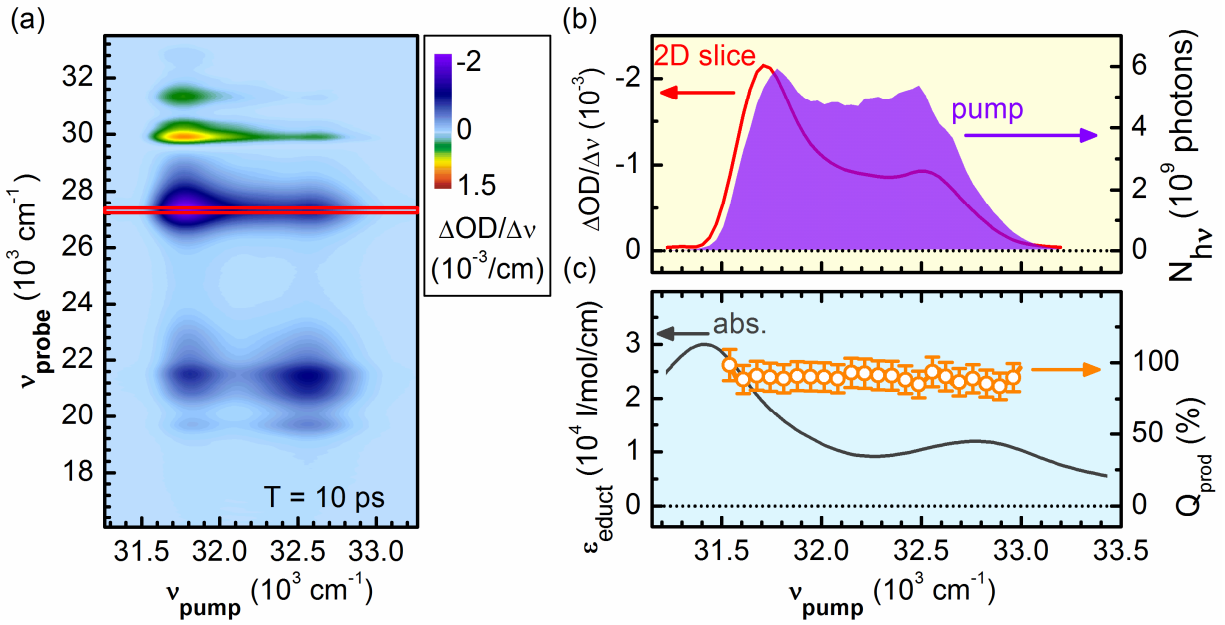

Fig. V.3. Calculation of the product quantum yield from a 2D measurement. (a) 2D measurement of pyrene for a population delay of 10 ps. (b) Overlay of the 2D slice along the pump axis for ν_{probe} = 27300 cm^{-1} (red line) and the spectral photon number distribution of the pump pulses (violet). (c) Absorption spectra of pyrene (black line) and the calculated efficiency Q_{prod} of the S_1 state formation after excitation into the S_2 state. Note, that the product quantum yield is 100 % as expected when there is no excimer formation within 100 ps.

Determination of the product yield (Q_{prod}). The concentration of the pyrene molecules dissolved in methanol (c_{educt}) was $(1.5 \pm 0.1) \cdot 10^{-3}$ mol/l. The beam size of the pump and probe pulses is 85 ± 2 µm and 50 ± 1 µm, respectively. Now that all necessary parameters of the experiment are determined the product quantum yield according to Eq. V.1 can be calculated from the 2D measurement. The result is shown in Fig. 4.3.6.

The uncertainty of the calculated quantum yield originating from the uncertainties of the individually measured parameters can directly be calculated by using the uncertainties of the individual parameters to be about 11 %. The calculated product quantum yield of the formation of the S_1 state after excitation into the S_2 state is constant for the whole spectral region of the pump pulses used (Fig. V.3c). This shows that there is no pump frequency dependence of the internal conversion from the S_2 to S_1 state for delays longer than 10 ps. The retrieved quantum yield is about 93 % when averaging over the complete spectral region. Note that for pyrene the reaction quantum yield of the formation of the S_1 state after excitation of the S_2 state is expected to be unity, and the result is within the uncertainty of the calculations. A further analysis of the error of the quantum yield calculation in a 2D experiment will be described in the following.

Frequency shift error analysis. In addition to the uncertainties originating from the uncertainty of the parameters used in the calculations there is yet another aspect that has to be kept in mind. Further uncertainty originates from an incorrect frequency calibration of the individually measured spectra, e.g., the pump spectrum and the absorption spectrum which are typically measured with different types of spectrometers. As for the quantum yield calculations one is multiplying or dividing these pump-frequency resolved spectra, an incorrect frequency calibration means an unphysical shift of the individual spectra with respect to each other. To demonstrate how such a shift influences the retrieved quantum yield values, the product quantum yield was calculated for different frequency shifts of the individual spectral distributions for the data shown in Fig. V.3. The result is shown in Fig. V.4.

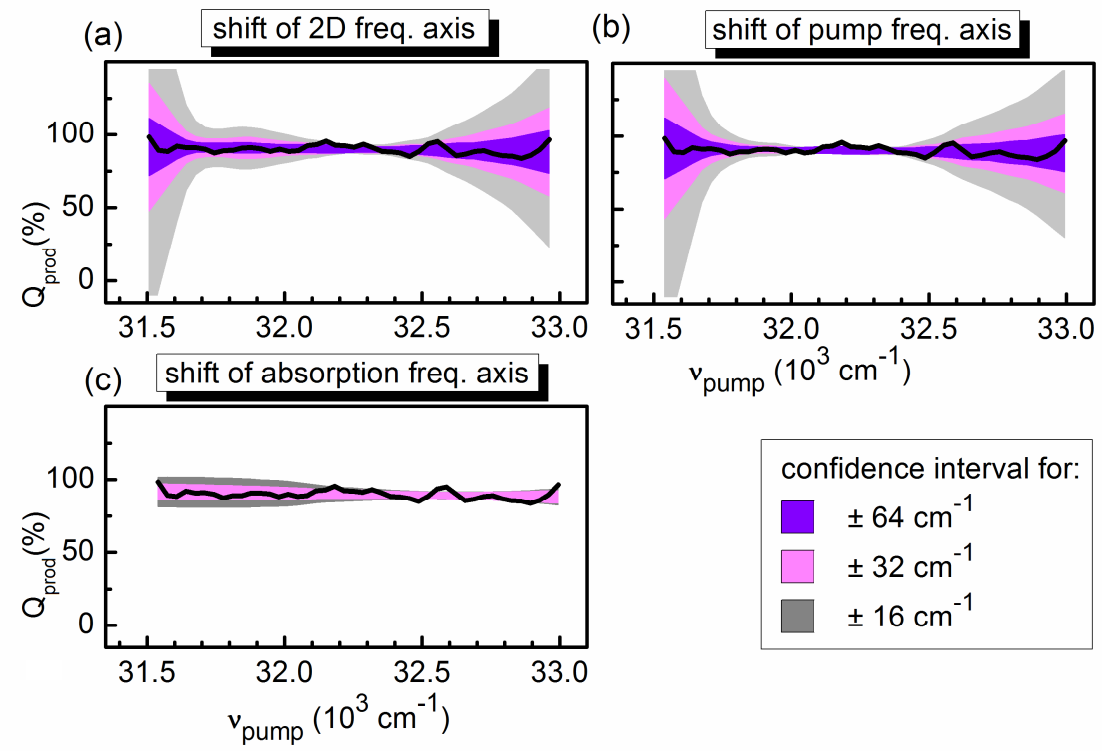

Fig. V.4. Illustration of the error of the retrieved quantum yield for incorrect frequency calibration of the individual spectra (2D, pump pulse and absorption spectra) used in the calculations for the data shown in Fig. V.4. The calculated product yield with correct frequency calibration is shown as a black line. The confidence interval was estimated by shifting the individual frequency axis and calculating the respective maximum product yield deviations. Influence of the pulse shaper calibration (a), pump pulse spectrometer calibration (b) and absorption spectrometer calibration (c). The relative frequency shift is 2 ‰ (violet, ±64 cm^{-1}), 1 ‰ (pink, ±32 cm^{-1}) and 0.5 ‰ (grey, ±16 cm^{-1}).

For each graph in Fig. V.4 the individual spectra, e.g., the 2D slice (Fig. V.4a), are shifted by the given values with respect to the frequency axis of the other spectra used in the calculation of the quantum yield. This procedure simulates an incorrect frequency calibration of the individual spectrometer used. The amplitude of the shifts is estimated to be in the order of 0.1 to 0.5 nm for a central wavelength of 310 nm (16 - 64 cm^{-1} for a central frequency of 32250 cm^{-1}). In Fig. V.4 the confidence interval for different amounts of frequency shifts was estimated by calculating the maximum change of the retrieved quantum yield value when shifting the individual frequency axis with respect to the other ones. The error in the observed quantum yields can exceed the error originating from the uncertainties of the individual parameters used

for calculation as it was shown in Fig. V.3 (about 11 %). The strongest effect of an incorrect frequency calibration is observed for the calibration of the frequency axis of the 2D spectrometer and the pump spectrometer. A shift of the absorption frequency axis is contributing less. The deviations of the calculated quantum yield (Fig. V.4a-c) show strong deviations at the borders while in the central part only a minor influence is observed. This is due to the fact, that at the borders the pump pulse spectrum has the strongest change in intensity for neighboring frequencies. A shift of the spectrum therefore strongly affects the amplitude at a certain frequency and thus the final quantum yield value. The same is true for a shift of the frequency axis of the 2D spectrometer as the shape of the 2D spectrum along the pump axis is a convolution with the pump-spectral intensity distribution. The absorption spectrum is less structured and therefore a frequency shift is influencing the quantum yield values less. This shows that one has to specifically take care of the frequency calibration of the pulse shaper itself.

From the results shown in Fig. V.4 it can be concluded that the frequency calibration is a crucial point when calculating the quantum yield from a 2D measurement. Additional effort has to be made to gauge the individual spectrometer to each other. However, a way to circumvent this problem is to use the same spectrometer for all measured spectra. While for the wavelength calibration of the pulse shaper one is generally using the same spectrometer as for the pump pulse measurement this is typically not the case for the absorption spectrometer. This can be done by building a fiber coupled absorption spectrometer with the same spectrometer.

Appendix A.VI: Details of the 2D-UV setup

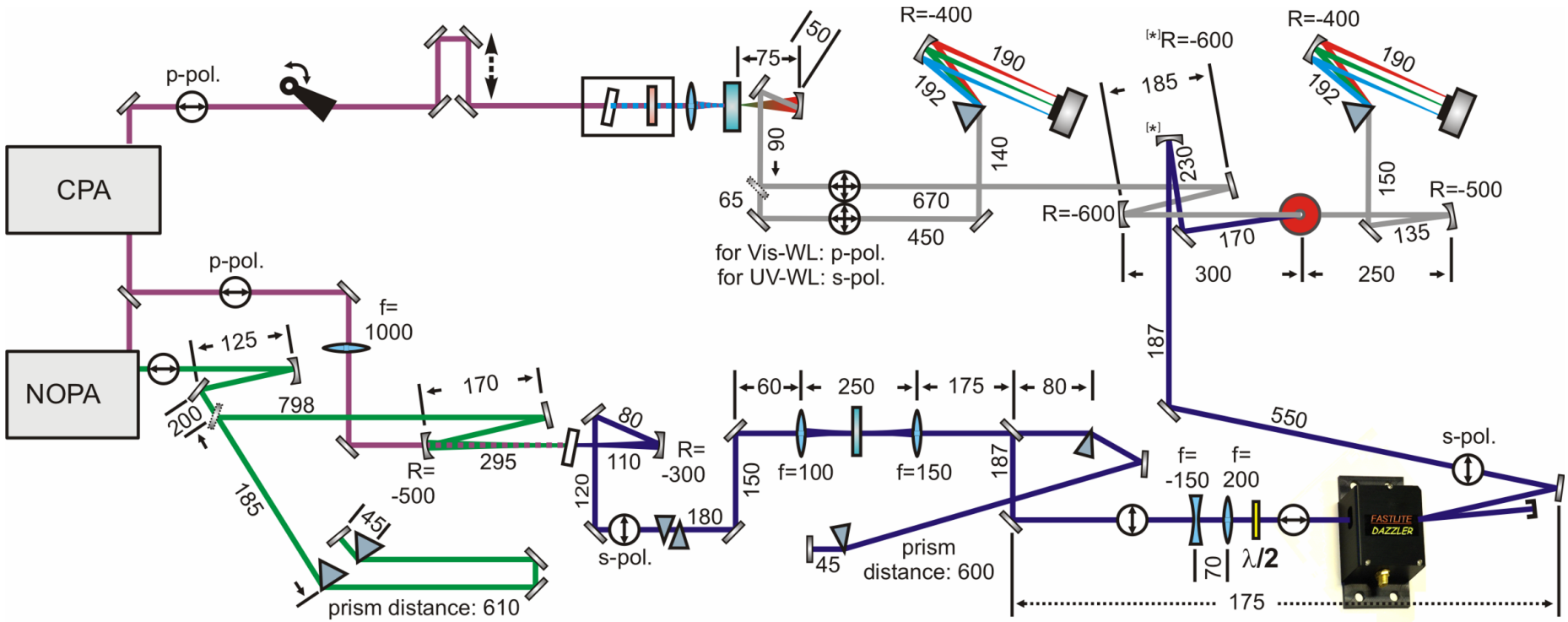

Fig. VI.1. Experimental setup with beam propagation distances. All values are given in mm. The polarization orientation of the individual beam parts are shown.

Appendix B.1

Two dimensional Fourier transform spectroscopy in the UV with sub-20 fs pump pulses and 250 – 720 nm supercontinuum probe

N. Krebs, I. Pugliesi, J. Hauer and E Riedle

Accepted for publication in New Journal of Physics (2013).

New Journal of Physics

Two-dimensional Fourier transform spectroscopy in the UV with sub-20 fs pump pulses and 250 – 720 nm supercontinuum probe

N Krebs[1], I Pugliesi[1], J Hauer[2] and E Riedle[1]

[1] *Lehrstuhl für BioMolekulare Optik, Ludwig-Maximilians-Universität (LMU), Oettingenstraße 67, 80538 München, Germany*

[2] *Photonics Institute, Vienna University of Technology, Gusshausstrasse 27, 1040 Vienna, Austria*

Abstract. Experimental realizations of two-dimensional electronic spectroscopy in the UV must so far contend with a limited bandwidth in both the excitation and particularly the probe frequency. The pump bandwidth is at best 1,500 cm^{-1} (FWHM) at a fixed wavelength of 267 nm or 400 cm^{-1} for tunable pulses. The use of a replica of the pump pulse as probe limits the observation of photochemical processes to the excitation region and makes the disentanglement of overlapping signal contributions difficult. We show that two-dimensional Fourier transform spectroscopy can be carried out in a shaper assisted collinear setup comprising fully tunable UV pulse pairs and supercontinuum probe spanning 250 - 720 nm. The pump pulses are broadened up to a useable spectral coverage of 2,000 cm^{-1} (25 nm at 316 nm) by self-phase modulation in bulk CaF_2 and compressed to 18 fs. By referencing the white light probe and eliminating pump stray light contributions, high signal-to-noise ratios even for weak probe intensities are achieved. Data acquisition times as short as 4 minutes for a selected population time allow the rapid recording of 2D spectra for photolabile biological samples even with the employed 1 kHz laser system. The potential of the setup is demonstrated on two representative molecules: pyrene and 2,2-diphenyl-5,6-benzo(2H)chromene. Well resolved cross peaks are observed and the excitation energy dependence of the relaxation processes is revealed.

1. Introduction

Two-dimensional (2D) spectroscopy has proven to be a powerful tool in unravelling electronic and vibrational couplings and the associated ultrafast dynamic processes [1]. This is afforded by spectrally resolving the pump pulse in addition to the probe pulse already resolved in standard femtosecond transient absorption spectroscopy. In the IR the technique has considerably increased our understanding of protein folding [2, 3] and solvation [4, 5]. In the visible it has provided deep insights in the workings of complex chromophoric systems such as the light harvesting complex and the photosynthetic reaction centres [6- 9], and vibronic and vibrational modulations in molecules [10] and molecular complexes [11]. In the UV only few results have so far been reported [12-16] as the technical development is still work in progress. Very recent first spectroscopic applications are the tryptophan-to-heme electron transfer in myoglobin [17], the ring opening of α-terpinene [18] and the excited state dynamics of 2-aminopurine dinucleotides [19] and chiral porphyrin dimers [16]. The limited bandwidth in the pump and probe pulse requires sophisticated analyses of the experimental data in order to extract the underlying dynamics. The probe spectrum range in these investigations is more or less identical to the pump range and thereby limited to the most congested region of the spectrum where ground state absorption (bleach), stimulated emission, excited state absorption and even a possible product absorption overlap.

The benefits of the extension of 2D spectroscopy into the ultraviolet (UV) have been envisioned in recent perspective articles [15, 20, 21] as it allows to address the absorption and ultrafast dynamics of aromatic amino acids in proteins and DNA bases and thus the investigation of the energy and charge transfer flow in these systems. The potential of this method is however even larger, as one can decipher spectrally overlapping bands in chromophore complexes and even in single chromophores. A prime example for this case is the mixing of the L_a/L_b states in arenes and polyenes [22, 23] as well as the coupling of nearly degenerate electronic states like they have been reported for diphenylmethane [24, 25]. In addition 2D-UV spectroscopy allows to investigate the excess energy dependence of photophysical and photochemical processes in chemical reactions involving UV absorbing chromophores.

Porting 2D spectroscopy into the UV spectral range must contend with several challenges. One is phase stability due to the mechanical fluctuations of the optical components, which is an order of magnitude more critical then in the MIR. For this problem the collinear shaper assisted approach used by Zanni and coworkers [26] in the IR and by Ogilvie and coworkers in the visible [27, 28] is the optimal solution as the shaper guaranties inherent phase stability. The second challenge is the generation of sufficient spectral bandwidth to cover a meaningful fraction of the absorption spectrum

and achieve a good match with the molecular absorption. Over the last few years several Fourier transform 2D-UV experiments have been reported in the literature, with a spectral bandwidth up to 1,500 cm^{-1} at a fixed wavelength [12, 15, 18, 29] or tunable with a bandwidth just above 300 cm^{-1} [13]. In all cases the pump and probe spectrum were equal. The spectral width is inadequate for most UV absorbing samples, where spectral features are often broader than 50 nm, e.g., for the nucleic acids. The third challenge is sufficiently low excitation density to avoid photoionization of the solute or/and the solvent, which has been reported for experiments involving DNA at excitation intensities from 10 GW/cm^2 onward [29-31].

Here we present a 2D-UV setup based on the shaper assisted pump-probe geometry. The UV pump pulses tunable between 240 and 370 nm are broadened by self-phase modulation to a Fourier limit below 16 fs [32]. In most 2D applications, a replica of the pump spectrum is used as probe. If the spectral bandwidth is large enough cross peaks can be resolved, but the probe window is restricted to the excitation region which is often highly congested [11]. We therefore combine our pump pulses with a CaF_2 supercontinuum allowing for a probe range spanning 250 – 720 nm. The potential of the setup is demonstrated on two representative molecules: pyrene and 2,2-diphenyl-5,6-benzo(2H)chromene.

2. Experimental setup

Figure 1 shows the setup used for 2D-UV spectroscopy. To generate UV pump pulses tunable over the whole UV spectral domain, the 6 μJ output of a single stage visible NOPA pumped by a 1 kHz Ti:sapphire amplifier system (CPA 2001; Clark MXR) is either frequency doubled (240 – 360 nm) or sum-frequency mixed with 80 μJ of the Ti:sapphire fundamental (300 – 370 nm) in a 56 μm thick BBO crystal [33]. The pump pulses with an energy of 3 μJ are then spectrally broadened by self-phase modulation in a 1 mm thick CaF_2 crystal as described in detail in ref. [32]. The broadened pulses are compressed to nearly their Fourier limit with the combination of a UV prism compressor and an acousto-optic programmable dispersive filter (AOPDF). The residual chirp is of fourth order and can be neglected. The AOPDF (DAZZLER™ model T-UV-250-400; Fastlite) also generates the phase-locked double pulses with a variable delay and controlled phase. Compressing the UV pulses and generating the double pulses needed for 2D in a single device is an ideal combination as it minimizes the losses compared to a multi-stage approach. The double pump pulses with typical single pulse energies of 80 nJ are focused into the sample by a slightly off-axis spherical mirror (R = -600 mm). The resulting focal diameter is about 100 μm with a negligible astigmatism (< 5%). The excitation fluence is up to $1.5 \cdot 10^{15}$ photons/cm^2 leading to a maximal excitation probability of about 5%. This

corresponds to a peak intensity up to 50 GW/cm^2. Measurements on methanol and acetonitrile show that no signal due to photoionization of the solvent is generated under these intensities. To achieve a clean spatial and temporal profile of the double pulses with the AOPDF, the geometric and Gaussian foci have to overlap at the sample position. This is achieved by the correct collimation of the beam entering the AOPDF. Specifically, an intermediate Gaussian focus has to be generated one focal distance before the R = -600 mm spherical mirror in front of the sample. For details see ref. [34].

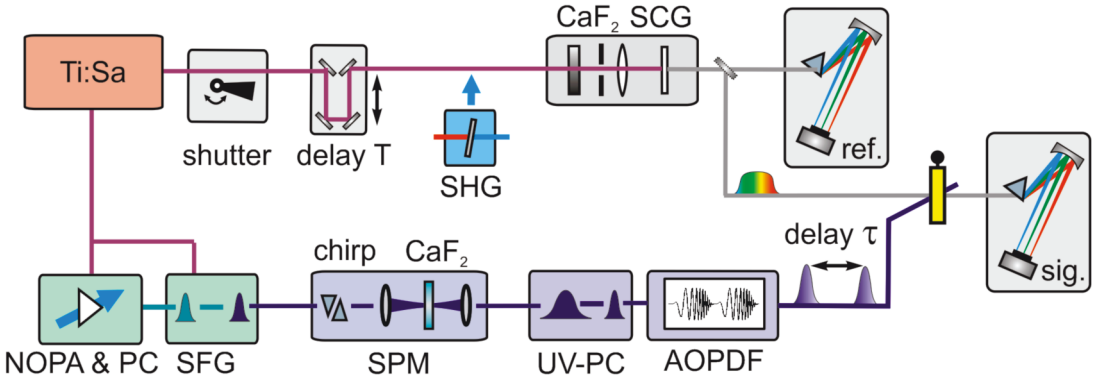

Figure 1. Scheme of the collinear 2D-UV setup. BS: beam splitter, PC: prism compressor, SFG: sum frequency generation, SPM: self-phase modulation, SHG: second harmonic generation, SCG: supercontinuum generation, AOPDF: acousto-optic dispersive filter.

For probing either a fraction of the UV pump pulse (about 2 nJ) or a white light supercontinuum (a few pJ/nm) is used. The delay time of the probe pulse relative to the second pump pulse is denoted as population time T in accordance with literature. The first pump pulse precedes the second one by the coherence time τ. The white light generated in a 4 mm thick CaF_2 crystal covers the spectral range of 290 - 720 nm when generated with the Ti:sapphire fundamental [35] and 250 – 360 nm when generated by the second harmonic of the Ti:sapphire fundamental [36]. The probe beam is focused into the sample by a spherical mirror (R = -600 mm) to a focal diameter of about 50 µm and subsequently spectrally dispersed in a prism-based spectrometer [35]. The spectrally resolved intensity of each laser shot is measured at the full 1 kHz repetition rate with a CCD array (S3902-512Q detector - Hamamatsu Photonics; electronics by Entwicklungsbuero Stresing). For probe referencing a fraction of the collimated probe beam is separated by a beam splitter in front of the sample and measured in a second identical prism spectrograph.

To characterize the phase stability between the two pump pulses generated by the AOPDF, their spectral interference is measured for an interpulse delay of 350 fs (see figure 2). The central frequency of the pulses is set to 32,258 cm^{-1} (310 nm). The phase deviation of an average of 75 laser shots is monitored over a period of half an hour (see figure 2(c)). A slight systematic drift of the phase is

observed on the long time scale which is attributed to a change of the beam pointing due to temperature deviations in the laboratory. The standard deviation of the phase is found to be 33 mrad over 30 minutes, which is less than λ/187 of the optical cycle. This is significantly better than the values reported for 2D-UV spectroscopy in the boxcar geometry, where the phase stability is measured to be about λ/88 [13]. Even the best reported stability at 800 nm of λ/157 [37] is surpassed. Since the measurement of the spectral interference pattern can be performed in parallel to the actual measurement, an even higher effective phase stability could be obtained by online feedback

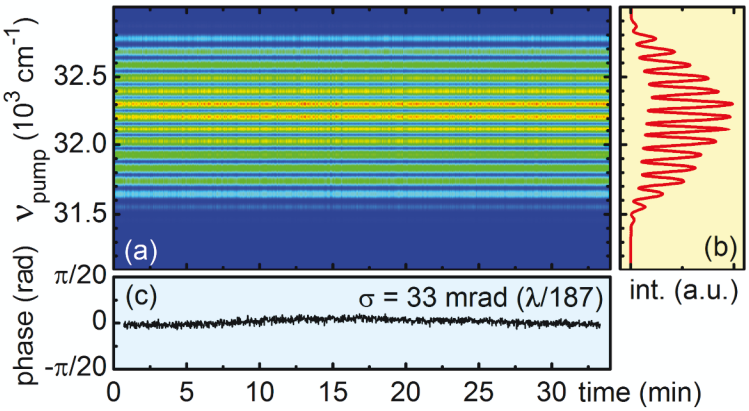

Figure 2. (a) Interpulse phase stability of the pump pulses with a central frequency of 32,258 cm^{-1} (310 nm) characterised by spectral interference. The interpulse delay τ is 350 fs. (b) shows the typical fringe pattern averaged over 75 laser shots and (c) the evaluated phase. The phase shows a long-term standard deviation of 33 mrad over half an hour, which is less than 1/187th of the optical cycle.

3. Measurement procedure: Referencing and stray light subtraction

To obtain a 2D spectrum for one population time T, i.e. the delay between the second pulse of the pump pulse pair and the probe, the probe spectral intensity is measured while the interpulse delay τ (coherence time) of the two pump pulses is scanned by the AOPDF. Both the pulse envelope and the interpulse phase of the electric field are shifted by the AOPDF, in order to ensure that the carrier envelope phase of the two pulses is identical. We measure 2.321 time points per optical cycle up to a maximum coherence time τ of about 150 fs depending on the system under investigation. The resulting step size (~ 0.45 fs at 310 nm) is in accordance with the numbers reported in the literature for 2D spectroscopy in the visible or IR [26, 28].

To remove the transient absorption background we use the phase cycling scheme as described in ref. [26]. For each coherence time τ the probe spectral intensity is measured once with the identical carrier

envelope phase for both pulses and once for the subsequent laser shot with the carrier envelope phase difference flipped by π for the first of the two pump pulses. The background free coherent contribution is obtained by subtraction of these two measurements.

For a 2D measurement the phase cycling scheme is not mandatory. The transient absorption background can also be separated in the course of the data evaluation by the Fourier transformation of the raw data as this contribution typically does not show modulations in the frequency range of the pump spectrum. However phase cycling has several important advantages. The subtraction automatically corrects for long term drifts of the CCD. The retrieved coherent contribution is doubled in size and thus the signal-to-noise ratio increases. Like the chopping of the pump beam in a pump-probe measurement, phase cycling doubles the number of laser shots in the acquisition of a 2D spectrum. However, the flipping of the phase on a shot-to-shot basis makes use of the high shot-to-shot intensity correlations of the laser and thus also increases the signal-to-noise ratio [38]. In spectroscopic terms, the suppression of the transient absorption background by phase cycling avoids the futile attempt to resolve fine structure on the excitation axis that is anyway hidden by the homogeneous broadening of the dissolved molecules.

To further increase the signal-to-noise ratio without increasing the total acquisition time, we combine phase cycling with single shot probe referencing [39]. For each laser shot the probe spectral intensity is measured after passing through the sample (Sig) and in addition in front of the sample (Ref). Inclusion of the reference measurement eliminates the noise on the probe spectral intensity and largely increases the fidelity of the measurement.

When just using the phase cycling scheme, for each coherence time τ_i and probe frequency ν_{probe} the above described signals are combined according to equation 1 on an alternating shot basis.

$$S_{2D}\left(\tau_i, T, \nu_{probe}\right) = Sig^{0}(\tau_i, \nu_{probe}) - Sig^{\pi}(\tau_i, \nu_{probe}) \tag{1}$$

The superscript refers to the interpulse carrier envelope phase difference being 0 or π. In order to include single shot referencing, the 2D raw signal is calculated according to equation 2.

$$S^{r}_{2D}\left(\tau_i, T, \nu_{probe}\right) = \left(\frac{Sig^{0}(\tau_i, \nu_{probe})}{Ref^{0}(\tau_i, \nu_{probe})} - \frac{Sig^{\pi}(\tau_i, \nu_{probe})}{Ref^{\pi}(\tau_i, \nu_{probe})} \right) Ref_{nopump}(\nu_{probe}) \tag{2}$$

Ref_{nopump} is the probe spectral intensity at the reference CCD when no pump pulse is present. The reference spectrum is measured as an average of 1000 laser shots before starting the τ-scan. This factor guaranties that the referencing does not change the shape of the 2D spectrum along the probe axis but only eliminates the noise. The results of equation 2 are averaged over 800 laser shots (400

pulse pairs).

An illustrative example of the raw data obtained with the above described acquisition procedure is shown in figure 3(a). The transient absorption background free interferogram was obtained for pyrene dissolved in methanol at T = 1 ps. The central wavelength of the pump pulses was set to 310 nm (32,258 cm^{-1}) to excite the S_2 ($^1B_{2u}$) ← S_0 (^1A_g) electronic transition. A fraction of the pump beam was used as probe. To better visualize the sinusoidal behaviour of the interferogram, here the step size of the coherence time τ was chosen to be 1/6 of the 1.03 fs optical cycle of the electric field.

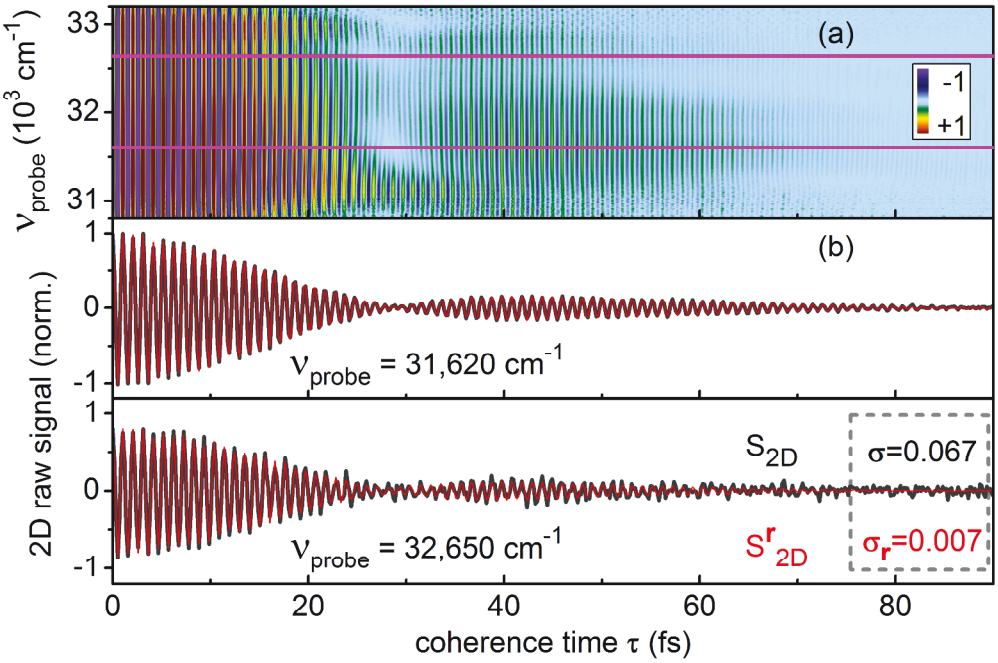

Figure 3. Measured phase-cycled 2D signal of pyrene in methanol at T = 1 ps prior to Fourier transformation. (a) 2D raw spectra measured with probe referencing. (b) Coherence time scans for ν_{probe} = 31,620 cm^{-1} and 32,650 cm^{-1} (pre-normalized intensity ratio 2:1) with (black) and without probe referencing (red). The standard deviations σ were evaluated for τ > 75 fs.

We observe modulations at the pump carrier frequency along the τ-axis (see figure 3(b)). These modulations originate from the polarization created by the pump pulses. The amplitude of these modulations vanish over time due to the finite temporal width of the pulses and the electronic dephasing of the molecule. Contrary to earlier measurements aimed at determining the dephasing time, we also observe a revival of the modulations peaking around the coherence time τ = 45 fs. The revival of the coherence is associated with a π phase shift in the high frequency component at τ = 30 fs.

To interpret this finding we look more closely at what is actually monitored in the 2D experiment. The

first pulse creates a polarization in the sample. This polarization is a Hertzian coherence between the ground state and the electronically excited state. It oscillates with the main transition energy that is equal to the carrier frequency of the pump pulse if it is tuned into resonance. Since our pump pulse is shorter than the typical electronic dephasing time of some ten femtoseconds [40, 41], the second phase-locked pump pulse encounters this freely oscillating polarization prior to significant dephasing. Depending on whether the electric field of the second pulse is in phase or out of phase, the additional polarization generated by the second pulse adds or subtracts to the one from the first pulse. For a static two-level system the frequency of the polarization does not evolve in time and the decrease in 2D signal is solely due to a stochastic decay of the polarization. In this simplified picture it is hard to explain why the sample polarization recurs after a complete disappearance and changes its phase by π. We would like to suggest that this is the intrinsic signature of the molecular energy structure and the ultrafast molecular dynamics following the optical excitation.

The experimental findings can be explained by two contributing transitions with distinct central frequencies and broad spectral bands. The nature of these transitions is not a priori known but they could be two vibronic side bands of the $S_2 \leftarrow S_0$ electronic transition. In this picture, the broadband pulse creates two polarizations with different oscillatory frequencies. These two polarizations can then beat and lead to the observed experimental behaviour, including the phase shift between the oscillations before and after the revival shown in figure 3(b).

An alternative explanation builds on the concept of a τ-dependent modulation of the electronic polarization due to structural motion. The first laser pulse induces a nuclear motion that can be associated with the time evolution of a vibronic wavepacket created in the excited and also the ground state. This motion is the consequence of the differing equilibrium geometry in the excited state as compared to the ground state, also seen in the Franck-Condon structure of the absorption band. The wavepacket propagates with time and the second pump pulse encounters a changed molecular configuration. We do not claim that we observe vibrational modulation along τ directly, rather the effect of structural motion on the electronic polarization.

Assuming two harmonic potentials for the electronic states that have the same curvature and are displaced to each other, the wavepacket motion induces a change in the S_2-S_0 potential energy spacing ΔE which is linear in the nuclear displacement. In the time domain the nuclear displacement oscillates periodically with the cosine of the frequency Ω of an effective mode associated with the wavepacket [42]. As a consequence also ΔE oscillates periodically, as previously reported for a molecular dimer [11, 43]. Thus the polarization created by the first laser pulse changes its frequency due to the nuclear motion. The second laser pulse subsequently interacts with a polarization that is detuned from the

pulse carrier frequency. As the detection averages over the length of the second pump pulse corresponding to about 25 cycles of the electric field, already a change of the polarization frequency of a few % can lead to a vanishing average. A typical vibrational frequency and energy spacing of 1400 cm^{-1} is just equal to 4.3 % of the transition frequency of 32,258 cm^{-1}.

With the above ingredients the time dependent modulation of the electronic polarization frequency can be described according to equation 3

$$\nu(t) = \frac{\Delta E(t)}{h} = \nu_0 + \frac{\delta E}{h} \times [\cos(\Omega t) - 1] \qquad (3)$$

where ν_0 is the initial frequency of the polarization, δE is the relevant vibrational energy and Ω its frequency. δE is on the order of the fundamental vibrational energy due to the displacement and curvature of the harmonic potentials. The frequency change of the polarization causes the electric field of the second pump pulse to get out of phase with the polarization which leads in turn to the vanishing amplitude at τ = 30 fs. As the nuclear geometry returns into the vicinity of the Franck-Condon geometry after one vibrational period $t = 2\pi/\Omega$, the frequency of the polarization returns to that of the pulse electric field and a revival of the coherence signal results. Due to the electronic dephasing, the amplitude of the revival is lower than the initial signal at τ = 0. Similar observations have been made in pump-probe experiments on the iodine molecule [44] and cesium [45].

Formally the two pictures, i.e. the τ-dependent modulation of the electronic polarization due to structural motion and the polarization beating are closely related and can both explain the experimental observations. An intensity dependent study should be able to elucidate and differentiate the suggested mechanisms in greater detail.

3.1. Performance of Single shot referencing

The intensity fluctuations of the probe pulses are the main source of noise in pump-probe experiments, as discussed in detail in ref. [38]. These fluctuations can be effectively eliminated by probe referencing [39]. The results are shown in figure 3(b) where the interferograms for the selected probe frequencies of 31,620 cm^{-1} and 32,650 cm^{-1} are compared with (red trace) and without (black trace) referencing. To calculate the increase in signal-to-noise ratio, the standard deviation of the base line for coherence times τ larger than 75 fs was calculated. The signal-to-noise ratio shows an increase by a factor of 10. This allows to use shorter averaging times for each τ-delay and is the major factor that reduces our acquisition time down to 4 minutes.

To obtain 2D spectra from the interferogram displayed in figure 3(a), the τ-axis is Fourier transformed

for each probe frequency. This yields the pump frequency axis. Since in collinear 2D spectroscopy the probe pulse both generates the 2D signal field and also serves as the local oscillator for heterodyne detection, the phase of the 2D signal is inherently correct. Unlike in the boxcar approach, phasing of the obtained amplitude spectra [46] is not required. The real part of the transformation obtained from the data in figure 3 is shown in figure 4(a) and (b) for the population times of 0.5 ps and 1 ps. It corresponds to the absorptive 2D spectrum. The sign of the obtained signals is opposite to that in pump-probe spectra (ΔOD) in accordance with common practice in 2D spectroscopy [8, 11, 46]. Ground state bleach and stimulated emission signals give rise to positive contributions while excited state absorption signals have negative contributions.

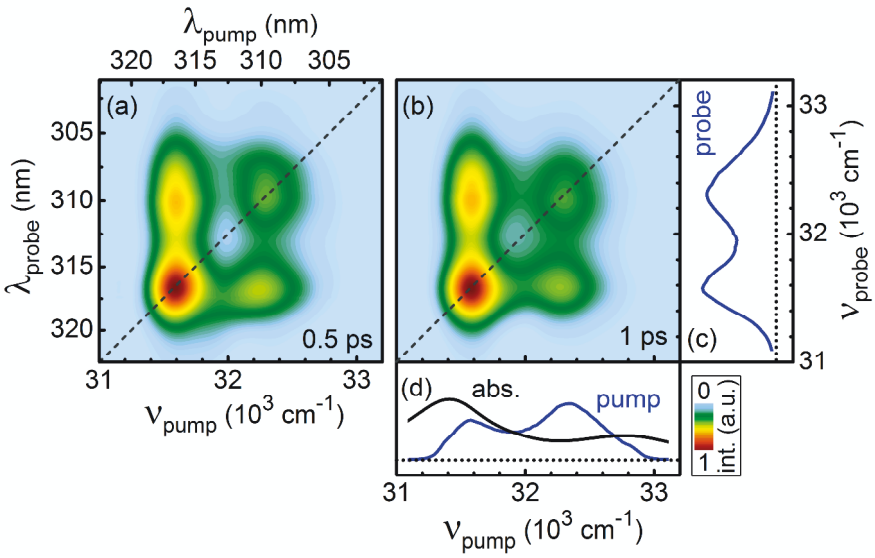

Figure 4. Absorptive 2D spectra of pyrene in methanol for the population times of (a) 0.5 ps and (b) 1 ps. The spectral intensity of the pulses (blue line) and the absorption spectrum of pyrene (black line) are shown in the right (c) and lower side panel (d).

All signals in the 2D spectra in figure 4 are positive and can be assigned to ground state bleach contributions of pyrene. The π phase shift observed in the interferogram of figure 3 leads to a dip in the real part of the Fourier transformation resulting in a double peak structure along the pump axis. The two diagonal peaks are reminiscent of the two vibronic bands in the absorption spectrum. As discussed below, this idea needs a closer consideration. In addition, due to the large spectral bandwidth of the pump pulses, off-diagonal peaks providing information on the correlation between vibronic bands are clearly resolved. The spacing of the off-diagonal peaks matches to the revival time of the electronic coherence observed in the interferogram in figure 3. When going from the population time of 0.5 ps to 1 ps we observe a decrease in intensity for the upper diagonal and the lower off-diagonal peak. As pyrene undergoes an ultrafast internal conversion from the S_2 $^1B_{2u}$ to the optically dark S_1 state within the first 100 fs after excitation, this change cannot be attributed to population

transfer from the upper to the lower vibronic level of the S_2 $^1B_{2u}$ state but rather has to be understood as a change in the excited state absorption of the S_1 state overlying with the ground state bleach region.

3.2. Performance of the dynamic pump stray light subtraction

The use of a replica of the pump pulse for probing limits the probe spectral window to the excitation region. As has just been demonstrated in the case of pyrene, this region is often congested by additional contributions from stimulated emission and excited state absorption. The often used way to cope with this situation is a complicated modelling of the 2D spectrograms and the underlying molecular response. An experimental alternative is to vary the probe spectrum independently from the pump spectrum and to use a much broader spectral range [28]. For the noncollinear boxcar geometry this is not readily possible as the broadband probe will be spatially dispersed when scattered by the transient grating in the sample. However the partially collinear geometry implemented here allows for probe pulses that are generated independently from the pump pulses.

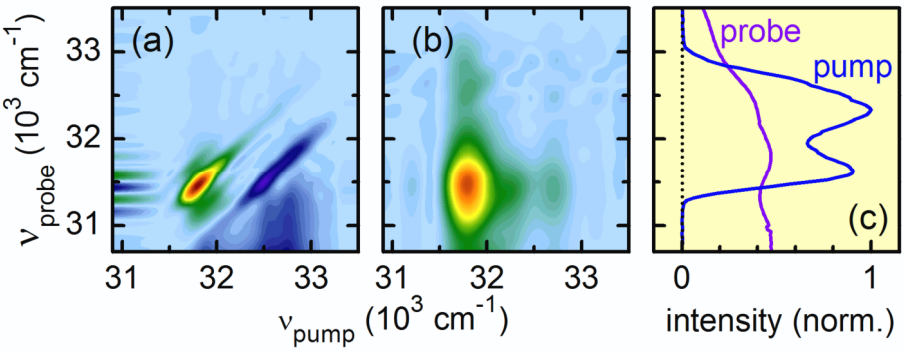

Figure 5. Demonstration of the benefit of pump stray light subtraction for weak probe pulses. The 775 nm pumped supercontinuum white light was used as probe. (a) 2D spectrum of pyrene in methanol without pump stray light subtraction for a population time of 1 ps; severe distortions in the excitation region are observed. (b) 2D spectrum with pump stray light subtraction; diagonal and cross-peaks in the excitation region are now clearly resolved. (c) Pump and probe spectrum.

The broadest probe spectra are obtained by supercontinuum generation. They have been successfully implemented in transient pump-probe setups [35, 36] and 2D-Vis spectroscopy [28]. As white light probes have relatively low intensities (few pJ/nm) compared to the pump pulses [47], even weak contributions of pump stray light can distort the 2D spectra in the spectral region of the pump pulse

spectrum (see figure 5(a)). Various procedures to minimize the influence of stray light have been proposed in the literature [46, 48]. Using well chosen polarization between the incident pulses has shown good results but needs precise adjustment and additional optical components [27]. It also changes the molecular response due to the differing polarization of electronic transitions [49]. Using an additional phase cycling scheme where the carrier envelope phase of both pump pulses is systematically changed was used successfully in the UV [12]. However, this technique needs phase stability between the pump and the probe pulses, which is not necessarily the case when the two are generated by differing nonlinear processes. To achieve applicability for all pump and probe combinations we have implemented the following technique. The pump stray light is measured when the probe beam is blocked with a computer controlled shutter. In this configuration only the pump stray light impinges on the signal spectrometer. This background is subtracted from the probe signal when the shutter is opened again after typically 200 laser shots. The procedure has to be repeated for each coherence time, as the pump spectral intensities of the double pulses changes slightly for each τ-delay.

As illustrated in figure 5(b), our stray light subtraction procedure eliminates the distortions in the spectral region of the pump. Again, well separated diagonal and cross-peaks are obtained as in the case where a replica of the pump was used as probe (see figure 4).

4. Measurement of the 2D spectrum of pyrene and chromene

Figure 6(a) shows the 2D spectrum of pyrene in methanol at a population time T = 1 ps obtained with the two supercontinua implemented in our setup. Note that in this figure for illustrative purposes the pump and probe axes have been turned around, i.e. the probe axis is the horizontal axis, while the pump axis is vertical. To eliminate the amplitude modulations of the probe spectrum from the 2D spectrum, the measurement values calculated via equation 2 have to be divided by the probe signal intensity recorded on the signal CCD when the pump is blocked (Sig_{nopump}) according to equation 4.

$$S_{2D}^{r}\left(\tau_i, T, \nu_{probe}\right) = \left(\frac{Sig^{0}(\tau_i, \nu_{probe})}{Ref^{0}(\tau_i, \nu_{probe})} - \frac{Sig^{\pi}(\tau_i, \nu_{probe})}{Ref^{\pi}(\tau_i, \nu_{probe})} \right) \frac{Ref_{nopump}(\nu_{probe})}{Sig_{nopump}(\nu_{probe})} \qquad (4)$$

As the white light detection ranges overlap between 300 – 340 nm (see figure 6(c)), the two measurements can be concatenated and scrutinized and together allow to probe more than one and a half octaves.

The UV supercontinuum visualizes not only the ground state bleach around the excitation region but also the ground state bleach corresponding to the $S_3 \leftarrow S_0$ absorption at 36,200 cm^{-1} (276 nm). With

the UV-Vis supercontinuum a strong excited state absorption to the red of the ground state bleach is visualized which extends over a very large range and is well structured. These features correspond to the excited state absorption of the S_1 state reached after the sub-100 fs internal conversion. They are distinct from the S_2 ESA determined in an auxiliary transient absorption measurement at 70 fs pump-probe delay. Integration of the 2D spectrum over the pump frequency yields a spectrum that nearly perfectly matches the pump-probe spectrum obtained for the same population time (see figure 6(b)). The amplitudes of the S_1 ESA bands in the visible spectral range show a clear excitation energy dependence. This suggests that the vibrational relaxation in the S_1 state is strongly dependent on the vibrational excess energy supplied to the initially excited S_2 state. A detailed interpretation of these observations is the subject of a forthcoming publication.

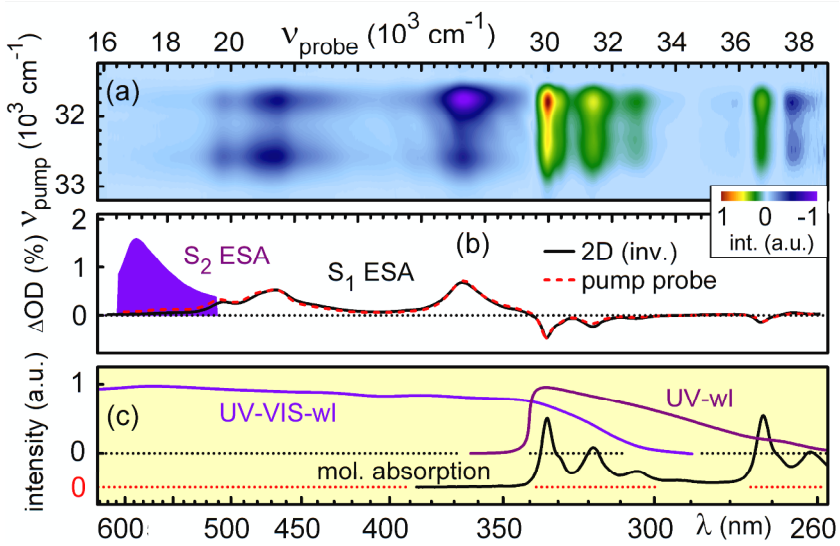

Figure 6. 2D spectrum (T = 1ps) of pyrene in methanol obtained with the UV and Vis supercontinua. The pump spectrum is centred at 32,258 cm^{-1} (310 nm). (a) Concatenated 2D spectrum probing the whole UV-Vis spectral domain. (b) Comparison between projected 2D spectrum (inverted) and pump-probe spectra at T = 1 ps (red hashed line) and at T = 75 fs (filled violet line). (c) Spectral intensity of the probe pulses and absorption spectrum of pyrene in methanol.

In figure 7 the ground state bleach (excitation) region obtained when using the UV supercontinuum as probe (see figure 7(a)) is compared to that obtained when a replica of the pump is used as probe. We observe distinct differences in the spacing between the diagonal and cross-peaks. When the SPM broadened UV pulses are used for both pump and probe the spacing between the bands is 700 cm^{-1}, which corresponds to the 45 fs revival in figure 3. With the supercontinuum, a diagonal-off diagonal spacing of 1380 cm^{-1} is obtained. This corresponds to the energy spacing of the vibronic progression

of the S_2 state. As has been demonstrated in the case of perylene diimides, the purely resolved absorption bands of these systems in solution are composed of several vibronic transitions each that can be resolved in a supersonic molecular beam [50]. The bandwidth of the SPM broadened UV pulses is still not large enough to cover the vibronic bands completely and thus excites a subensemble of these transitions.

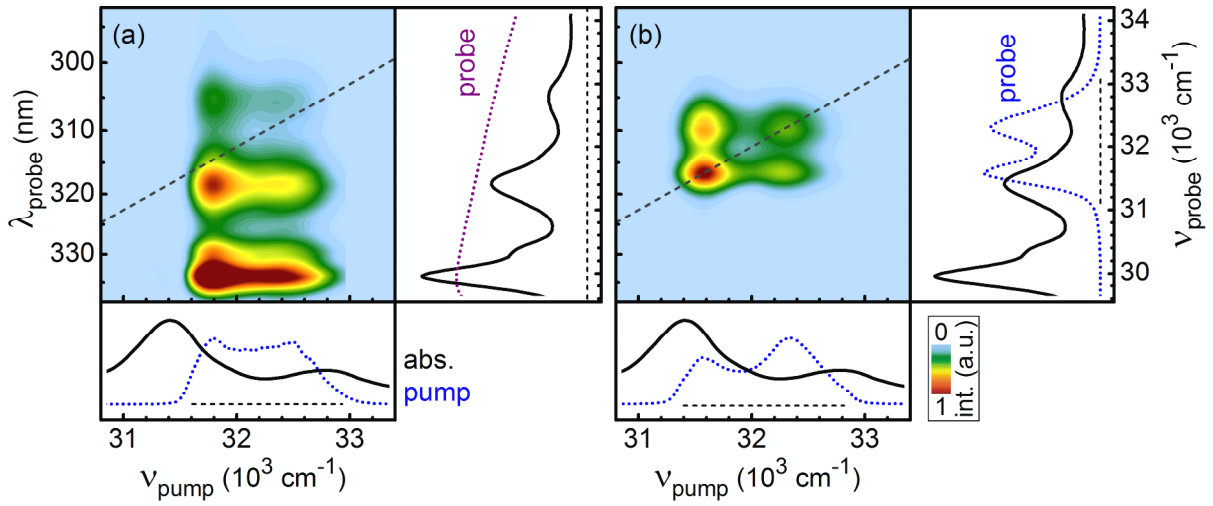

Figure 7. Comparison of the excitation region probed with the UV-white light (a) and the replica of the pump pulse (b). The 2D spectrum in (b) is retrieved according to equation 2 while for (a) the spectral amplitude modulations of the UV-white light have been eliminated by using equation 3 prior to Fourier transformation.

As mentioned in the previous section, the dynamics of the ground state bleach diagonal and cross peaks in the 2D spectra of figure 4 is not due to population transfer from the upper to the lower vibronic level of the S_2 $^1B_{2u}$ state but due to excited state absorption of the S_1 state overlying the ground state bleach region. With the supercontinuum probe this excited state absorption can be visualized directly and completely. Now a disentanglement between ground state bleach and excited state absorption is easily possible, e.g., by subtraction of an appropriately scaled steady state absorption spectrum. There is no need for complicated temporal and spectral analyses, which are common place in 2D applications, where the probe window is confined to the excitation region [18].

The time evolution of diagonal and cross-peaks contains valuable information on the population and coherence transfer in multichromophoric systems or the vibrational excess energy dependence of photophysical and photochemical processes. The capability to measure 2D spectra at several different population times in order to unambiguously resolve the dynamics is therefore of crucial importance. As illustrative example we have chosen the photochromic reaction of 2,2-diphenyl-5,6-

benzo(2H)chromene (5,6-DPBC), which has been extensively investigated with fluorescence [51, 52] and time resolved techniques [53-55].

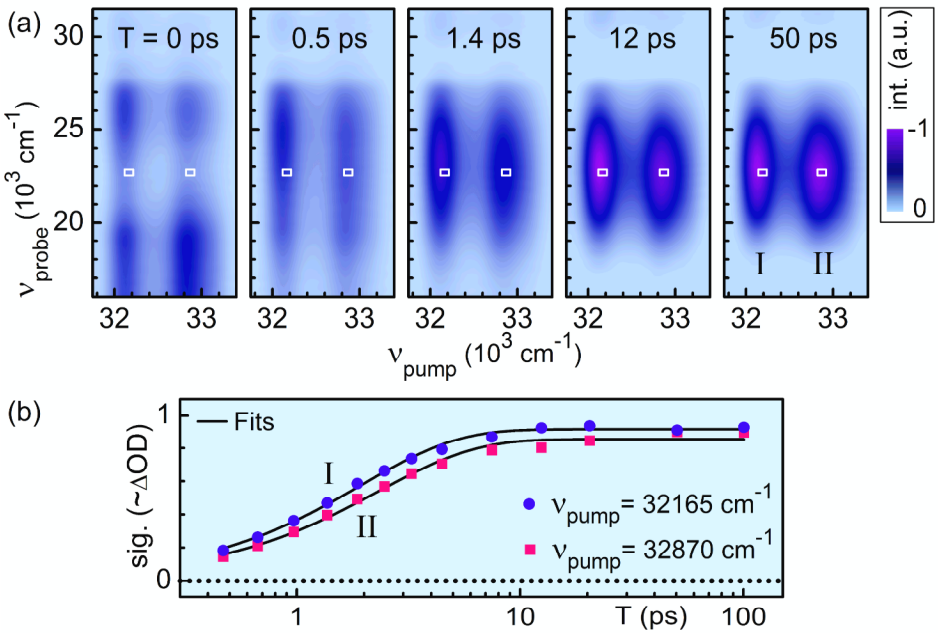

Figure 8. (a) 2D-UV measurements of 5,6 DPBC in ACN for selected population times T measured with visible white light probing. The 2D intensity was normalized to the maximum of the T = 50 ps spectrum. The spectra show the formation of the absorption of the ring-opened photoproduct. (b) Time evolution of the product band at the pump frequency maxima of 32,165 cm^{-1} and 32,870 cm^{-1}, for the probe frequency of 22,920 cm^{-1}. The integration region is marked by white boxes in (a).

When irradiated with UV light, 5,6-DPBC undergoes a pericyclic ring opening which is accompanied by the rise of a broad spectral feature centred at 23,529 cm^{-1} (425 nm). This absorption is attributed to the ring-opened form [56]. The rise of this band is clearly visible in the 2D spectra shown in figure 8(a), which have been obtained by excitation into the S_2 band of 5,6-DPBC with pump pulses centred at 32,415 cm^{-1} (308.5 nm). The pump pulses were broadened by SPM to cover two vibronic bands of the S_2 absorption. This affords the double-band structure of the product absorption along the pump frequency axis. To obtain the temporal evolution of the product band, 2D spectra of 5,6-DPBC were recorded for 13 population times. With an acquisition time of 4 minutes per spectrum, the total measurement was completed in less than one hour. The high quality of the measurements becomes visible when the time traces of the product band (see figure 8(b)) are obtained by integration over just 120 cm^{-1} around the band maximum along the probe axis (22,920 cm^{-1}) and 65 cm^{-1} around the band maxima along the pump axis (32,165 cm^{-1} and 32,870 cm^{-1}; marked by white boxes in figure 8(a)). The high signal-to-noise ratio of the traces is afforded by the short acquisition time which avoids long

term drifts of the setup.

Due to the high signal-to-noise ratio in the time traces, we can precisely monitor the dynamics of the product formation as a function of excitation energy. We observe an excitation dependent rise of the product band. The rise time steadily increases from 1.7 ps at 32,000 cm^{-1} to 2.4 ps at 33,240 cm^{-1}. The earlier pump-probe measurements identified three time constants in the ring-opening of 5,6-DPBC, a 400 fs time, a few ps time and a 10 ps time [54, 55]. However, the pump-probe investigations did not yield sufficient information for an univocal assignment, as to which time constant can be associated with the ring-opening process. Due to the excess energy dependence observed in the 2D measurements, the few ps time constant can now be assigned to the ring-opening, i.e. the product formation with certainty. Intuitively, an increase in supplied vibrational excess energy should lead to a speed up in the product formation. Here however we observe the opposite behaviour. This indicates that with increasing excess vibrational energy, the vibronic wavepacket needs more time to pass through the conical intersection responsible for product formation. This is similar to recent reports on carotenoids [57, 58].

The results obtained on 5,6-DPBC show the power of 2D-UV spectroscopy. Due to its inherent excitation energy resolution it allows to systematically investigate the dependence of photophysical and photochemical processes on the vibrational excess energy, thus giving insights in the vibronic wavepacket dynamics.

5. Discussion and conclusions

We have presented a shaper assisted 2D-UV setup comprising UV pump pulses tunable between 240 and 370 nm and probe supercontinua spanning the range 250 – 720 nm. The UV acousto-optic programmable dispersive filter that generates the double pump-pulses affords a phase stability that is measured to $\lambda/187$ for 30 minutes. The incorporated single shot referencing of the probe increases the signal-to-noise ratio by a factor of 10 for equal acquisition time and affords an acquisition time of just 4 minutes for a 2D spectrum at a selected population time even for the 1 kHz repetition rate laser system.

Tthe bandwidth of our pump pulses is roughly equal to the best value reported for just a fixed wavelength generated by frequency tripling in a gas filled capillary [15, 18]. It is more than three times as large as achieved for tunable pulses [13]. The pump pulses broadened by self-phase modulation up to a spectral width of 25 nm at 310 nm allow to cover more than one vibronic feature of UV absorbing chromophores leading to clearly resolved diagonal and cross peaks in the 2D spectra.

These pulses are compressed to nearly their Fourier limit of sub-20 fs and allow for a temporal resolution better than 30 fs in combination with the supercontinuum probe. At present the chirp of the supercontinuum puts a lower limit to the shortest population times we can observe. If we consider the full spectral width of the probe, only times slightly below 1 ps are accessible. However, a limited range of 1,500 cm^{-1} that is at best available in other 2D-UV setups only amounts to a 75 fs group delay between the half-height frequencies. This is just about the same time range that is lost to observation in one-color transient grating geometry 2D experiments as it is obscured by the coherent artifact [15, 18]. We can expect a much smaller group velocity dispersion when parts of the continuum spectrum are amplified in a broadband NOPA and transferred to the UV by frequency upconversion with a tunable near infrared pulse. In earlier work we already compressed a 5,000 cm^{-1} bandwidth to 5.7 fs [59]. Even the direct compression of the supercontinuum is within sight [60].

Due to the ultrabroad supercontinuum probe we are not confined to investigate photochemical and photophysical processes within the excitation region [16, 18], where it is often necessary to disentangle overlapping signal contributions in order to understand the dynamics. The complicated temporal and spectral analyses for the separation of overlapping contributions coming from different states or chromophores can be circumvented by exploiting the fact that different states or chromophores have distinct excited state absorption signals well outside of the absorption region [36]. As the excited state absorption is typically to the red of the UV absorption, it is often conveniently located in the readily accessible visible region. This situation is exemplarily demonstrated with the 2D spectra of pyrene, once obtained with a probe that is a replica of the pump pulse and once with the supercontinua.

With the example of 2,2-diphenyl-5,6-benzo(2H)chromene we show that white light probing is essential for the investigation of the photochromic ring opening reaction. The ground state bleach is relatively weak with a molar absorption coefficient of around 5,000 $M^{-1}cm^{-1}$ and only shows broad spectral features. The absorption band of the ring-opened form around 425 nm lies well outside the excitation region and is about 10 times stronger. Even if the ground state bleach would be resolved with further increased sensitivity, it would not report on the photochemical reaction as the bleach is not recovered upon the ring opening. Only the stimulated emission signal would decay, but it is typically hard to identify in polar solvents as it is strongly influenced by solvation in the ultrafast time regime. The product absorption on the other hand is a unambiguous signature of the product formation.

The excitation energy resolved measurements that helped unravelling the complex reaction dynamics of the photoswitch will be essential in the investigation of the target systems envisioned for 2D-UV,

such as DNA and proteins [61]. For the measurement of 2D spectra of DNA model systems in aqueous solutions, the intensity might have to be limited to a few GW/cm^2 to avoid contributions from ionization of the solute or the solvent [31]. In the measurements presented here, the solvents methanol and acetonitrile do not produce any lasting signal even at the used peak intensities of 50 GW/cm^2. The amplitude of the coherent artifact is in all cases less than the molecular signal, in strong contrast to the results obtained in the transient grating geometry setups [13, 15, 18]. Such intensities have been reported to generate solvated electrons in buffered aqueous solutions. However, it is not clear whether the solvated electrons have been generated via multiphoton processes in the solvent as discussed in [31] or due to single photon induced formation of a $\pi\sigma^*$ state in the solute [62, 63, 64]. The implicit need for systematic intensity variations in 2D-UV spectroscopy can be carried out with our setup by purely electronic means. We believe that the sensitivity at largely reduced excitation intensities will still be sufficient due to the referencing scheme integral to our setup and the intrinsic smoothing of the Fourier transform.

Acknowledgements

We thank Niklas Christensson and Harald Kauffmann for valuable discussions and suggestions. This work was supported by the Austrian Science Fund within the framework of the Special Research Program F16 (Advanced Light Sources), by the SFB749 and by the DFG-Cluster of Excellence: Munich-Centre for Advanced Photonics. J. H. acknowledges funding by the Austrian Science Fund (FWF): START project Y 631-N27.

6. References

[1] Jonas D M 2003 *Annu. Rev. Phys. Chem.* **54** 425

[2] Hamm P, Helbing J and Bredenbeck J 2008 *Annu. Rev. Phys. Chem.* **59** 291

[3] Hunt N T 2009 *Chem. Soc. Rev.* **38** 1837

[4] Elsaesser T 2009 *Acc. Chem. Res.* **42** 1220

[5] Fayer M D, Moilanen D E, Wong D, Rosenfeld D E, Fenn E E and Park S 2009 *Acc. Chem. Res.* **42** 1210

[6] Brixner T, Stenger J, Vaswani H M, Cho M, Blankenship R E and Fleming G R 2005 *Nature* **434** 625

[7] Cheng Y-C and Fleming G R 2009 *Annu. Rev. Phys. Chem.* **60** 241

[8] Milota F, Sperling J, Nemeth A, Abramavicius D, Mukamel S and Kauffmann H F 2009 *J. Chem. Phys.* **131** 054510

[9] Wong C Y, Alvey R M, Turner D B, Wilk K E, Bryant D A, Curmi P M G, Silbey R J and Scholes G D 2012 *Nature Chem.* **4** 396

[10] Mančal T, Christensson N, Lukeš V, Milota F, Bixner O, Kauffmann H F and Hauer J 2012 *J. Phys. Chem. Lett.* **3** 1497

[11] Bixner O, Lukeš V, Mančal T, Hauer J, Milota F, Fischer M, Pugliesi I, Bradler M, Schmid W, Riedle E, Kauffmann H F and Christensson N 2012 *J. Chem. Phys.* **136**, 204503

[12] Tseng C, Matsika S and Weinacht T C 2009 *Opt. Express* **17** 18788

[13] Selig U, Schleussner C-F, Foerster M, Langhojer F, Nuernberger P and Brixner T 2010 *Opt. Letters* **35** 4178

[14] Auböck G, Consani C, Van Mourik F and Chergui 2012 M *Opt. Letters* **37** 2337

[15] West B A and Moran A M 2012 *J. Phys. Chem. Lett.* **3** 2575

[16] Koch F, Kullmann M, Selig U, Nuernberger P, Götz D C G, Bringmann G and Brixner T 2013 *New J. Phys.* **15** 025006

[17] Consani C, Auböck G, van Mourik F and Chergui M 2013 *Science* DOI: 10.1126/science.1230758

[18] West B A, Molesky B P, Montoni N P and Moran A M 2013 *New J. Phys.* **15** 025007

[19] Widom J R, Johnson N P, von Hippel P H and Marcus A H 2013 *New J. Phys.* **15** 025028

[20] Cannizzo A 2012 *Phys. Chem. Chem. Phys.* **14** 11205

[21] Lewis K L M and Ogilvie J P 2012 *J. Phys. Chem. Lett.* **3** 503

[22] Tavan P and Schulten K 1987 *Phys. Rev. B* **36** 4337

[23] Schmidt M and Tavan P J 2012 *Chem. Phys.* **136** 124309

[24] Pillsbury N R, Stearns J A, Müller C W, Plusquellic D F and Zwier T S 2008 *J. Chem. Phys.* **129** 114301

[25] Stearns J A, Pillsbury N R, Douglass K O, Müller C W, Zwier T S and Plusquellic D F 2008 *J. Chem. Phys.* **129** 224305

[26] Shim S-H and Zanni M 2009 *Phys. Chem. Chem. Phys.* **11** 748

[27] Myers J A, Lewis K L M, Tekavec P F and Ogilvie J P 2008 *Opt. Express* **16** 17420

[28] Tekavec P F, Myers J A, Lewis K L M and Ogilvie J P 2009 *Opt. Letters* **34** 1390

[29] West B A, Womick J M and Moran A M 2011 *J. Phys. Chem. A* **115** 8630

[30] Reuther A, Iglev H, Laenen R and Laubereau A 2000 *Chem. Phys. Lett.* **325** 360

[31] Pecourt J-M L, Peon J and Kohler B 2001, *J. Am. Chem.Soc.* **123** 10370

[32] Krebs N, Pugliesi I and Riedle E 2013 *Appl. Sci.* **3** 153

[33] Kozma I Z, Baum P, Lochbrunner S and Riedle E 2003 *Opt. Express* **11** 3110

[34] Krebs N, Probst R A and Riedle E 2010 *Opt. Express* **18** 6164

[35] Megerle U, Pugliesi I, Schriever C, Sailer C F and Riedle E 2009 *Appl. Phys. B* **96** 215

[36] Riedle E, Bradler M, Wenninger M, Sailer C F and Pugliesi I 2013 *Faraday Disc.* DOI: 10.1039/C3FD00010A

[37] Turner D B, Stone K W, Gundogdu K and Nelson K A 2011 *Rev. Sci. Instrum.* **82** 081301

[38] Schriever C, Lochbrunner S, Riedle E and Nesbitt D J 2008 *Rev. Sci. Instrum.* **79** 013107

[39] Dobryakov A L, Kovalenko S A, Weigel A, Pérez-Lustres J L, Lange J, Müller A and Ernsting N P 2010 *Rev. Sci. Instrum.* **81** 113106

[40] Bigot J-Y, Portella M T, Schoenlein R W, Bardeen C J, Migus A and Shank C V 1991 *Phys. Rev. Lett.* **66** 1138

[41] Nibbering E T J, Wiersma D A and Duppen K 1991 *Phys. Rev. Lett.* **66** 2464

[42] Wolfseder B, Seidner L, Domcke W, Stock G, Seel M, Engleitner S and Zinth W *Chem. Phys.*

233 323

[43] Prall B S, Parkinson D Y, Ishikawa N and Fleming G R 2005 *J. Phys. Chem. A* **109** 10870

[44] Katsuki H, Chiba H, Girard B, Meier C and Ohmori K 2006 *Science* **311** 1589

[45] Blanchet V, Nicole C, Bouchene M-A and Girard B 1997 *Phys. Rev. Lett.* **78** 2716

[46] Brixner T, Mančal T, Stiopkin I V and Fleming G R 2004 *J. Chem. Phys.* **121** 4221

[47] Bradler M, Baum P and Riedle E 2009 *Appl. Phys. B* **97** 561

[48] Augulis R and Zigmantas D 2011 *Opt. Express* **19** 13126

[49] Read E L, Engel G S, Calhoun T R, Mančal T, Ahn T K, Blankenship R E and Fleming G R 2007 *Proc. Natl. Acad. Sci. USA* **104** 14203

[50] Wewer M and Stienkemeier F 2005 *Phys. Chem. Chem. Phys.* **7** 1171

[51] Becker R S and Michl J 1966 *J. Am. Chem. Soc.* **88** 5931

[52] Becker R S, Pelliccioli A P, Romani A and Favaro G 1999 *J. Am. Chem. Soc.* **121** 2104

[53] Gentili P L, Danilov E, Ortica F, Rodgers M A J and Favaro G 2004 *Photochem. Photobiol. Sci.* **3** 886

[54] Moine B, Buntinx G, Poizat O, Rehault J, Moustrou C and Samat A 2007 *J. Phys. Org. Chem.* **20** 936

[55] Moine B, Réhault J, Aloïse S, Micheau J-C, Moustrou C, Samat A, Poizat O and Buntinx G 2008 *J. Phys. Chem. A* **112** 4719

[56] Ottavi G, Favaro G and Malatesta V 1998 *J. Photochem. Photobiol. A: Chem.* **115** 123

[57] Billsten H H, Pan J, Sinha S, Pascher T, Sundström V and Polívka T 2005 *J. Phys. Chem. A* **109** 6852

[58] Larsen D S, Papagiannakis E, van Stokkum I H M, Vengris M, Kennis J T M and van Grondelle R 2003 *Chem. Phys. Lett.* **381** 733

[59] Baum P, Breuer M, Riedle E and Steinmeyer G 2006 *Opt. Lett.* **31** 2220

[60] Hassan M, Wirth Grguras A I, Moulet A, Luu T, Gagnon J, Pervak V, and Goulielmak E 2012 *Rev. Sci. Instrum.* **83** 111301

[61] Abramavicius D, Jiang J, Bulheller B M, Hirst J D and Mukamel S 2010 *J. Am. Chem. Soc.* **132** 7769

[62] Sobolewski A L, Domcke W, Dedonder-Lardeux C and Jouvet C 2002, *Phys. Chem. Chem. Phys.* **4** 1093

[63] Perun S, Sobolewski A L and Domcke W 2005 *Chem. Phys.* **313** 107

[64] Nix M G D, Devine A L, Cronin B and Ashfold M N R 2007 *J. Chem. Phys.* **126** 124312

Appendix B.2

Pulse compression of ultrashort UV pulses by self-phase modulation in bulk material

N. Krebs, I. Pugliesi, and E. Riedle

Applied Sciences **3**, 153 - 167 (2013).

Appl. Sci. **2013**, *3*, 153-167; doi:10.3390/app3010153

OPEN ACCESS

applied sciences

ISSN 2076-3417

www.mdpi.com/journal/applsci

Article

Pulse Compression of Ultrashort UV Pulses by Self-Phase Modulation in Bulk Material

Nils Krebs, Igor Pugliesi and Eberhard Riedle *

Lehrstuhl für BioMolekulare Optik, Ludwig-Maximilians-Universität München (LMU), 80538 München, Germany; E-Mails: nils.krebs@physik.uni-muenchen.de (N.K.); igor.pugliesi@physik.uni-muenchen.de (I.P.)

* Author to whom correspondence should be addressed; E-Mail: riedle@physik.lmu.de; Tel.: +49-89-2180-9210; Fax: +49-89-2180-9202.

Received: 21 December 2012; in revised form: 5 February 2013 / Accepted: 6 February 2013 / Published: 8 February 2013

Abstract: The bandwidth of ultrafast pulses in the UV is limited by the finite acceptance bandwidth of the nonlinear crystals used for their generation. For fundamental laser pulses it is well established that spectral broadening can be used to overcome intrinsic bandwidth limits. We show that self-phase modulation of UV pulses in bulk materials leads to large spectral broadening and allows for a significant reduction of the pulse duration. We find that for pulse energies in the range of a few μJ, a thin crystal is favorable due to the strong dispersion in the UV and the limitations set by self-focusing. In contrast to spectral broadening in gaseous media, the self-focus has to lie outside the crystal to avoid beam break up. We focus UV pulses into a 1 mm thick CaF_2 crystal. For moderately short input pulses, a shortening factor up to 2.4 is achieved: the 120 fs long third harmonic output of a Ti:sapphire amplifier is compressed down to 50 fs FWHM. For a central wavelength of 315 nm, we generate pulses as short as 14.9 fs after compression with an UV pulse shaper. In both cases the resulting beam shape is close to Gaussian and fully usable for spectroscopic experiments. We use the pulses in a collinear 2D-UV experiment and clearly resolve vibronic off-diagonal peaks of the S_2 $^1B_{2u}$ vibronic progression of pyrene.

Keywords: ultrashort optical pulses; ultraviolet; UV; self-phase modulation; pulse compression

---

1. Introduction

For nonlinear optics and time resolved spectroscopic studies of atoms, molecules and biological processes there is a rising need for ultrashort light pulses in the UV and deep UV spectral domain. Straightforward frequency upconversion of short visible pulses in non-linear crystals already allows for the generation of sub-20 fs UV pulses [1] and 30 fs pulses down to 189 nm [2]. The phase-matching bandwidth can be increased by advanced angular dispersion methods leading to sub-10 fs pulses [3,4]. Other important techniques capable of generating UV pulses are four wave mixing in a gas filled hollow wave guide providing sub-10 fs pulses at 270 nm [5]. Third harmonic generation of the fundamental pulses at around 800 nm provide sub-30 fs pulses in air [6] or even 3-fs pulses in a Neon filled gas cell [7]. These techniques are characterized by a low conversion efficiency and require an elaborate experimental implementation.

Pulse shortening can also be achieved through spectral broadening of longer UV pulses typically generated by frequency up conversion. Spectral broadening can be achieved by nonlinear phase modulation of the UV pulse in an optically transparent medium. In cross phase modulation the nonlinearity is induced by an auxiliary high intensity laser pulse. To increase the interaction length, gas filled hollow waveguides are often used. With this approach cross phase modulation between the fundamental and the third harmonic of a Ti:sapphire laser amplifier allows to compress the 266 nm pulses by a factor of 2 down to 23 fs [8]. For a 35 fs Ti:sapphire laser system this process helps to further broaden the intense 266 nm pulses originating from four-wave-mixing of blue and red pulses down to a length of 8-fs [9].

Efficient spectral pulse broadening in gas-filled hollow fibers or gas cells has also been achieved by self-phase modulation (SPM). With input pulse lengths of around 100 fs, deep UV pulses with an pulse energy of several hundred μJ as short as 20 fs centered at 268 nm [10] and 25 fs centered at 248 nm [11] were obtained. This technique however needs high input UV pulse energies up to several hundred μJ due to the low nonlinearity of the gas. Such high energy pulses are typically not available in spectroscopic setups, particularly at high repetition rates, and therefore the practical use of spectral broadening in gases is limited.

Bulk materials and fibers in contrast offer medium to high nonlinearities and are suitable candidates for nonlinear phase modulation. In single-mode fibers the pulse power is typically limited to tens of nJ. Fibers are therefore best suited for high repetition laser systems [12]. Bulk materials can be operated at any input energy as the thickness of the material can be suitably adjusted so that self-focusing in the crystal is controlled and any serious beam distortion or material destruction can be avoided. Spectral broadening by SPM in bulk material has been first observed in the visible by Alfano *et al.* [13] and later in the UV by Hata *et al.* [14]. Theoretically, it was shown that in bulk material cross phase modulation should be capable of generating chirp free nearly-single cycle pulses [15]. The shortening of IR and VIS pulses by SPM in bulk materials has been realized successfully in the 1980s [16,17] and it was envisioned that this approach can be extended into the UV spectral domain [17].

In this paper we demonstrate that SPM can indeed be used to shorten UV pulses below their input Fourier limit. Taking into account the nonlinear processes of self-focusing and SPM we use simulations to find the optimal conditions for UV spectral broadening in common crystals. We then describe our experimental results on spectral broadening of UV pulses in a CaF_2 plate and describe the

way to achieve shorter pulses by incorporating a few supplemental parts into the setup. Compression of the pulses to nearly their Fourier limit is demonstrated by implementing an acousto-optical pulse shaper not necessary if the residual higher order chirp is of no concern.

Finally we apply the broadened UV pulses as pump and probe in a collinear two-dimensional experiment that allows us to resolve the spectral correlations of two vibrational bands of pyrene due to the enlarged spectral window of the pulses.

2. Parameter Optimization for Spectral Broadening

SPM modifies the spectral content of a laser pulse. The result of this modification is influenced by several experimental factors such as the pulse intensity, the wavelength and the nonlinear material properties. When an intense laser pulse propagates through a medium it induces a dynamic refractive index change $n(t) = n_0 + n_2 I(t)$ due to the third-order Kerr nonlinearity n_2. This leads to self-focusing, self-steepening and SPM. In the case of SPM, n_2 causes a change of the phase of the electric field in the pulse itself. For an input pulse with spatial and temporal intensity profile $I(r,t)$, this nonlinear phase variation accumulates over the propagation direction z in a medium with thickness l according to the *B integral*:

$$B(r,t) = \frac{\omega_0}{c} \int_0^l n_2 \cdot I(z,r,t)\, dz \tag{1}$$

Here ω_0 is the initial circular frequency, c the speed of light and r parameterizes the spatial intensity distribution perpendicular to the propagation direction. The accumulated phase shift results in a corresponding frequency shift and thus a broadening or narrowing of the pulse spectrum.

A quantification of the maximum frequency shift due to SPM is given by

$$\Delta\omega_{\max} = \omega(t) - \omega_0 = -\left(\frac{\partial}{\partial t} B(t) \right)_{\max} \tag{2}$$

where the maximum frequency shift $\Delta\omega_{\max}$ is typically located at the maximum slope of the leading and trailing edge of the pulse intensity.

From Equations (1) and (2) one can conclude that high intensities and a long propagation distance in a material with a large positive n_2 is favorable to maximize spectral broadening through SPM. However, in bulk materials the large dispersion experienced by a UV pulse has to be taken into account. This leads to a reduction of the pulse intensity and thus the accumulated phase. A further limiting factor is the nonlinear process of self-focusing. As often mentioned in the literature, if the self-focus lies within the crystal length, severe beam distortions, beam breakup [14] or ultimately filamentation occurs [10,18].

To illustrate the influence of the material's dispersion on SPM we calculated the *B integral* (Equation (1)) for different thicknesses of a CaF_2 crystal ($n_2 = 1.92 \times 10^{-16}$ cm^2/W [19]). The results for a 25 fs long UV pulse centered at 308 nm with a pulse energy of 3μJ are shown in Figure 1. One should note, that for a given crystal thickness we optimize the beam focusing to a minimal beam waist radius w for which the self-focal length is 1.25 times the crystal length (see orange line in Figure 1). This puts the self-focus outside the crystal and ensures that beam distortions do not occur. The

self-focal length for a pulse with a power P focused to a beam waist w can be calculated according to Equation (3).

$$z_{SF}(w) = \frac{0.183\,\rho_0(w)}{\sqrt{\left(\sqrt{P/P_{cr}(n_2)} - 0.852\right)^2 - 0.0219}} \quad (3)$$

with ρ_0 being the Rayleigh length and P_{cr} the critical self-focusing power threshold [20,21]. In the simulations, the change in the peak intensity due to self-focusing and self-steepening is neglected. The spatial intensity distribution is assumed to be Gaussian and the input pulses are Fourier limited. For the calculation of the *B integral* we integrate over the whole beam profile.

Figure 1. Amount of self-phase modulation (SPM) for 25 fs, 308 nm, 3 µJ UV pulses broadened in a CaF_2 crystal. Calculated B-integral at increasing levels of theory for varied crystal length. The input beam waist is set to a value for which the self-focal length is 1.25 × the crystal length.

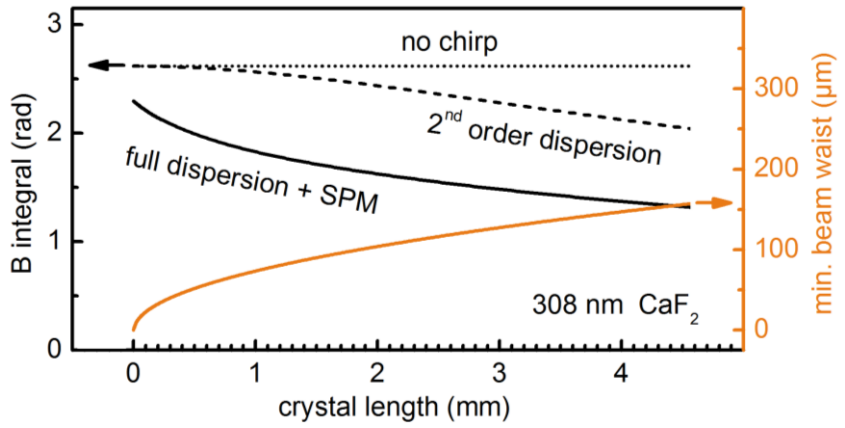

The B integral does not vary with the crystal length when no material dispersion is included in the simulation (Figure 1, dotted line) as the self-focal length is kept 1.25 times the crystal length for the different crystal thicknesses. As soon as 2nd order dispersion is considered (for a formula see, e.g., [20]), the *B integral* starts dropping steadily when the crystal thickness exceeds 1 mm and converges to zero for long crystals (Figure 1, dashed line). The effect is even more dramatic when the full material dispersion is introduced by using virtual femtosecond laboratory software Lab2 [22]. The resulting *B integral* (Figure 1, continuous line) shows a pronounced decrease even for crystals thinner than a few mm.

To find the optimal experimental conditions for a specific crystal thickness and a given minimal beam waist, we varied the input pulse energies and the type of bulk materials (Figure 2). To get direct information on the achieved broadening we calculated the compressibility factor, which is the Fourier limit of the broadened pulse spectrum after propagating through the material divided by the initial Fourier limited pulse length (25 fs for all simulations).

Figure 2a shows, that for a fixed crystal length an increase of the input pulse energy increases the achievable compressibility factor. This behavior can be understood from Equations (1) and (3). The self-focal length scales roughly inversely with the square root of the pulse power P, while the pulse

intensity is directly proportional to the power. Therefore, the compressibility factor can be estimated to roughly scale with $\sqrt{P}$.

Figure 2. Compressibility factor (ratio between input and output Fourier limit) for a 25 fs pulse. Results for varied input energies, pulses centered at 308 nm, and a CaF_2 crystal (**a**) and for different crystals with 266 nm pulses of 3 μJ energy (**b**). The input beam waist is set to a value for which the calculated self-focal length is 1.25 × the crystal length.

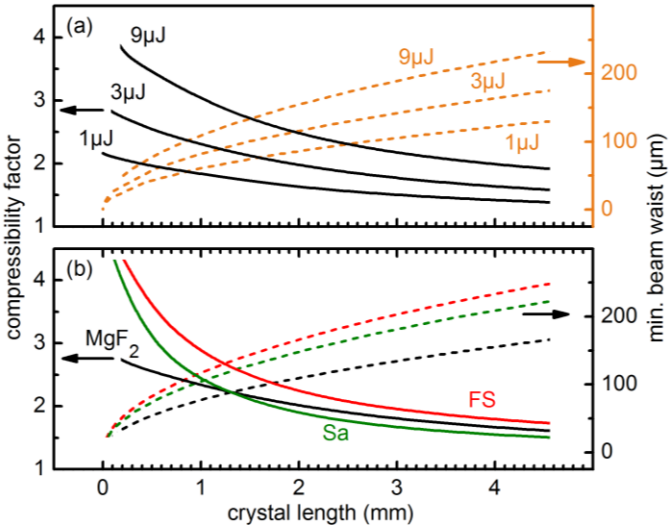

In Figure 2b the simulation results for different materials are shown. The n_2 values of MgF_2 (1.5×10^{-16} cm^2/W), fused silica (7.8×10^{-16} cm^2/W) and Sapphire (6.0×10^{-16} cm^2/W) at 266 nm were taken from the literature [19,23]. The simulations show that a larger n_2 generally leads to an increase of the compressibility factor. However, the differing dispersion of the materials can change this general trend (see crossing of MgF_2 and Sa curves in Figure 2b).

The simulations show that due to the pronounced dispersion in the UV, it is favorable to use short crystals with tight focusing. This is unlike spectral broadening in gases, where meter-long propagations are needed due to the much lower n_2 values. 1 mm thick crystals lead to compressibility factors between 2 to 2.5 for Fourier limited Gaussian pulses with energies of a few μJ. The required beam waist radius lies in the order of 100 μm. These parameters are experimentally sensible.

3. Experimental Setup

A schematic of the setup, which comprises the generation, broadening and characterization of UV pulses, is shown in Figure 3. Tunable visible pulses were generated from a single-stage noncollinear parametric amplifier (NOPA) pumped by a 1-kHz Ti:Sa amplifier system (CPA 2001; Clark MXR) and optimally compressed by a pair of fused silica Brewster prisms. UV pulses with a typical pulse length of 25 fs were generated by frequency doubling or sum frequency mixing the NOPA pulses with the CPA fundamental in BBO crystals with a thickness of 53 μm. For the frequency doubling we typically obtain < 1 μJ which corresponds to an efficiency of < 15%. For the sum frequency mixing both beams were collinearly overlapped and the CPA fundamental was focused with a fused silica lens to match the focal size of the beam of the visible pulse in the BBO. Typical energies of 4 μJ are achieved with a visible to UV efficiency of 50 %.

To introduce a variable positive chirp the UV pulses pass through a set of UV antireflection coated movable fused silica wedges (apex angel 45°) with counter oriented apexes [24]. To obtain a clean and spatially symmetric beam profile, which is advantageous for SPM, we introduce an aperture accepting a minimal loss of energy. The UV beam is then focused with the f = 150 mm antireflection coated fused silica lens L1 into a few mm thick crystal which spectrally broadens the pulses due to SPM. The position of the crystal relative to the soft focus of the UV beam can be adjusted to obtain maximum broadening without impairing the spatial mode due to self-focusing inside the crystal. A second fused silica lens L2 (f = 100 mm), that can be translated along the beam axis, recollimates the spectrally broadened UV pulse. This not only accounts for the change in divergence caused by the partial self-focusing in the crystal but also adjusts the collimation of the beam such that the specific requirements for pulse shaping with an acousto-optic programmable dispersive filter (AOPDF) are met [1]. Specifically, the intermediate beam waist of the broadened UV pulse after the AOPDF has to be located one focusing length in front of the focusing element which is used to focus the beam into the interaction region, e.g., the sample.

Figure 3. Setup for the generation, compression and characterization of UV pulses spectrally broadened by SPM. PC: prism compressor; SFM (SHG): sum frequency (second harmonic) generation; FS-W: Fused silica wedges; Ap: aperture; L1, L2 lenses.

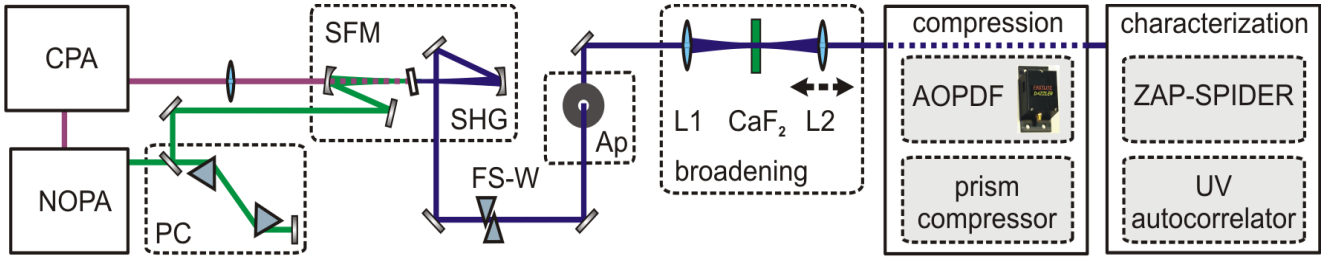

The compression of the positively chirped broadened UV pulses is achieved by either a second UV prism compressor or a combination of a UV prism compressor and an AOPDF (DAZZLER™ model T-UV-250-400; Fastlite) [25] for higher order chirp correction. The prisms are UV antireflection coated and have an apex angle of 45°. The throughput of the UV PC is roughly 93%. In the PC-AOPDF combination the precompression with the UV PC permits a larger bandwidth of the AOPDF because the acoustic wave is less chirped and thus less elongated within the shaper crystal.

To measure the pulse lengths obtained in the simple setup where only a UV-PC is used to compress the broadened pulses, we employ a newly developed UV autocorrelator [26] based on two photon absorption in a 173 μm thick BBO crystal. To check if the higher order chirp contributions of the UV-broadened pulses can be compensated for by the PC-AOPDF combination, we characterized the spectral phase with a ZAP-SPIDER [27].

4. Results and Discussion

4.1. Experimental Characterization of Self-Phase Modulation Broadened UV Pulses

With the insights gained by the simulations, we experimentally tested the broadening of UV pulses by focusing them into a CaF_2 crystal and subsequently compensate the phase of the broadened spectra.

First we tuned the chirp of the input pulse and investigated the influence of the peak intensity on the SPM process. Subsequently, we varied the type and thickness of the broadening crystal.

When the UV beam is tightly focused into a crystal we observe changes in the spectral intensity distribution (see Figure 4d–f). Experimental conditions can be found that allow the generation of new frequency components due to SPM.

Figure 4. Correlation between the peak intensity and the measured output energy (**a**), output Fourier limit (**b**) and the calculated self-focal length (**c**) obtained by moving a 1 mm CaF_2 crystal relative to the beam focus of a positively chirped pulse centered at 312 nm. Measured spectra and calculated Fourier limits of the input pulse (**d**) and output pulses for selected crystal positions (**e**, **f**).

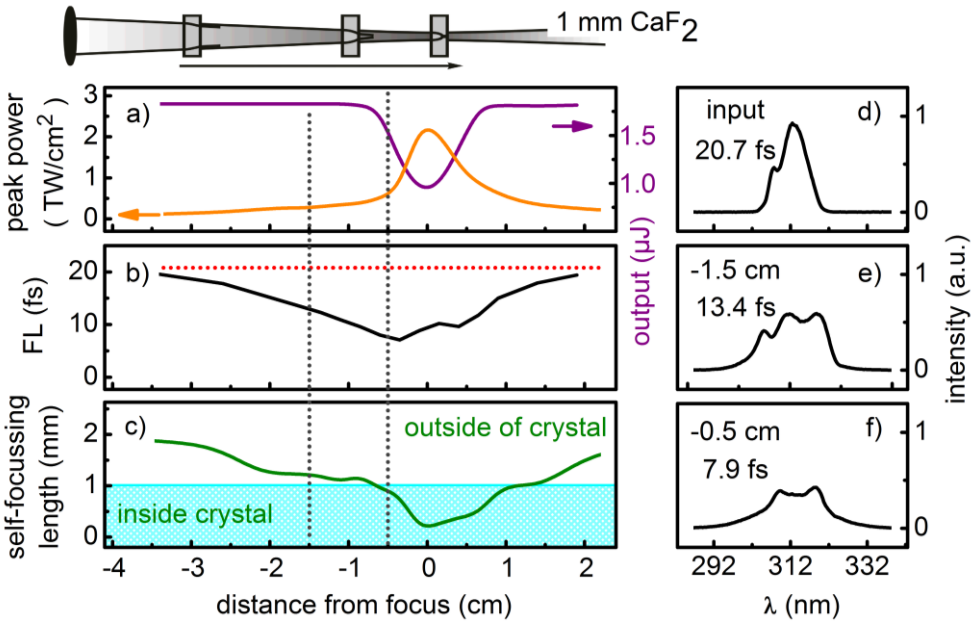

As commonly known for SPM of ultrashort laser pulses, we find that for a negatively chirped input pulse spectral narrowing occurs. For positively chirped pulses—the red components arrive before the blue ones—the output spectra are broadened [28]. Furthermore, for a specific positive chirp (measured to be about 260 fs^2) spectra with a square like shape which are symmetric about the central frequency can be generated. Pulses with such spectra correspond to the maximal broadening observed in the experiment while the beam profile still has a homogeneous spatial intensity distribution. These characteristics are advantageous for applications like pump-probe spectroscopy.

A simple way to vary and optimize the beam waist for a given crystal length and type and thus precisely adjust the peak intensity while using the full pulse energy is to move the crystal with respect to the focus of the UV beam. For this experiment we chose a 1 mm CaF_2 crystal which we move through the focus of a positively chirped pulse centered at 312 nm with a pulse energy of 1.96 µJ. The pulse length of the input pulse was measured by the UV-AC and found to be 63 fs. To determine the peak intensity at the entrance of the crystal we measured the size of the beam profile at the respective crystal positions with a CCD camera.

When moving the crystal towards the focus, the output energy remains constant and is equal to the input energy minus the losses due to reflection. A drop in the output energy occurs for crystal positions

within ± 1 cm of the focus. This resembles the profile of a *z-scan* and is therefore attributed to multi-photon absorption (MPA) (Figure 4a, purple line). For every position of the crystal we measure the spectrum and calculated the Fourier limit of the output pulse (Figure 4b). The Fourier limit steadily decreases from 20.6 fs (input spectrum) down to 8 fs when the crystal is placed near the focus. In addition to the above measurements the self-focal length was determined for all respective crystal positions (see Figure 4c). The calculations were done by taking into account the convergence or divergence caused by the focusing of the beam according to ref. [29]. For crystal positions within ± 1 cm of the focus we obtain a self-focal length smaller than the crystal thickness.

When comparing the three plots in Figure 4a–c, it becomes clear, that the MPA induced drop in output power accompanied by increased shot-to-shot fluctuations occurs when the self-focus lies within the crystal. Although in this regime the Fourier limit is well below 10 fs (Figure 4f), the beam undergoes beam breakup [14] accompanied with a strong divergence after the crystal. Furthermore, it shows enhanced fluctuations both in the spatial and spectral intensity distribution. As can be seen from Figure 4b, putting the self-focus just outside the crystal still delivers a sizable spectral broadening down to a Fourier limit of 13.4 fs (Figure 4e, 1.5 cm in front of the beam focus) without undesirable beam distortions and no loss in output energy. This regime delivers broadened pulses feasible for further applications and justifies the focusing assumptions made in our previous simulations. The resulting change in beam divergence due to the moderate self-focusing is then compensated for by the recollimation lens L2.

We investigated the spectral broadening by SPM in Sapphire, CaF_2, LiF_2 and fused silica crystals of various thicknesses between 0.5–4 mm. For each crystal we work in the regime with optimum SPM broadening as discussed before. In accordance with our theoretical simulations we find that crystals with a higher n_2 lead to broader pulses. With the smallest n_2, LiF_2 delivers the smallest broadening. Although sapphire has a larger n_2 than CaF_2, experimentally we observe slightly better broadening in CaF_2. Fused silica gives similar results to CaF_2. However impurities cause large beam scattering.

When trying different crystal thicknesses, we achieve larger broadening with thinner crystals as predicted by the theory. Best results are obtained for a 0.5 mm CaF_2 plate with a compressibility factor of ~2. However, the required tight focusing leads to unwanted multi-photon absorption and to beam distortions caused by the progressive deterioration of the crystal. Therefore we employ 1 and 2 mm thick CaF_2 disks for the compression experiments discussed below.

The experimentally achieved spectral broadening is generally about 25% less than the calculated values in section 2. We believe that this is due to the chirp of the pulses neglected in the calculations as well as the deviations of the beam profile from a Gaussian like intensity distribution, which lead to significant spatial distortions well before the self-focus length reaches the crystal length.

4.2. Compression of Self-Phase Modulated UV Pulses

The availability of sub-25 fs UV pulses generated by parametric amplification and conversion is in general limited in optic laboratories. More often the third harmonic of the Ti:sapphire system is used directly. To show that SPM can be used in such a configuration we employ the third harmonic of our CPA laser as the initial pulse. Pulses centered at 257 nm with an energy of about 1.5 μJ are spectrally broadened in a 1 mm thick CaF_2 crystal (Figure 5). The pulses are subsequently compressed by a UV-PC and then measured with the UV autocorrelator. When the full spatial beam profile is used, we

obtain a reduction of the initial Fourier limit of 80 fs down to 49 fs (Figure 5a). The measured autocorrelation trace (Figure 5b) shows that the Gaussian shape of the input pulse is conserved. The measured pulse length FWHM changes from 120 fs to 73 fs. When only the central part of the broadened pulses is selected by an aperture (pulse energy reduced by 30%), we obtain a much broader spectrum, as the spatial intensity is higher in the central part. The initial Fourier limit of 80 fs is shortened by nearly a factor of 3 down to 29 fs (Figure 5c). The measured pulse length is 50 fs (Figure 5d). The autocorrelation trace of the broadened pulses shows deviations from a Gaussian shape due to higher order dispersion which could be eliminated by a more sophisticated compression scheme.

Figure 5. Pulse compression of the 120 fs third harmonic of the CPA by SPM broadening in a 1 mm CaF_2 crystal and chirp compensation by a prism compressor. Dotted lines: input pulses; solid lines: spectrally broadened pulses. Spectra (**a**, **c**) and autocorrelation measurements (**b**, **d**) of the complete beam profile (blue lines) and the central part of the beam profile (red lines).

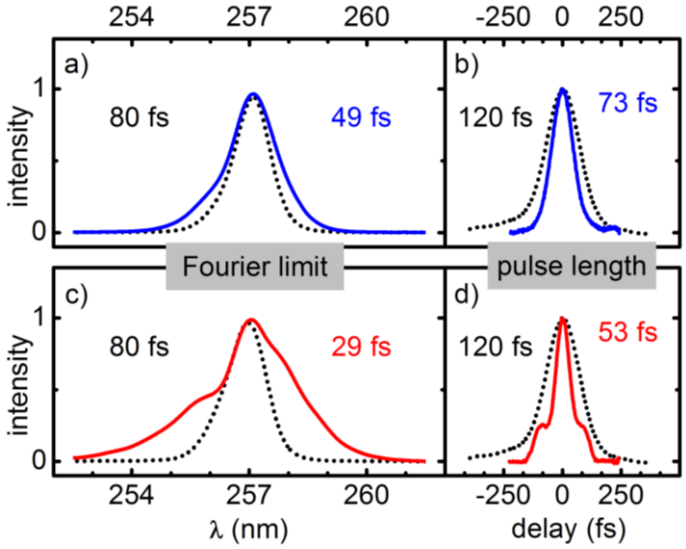

To show that the spectrally broadened pulses are compressible near to the Fourier limit, we employed an UV-PC in combination with an AOPDF to compensate for all orders of dispersion. We compressed SPM broadened pulses centered at 273 nm, generated by frequency doubling the output of the NOPA. Due to the low input energy of 0.7 μJ, we used a 2 mm thick CaF_2 crystal for broadening. The recollimation lens L2 was moved in order to compensate for the SPM induced change in beam divergence while the specific collimation requirements of the AOPDF are met (see ref. [1] for details). According to the literature [17], for a Gaussian beam profile SPM can lead to different frequency chirps across the transverse beam profile related to the spatial intensity profile. Therefore an aperture was used to block the outer parts of the beam. This reduced the pulse energy by about 20%. In order to compensate the chirp of the pulse, the spectral phase was measured by a ZAP-SPIDER and the obtained phase function was then recursively used in the AOPDF to completely flatten the phase. The results are shown in Figure 6a and b together with the temporal profile. We are able to obtain a flat spectral phase and the pulse length is reduced to 19.8 fs, which is close to the Fourier limit of 19 fs.

Figure 6. Pulse compression of sub-30 fs UV pulses generated by SHG (**a**, **b**) and SFG (**c**, **d**) of visible noncollinear parametric amplifier (NOPA) pulses by SPM broadening in a 2 mm (**a**, **b**) or 1 mm (**c**, **d**) CaF_2 crystal. Dotted lines: input pulses; solid lines: spectrally broadened pulses. Compression to a flat spectral and temporal phase (dashed lines) was achieved by the use of an acousto-optic pulse shaper and measured by a ZAP-SPIDER.

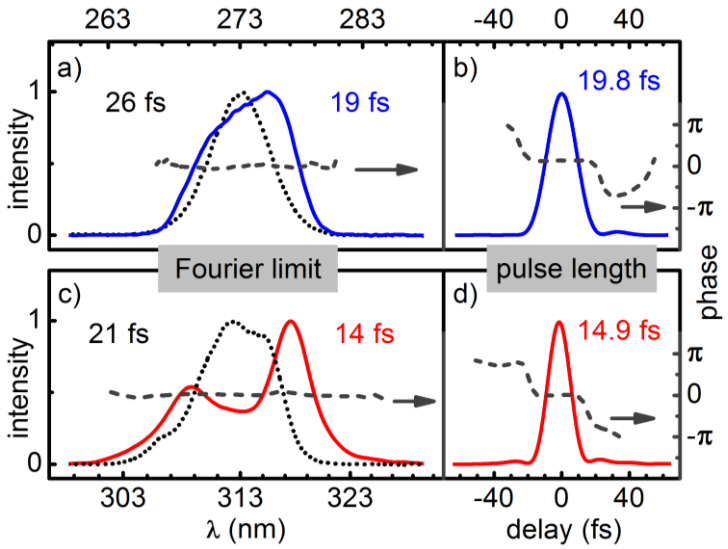

For the pulses with a central wavelength at 313 nm generated by sum frequency mixing the thickness of CaF_2 disk was changed to 1 mm as more energy (2.1 μJ) was available. The broadened pulses can again be compressed well below the input Fourier limit to 14.9 fs. This corresponds to a reduction of the pulse length by a factor of about 1.5 of the initial 22 fs long pulses. The energy after the PC was typically about 2 μJ and that of the compressed pulses after the shaper was about 200 nJ, which corresponds to the 10% overall efficiency of the shaper device. This is an order of magnitude higher compared to the output energies obtained previously with the AOPDF [1].

4.3. Effects of Self-Phase Modulation on the Beam Profile

To investigate the influence of SPM on the beam profile, we use the nearly perfect Gaussian shaped (M^2 ~1.05) third harmonic of a Yb:KYW laser (JenLas D2.fs JenOptik GmbH) as input. Pulses with an energy of 310 nJ and a duration of 173 fs are focused with a fused silica lens (f = 50 mm) into a 3 mm thick Sapphire disk. In analogy to the experiments in section 4, the disk is moved relative to the focus along the beam propagation to change the peak intensity and thus the amount of SPM. The beam profile is measured after a second recollimation lens.

When the disk is placed in the focus, we observe strong spectral broadening but severe beam profile distortions as the self-focus lies inside the crystal (see Figure 7b,f). The ring pattern is caused by the interference of spatial variations of self-phase modulation, as explained in refs. [30,31]. Moving the crystal away from the focus significantly reduces the distortions while the spectral broadening is still respectable. Already 2 mm after the focus a symmetric beam profile is obtained with a broadening that reduces the Fourier limit from 133 fs to 31 fs (see Figure 7d,h). The outer rings in the beam profile can be cut off with an aperture and the inner part then has a beam profile that is comparable with a

Gaussian beam. The analysis of the measured intensity profile (pink rings in Figure 7a–d) shows that this typically reduces the usable pulse energy to 30%.

Figure 7. Effect of SPM broadening on the beam profile and spectrum of the third harmonic (342 nm) of the Yb:KYW JenLas laser for various peak powers in a sapphire crystal. The Gaussian shaped (M^2 ~1.05) input profile and spectrum are shown in (**a**) and (**e**). The crystal was placed in the focus (**b**, **f**), 1 mm (**c**, **g**) and 2 mm (**d**, **h**) behind the focus. Pink circles indicate the beam energy for various apertures given in percent of the total energy. Fourier limits are given in blue.

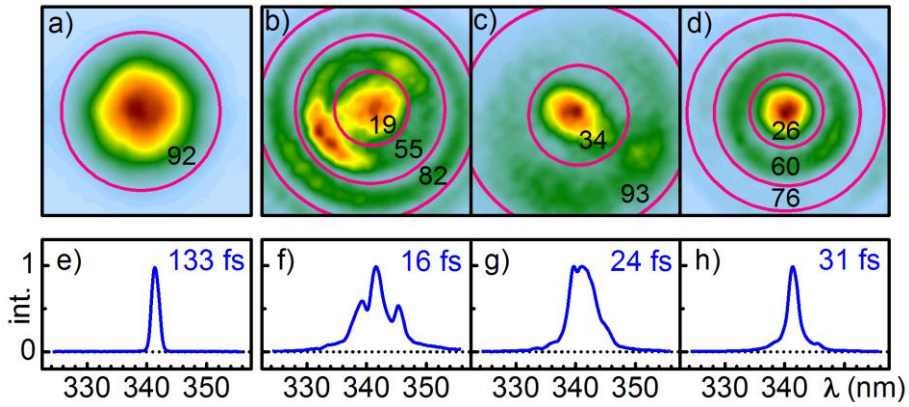

5. Application: Collinear Two-Dimensional Spectroscopy on Pyrene

Two-dimensional electronic spectroscopy can be regarded as an excitation frequency resolved pump-probe experiment. The measurable excitation window is determined by the spectral bandwidth of the excitation. Pulses with a spectral width large enough to cover the transitions to a multitude of vibronic or even electronic states are therefore an essential requirement. In contrast to 2D-Vis [32,33], where a bandwidth up to 150 nm can be reached, experimental realizations in the UV are so far limited to about 5 nm [34–36].

We therefore introduce SPM broadened pulses in our collinear 2D-UV experiment. The central wavelength is set to 312 nm to excited the S_2 $^1B_{2u}$←S_0 electronic transition of the test molecule pyrene. We use the same experimental parameters as determined above (1 mm CaF_2 and 2.5 μJ input energy) and achieve a FWHM bandwidth of 13 nm. This pulse spectrum is large enough to cover two vibronic bands of the absorption spectrum (see Figure 8c, black line).

The 2D experiment is carried out in a pulse shaper assisted pump-probe geometry, as described in refs. [34,37]. After the SPM stage the UV beam is compressed with a UV prism compressor and then split into a pump and a probe beam. The pump passes through the AOPDF, which is used to resolve the excitation frequency by generating phase locked double pulses and scanning their interpulse delay. Additionally the shaper compensates for the higher order chirp. Both pump and probe are focused inside a 120 μm thick flow cell as described in ref. [38]. The energy of the pump pulse in the cell is 63 nJ at a duration of the sub-pulses of 22 fs and the probe energy is about 2 nJ. After the sample cell the probe is spectrally resolved in a prism based CCD spectrometer. To increase the signal-to-noise ratio a fraction of the probe beam is used as a reference in a second prism based spectrometer [39].

Figure 8. SPM broadened UV pulses in collinear two-dimensional spectroscopy as pump and probe pulses. The absorptive signal resolves the pump-probe frequency correlation of the ground-state bleach of Pyrene in methanol for a population delay of 100 ps (**a**). The spectral intensity of the pulses (blue hashed areas) and the absorption spectrum of Pyrene (black line) are shown in the right (**b**) and lower side panel (**c**).

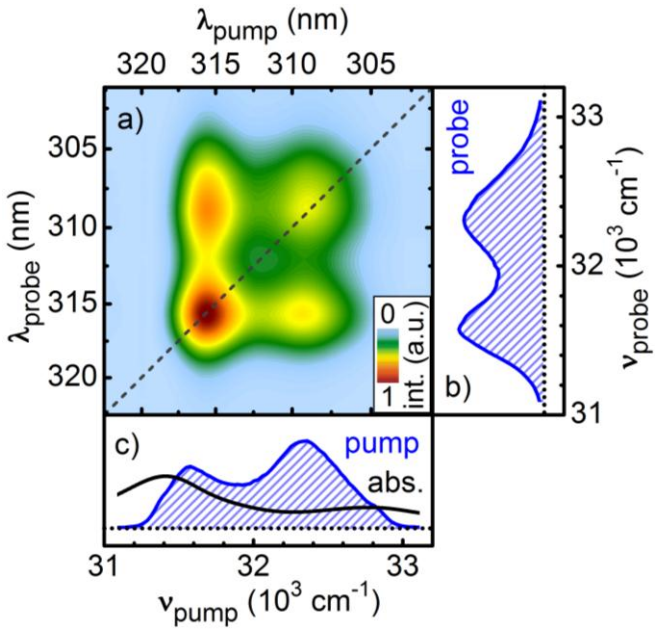

In Figure 8a the absorptive part of the 2D-UV measurement of pyrene dissolved in methanol is shown for a pump-probe delay of 100 ps. All signals in the 2D spectrum are positive and are assigned to ground state bleach contributions of pyrene. The two diagonal peaks correspond to the two vibronic bands in the absorption spectrum. In addition, due to the large spectral bandwidth of the pump pulses, the off-diagonal peaks describing the correlation between the vibronic bands are clearly resolved for the first time.

6. Summary and Perspectives

In this work we have shown that SPM in bulk materials can be readily used to broaden the spectrum of μJ femtosecond UV pulses and to reduce the pulse length. The broadening stage is most conveniently incorporated into an optical setup by using two lenses or spherical mirrors with a slight off-axis geometry and a crystal plate and thus relies only on components present in most ultrafast spectroscopy laboratories. There is no need for a specially designed fiber or meter long gas cells.

By focusing the UV beam into the crystal the high pulse intensity leads to self-phase modulation and self-focusing. In contrast to techniques using gas filled cells [10] where self-focusing induced filamentation is a prerequisite for broadening, we find that the self-focus should be kept just outside the crystal, about 25% of the crystal thickness. This leads to broadening without serious beam distortions and to no beam break-up. Under this condition the pulse energy is nearly conserved as multi-photon absorption is minimized. It allows a maximum achievable broadening of up to a factor of three. Thin crystals with high nonlinearity in conjunction with reasonably tight focusing are found optimal as this keeps the negative influence of the strong group delay dispersion in the UV and the

associated pulse lengthening to a minimum. A slight up chirp of the input pulse helps to enhance the broadening. Experimentally we find that a few millimeter thick CaF_2 crystal delivers the best results in terms of broadening and transmission efficiency. Once the pulse energy and length, and the crystal thickness is known, the beam size at the plate can be determined from the well known formula for the self-focal length.

Temporal compression of the broadened pulses is done with a simple prism compressor for the regime down to about 50 fs. A compression by a factor of two to three is demonstrated. For even shorter pulses an AOPDF (DAZZLER) is added for the compensation of higher order chirp components. For pulses at 312 nm and 273 nm this allowed for a near Fourier limited compression down to 15 fs and 20 fs. If the pulses do not have to be perfectly compressed, even larger spectral broadening can be achieved.

The beam profile is quite acceptable for spectroscopic applications. The use of a circular aperture to select the central part of beam is often helpful. Still many tens of percent of the pulse energy can be utilized with the resulting new-Gaussian transversal profile.

We expect that SPM in bulk material can be employed for a large range of energies as the focusing conditions can be adapted for pulses less than a μJ to tens of μJ. Although here we only investigated the broadening of 120 and 25 fs input pulses, we envision that pulses at various pulse length can be broadened and compressed. The method likely will be best suited to situations where just an extra factor around two is needed for a successful experiment. This is, to our own experience, quite often the case.

Acknowledgments

We thank Thomas Ganz for valuable discussions and suggestions. This work was supported by the Austrian Science Fund within the framework of the Special Research Program F16 (Advanced Light Sources), by the SFB749 and by the DFG-Cluster of Excellence: Munich-Centre for Advanced Photonics.

References

1. Krebs, N.; Probst, R.A.; Riedle, E. Sub-20 fs pulses shaped directly in the UV by an acousto-optic programmable dispersive filter. *Opt. Express* **2010**, *18*, 6164–6171.
2. Homann, C.; Lang, P.; Riedle, E. Generation of 30 fs pulses tunable from 189 to 240 nm with an all-solid-state setup. *J. Opt. Soc. Am. B* **2012**, *29*, 2765–2769.
3. Baum, P.; Lochbrunner, S.; Riedle, E. Generation of tunable 7-fs ultraviolet pulses: achromatic phase matching and chirp management. *Appl. Phys. B* **2004**, *79*, 1027–1032.
4. Zhao, B.; Jiang, Y.; Sueda, K.; Miyanaga, N.; Kobayashi, T. Sub-15fs ultraviolet pulses generated by achromatic phase-matching sum-frequency mixing. *Opt. Express* **2009**, *17*, 17711–17714.
5. Kida, Y.; Liu, J.; Kobayashi, T. Single 10-fs deep-ultraviolet pulses generated by broadband four-wave mixing and high-order dispersion compensation. *Appl. Phys. B* **2011**, *105*, 675–679.
6. Backus, S.; Peatross, J.; Zeek, Z.; Rundquist, A.; Taft, G.; Murnane, M.M.; Kapteyn, H.C. 16-fs, 1-μJ ultraviolet pulses generated by third-harmonic conversion in air. *Opt. Lett.* **1996**, *21*, 665–667.
7. Reiter, F.; Graf, U.; Schultze, M.; Schweinberger, W.; Schröder, H.; Karpowicz, N.; Azzeer, A.M.; Kienberger, R.; Krausz, F.; Goulielmakis, E. Generation of sub-3 fs pulses in the deep ultraviolet. *Opt. Lett.* **2010**, *35*, 2248–2250.

8. Noack, F.; Steinkellner, O.; Tzankov, P.; Ritze, H.-H.; Herrmann, J.; Kida, Y. Generation of sub-30 fs ultraviolet Raman induced phase modulation in nitrogen. *Opt. Express* **2005**, *13*, 2467–2474.
9. Durfee III, C.G.; Backus, S.; Kapteyn, H.C.; Murnane, M.M. Intense 8-fs pulse generation in the deep ultraviolet. *Opt. Lett.* **1999**, *24*, 697–699.
10. Ghotbi, M.; Trabs, P.; Beutler, M. Generation of high-energy, sub-20-fs pulses in the deep ultraviolet by using spectral broadening during filamentation in argon. *Opt. Lett.* **2011**, *36*, 463–465.
11. Nagy, T.; Simon, P. Generation of 200-μJ, sub-25-fs deep-UV pulses using noble-gas-filled hollow fiber. *Opt. Lett.* **2009**, *34*, 2300–2302.
12. Ganz, T.; Pervak, V.; Apolonski, A.; Baum, P. 16 fs, 350 nJ pulses at 5 MHz repetition rate delivered by chirped pulse compression in fibers. *Opt. Lett.* **2011**, *36*, 1107–1109.
13. Alfano, R.R.; Shapiro, S.L. Observation of self-phase modulation and small-scale filaments in crystals and glasses. *Phys. Rev. Lett.* **1970**, *24*, 592–594.
14. Hata, K.; Watanabe, M.; Watanabe, S. Nonlinear Processes in UV Optical Materials. *Appl. Phys. B* **1990**, *50*, 55–59.
15. Spanner, M.; Ivanov, M.Y.; Kalosha, V.; Hermann, J.; Wiersma, D.A.; Pshenichnikov, M. Tunable optimal compression of ultrabroadband pulses by cross-phase modulation. *Opt. Lett.* **2003**, *28*, 749–751.
16. Petrov, V.; Rudolph, W.; Wilhelmi, B. Compression of high-energy femtosecond light pulses by self-phase modulation in bulk media. *J. Mod. Opt.* **1989**, *36*, 587–595.
17. Rolland, C.; Corkum, P.B. Compression of high-power optical pulses. *J. Opt. Soc. Am. B* **1988**, *5*, 641–647.
18. Tzortzakis, S.; Lamouroux, B.; Chiron, A.; Franco, M.; Prade, B.; Mysyrowicz, A.; Moustaizis, S.D. Nonlinear propagation of subpicosecond ultraviolet laser pulses in air. *Opt. Lett.* **2000**, *25*, 1270–1272.
19. Kim, Y.P.; Hutchinson, M.H.R. Intensity-Induced Nonlinear Effects in UV Window Materials. *Appl. Phys. B* **1989**, *49*, 469–478.
20. Diels, J.-C.; Rudolph, W. *Ultrashort Laser Pulse Phenomena*; Academic Press: London, UK, 1995.
21. Fibich, G.; Gaeta, A.L. Critical power for self-focusing in bulk media and in hollow waveguides. *Opt. Lett.* **2000**, *25*, 335–337.
22. Schmidt, B.; Hacker, M.; Stobrawa, G.; Feurer, T. LAB2-A Virtual Femtosecond Laser Lab. Available online: http://www.lab2.de (accessed on 1 September 2012).
23. DeSalvo, R.; Said, A.A.; Hagan, D.J.; Van Stryland, E.W.; Sheik-Bahae, M. Infrared to Ultraviolet Measurements of Two-Photon Absorption an n_2 in Wide Bandgap Solids. *IEEE J. Quantum Electron.* **1996**, *32*, 1324–1333.
24. Kozma, I.Z.; Baum, P.; Lochbrunner, S.; Riedle, E. Widely tunable sub-30 fs ultraviolet pulses by chirped sum frequency mixing. *Opt. Express* **2003**, *11*, 3110–3115.
25. Coudreau, S.; Kaplan, D.; Tournois, P. Ultraviolet acousto-optic programmable dispersive filter laser pulse shaping in KDP. *Opt. Lett.* **2006**, *31*, 1899–1901.
26. Homann, C.; Krebs, N.; Riedle, E. Convenient pulse length measurement of sub-20-fs pulses down to the deep UV via two-photon absorption in bulk material. *Appl. Phys. B* **2011**, *104*, 783–791.
27. Baum, P.; Lochbrunner, S.; Riedle, E. Zero-additional-phase SPIDER: full characterization of visible and sub-20-fs ultraviolet pulses. *Opt. Lett.* **2004**, *29*, 210–212.

28. Oberthaler, M.; Höpfel, R.A. Special narrowing of ultrashort laser pulses by self-phase modulation in optical fibers. *Appl. Phy. Lett.* **1993**, *63*, 1017–1019.
29. Yariv, A. *Quantum Electronics*, 3rd ed.; John Wiley & Sons: New York, NY, USA, 1988; p. 487.
30. Nascimento, C.M.; Alencar, M.A.R.C.; Chávez-Cerda, S.; da Silva, M.G.A.; Meneghetti, M.R.; Hickmann, J.M. Experimental demonstration of novel effects on the far-field diffraction patterns of a Gaussian beam in a Kerr medium. *J. Opt. A: Pure Appl. Opt.* **2006**, *8*, 947–951.
31. Garcia Ramirez, E.V.; Arroyo Carrasco, M.L.; Mendez Otero, M.M.; ChavezCerda, S.; Iturbe Castillo, M.D. Far field intensity distributions due to spatial selfphase modulation of a Gaussian beam by a thin nonlocal nonlinear media. *Opt. Express* **2010**, *18*, 22067–22079.
32. Christensson, N.; Milota, F.; Nemeth, A.; Pugliesi, I.; Riedle, E.; Sperling, J.; Pullerits, T.; Kauffmann, H.F.; Hauer, J. Electronic Double-Quantum Coherences and Their Impact on Ultrafast Spectroscopy: The Example of β-Carotene. *J. Phys. Chem. Lett.* **2010**, *1*, 3366–3370.
33. Bixner, O.; Lukeš, V.; Maňcal, T.; Hauer, J.; Milota, F.; Fischer, M.; Pugliesi, I.; Bradler, M.; Schmid, W.; Riedle, E.; *et al*. Ultrafast photo-induced charge transfer unveiled by two-dimensional electronic spectroscopy. *J. Chem. Phys.* **2012**, *136*, 204503.
34. Tseng, C.-H.; Matsika, S.; Weinacht, T.C. Two-Dimensional Ultrafast Fourier Transform Spectroscopy in the Deep Ultraviolet. *Opt. Express* **2009**, *17*, 18788–18793.
35. Selig, U.; Schleussner, C.-F.; Foerster, M.; Langhojer, F.; Nuernberger, P.; Brixner, T. Coherent two-dimensional ultraviolet spectroscopy in fully noncollinear geometry. *Opt. Lett.* **2011**, *35*, 4178–4180.
36. West, B.A.; Womick, J.M.; Moran, A.M. Probing Ultrafast Dynamics in Adenine With Mid-UV Four-Wave Mixing Spectroscopies. *J. Phys. Chem. A* **2011**, *115*, 8630–8637.
37. Shim, S.-H.; Zanni, M.T. How to turn your pump–probe instrument into a multidimensional spectrometer: 2D IR and Vis spectroscopies via pulse shaping. *Phys. Chem. Chem. Phys.* **2009**, *11*, 748–761.
38. Megerle, U.; Pugliesi, I.; Schriever, C.; Sailer, C.F.; Riedle, E. Sub-50 fs broadband absorption spectroscopy with tunable excitation: putting the analysis of ultrafast molecular dynamics on solid ground. *Appl. Phys. B* **2009**, *96*, 215–231.
39. Dobryakov, A.L.; Kovalenko, S.A.; Weigel, A.; Pérez-Lustres, J.L.; Lange, J.; Müller, A.; Ernsting, N.P. Femtosecond pump/supercontinuum-probe spectroscopy: Optimized setup and signal analysis for sinlge shot spectral referencing. *Rev. Sci. Instrum.* **2010**, *81*, 113106.

Appendix B.3

Convenient pulse length measurement of sub-20-fs pulses down to the deep UV via two-photon absorption in bulk material

C. Homann, N. Krebs, and E. Riedle

Appl. Phys. B **104**, 783 - 791 (2011)

Appl Phys B (2011) 104:783–791
DOI 10.1007/s00340-011-4683-0

Applied Physics B
Lasers and Optics

Convenient pulse length measurement of sub-20-fs pulses down to the deep UV via two-photon absorption in bulk material

C. Homann · N. Krebs · E. Riedle

Received: 18 March 2011 / Revised version: 15 June 2011 / Published online: 6 August 2011

Abstract The beam attenuation by two-photon absorption in thin crystals and glass plates is utilized for directly measuring the intensity autocorrelation of UV femtosecond pulses without the need for an auxiliary pulse. We give a full description of the newly developed setup for operation from the blue down to the deep UV. The conditions that must be met to achieve reliable measurements are investigated. The choice of the two-photon-absorbing material governs the attainable wavelength range, the material thickness determines the shortest pulse that can be reliably characterized and high intensities influence the derived pulse duration due to saturation effects. The performance of the UV autocorrelator is demonstrated for pulses with durations below 20 fs, with energies of 3 nJ and with central wavelengths from the visible down to 195 nm. 2-Hz update rates are achieved at the 1-kHz repetition rate of the laser. The wavelength dependence of the two-photon-absorption coefficient of BBO is determined by z-scan measurements and we find that it decreases much faster at longer wavelengths than is expected from the linear absorption spectrum.

1 Introduction

Ultra-short pulses in the UV are essential prerequisites for the investigation of the primary processes in physics, chemistry and biology. Particularly small molecules do not absorb in the visible, and two- or multi-photon excitation can lead to unwanted complexity in the interpretation. Tunable UV pulses with sufficient energy of a few μJ can be readily generated by second-harmonic generation (SHG) or sum-frequency generation (SFG) of tunable visible pulses generated in noncollinear parametric amplifiers (NOPAs) in thin nonlinear crystals [1, 2]. With some care, even pulse lengths below 20 fs can be reached in the UV [3, 4].

The characterization of the UV pulses turns out to be more demanding than the generation. The method of phase-matched second-harmonic autocorrelation in nonlinear crystals—intensity or fringe resolved—that is widely used in the visible and near infrared cannot be used in the UV due to the lack of suitable crystals. Even if new crystals were found, the resulting second harmonic would be in the vacuum UV (VUV) and therefore hard to handle.

A viable alternative is SFG or difference-frequency generation (DFG). This does, however, require an additional auxiliary pulse of comparable shortness and known duration. From a practical standpoint, any mixing scheme is cumbersome as the time zero has to be regained after any alteration of the optical system.

When a full characterization of the pulse and its spectral and temporal phases is needed, this effort is justified and spectral phase interferometry for direct electric-field reconstruction (SPIDER) [5, 6] and X-FROG (cross-correlation frequency-resolved optical gating) [7] are well established. Recently, a shaper-assisted cross-correlation setup was introduced that is free of external references, additional pulses and a spectrometer, which employs a two-dimensional shaper that works in the UV and uses a solar blind multiplier as nonlinear detector [8].

However, for spectroscopic work and day to day application a much simpler setup is needed to optimally compress the UV pulses and monitor the length for the subsequent interpretation of the data. A number of techniques have been

C. Homann · N. Krebs · E. Riedle (✉)
Lehrstuhl für BioMolekulare Optik,
Ludwig-Maximilians-Universität (LMU), Oettingenstraße 67,
80538 München, Germany
e-mail: riedle@physik.lmu.de
Fax: +49-89-21809202

tested to directly characterize UV pulses. Multiple FROG techniques like transient-grating (TG), self-diffraction (SD) and polarization gating (PG) FROG have successfully been transferred to the UV spectral region [9, 10]. If the diffracted beam is not analyzed in a spectrometer, the TG- or SD-FROG signal renders a third-order autocorrelation and the desired information on the pulse length. We notice that these methods are not often invoked in spectroscopic publications and we can only speculate that too high a pulse energy is required or the beam shape influences the measured value of the pulse length.

Since $\chi^{(2)}$ processes are not attractive for the UV, several techniques exploiting two- or multi-photon absorption as nonlinear process have been investigated for the UV spectral domain. They can be arranged in two categories: measuring the generated charge or induced fluorescence, or measuring the depletion—both in dependence on the temporal overlap of two replicas of the UV pulse. The first approach has been realized with CsI as photocathode in a photomultiplier tube, but with the problem of suppressing the one-photon absorption background in the photomultiplier tube material [11]. In fused silica, microstructured electrodes on top of the substrate are required, that are complex to manufacture, together with a high bias voltage that leads to a high dark current [12]. Recently, diamond pin diodes have been developed, that allow pulse length measurements down to a wavelength of 225 nm, but again with a complex fabrication procedure and limited durability [13].

For gas-phase and in particular molecular beam experiments, opportunities like the two-photon induced fluorescence of xenon excimers for measuring sub-picosecond pulse durations at 248 nm [14] or the ionization of rare gases [15] arise. These methods are, however, not easily incorporated into typical laser setups.

Two-photon absorption (TPA) of even modest energy femtosecond pulses is present in liquids and bulk materials if the photon energy is larger than half the absorption edge. To utilize this for autocorrelation measurements, a strong pump and a weak probe beam, both derived from the pulse to be characterized, are spatially overlapped in the medium. Both beams are individually depleted by TPA; however at temporal overlap an additional contribution due to TPA with one photon from each beam arises. This two-beam contribution creates the autocorrelation signal.

In solution, an autocorrelation trace of 180-fs pulses in a 1-mm water cell at 282 nm [16] and even 30-fs pulses in a 50-µm water film have been reported [17]. In 1991, Dadap et al. [18] successfully demonstrated the applicability of TPA in diamond for pulse length measurements. They showed autocorrelation traces of 180-fs pulses at 310 nm and claimed that their method is applicable in a wavelength range from 220 nm to 550 nm.

Despite these promising reports, TPA depletion has not been widely used. Traditionally, the background-free signal of SHG seems to have been important for the fluctuating sources of early days and insensitive detection. Now, laser systems and parametric converters as well as SHG schemes are available with pulse fluctuation below 1% and high enough repetition rate to allow for rapid data taking. Transient spectroscopy has matured greatly and readily allows us to detect broadband transmission changes below 10^{-4} [19, 20] and even 10^{-6} for single detection wavelengths [21].

In this work we report on our investigation about the suitability of different materials for TPA depletion, the experimental conditions needed to perform reliable measurements and the methods used for evaluation of the raw data. The resulting UV autocorrelator is found to be a highly stable and simple device capable of characterizing pulses from the blue down into the VUV, with durations shorter than 20 fs and for nJ pulse energies. Practical guidelines for the implementation are given at the end.

2 Experimental setup and design considerations

The layout of the UV autocorrelator is shown in Fig. 1a. It is similar to standard autocorrelators for the visible or near infrared. However, no nonlinear crystal for frequency mixing

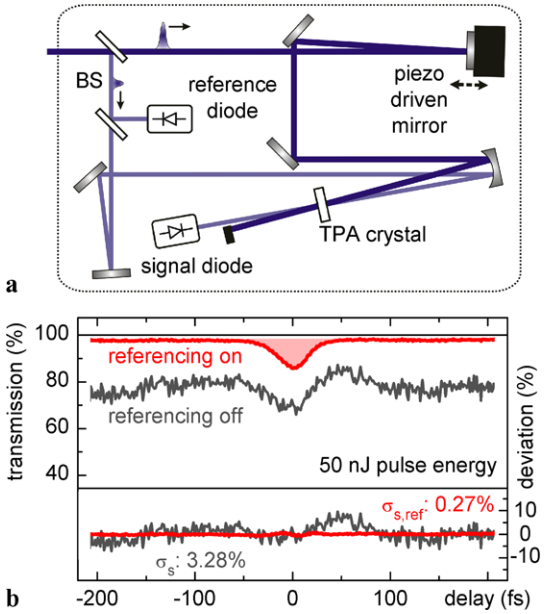

Fig. 1 (**a**) Layout of the autocorrelator setup. BS: beam splitter (fused silica, 160 µm). (**b**) Typical measured signal (single scan of 0.5-s duration, each individual laser shot detected and shown) of a pulse with an energy of 50 nJ and a central wavelength of 277 nm, with (*red curve*) and without (*grey curve*) using a second diode for pulse energy referencing. The *lower panel* shows the significant reduction of noise by referencing (Gaussian fit subtracted from the measured data)

of two pulse replicas is used. Instead, the attenuation at temporal overlap of the weaker of the two beams is monitored.

To generate the pump and probe pulses, the input beam is split by a thin fused silica cover slip (thickness 160 µm, Esco Products Inc.), which introduces only a negligible amount of dispersion for typical experimental conditions. The front-side reflection of the cover slip is used as probe pulse. It is temporally and also spatially separated from the back-side reflection at the measurement point. However, the back-side reflection doubles the total signal from the photodiode while the signal due to the two-photon interaction is not influenced by the second reflection due to the lack of temporal overlap. One might therefore consider a wedged substrate. We prefer to allow for this effect in the data evaluation.

Since the depletion in the probe beam due to TPA of one pump and one probe photon is proportional to the pump pulse intensity, a strong pump pulse is desirable. When using s-polarized light, the reflection at 45° off the fused silica cover slip yields a favorable energy ratio of ∼15 : 1 for pump and probe out of the total available pulse. An identical cover slip in the path of the reflected probe pulses compensates for the dispersion in the path of the pump pulses. The reflection off this plate is used for referencing (see Fig. 1a). With p-polarized light, the energy ratio between pump and probe increases to ∼100 : 1, which might lead to hardly detectable probe and reference pulses. In this case, the use of appropriately coated beam splitters or an angle far from Brewster's angle might be preferential.

The delay between the pump and probe pulses is controlled by a piezo-based delay line, yielding a maximum delay of approximately 500 fs, which was calibrated interferometrically with a HeNe laser [22]. The piezo position is scanned via a sawtooth-shaped voltage with a frequency of 2 Hz, generated by a home-built circuit. An additional manual delay line is helpful for initially adjusting the temporal overlap. Both pulses are then focused by the same spherical mirror (radius of curvature 500 mm) into the two-photon-absorbing medium.

The depleted probe beam as well as the reference beam are detected on large-area (5×5 mm^2) photodiodes (S1227-66BQ; Hamamatsu Photonics K.K.) integrated in a home-built amplifier circuit [21]. The large area ensures that the whole beam profiles are measured without the need for additional focusing optics even for slight self focusing or beam distortion. The spectrally integrated detection avoids problems with a possible frequency redistribution due to cross-phase modulation. The photodiodes and the piezo driver voltage are read out simultaneously by a multi-channel digitizer board (NI 6132; National Instruments) for each laser shot and displayed without smoothing or next-neighbor averaging.

Tunable UV pulses for the test of the autocorrelator were generated by frequency doubling the output of a single-stage NOPA pumped by a 1-kHz Ti:Sa amplifier system (CPA 2001; Clark MXR). The pulses were pre-compressed in the visible by a pair of fused silica Brewster prisms [3] and frequency doubled in BBO crystals with thicknesses between 30 µm and 100 µm depending on the spectral width of the particular visible pulses. For wavelengths below 225 nm, the primary UV pulses were mixed with the fundamental Ti:Sa pulses in a second BBO crystal. To adjust the UV pulse energy, a $\lambda/2$ retarder is inserted in front of the doubling crystal. Before entering the autocorrelator setup, the pulses are reflected off three dielectric mirrors to strongly suppress the visible background.

3 Results and discussion

Figure 1b shows a typical single scan from 400 consecutive laser shots, recorded with our setup for input pulses with an energy of 50 nJ at a central wavelength of 277 nm measured in a BBO crystal (134-µm thick) as the two-photon-absorbing medium. BBO was chosen for its availability in thin samples and the high TPA coefficient. The depleted probe beam, detected on the signal diode, is subject to pulse energy fluctuations, that can be similar in magnitude to the autocorrelation depletion signal (grey curve). By dividing the signal through the pulse energy reference, we compensate for these fluctuations to first order. This enhances the signal to noise ratio by more than an order of magnitude (red curve) from a standard deviation of $\sigma_s = 3.28\%$ to $\sigma_{s,ref} = 0.27\%$, as can be seen after subtracting a Gaussian function from the measured data (lower panel in Fig. 1b). As a consequence, a maximum transmission change of less than 1% is sufficient in single-scan mode for a usable autocorrelation. An even better noise level can be obtained by modest signal averaging over repeated scans and the detectivity is accordingly increased to the 1‰ range, well below the pump laser noise. We find it important that the full beam profiles are detected on each diode and that the diodes are both operated in their linear response regime.

A slight asymmetry in the autocorrelation trace is observed as depletion offset of about 1% when the pump precedes the probe. This is due to long-living free-carrier absorption and the different intensities in the pump and the probe beams [23]. This offset is negligible for the practical application of the autocorrelator.

At high energies, we additionally see a self-diffracted beam in the direction $2\vec{k}_{pump} - \vec{k}_{probe}$. In our case, when working at energies below 100 nJ, the diffracted energy is so low that it does not disturb the depletion autocorrelation measurement. A possibility to avoid the diffracted beam is to rotate the polarization of either pump or probe beam so that their polarizations are orthogonal. However, this also reduces the two-beam TPA cross section and hence the depletion signal.

To retrieve a precise value for the pulse length from the measured autocorrelation trace, we perform a deconvolution based on the following theoretical considerations.

Since the one-photon absorption can be neglected, the coupled differential equations describing the decrease of the pump intensity I_{pump} and the probe intensity I_{probe} due to TPA after propagating the distance x read

$$\frac{dI_{\mathrm{pump}}}{dx} = -\beta I_{\mathrm{pump}}^2 - \beta I_{\mathrm{pump}} I_{\mathrm{probe}}, \tag{1}$$

$$\frac{dI_{\mathrm{probe}}}{dx} = -\beta I_{\mathrm{probe}}^2 - \beta I_{\mathrm{pump}} I_{\mathrm{probe}}, \tag{2}$$

with the TPA coefficient β. The attenuation of the pump/probe pulse is due to a delay time independent term from the TPA of the pulse itself and the delay time dependent interaction of both pulses. For input pulses with the spatial and temporal profile described by $I^0(r,t)$, e.g. Gaussian input pulses with pulse length τ (FWHM) and beam waist w_0 : $I^0(r,t) = I_0 \exp(-4\ln 2 t^2/\tau^2 - 2r^2/w_0^2)$, the solution for I_{probe} is given by

$$I_{\mathrm{probe}}(x,r,t,\Delta t) = \frac{I^0_{\mathrm{probe}}(r,t)}{1+\beta x (I^0_{\mathrm{pump}}(r,t-\Delta t) + I^0_{\mathrm{probe}}(r,t))}, \tag{3}$$

with the pump–probe delay Δt. In the autocorrelation measurement, the time delay Δt is scanned while the probe pulse is integrated in space, time and frequency by the photodiode. For Gaussian pulses, this leads to an autocorrelation trace with a width depending on the pulse length τ and the intensity of the input pulses. For low intensities, the trace can be deconvoluted with a factor of $\sqrt{2}$, according to the procedure in SHG autocorrelation [24]. A derivation of the asymptotic equality of the TPA depletion curve and the autocorrelation function is given in [25]. For higher intensities, a broadening of the autocorrelation trace is predicted as well, as seen in the experiment.

Figure 2a shows the increase of the measured autocorrelation width by 19% when the input pulse energy is increased to a maximum of 200 nJ, corresponding to a pump pulse peak intensity of 470 GW/cm^2 and a maximum probe depletion of 68%. To compare the measurements with theory, we calculated the autocorrelation traces by numerically integrating (3) for different pump–probe delays Δt and using the experimentally determined values for β = 0.85 cm/GW (see Sect. 4), crystal thickness 173 µm (BBO) and surface reflection losses of 1.05%. The retrieved autocorrelation widths (red line in Fig. 2a) show excellent agreement with the measured ones (circles in Fig. 2a) for a pulse length τ of 22 fs.

As a rule of thumb, we found that the measured autocorrelation width can be deconvoluted with a factor of $\sqrt{2}$ when

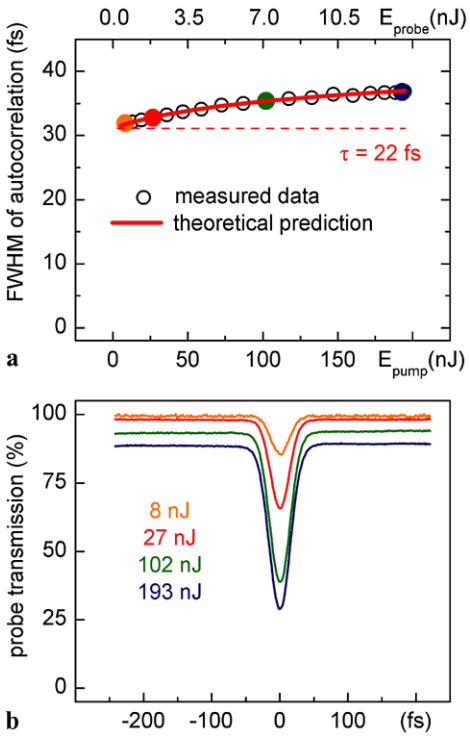

Fig. 2 (**a**) Measured and calculated widths of the depletion autocorrelation signal with increasing pulse energy. For probe transmission changes smaller than 15%, the pulses can be deconvoluted with good accuracy by a factor of $\sqrt{2}$ for Gaussian pulses. (**b**) Shows selected traces at different pump energies; the baseline offset is due to the TPA of the probe beam itself

the transmission change is smaller than 15%, and an overestimate of 5% is accepted. We define the transmission change as the probe depletion at zero time delay normalized by the total signal from the probe pulse far from temporal overlap. The stated values for the transmission change are corrected to only the front-side reflection.

In phase-matched SHG autocorrelation, the finite phase-matching bandwidth can limit the precision of the measurement. This is particularly important for chirped pulses, as the extreme spectral components are suppressed and too short a value is determined [26]. In the TPA depletion, such a limitation is not present. The only consequence of the material dispersion that can lead to distorted pulse length measurements is the pulse lengthening introduced by the TPA medium.

A first-order approximation of the pulse duration after propagating through a medium of length L for an initially Fourier-limited Gaussian pulse with pulse duration τ_0 and central wavelength λ_c is given by

$$\tau = \tau_0 \sqrt{1 + \left(\frac{4\ln 2 L \lambda_c^3}{2\pi c^2 \tau_0^2} \frac{d^2 n(\lambda)}{d\lambda^2}\bigg|_{\lambda_c} \right)^2} \tag{4}$$

(compare e.g. [27]), with c being the speed of light in vacuum. To help estimating the expected pulse lengthening

with this formula, calculated values for the second derivative of the refractive index with respect to the wavelength are shown for selected materials in Fig. 3a. Figure 3b indicates down to which minimal pulse duration the respective materials with a thickness of 200 µm can be used when accepting a maximal pulse lengthening of 20%. For example, when working at a central wavelength of 300 nm and using a 200-µm-thick BBO crystal as TPA medium, pulses with a Fourier limit of 18 fs (or larger) are lengthened by (less than) 3.6 fs. If even shorter pulses are to be measured, a material with less dispersion (e.g. sapphire or fused silica) has to be used, or a thinner crystal is needed, however at the expense of a decreasing transmission change.

Apart from their differing dispersion, the various materials vary strongly in the strength and wavelength dependence of their β values, which makes them well suited for selected intensity regimes and wavelength regions. As a general rule, β increases with decreasing wavelength. Each material can only be used above the one-photon absorption edge—indicated in Fig. 3 with the dashed vertical lines. We summarize the relative merit of the various TPA materials tested in our investigations in Fig. 4. The raw measured signals were scaled according to the varying pulse length, energy and focal spot size.

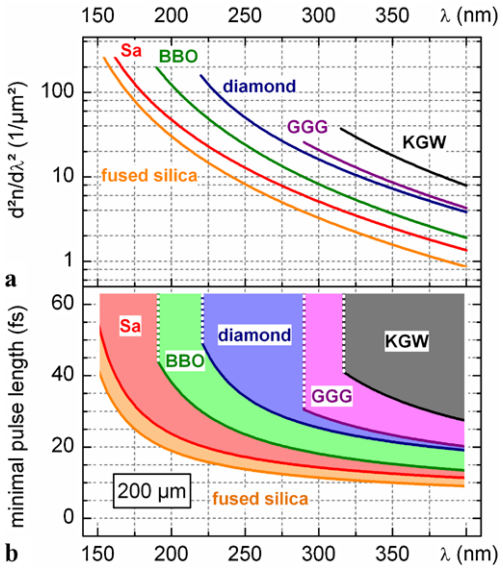

Fig. 3 (**a**) Calculated second derivatives of the refractive index with respect to wavelength for different materials to estimate the pulse lengthening due to dispersion with (4). (**b**) The *lines* indicate the calculated Fourier limit of pulses which are elongated by 20% due to dispersion in materials with a thickness of 200 µm. The *filled areas* mark the conditions where the pulse lengthening is below 20%

BBO is highly suited for measurements in the wide wavelength region from 195 nm up to 330 nm, and has the advantage that it is often available in a variety of thicknesses in laser laboratories. Please note that the crystal cut is of no relevance, as the TPA depletion autocorrelator does not rely on phase matching but on the high β that only depends weakly on the orientation. We checked this fact by comparing the TPA depletion of the more common β-BBO with similar size α-BBO crystals and found no significant difference.

In the course of our measurements, we found that sapphire shows a very similar transmission change compared to BBO in the investigated wavelength region, but with considerably smaller dispersion. However, sufficiently thin samples might not be at hand easily. Fused silica shows even less dispersion; however, only very small transmission changes are observed due to its low β value [28]. We found YAG samples that show a good TPA strength at 250 and 300 nm, but there are doubts about the UV transmission of YAG. The dispersion of YAG is even somewhat lower in the deep UV than that of BBO.

For pulses with central wavelengths above 330 nm, materials with a smaller band gap are needed, as the TPA strength of the materials discussed so far starts to vanish (see Fig. 4). We found that diamond is well suited for measurements up to about 360 nm and potassium gadolinium tungstate (KGW) extends the accessible wavelength region even further into the visible. KGW shows a very large transmission change due to its unusually high β [29]. It is therefore advantageous for primarily finding the autocorrelation sig-

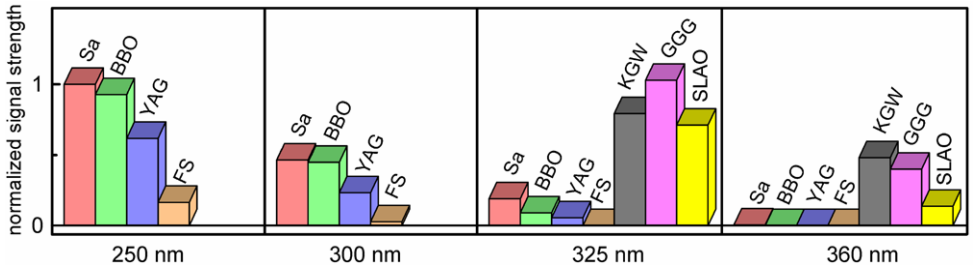

Fig. 4 Normalized two-photon absorption strength of various materials in dependence on the pulse wavelength. Sa = standard grade sapphire, BBO = barium borate, YAG = yttrium aluminium garnet, FS = UV grade fused silica, KGW = potassium gadolinium tungstate, GGG = gadolinium gallium garnet, SLAO = strontium lanthanum aluminate

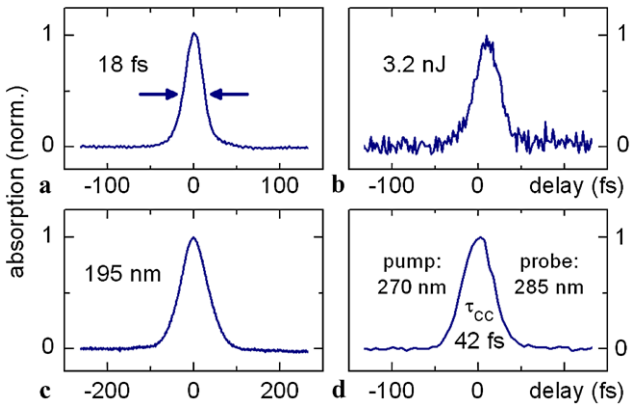

Fig. 5 Measured auto- and cross-correlation traces showing the applicability of our concept to (**a**) pulse durations below 20 fs ($\lambda_c = 300$ nm), (**b**) pulse energies down to 3.2 nJ ($\lambda_c = 277$ nm), (**c**) central wavelengths down to 195 nm, (**d**) cross correlation of pulses in the UV spectral region, where neither sum- nor difference-frequency mixing are possible

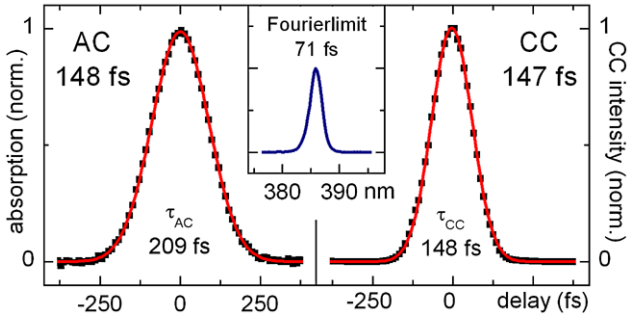

Fig. 6 Comparison of the autocorrelation (width τ_{AC}) of a frequency-doubled Ti:Sa laser ($\lambda_c = 386$ nm) measured in a KGW crystal with a thickness of 500 µm to the cross correlation (width τ_{CC}) with a 20-fs NOPA pulse

nal, but has the drawback of being strongly dispersive (see Fig. 3) even in the near-UV spectral domain [30].

Due to the dispersion problems encountered with KGW, we investigated even less well known crystals with respect to their applicability for TPA autocorrelation measurements. Salt crystals like NaCl, KCl and KBr look very promising according to an early report of the β value [31], but, at the longer-wavelength region of interest, we did not find similarly large values, and the damage threshold was only moderate. MgO showed a TPA signal twice as large as BBO at 310 nm with a very similar dispersion, but no signal at 360 nm. For $MgAl_2O_4$, no signal was found at 310 and 360 nm. BK7 and CaF_2 showed no significant signals at any tested wavelength.

Very useful materials in the near UV are gadolinium gallium garnet (GGG) and strontium lanthanum aluminate (SLAO). The dispersion of GGG [32] is much lower than that of KGW (see Fig. 3) and close to that of diamond. GGG of good crystal quality is easier to obtain than for diamond that is typically supplied as polycrystalline material. We particularly suggest thin samples of GGG for measurements in the spectroscopically important range around 350 nm.

With the proper choice of the TPA material, an adequate thickness and a moderate pulse intensity and by using the referencing technique, autocorrelation measurements can be performed for a large variety of experimental conditions.

To demonstrate the capability to measure pulses below 20 fs, we generated pulses with a central wavelength of 297 nm and a Fourier limit of 12 fs, which were compressed down to 18 fs by optimizing the prism compressor in the visible (Fig. 5a). The trace is almost of Gaussian shape, as expected from the nearly Gaussian like spectrum, with slight wings due to residual higher-order chirp. Due to the high sensitivity achieved through the pulse energy referencing (see beginning of Sect. 3), pulses with energies of only 3.2 nJ (sum of pump and probe) at kHz repetition rate and a duration of 24 fs at a central wavelength of 277 nm were successfully measured in a 135-µm-thick BBO crystal (Fig. 5b). Even pulses with central wavelengths as short as 195 nm can be characterized without difficulty (pulse length 55 fs, see Fig. 5c). We expect that UV grade sapphire with its optical band gap of 8.8 eV [33] allows for TPA autocorrelation measurements down to about 150 nm.

Our scheme also allows measuring the cross correlation of UV pulses with closely spaced central frequencies by two-color TPA, where neither SFG nor DFG are feasible. As an example, Fig. 5d shows a cross correlation of pulses with 270 nm and 285 nm in BBO with a width of 42 fs. To our knowledge, no crystal is currently available that allows phase matching to the sum or difference frequency of nominally 139 nm or 5130 nm. In addition, the TPA autocorrelator avoids any erroneous measurements of chirped pulses, such as can easily be made with phase-matched schemes [26].

Our concept also readily applies to measure pulses with durations in the range of hundreds of femtoseconds, where spectrometer-based pulse characterization methods, e.g. SPIDER and FROG, are troublesome due to the narrow spectra involved and the accompanying need of high-resolution spectrometers. The only limiting factor in our case is the travel range of the piezo. A measurement of the frequency-doubled output of our Ti:Sa amplifier system in a 500-µm-thick KGW crystal yields a pulse duration of 148 fs (Fig. 6). Calculations show that the pulse lengthening introduced by the KGW crystal amounts to only 1 fs in this case. For comparison, we measured the cross correlation with a 20-fs NOPA pulse at 540 nm by SFG. The derived pulse lengths agree within experimental accuracy and confirm the validity of the TPA depletion measurements.

4 Wavelength dependence of one- and two-photon absorption in BBO

The band gap of β-BBO has been reported as 6.4 eV [34], corresponding to a one-photon-absorption band edge at 193 nm. This suggests that autocorrelation measurements based on TPA should be feasible up to 386 nm. However, the observed depletion at wavelengths significantly below this value was found to be extremely small. To the best of our knowledge, for this wavelength region there is no coherent set of values for the TPA coefficient β of BBO reported in the literature. We therefore conducted z-scan measurements at different wavelengths to determine β_{BBO} between 250 nm and 340 nm.

Figure 7a depicts the schematic setup for measuring open-aperture z-scans. A detailed description of this technique can be found in [35]. The transmission through a BBO crystal (thickness 173 µm) was measured in dependence on its position along the focused beam (radius of curvature of focusing mirror 500 mm). For an accurate determination of the respective intensities incident on the crystal, the beam size was recorded with a beam profiler at every position. Additionally, we measured for every wavelength the pulse duration, pulse energy and crystal reflectivity. Again, referencing was used to enhance the signal to noise ratio.

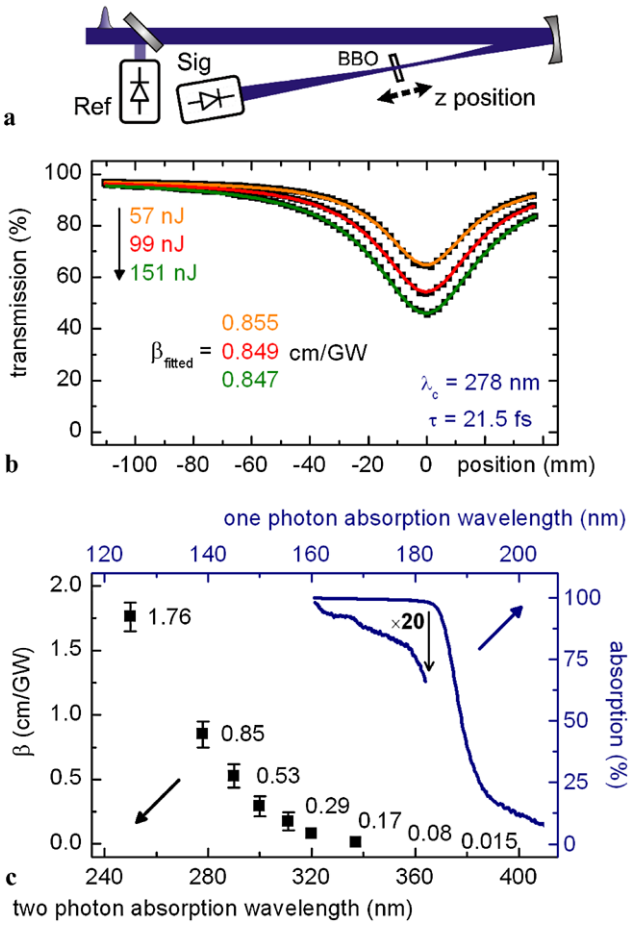

Fig. 7 (**a**) Layout of the setup for open aperture z-scan measurements. (**b**) Experimental data with different pulse energies but otherwise unchanged parameters (*black squares*) and the fits to the measured data with the TPA coefficient β being the only fit parameter (*colored lines*). (**c**) Obtained β coefficients for different central wavelengths (*black squares*) and measured one-photon absorption (*blue line*) of a 173-µm-thick BBO crystal

Exemplarily, we show measurements at a central wavelength of 278 nm for three different pulse energies in Fig. 7b together with their associated fits. The observed z dependence is modeled by (3) with $I_{\mathrm{pump}} = 0$ and integrating over the beam profile and t. For the different energies, and accordingly intensity regimes, we obtain an absolute value of the fitting parameter β of 0.85 cm/GW. Figure 7c summarizes our results for different wavelengths. For the investigated β-BBO crystal, the TPA coefficient decreases from 1.76 cm/GW at 250 nm to 0.015 cm/GW at 337 nm (black squares). This is in good agreement with earlier measurements at two wavelengths [36]. At longer wavelengths, the decrease in transmission was too weak to be detected. We note that for selected wavelengths we also conducted z-scan measurements of other BBO crystals. We found that the β-values can vary up to 20% from sample to sample, somewhat more than the variation of the $\chi^{(2)}$ value reported [37].

For comparison, we also measured the one-photon absorption of the crystal in a VUV spectrophotometer (blue line). Remarkably, there exists a wavelength region from about 170 nm to 185 nm where the crystal is nearly opaque due to one-photon absorption but the corresponding TPA is hardly measurable. It has been postulated that the direct band gap of BBO is significantly higher than the effective linear absorption cutoff at about 190 nm and possible reasons for the increasing absorption at wavelengths below 193 nm were discussed [36]. In view of our TPA coefficient measurements, one could reassign the direct band gap of BBO to 160 nm or 7.76 eV. Alternatively, symmetry considerations might render a differing absorption cutoff for one- and two-photon absorption. The first interpretation is not unlikely, as we see some finite transmission for the 173-µm BBO crystal between 160 nm and 185 nm in accordance with [34].

5 Guidelines for a reliable measurement

In summary, to achieve a quick and accurate pulse length measurement with TPA-induced depletion, we suggest the following procedure:

- Choose the correct two-photon-absorbing material according to the central wavelength of the pulse to be measured. We suggest sapphire for the wavelength range 150 nm to 270 nm, BBO for the range 200 nm to 330 nm and GGG for wavelengths longer than 320 nm (for details, see Fig. 4).

- Position the material in the focus of pump and probe beams, which can be easily achieved by minimizing the transmission of a single beam (preferably the pump beam) by moving the material along the beam propagation direction.
- Select the front reflection from the first beam splitter as probe beam.
- After overlapping pump and probe spatially at the focal point, e.g. by using a pinhole or a beam profiler, the temporal overlap is found by looking for a change in probe transmission when changing the delay between the beams. For this, the probe detector should be well centered and have a sensitive area that is larger than the beam.
- For finding the autocorrelation signal for the first time, reasonably high energies and thick crystals (up to ∼1 mm) are advantageous.
- To get an accurate measurement of the pulse length and to avoid pulse lengthening, the transmission change and the dispersion introduced by the crystal must be controlled.
- The transmission change induced on the probe by the pump pulse, which is determined by the pulse intensities, the TPA coefficient and the thickness of the crystal, should be smaller than 15%.
- The suitable thickness of the measurement crystal depends on the spectral width (Fourier limit) of the pulse and the chosen material due to chirp (for details, see Fig. 3).
- For these conditions, the pulse length can be calculated within an error of 5% from the measured autocorrelation width by deconvolution with a factor of $\sqrt{2}$ for a Gaussian pulse.
- A strong improvement of the signal to noise ratio is gained by referencing the autocorrelation signal to the beam energy fluctuations.

6 Outlook and perspectives

In conclusion, we have demonstrated that probe beam depletion caused by two-photon absorption from the simultaneous interaction with a stronger pump pulse is a well-suited method to determine the pulse length of UV femtosecond pulses. Measurements seem possible down to 150 nm and have explicitly been demonstrated for 3-nJ pulses at 1-kHz repetition rate—regimes that are at least difficult to access with other methods. In particular, the length of the second, third, fourth and fifth harmonics of the broadly used Ti:Sa systems can be readily measured. Any available thin plate with a band gap energy of $E_{\mathrm{gap}}/2 < h\nu_{\mathrm{laser}} < E_{\mathrm{gap}}$ and a sufficiently high TPA coefficient can be employed.

In contrast to sum- and difference-frequency mixing, which are restricted by the need for phase matching, TPA is not hampered by this constraint. In addition, the detector is simply positioned in the probe beam and no weak deflected or converted beam has to be found. We demonstrate measurements of pulses with a duration from sub-20 fs to hundreds of femtoseconds. In principle, the only limit for long pulse durations is the travel range of the piezo used, while the shortest pulse durations are only limited by the small material dispersion.

Our setup is simple and robust, and it renders pulse lengths at 2-Hz update rate for the 1-kHz laser system used. This corresponds to 400 data points per curve. For higher repetition rates of the laser, proportionally faster updates seem feasible with suitable electronics and scanning mechanics. The autocorrelator can easily be incorporated into existing experimental setups where the pulse length is an important parameter, e.g. in pump–probe setups [19]. As a matter of fact, the sensitive detection schemes developed for pump–probe schemes are the basis of the autocorrelator setup. Because there is no need for an additional auxiliary pulse, such as for example in cross-correlation measurements, our setup does not require finding time zero after an adjustment of the compressor. It therefore readily permits the online minimization of the pulse duration. The measured correlation width is a monotonic function of the true pulse length even for too high an intensity and therefore the pulse length minimization is a highly stable procedure. For too thick a TPA plate, the minimal pulse length obtainable by variation of the linear chirp, e.g. by variation of the insertion in a prism compressor, is still found. This minimal length is reached halfway through the TPA plate and from the known dispersion the necessary compression correction for the shortest pulse at the front end can be determined.

The characterization of the wavelength-dependent two-photon-absorption coefficient in BBO reveals a discrepancy between the one- and two-photon absorption edges. This discrepancy is quite advantageous for pumping of a BBO-based OPA in the UV. Is seems feasible down to a wavelength of approximately 330 nm. This agrees well with previous work, which showed that pumping at 266 nm yields only very low output energies, mainly due to TPA of the pump [38]. Pumping at 343 nm—the third harmonic of the increasingly available femtosecond systems based on Yb^+—provided high conversion efficiencies [39] and tunability throughout the visible [40].

Acknowledgements The authors thank Peter Lang and Alexandra Waritschlager for valuable experimental assistance, Johannes Piel for an early demonstration of the feasibility and Andreas Ulrich for the VUV measurement. The work was supported by the DFG Cluster of Excellence: Munich Centre for Advanced Photonics and the SFB 749. C.H. gratefully acknowledges the International Max Planck Research School on Advanced Photon Science.

References

1. M. Beutler, M. Ghotbi, F. Noack, D. Brida, C. Manzoni, G. Cerullo, Opt. Lett. **34**, 710 (2009)
2. I.Z. Kozma, P. Baum, S. Lochbrunner, E. Riedle, Opt. Express **11**, 3110 (2003)
3. P. Baum, S. Lochbrunner, E. Riedle, Appl. Phys. B **79**, 1027 (2004)
4. N. Krebs, R.A. Probst, E. Riedle, Opt. Express **18**, 6164 (2010)
5. C. Iaconis, I.A. Walmsley, Opt. Lett. **23**, 792 (1998)
6. P. Baum, S. Lochbrunner, E. Riedle, Opt. Lett. **29**, 210 (2004)
7. S. Linden, J. Kuhl, H. Giessen, Opt. Lett. **24**, 569 (1999)
8. J. Möhring, T. Buckup, M. Motzkus, Opt. Lett. **35**, 3916 (2010)
9. S. Backus, J. Peatross, Z. Zeek, A. Rundquist, G. Taft, M.M. Murnane, H.C. Kapteyn, Opt. Lett. **21**, 665 (1996)
10. D.J. Kane, A.J. Taylor, R. Trebino, K.W. DeLong, Opt. Lett. **19**, 1061 (1994)
11. Y. Takagi, Appl. Opt. **33**, 6328 (1994)
12. A.M. Streltsov, J.K. Ranka, A.L. Gaeta, Opt. Lett. **23**, 798 (1998)
13. N.F. Kleimeier, T. Haarlammert, H. Witte, U. Schühle, J.-F. Hochedez, A. BenMoussa, H. Zacharias, Opt. Express **18**, 6945 (2010)
14. M.H.R. Hutchinson, I.A. McIntyre, G.N. Gibson, C.K. Rhodes, Opt. Lett. **12**, 102 (1987)
15. S.A. Trushin, W. Fuss, K. Kosma, W.E. Schmid, Appl. Phys. B **85**, 1 (2006)
16. A. Reuther, A. Laubereau, D.N. Nikogosyan, Opt. Commun. **141**, 180 (1997)
17. A.E. Jailaubekov, S.E. Bradforth, Appl. Phys. Lett. **87**, 021107 (2005)
18. J.I. Dadap, G.B. Focht, D.H. Reitze, M.C. Downer, Opt. Lett. **16**, 499 (1991)
19. U. Megerle, I. Pugliesi, C. Schriever, C.F. Sailer, E. Riedle, Appl. Phys. B **96**, 215 (2009)
20. A.L. Dobryakov, S.A. Kovalenko, A. Weigel, J.L. Pérez-Lustres, J. Lange, A. Müller, N.P. Ernsting, Rev. Sci. Instrum. **81**, 113106 (2010)
21. C. Schriever, S. Lochbrunner, E. Riedle, D.J. Nesbitt, Rev. Sci. Instrum. **79**, 013107 (2008)
22. I.Z. Kozma, P. Baum, U. Schmidhammer, S. Lochbrunner, E. Riedle, Rev. Sci. Instrum. **75**, 2323 (2004)
23. Y. Tomita, M. Shibata, J. Bergquist, J. Appl. Phys. **72**, 1075 (1992)
24. K. Sala, G. Kenney-Wallace, G. Hall, IEEE J. Quantum Electron. **16**, 990 (1980)
25. Y. Tomita, M. Shibata, J. Bergquist, J. Appl. Phys. **72**, 2102 (1992)
26. S. Lochbrunner, P. Huppmann, E. Riedle, Opt. Commun. **184**, 321 (2000)
27. J.-C. Diels, W. Rudolph, *Ultrashort Laser Pulse Phenomena* (Academic Press, San Diego, 1996)
28. A. Dragomir, J.G. McInerney, D.N. Nikogosyan, P.G. Kazansky, Appl. Phys. Lett. **80**, 1114 (2002)
29. A.I. Vodchits, V.P. Kozich, V.A. Orlovich, P.A. Apanasevich, Opt. Commun. **263**, 304 (2006)
30. M.C. Pujol, M. Rico, C. Zaldo, R. Solé, V. Nikolov, X. Solans, M. Aguiló, F. Díaz, Appl. Phys. B **68**, 187 (1999)
31. R. Pizzoferrato, M. Casalboni, R. Francini, U.M. Grassano, F. Antonangeli, M. Piacentini, N. Zema, F. Bassani, Europhys. Lett. **2**, 571 (1986)
32. D.L. Wood, K. Nassau, Appl. Opt. **29**, 3704 (1990)
33. R.H. French, J. Am. Ceram. Soc. **73**, 477 (1990)
34. R.H. French, J.W. Ling, F.S. Ohuchi, C.T. Chen, Phys. Rev. B **44**, 8496 (1991)
35. M. Sheik-Bahae, A.A. Said, T.-H. Wei, D.J. Hagan, E.W. van Stryland, IEEE J. Quantum Electron. **26**, 760 (1990)
36. R. DeSalvo, A.A. Said, D.J. Hagan, E.W. van Stryland, M. Sheik-Bahae, IEEE J. Quantum Electron. **32**, 1324 (1996)
37. D.J. Armstrong, W.J. Alford, T.D. Raymond, A.V. Smith, Appl. Opt. **35**, 2032 (1996)
38. P. Tzankov, T. Fiebig, I. Buchvarov, Appl. Phys. Lett. **82**, 517 (2003)
39. D. Herrmann, C. Homann, R. Tautz, M. Scharrer, P.St.J. Russell, F. Krausz, L. Veisz, E. Riedle, Opt. Express **18**, 18752 (2010)
40. C. Homann, C. Schriever, P. Baum, E. Riedle, Opt. Express **16**, 5746 (2008)

Appendix B.4

Shaped sub-20 fs UV Pulses: Handling Spatio-Temporal Coupling

N. Krebs, R. A. Probst, and E. Riedle

Ultrafast Phenomena XVII, M. Chergui, D. Jonas, E. Riedle, R.W. Schoenlein, A. Taylor, eds. (Oxford University Press, Inc., New York 2011), 814 - 816.

Shaped sub-20 fs UV Pulses: Handling Spatio-Temporal Coupling

Nils Krebs, Rafael A. Probst, and Eberhard Riedle

LS für BioMolekulare Optik, LMU, Oettingenstr. 67, München, Germany
E-mail: nils.krebs@physik.uni-muenchen.de

1. Spatio-temporal coupling in a shaper: guiding the pulse to the focus. When shaping ultrashort UV and visible pulses it has become increasingly evident that in critical applications the coupling between the temporal structure of the pulse and its spatial profile has to be considered properly. Shaping in the visible and subsequent transformation into the UV by nonlinear frequency conversion was used to produce ultrashort shaped UV pulses [1] but the applications are restricted because the conversion process is seriously affected by the temporal pulse shape. Even when shaping directly in the UV, the spatio-temporal coupling is inherent in all common shaping devices and needs to be considered, especially for broadband sub-20 fs pulses that are needed for molecular coherent control. Therefore, when shaping UV pulses a practicable and reliable procedure to handle the shaper's spatio-temporal coupling is indispensable to produce clean output pulses.

Here we present a setup using a commercially available acousto-optic programmable dispersive filter (AOPDF) that is used to shape the second harmonic of a noncollinear optical parametric amplifier (NOPA) tunable between 240 - 400 nm [2]. The second harmonic is free of lateral chirp and quasi-collimated by a telescope before being actually shaped in the AOPDF. This is necessary because the AOPDF generates lateral displacement in the diffracted beam and one has to consider geometric as well as Gaussian optics explicitly when focusing the shaped pulse into the interaction region, typically the spectroscopic sample. Pulses with nearly Fourier limited durations down to 16.8 fs and energies around 50 nJ are shown. We generated and characterized clean arbitrary pulse shapes like square pulses and complex pulse sequences where the subpulses were manipulated individually in intensity, temporal delay, chirp, relative phase and central wavelength.

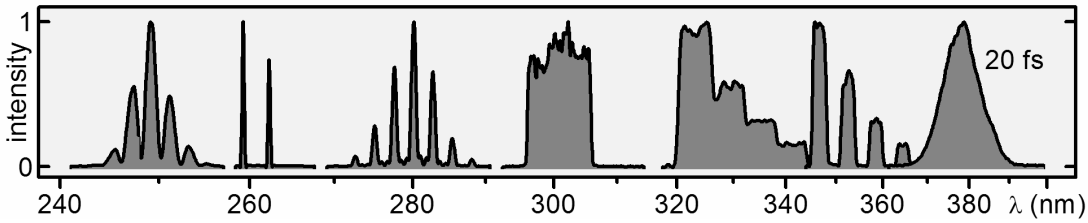

Fig. 1. Spectra of tunable amplitude modulated UV pulses suitable for sub-20 fs duration and with energies of about 50 nJ.

2. Readily wavelength tunable setup (240 – 400 nm) for shaped sub-20 fs UV pulses. The setup is composed of a Ti:Sa amplifier system at 1 kHz repetition rate (CPA 2001; Clark MXR) pumping a dispersion reduced broadband NOPA delivering visible pulses with typically 10 μJ and sub-20 fs

Fourier limits. The NOPA output is focussed into a 30 μm BBO crystal for type I second harmonic generation (SHG). The SHG potentially creates angular chirp in the plane of the crystal axis, as the efficiency for every wavelength is dependent on the incident angle. To compensate for this, the angle of the NOPA crystal was slightly detuned, while the homogeneity of the UV beam was monitored with a fiber coupled spectrometer. About half of the material dispersion of the AOPDF is precompensated by an UV prism compressor. The AOPDF is based on a 50 mm long KDP crystal and has a shaping window of 4 – 3 ps in the spectral range of 250 – 400 nm with a typical efficiency of 20 %. Figure 1 shows measured UV pulses that were amplitude shaped by the AOPDF. The bandwidth and Fourier limit of the generating input pulses ensure the capacity for sub-20 fs pulses with complex structures.

3. Gaussian vs. geometric optics: correct focusing of the ultrashort pulses. A broad spectrum and a flat spectral phase are indispensable prerequisites for a Fourier limited ultrashort pulse. Equally important is the fact that all spectral components spatially overlap in the interaction region. As the AOPDF creates delay dependent lateral displacement, a properly designed beam focusing geometry is needed.

In the AOPDF crystal the shaped light is diffracted under an angle to the incident optical beam by an acoustic wave propagating collinearly with the incident beam. The acoustic wave is elongated in the crystal and therefore different parts of the shaped beam are diffracted with a varying lateral displacement but parallel when exiting the AOPDF. A parallel shift up to 960 μm was observed, e.g., when two narrow band pulses are separated by the maximum shaping window delay. However, the two beams are still parallel and when they are imaged into the interaction region, e. g., by a focussing mirror, can be treated as geometric rays that cross at the classical focal distance f after the mirror. But it is crucial to keep in mind, that geometric optics is only an approximation for the propagation of light. Gaussian optics determines that the beam waist position after a focussing element depends on the beam parameters of the incident beam. The beam waist in the interaction region is located at the distance f, and therefore matches the geometric focus, only if the incident beam has an intermediate beam waist at the distance -f in front of the focusing element.

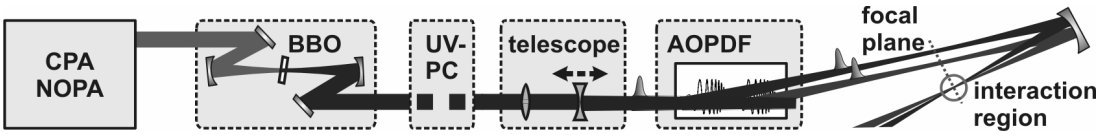

Fig. 2. Schematic of the setup. Gaussian beam propagation is illustrated by the width of the beam.

To match geometric and Gaussian focussing and thereby ensure the spatial overlap of the pulse components simultaneously with the highest intensity, the former condition has to be fulfilled. Experimentally this was done by adjusting the position of the intermediate beam waist, located well after the AOPDF with the telescope, while monitoring the interaction region with a beam camera (fig.

2). This enabled us to compress pulses to nearly their Fourier limit of below 20 fs, while in measurements without adjusted focussing geometry the pulses couldn't be compressed to less than 60 fs by optimizing the spectral phase.

4. Compression and shaping of structured sub-20 fs pulses. For the generation of arbitrarily shaped UV pulses one generally starts with a Fourier limited pulse with sufficient bandwidth and applies a well defined amplitude and phase mask. Therefore we use the AOPDF first to compress the pulse and then shape it. For pulse characterization we use either zero-additional-phase spectral phase interferometry for direct electric-field reconstruction (ZAP-SPIDER) or type-I difference frequency cross correlation with a 13.5 fs FWHM auxiliary pulse centered at 530 nm.

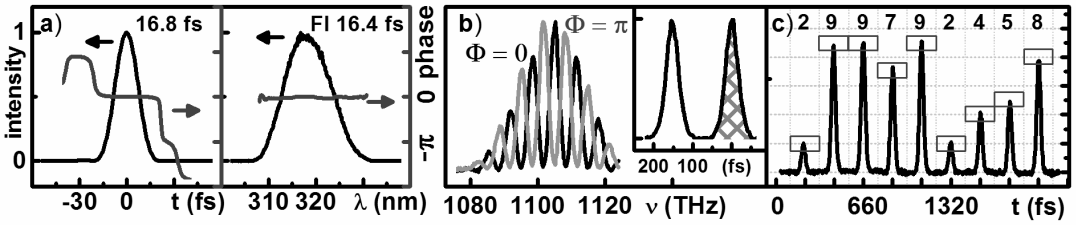

Fig. 3. (a) ZAP-SPIDER measurement of a pulse centered a 318 nm. The Gaussian type spectrum (right) and flat phase leads to a clean pulse in the time domain (left). (b) Short double pulses with defined interpulse phase Φ. (c) Cross correlation of a 9-fold pulse sequence where the SI value of the speed of light is encoded via the subpulse intensity.

To demonstrate the capability of the shaping device over its whole spectral range we first compressed pulses at two distinct wavelengths. We retrieved nearly Fourier limited pulses as short as 19.5 fs at 260 nm and 16.8 fs at 318 nm, the latter measurement is shown in figure 3a). Both in the spectral and the temporal domain the phase vanishes nearly perfectly. Full control over amplitude and phase is demonstrated by generating arbitrarily shapes, like double pulses with defined interpulse phase (fig. 3b) and complex pulse sequences. Satellite free pulse sequences with individually adjustable subpulse intensities are easily at hand once the phase mask for optimal compression is known. The intensity can be controlled to a precision of better than 4 bit (fig. 3c). We also performed experiments were the subpulse chirp and interpulse phase are controlled. Finally we used a broadband input spectrum to generate a double pulse with distinct frequency components, centered at 314 nm and 324 nm and subpulse lengths of 60 fs.

Having measured clean shaped UV pulses indicates that the observed spatio-temporal coupling of the AOPDF can be circumvented when the beam propagation is considered carefully. In the future the pulse duration could further be decreased as the maximum bandwidth of the AOPDF can provide for pulses down to 6 fs duration.

1 C. Schriever, S. Lochbrunner, M. Optiz and E. Riedle, "19 fs shaped ultraviolet pulses", Opt. Lett. **31**, 543-545 (2006).

2 N. Krebs, R. A. Probst and E. Riedle, "Sub-20 fs pulses shaped directly in the UV by an acousto-optic programmable dispersive filter", Opt. Express **18**, 6164-6171 (2010).

Appendix B.5

Sub-20 fs pulses shaped directly in the UV by an acousto-optic programmable dispersive filter

N. Krebs, R. A. Probst, and E. Riedle

Opt. Express 18, 6164–6171 (2010)

Sub-20 fs pulses shaped directly in the UV by an acousto-optic programmable dispersive filter

N. Krebs, R. A. Probst and E. Riedle*

Lehrstuhl für BioMolekulare Optik, Fakultät für Physik, Ludwig-Maximilians-Universität, Oettingenstrasse 67, 80538 München, Germany

**Eberhard.Riedle@physik.uni-muenchen.de*

Abstract: Direct pulse shaping in the UV was used to compress and structure pulses throughout the range of 250 – 400 nm. Broadband pulses generated by SHG of a NOPA were used as input to an acousto-optic programmable dispersive filter. As this shaper creates lateral dispersion, aspects of Gaussian and geometric optics had to be considered for the design of the beam path. Special care was taken to produce a homogeneous input beam. We show nearly Fourier-limited pulses as short as 16.8 fs at 320 nm and 19.5 fs at 260 nm. Full control over amplitude and phase is demonstrated by generating arbitrary shapes like square pulses and complex pulse sequences. The subpulses were manipulated individually in intensity, temporal delay, chirp, relative phase and central wavelength.

OCIS codes: (230.1040) Acousto-optical devices; (320.0320) Ultrafast optics; (320.5540) Pulse shaping.

References and links

1. P. Baum, S. Lochbrunner, and E. Riedle, "Tunable sub-10-fs ultraviolet pulses generated by achromatic frequency doubling," Opt. Lett. **29**(14), 1686–1688 (2004).
2. D. Herrmann, L. Veisz, R. Tautz, F. Tavella, K. Schmid, V. Pervak, and F. Krausz, "Generation of sub-three-cycle, 16 TW light pulses by using noncollinear optical parametric chirped-pulse amplification," Opt. Lett. **34**(16), 2459–2461 (2009).
3. T. Brixner, and G. Gerber, "Quantum control of gas-phase and liquid-phase femtochemistry," ChemPhysChem **4**(5), 418–438 (2003).
4. H. Rabitz, M. Motzkus, K. Kompa, and R. de Vivie-Riedle, "Whither the future of controlling quantum phenomena?" Science **288**(5467), 824–828 (2000).
5. S.-H. Shim, and M. T. Zanni, "How to turn your pump-probe instrument into a multidimensional spectrometer: 2D IR and Vis spectroscopies via pulse shaping," Phys. Chem. Chem. Phys. **11**(5), 748–761 (2009).
6. A. W. Weiner, "Femtosecond pulse shaping using spatial light modulators," Rev. Sci. Instrum. **71**(5), 1929–1960 (2000).
7. M. A. Dugan, J. X. Tull, and W. S. Warren, "High-resolution acousto-optic shaping of unamplified and amplified femtosecond laser pulses," J. Opt. Soc. Am. B **14**(9), 2348–2358 (1997).
8. A. Monmayrant, A. Arbouet, B. Girard, B. Chatel, A. Barman, B. J. Whitaker, and D. Kaplan, "AOPDF-shaped optical parametric amplifier output in the visible," Appl. Phys. B **81**(2-3), 177–180 (2005).
9. T. Tanigawa, Y. Sakakibara, S. Fang, T. Sekikawa, and M. Yamashita, "Spatial light modulator of 648 pixels with liquid crystal transparent from ultraviolet to near-infrared and its chirp compensation application," Opt. Lett. **34**(11), 1696–1698 (2009).
10. M. Roth, M. Mehendale, A. Bartelt, and H. Rabitz, "Acousto-optical shaping of ultraviolet femtosecond pulses," Appl. Phys. B **80**(4-5), 441–444 (2005).
11. D. S. N. Parker, A. D. G. Nunn, R. S. Minns, and H. H. Fielding, "Frequency doubling and Fourier domain shaping the output of a femtosecond optical parametric amplifier: easy access to tuneable femtosecond pulse shapes in the deep ultraviolet," Appl. Phys. B **94**(2), 181–186 (2009).
12. C. Schriever, S. Lochbrunner, M. Optiz, and E. Riedle, "19 fs shaped ultraviolet pulses," Opt. Lett. **31**(4), 543–545 (2006).
13. P. Nuernberger, G. Vogt, R. Selle, S. Fechner, T. Brixner, and G. Gerber, "Generation of shaped ultraviolet pulses at the third harmonic of titanium-sapphire femtosecond laser radiation," Appl. Phys. B **88**(4), 519–526 (2007).
14. A. Rondi, J. Extermann, L. Bonacina, S. M. Weber, and J.-P. Wolf, "Characterization of a MEMS-based pulse-shaping device in the deep ultraviolet," Appl. Phys. B **96**(4), 757–761 (2009).
15. M. Hacker, G. Stobrawa, R. Sauerbrey, T. Buckup, M. Motzkus, M. Wildenhain, and A. Gehner, "Micromirror SLM for femtosecond pulse shaping in the ultraviolet," Appl. Phys. B **76**, 711–714 (2003).

#122651 - $15.00 USD Received 12 Jan 2010; revised 5 Mar 2010; accepted 5 Mar 2010; published 11 Mar 2010

16. J. Möhring, T. Buckup, C. S. Lehmann, and M. Motzkus, "Generation of phase-controlled ultraviolet pulses and characterization by a simple autocorrelator setup," J. Opt. Soc. Am. B **26**(8), 1538–1544 (2009).
17. B. J. Pearson, and T. C. Weinacht, "Shaped ultrafast laser pulses in the deep ultraviolet," Opt. Express **15**(7), 4385–4388 (2007).
18. S. Coudreau, D. Kaplan, and P. Tournois, "Ultraviolet acousto-optic programmable dispersive filter laser pulse shaping in KDP," Opt. Lett. **31**(12), 1899–1901 (2006).
19. S. Weber, M. Barthélemy, and B. Chatel, "Direct shaping of tunable UV ultra-short pulses," Appl. Phys. B **98**(2-3), 323–326 (2010).
20. J. Hebling, "Derivation of the pulse front tilt caused by angular dispersion," Opt. Quantum Electron. **28**(12), 1759–1763 (1996).
21. V. Petrov, F. Noack, W. Rudolph, and C. Rempel, ""Intracavity Dispersion Compensation and Extracavity Pulse Compression Using Pairs of Prisms", Exp," Tech. Phys. **36**, 167–173 (1988).
22. P. Baum, S. Lochbrunner, and E. Riedle, "Zero-additional-phase SPIDER: full characterization of visible and sub-20-fs ultraviolet pulses," Opt. Lett. **29**(2), 210–212 (2004).
23. P. Baum, M. Breuer, E. Riedle, and G. Steinmeyer, "Brewster-angled chirped mirrors for broadband pulse compression without dispersion oscillations," Opt. Lett. **31**(14), 2220–2222 (2006).
24. I. Z. Kozma, P. Baum, U. Schmidhammer, S. Lochbrunner, and E. Riedle, "Compact autocorrelator for the online measurement of tunable 10 femtosecond pulses," Rev. Sci. Instrum. **75**(7), 2323–2327 (2004).
25. M. M. Wefers, and K. A. Nelson, "Space-Time Profiles of Shaped Ultrafast Optical Waveforms," IEEE J. Quantum Electron. **32**(1), 161–172 (1996).
26. M. V. Klein, and T. E. Furtak, *Optics*, (John Wiley & Sons, New York, 1986), Chap. 7, p. 477.
27. F. Frei, A. Galler, and T. Feurer, "Space-time coupling in femtosecond pulse shaping and its effects on coherent control," J. Chem. Phys. **130**(3), 034302 (2009).
28. D. C. Edelstein, E. S. Wachman, L. K. Cheng, W. R. Bosenberg, and C. L. Tang, "Femtosecond ultraviolet pulse generation in β-BaB_2O_4," Appl. Phys. Lett. **52**(26), 2211–2213 (1988).
29. J. C. Vaughan, T. Feurer, K. W. Stone, and K. A. Nelson, "Analysis of replica pulses in femtosecond pulse shaping with pixelated devices," Opt. Express **14**(3), 1314–1328 (2006).

1. Introduction

Advanced nonlinear optics allows the generation of extremely short light pulses tunable from the UV to the infrared. The pulse duration approaches the period of the carrier wave [1]. In this regime the control of the pulse spectrum and the spectral phase becomes increasingly important. The technical capability of deliberate pulse shaping opens new opportunities of optimal compression [2], coherent control [3,4] and two-dimensional spectroscopy [5].

Various methods for ultrafast pulse shaping have been demonstrated: 4-f shapers based on liquid crystal displays (LCD) [6] and on acousto-optic modulators (AOM) [7] as well as more direct acousto-optic programmable dispersive filters (AOPDF) [8]. Due to technical reasons these methods were largely limited to the visible and infrared spectral range. A vast class of molecules and attractive materials does, however, require UV light for electronic excitation or manipulation of reaction dynamics. Advanced devices promise to improve this situation [9,10], they await their combination with competitive tunable UV sources.

Direct frequency doubling of shaped sub-100 fs visible or NIR pulses allows only selected pulse shapes in the UV [11]. More flexibility is given by sum frequency mixing of shaped pulses with stretched fixed frequency auxiliary pulses and resulted in tunable 19 fs shaped UV pulses [12] and 150 fs at the third harmonic of a Ti:Sa laser [13]. However, coupling between the shaping and the efficiency is still encountered. With micromirrors (MEMS) direct shaping of UV pulses has been demonstrated, yet at very low duty cycle and efficiency. The reported results are so far limited to 78 fs at 404 nm [14], 104 fs at 266 nm [15] and 30 fs in a limited range around 324 nm [16]. Despite reasonable efficiency and a predicted operational range down to 180 nm, the use of a fused silica AOM in a 4-f setup has only been shown for 88 fs pulses at 400 nm [10] and 55 fs at 260 nm [17].

With the newly available AOPDF for UV operation, that is based on a KDP crystal [18], significant progress can be expected. The principal applicability of the new unit to UV pulses on the 50 to 100 fs range has already been demonstrated [19]. Compression close to the Fourier limit can, however, not be derived from the figures and information given in the report. In the present contribution we report on a detailed investigation of the use of this compact and easily adjustable device for the full range from 250 to 400 nm. The UV pulses are derived from the broadband visible pulses of a noncollinear optical parametric amplifier (NOPA). Compression to below 20 fs as well as complex pulse structures are obtained and the pulses

#122651 - $15.00 USD Received 12 Jan 2010; revised 5 Mar 2010; accepted 5 Mar 2010; published 11 Mar 2010

are fully characterized. Contrary to most previous shaping efforts the collimation and focusing of the beams into interaction region of the spectroscopic experiment was considered explicitly. This proved necessary since proper pulse compression was not possible with the initially chosen beam geometry. The correct combination of geometric and Gaussian optics proved to be crucial for the generation of clean pulses.

2. Experimental setup

The basis for the shaped UV pulses and their characterization (see Fig. 1) are two single-stage NOPAs pumped by a 1 kHz Ti:Sa amplifier system (CPA 2001; Clark MXR). The output of NOPA 1 is compressed by a prism compressor (PC) and then focused by mirror M1 into a 30 µm thick BBO crystal for type I second harmonic generation (SHG). The SHG potentially creates angular dispersion, because the maximum efficiency for every wavelength depends on the incident angle. Thus the recollimated UV beam would have a spatial chirp in the vertical direction. A further possible source of angular chirp is a nominally imperfect alignment of the NOPA. The angular dispersion is equivalent to a pulse front tilt [20]. We compensate the horizontal component by a slight rotation of the second prism in the PC [21] while monitoring the UV beam with a fiber coupled spectrometer. To precompensate the vertical chirp caused by the SHG, we slightly change the angle of the amplifier crystal in the NOPA from the nominally correct value for achromatic phase matching and utilize the slight divergence of the seed light.

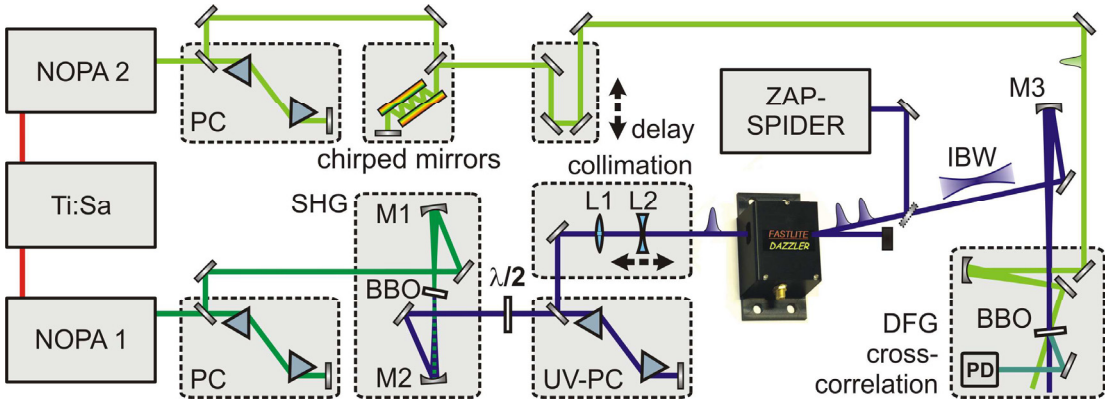

Fig. 1. Setup for the generation and characterization of shaped UV-pulses. PC: prism compressor; SHG (DFG): second harmonic (difference frequency) generation; λ/2: half-wave plate; M1 to M3: spherical focusing mirrors; L1 and L2: lenses; IBW: intermediate beam waist.

The UV polarization is rotated by an achromatic half-wave plate. Half of the material dispersion of the AOPDF is compensated by an UV-PC. This permits a higher temporal shaping window and a larger bandwidth of the AOPDF because the acoustic wave is less chirped and thus less elongated within the crystal length.

Mirror M2 cannot lead to a perfect collimation of the UV beam propagating toward the UV-PC and the AOPDF due to the inherent divergence of the Gaussian beam. The quasi-collimation can only be adjusted for a nearly parallel beam in some selected region and an intermediate beam waist (IBW in Figs. 1 and 3) downstream. To position the location of the IBW behind the AOPDF and to adjust the beam size inside the AOPDF suitably, we use a refractive telescope (L1 and L2) in front of the AOPDF.

The AOPDF (Dazzler™ model T-UV-250-400; Fastlite) [18] is based on a 50 mm long KDP crystal and offers a temporal shaping window of 4 - 3 ps in the spectral range of 250 - 400 nm. The previously reported 75 mm crystal renders a somewhat longer shaping window, yet at the cost of additional linear and higher order dispersion, independent of the pulse duration. The efficiency of the shaper is typically 20% at the 1 kHz repetition rate of the system. The shaped diffracted beam is geometrically separated from the direct beam.

#122651 - $15.00 USD Received 12 Jan 2010; revised 5 Mar 2010; accepted 5 Mar 2010; published 11 Mar 2010

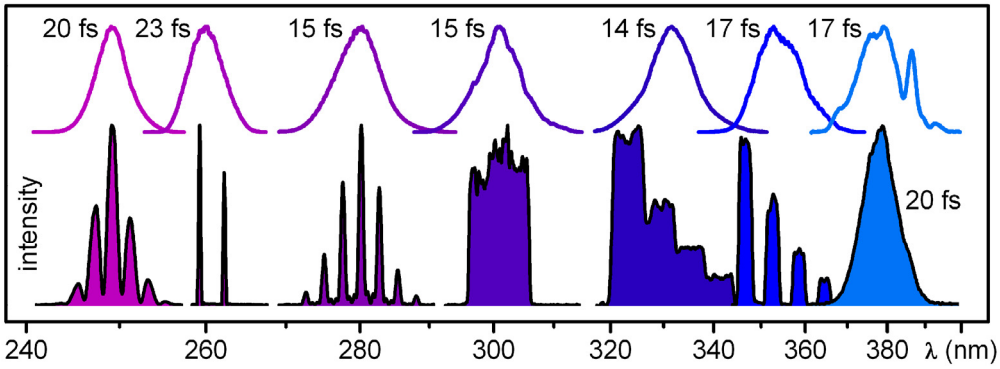

Fig. 2. Spectra of shaped frequency-doubled NOPA pulses tunable between 250 and 390 nm and their Fourier limit. Top: unmodulated; bottom: modulated by the AOPDF.

For pulse characterization we use either ZAP-SPIDER [22] or type I difference frequency cross correlation and XFROG. Visible auxiliary pulses for the cross correlation are provided by NOPA 2 tuned to 530 nm. The pulse is compressed by a combination of a PC and Brewster-angled chirped mirrors [23]. The Gaussian pulse duration was determined with an autocorrelator [24] to 13.5 fs FWHM. Cross correlation with the shaped UV pulses is done in 25 to 62 μm thick BBO crystals and measured with an integrating photodiode or - for the XFROG - a spectrometer.

The combination of NOPA and SHG allowed us to produce tunable UV pulses over a wide range in the UV. Modulated and unmodulated broadband output spectra of the AOPDF are shown in the Fig. 2. Fourier limits down to 14 fs were obtained, representative values are indicated at the top of Fig. 2. The minimal pulse length at short wavelength is limited mainly by the phase matching bandwidth of the BBO. For the longest wavelength the spectrum is structured due to the proximity to the Ti:Sa fundamental. Amplitude shaping can be used, e.g., to produce clean Gaussian pulse shapes (spectrum at 380 nm) or selective excitation of different electronic molecular absorption bands or vibrational modes (260 nm or 350 nm). The diffracted UV pulses have an energy of typically 10 - 50 nJ depending on the spectral shaping.

3. Focusing geometry alignment: Gaussian vs. geometric optics

A broad spectrum and a flat spectral phase are indispensable prerequisites for a Fourier-limited ultrashort pulse. Equally important is the fact that all spectral components spatially overlap, generally in the focus of a lens or mirror used to concentrate the pulse in the interaction region of the spectroscopic experiment. The AOPDF displaces parts of the pulse diffracted at different positions along the KDP crystal differently. Consequently a properly designed beam focusing geometry is needed that is described in the following.

The acousto-optical interaction rotates the polarization from the extraordinary to the ordinary axis. At the same time, it deflects the wave-vector and the Poynting vector of the light, yet not in the same manner, which is due to the crystal walk-off. The angle of the Poynting vector determines the beam path inside the acousto-optical crystal and therefore possible lateral spatial effects: The subpulses of a pulse sequence are diffracted at different positions and therefore are emitted from the AOPDF with a parallel shift of up to 960 μm [see Fig. 3(a) for a double pulse]. The angle between the diffracted and the directly transmitted beam after the AOPDF is, however, purely determined by the wave-vectors. For simplicity, the refraction of the beams at the crystal/air interface is ignored in Fig. 3(a). Not only well separated double pulses but also the components of a compact pulse are affected by this effect. In addition, the AOPDF is typically used to compensate its intrinsic material dispersion by a strongly negatively chirped acoustic signal. This means that different spectral components are scattered at different locations and a spatial chirp results even for an optimally compressed pulse. Interestingly this issue is not addressed in the dominant application of AOPDFs, the phase correction for shortest amplified light pulses [2].

#122651 - $15.00 USD Received 12 Jan 2010; revised 5 Mar 2010; accepted 5 Mar 2010; published 11 Mar 2010

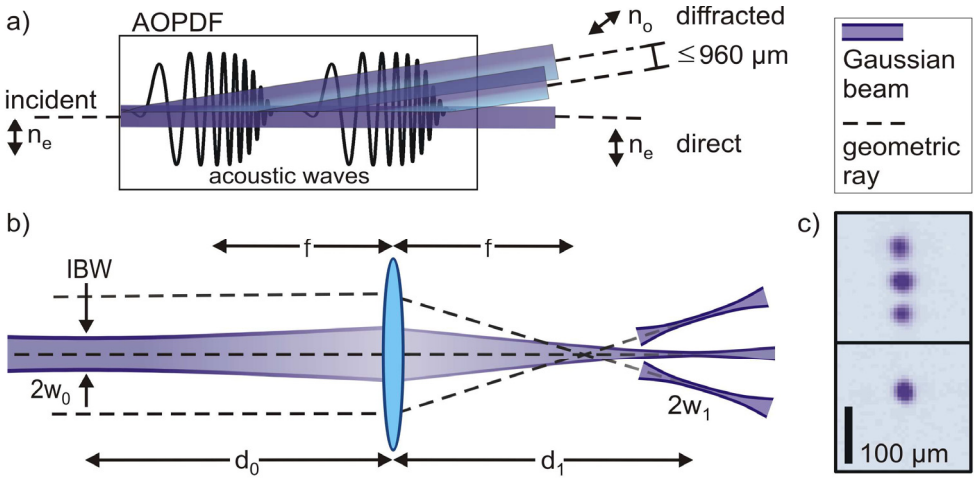

Fig. 3. Geometric and Gaussian optics relevant for the use of the AOPDF. (a) Spatial chirp and parallel displacement of diffracted subpulses, e.g., for a double pulse. (b) Focusing of three transversally shifted Gaussian beams without proper positioning of the intermediate beam waist (IBW). (c) Measured beam profile of a triple pulse in the Gaussian focus with improper (top) and adjusted (bottom) collimation.

It has been argued that an analogous complication is also encountered in LCD based 4-f shapers [25]. The optical layout described below might also be helpful in these setups. In principal, the parallel shift can be compensated by a double pass geometry, however, at the cost of a dramatically lowered overall efficiency. We therefore choose an alternative approach depicted in Fig. 3(b).

The transversally displaced components propagate in parallel after exiting the AOPDF. The are focused to the interaction region of the spectroscopic experiment or the pulse characterization (mirror M3 in Fig. 1 or lens in Fig. 3) and intersect in the geometric focus. The highest intensity is reached in the Gaussian focus of each subbeam or subpulse. The challenge is to overlap the two loci. In our initial setup the three subpulses generated by the AOPDF did indeed not overlap in the Gaussian focal plane as shown in the upper part of Fig. 3(c). By variation of the input signal to the AOPDF we confirmed that indeed each one of the spots corresponds to one of the delayed subpulses. This was also corroborated by cross correlation measurements. When a large size of the visible auxiliary beam was used, the full triple-pulse was found. Only a single sub-pulse was observed, however, when the beam size was adjusted to the one of the individual UV subbeam.

The propagation of a Gaussian beam through a focusing lens can be calculated analytically in the paraxial approximation. We consider a beam with an intermediate beam waist (IBW) w_0 at the distance d_0 in front of the lens and an incident Rayleigh length $z_0 = \pi \cdot w_0^2 / \lambda$. The distance d_1 of the Gaussian focus after the lens with focal length f is given by Eq. (1) [26].

$$d_1 = f + \frac{f^2 (d_0 - f)}{(d_0 - f)^2 + z_0^2}. \qquad (1)$$

This formula implies that the position of the Gaussian focus depends not only on the distance of the IBW from the lens, but also on the waist size. For geometric optics z_0 is zero and Eq. (1) reduces to the well known lens formula. If the distance d_0 can be chosen to be identical to f, d_1 becomes identical to f and the Gaussian focus will coincide with the intersection of the parallel rays, i.e. the geometrical focus.

We chose a position of the focusing mirror at roughly its focal length behind the IBW and fine tuned the collimation telescope (see Fig. 1) to set $d_0 = f$. To optimize the alignment, a beam camera is placed into the geometric focus. This location is determined by the position where pulses with different delay generated by the AOPDF overlap. Subsequently, the Gaus-

#122651 - $15.00 USD Received 12 Jan 2010; revised 5 Mar 2010; accepted 5 Mar 2010; published 11 Mar 2010

sian focus is positioned in the same plane by moving one of the lenses in the telescope. The perfect overlap shown in the lower part of Fig. 3(c) results. Finally, the lack of any remaining spatial chirp is confirmed by the use of the AOPDF as a tunable narrow spectral filter. This means that there is no more spatio-spectral coupling. Together with the demonstrated temporal compression very close to the Fourier limit (see Sec. 4), we can conclude that there is no more relevant spatio-temporal coupling.

We note that it has been suggested to place the focusing lens after a 4-f shaper one focal length after the shaper's last grating [27], in close analogy to our situation. To avoid the reflection losses and the chirp introduced by the telescope, in principle the recollimation mirror after the SHG could be used to adjust the focal position. Unfortunately, the given beam size and the length of the UV compressor make this impractical.

4. Sub-20 fs tunable UV pulses and arbitrary spectral and temporal shapes

The generation of arbitrarily shaped UV pulses requires Fourier limited input pulses and the application of well known amplitude and phase filters [6,13]. In our setup the input pulses generated by SHG of the NOPA are not Fourier limited and we therefore use the AOPDF both to compress and shape them. For this purpose the alignment considerations detailed in Sec. 3 are applied. Before we demonstrate the extensive shaping capabilities, we first describe the optimal compression of the tunable UV pulses.

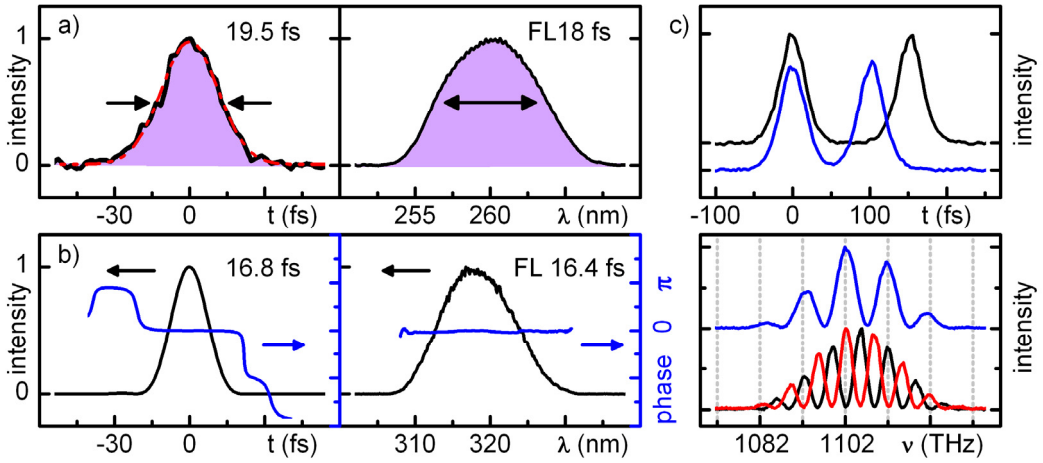

Fig. 4. (a) Cross correlation and spectrum of a pulse at 260 nm compressed to 19.5 fs FWHM. (b) ZAP-SPIDER measurement of a 16.8 fs pulse at 319 nm. (c) Cross correlations and spectra of double pulses at 260 nm with 100 fs (blue) and 150 fs (black) interpulse delay. The subpulses of the latter are in-phase (black spectrum), and opposite in phase (red spectrum).

Figure 4(a) shows the spectrum of a pulse centered at 260 nm together with the measured cross correlation (CC) curve. No amplitude shaping was used and progressive orders of the phase filter applied by the AOPDF were optimized for the shortest possible CC time. From the Gaussian shape of the spectrum we conclude that the temporal shape is also Gaussian. With the measured FWHM of the CC we can use a straight forward deconvolution procedure [28] utilizing the pulse length of the visible auxiliary pulse to determine the actual length of the UV pulse of 19.5 fs. This is within 10% of the Fourier limit despite the very short wavelength. Even for such a short pulse the pulse lengthening in the CC crystal by the group velocity dispersion can be neglected and only the group velocity mismatch between UV and visible pulse and the timing jitter of 1.3 fs added by the AOPDF electronics have to be considered.

Pulses at 320 nm could readily be compressed to 16.8 fs as measured by ZAP-SPIDER [22]. The identical value was found by the CC measurement and the comparison confirms the validity of our deconvolution procedure. Both in the spectral and the temporal domain the phase vanishes nearly perfectly [see Fig. 4(b)].

The optimal compression at a selected wavelength renders the necessary phase filter to compensate all unbalanced dispersion encountered by the UV pulses. This filter is applied as

#122651 - $15.00 USD Received 12 Jan 2010; revised 5 Mar 2010; accepted 5 Mar 2010; published 11 Mar 2010

an acoustic pulse with the appropriate fine structure and synchronization to the AOPDF. A straight forward addition of a filter function renders any desired pulse shape. This is demonstrated in Fig. 4(c) for satellite free double pulses at 260 nm. In this case the above mentioned acoustic pulse is applied twice with the acoustic delay corresponding to the optical delay of 100 or 150 fs. For the double pulses separated by 100 fs (shown in blue) the resulting spectrum is modulated with a 10 THz spacing. The pulse spacing of 150 fs decreases the spectral period (see lower part of Fig. 4(c). The relative phase of the two subpulses with respect to the carrier wave determines the position of the fringes: for in-phase pulses there is a maximum at the center of the spectrum (black curve) while for pulses with opposite phase two equal height maxima are found symmetrically displaced (red curve).

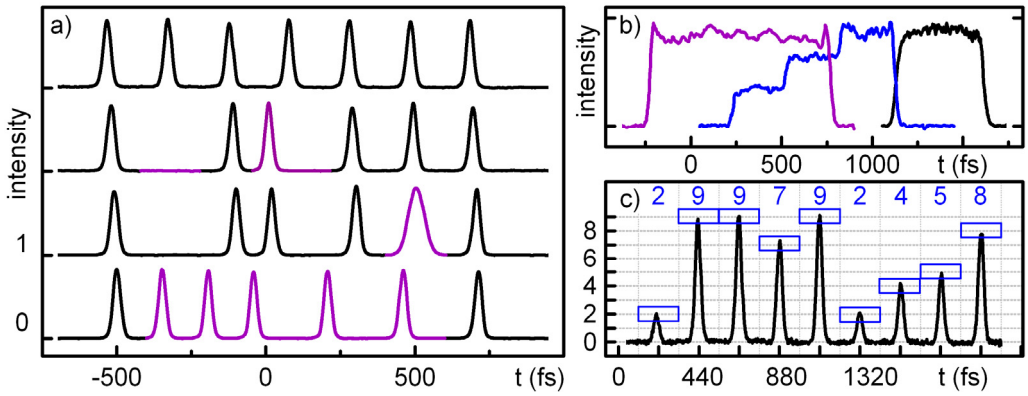

Fig. 5. Cross correlation of structured pulses at 319 nm (a) and 260 nm (b, c). (a) Pulse trains of 21 fs pulses subsequently manipulated. (b) 1 ps square pulse (violet), stairs with 300 fs broad equal amplitude steps (blue), 500 fs square pulse (black). (c) Value of the speed of light encoded on a pulse train via the subpulse intensity.

Multiple subpulses at 319 nm, with an individual length of 21 fs and without additional satellites outside the displayed window are shown in Fig. 5(a). Out of the 7 pulses individual ones can be left out, shifted and broadened (by chirp) at will. In Fig. 5(b) we show pulses at 260 nm with a distinct flat top temporal profile and a staircase one. These pulses are chirped to utilize the energy contained in the broad spectrum of the input pulses.

It should be noted that not only the subpulse spacing but also the energy of all the subpulses can be precisely controlled. For equally intense subpulses the acoustic power has to be properly limited to avoid nonlinear amplitude filtering. The high degree of amplitude control is elaborated in Fig. 5(c) where the SI value of the speed of light is encoded to 9 digits with about 4 bit vertical precision. For this equally spaced pulse sequence the energy contained in each subpulse was adjusted with a single iteration.

So far we have shown pulse sequences with identical spectral content for all subpulses. For coherent control experiments shaped pulses are needed with differing spectra of the subpulses. This can be readily achieved with our setup. Figure 6(a) shows a pair of 58 fs pulses generated from a common input pulse (black spectrum on the right). The XFROG measurement agrees very well with the CC trace [Fig. 6(b)] and the individual spectra of the subpulses. To decrease the spectral smearing in the XFROG, the probe pulse was spectrally narrowed.

#122651 - $15.00 USD Received 12 Jan 2010; revised 5 Mar 2010; accepted 5 Mar 2010; published 11 Mar 2010

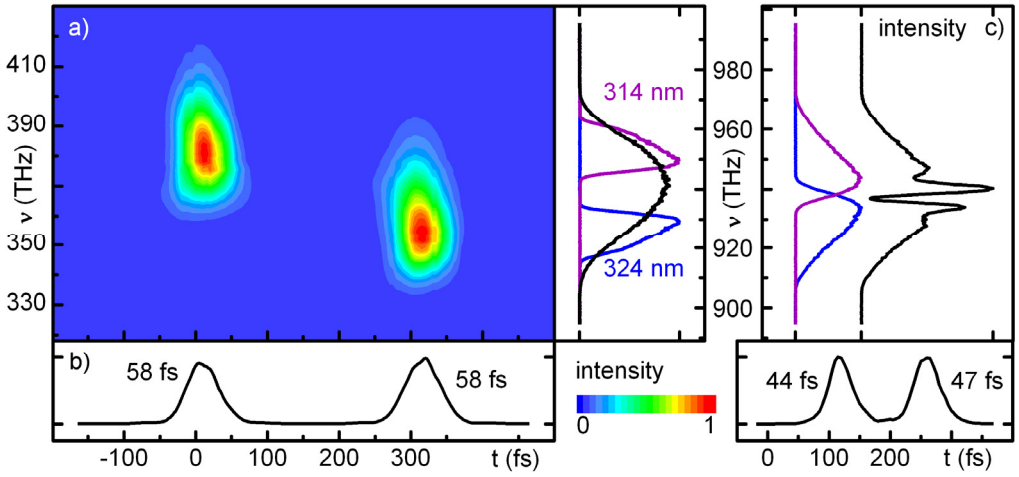

Fig. 6. Cross correlation of double pulses with differing wavelength. (a) XFROG (left) of pulses with disjunct spectra (right) and input spectrum (black). (b) Corresponding cross correlation and pulse durations. (c) Cross correlation (bottom) and spectra (top) of subpulses with 12 nm bandwidth; colored: individual spectra; black: double-pulse spectrum.

For subpulses with overlapping spectra [see Fig. 6(c)] the joint spectrum is modulated in the center according to the temporal separation of the sub-50 fs pulses. The phase of the fringes can be adjusted by the relative phase of the two pulses.

5. Conclusions and perspectives

In this work we have demonstrated that the combination of a broadband NOPA with SHG in a thin BBO crystal and direct pulse shaping in a commercially available AOPDF allow the generation of fully tunable UV pulses with a duration below 20 fs or an arbitrary temporal shape. A further shortening of the pulses could be reached with achromatic phase matching [1]. Since the UV Dazzler^{TM} is specified for an instantaneous bandwidth of 15% of the optical carrier frequency, we can expect pulses or pulse structures as short as 6 fs. This is well in the regime of vibrational time scales needed for the most demanding coherent control schemes [3,4].

Increased output pulse energy could be achieved by sum frequency mixing of the NOPA pulses with a sizable fraction of the pump pulses. This would come at the cost of reduced tuning at short wavelengths. Alternatively a two-stage NOPA should provide higher output, but at present it is quite challenging to operate it with a clean enough spatial mode.

The crucial issue that was solved in this work was the proper combination of geometric and Gaussian optics. As with any cutting-edge ultrafast setup, the desired ultrafast pulses are only assured at one position along the beam propagation. This is not only necessary and ensured with respect to the spectral components but also in the spatial domain. In the described setup this position is presently at the focus of the cross correlation or the ZAP-SPIDER. The envisioned spectroscopic investigations will be performed in this spot.

The direct shaping in the AOPDF delivers fully controlled UV pulses with unprecedented shortness and full tunability. The operational principle of the AOPDF intrinsically avoids the generation of replica pulses encountered in pixelated devices like LCDs in a 4-f shaper [29]. This will be of great advantage for 2D UV spectroscopy that now can be implemented readily with the phase locked double pulses [5]. The presently limited update rate of the AOPDF is only due to the technical implementation but can easily be upgraded to the kHz repetition rate of the laser system. A 100% duty cycle will then be available for the most demanding experiments.

Acknowledgments

The authors thank Peter Baum, Trung Thuan Doan and Fastlite for technical assistance and Pascal Tournois for fruitful discussions. The work was supported by the DFG-Cluster of Excellence: Munich-Centre for Advanced Photonics and by the Austrian Science Fund within the Special Research Program F16 (Advanced Light Sources).

#122651 - $15.00 USD Received 12 Jan 2010; revised 5 Mar 2010; accepted 5 Mar 2010; published 11 Mar 2010

Danksagung

Ich möchte mich an dieser Stelle bei allen Personen herzlich bedanken die mich im Laufe meiner Promotion mit Rat und Tat unterstützt haben.

Mein besonderer Dank gilt meinem Doktorvater **Herr Prof. Dr. Eberhard Riedle**, der mir ermöglicht hat an den vielen spannenden wissenschaftlichen Fragestellungen und deren Lösungen zu arbeiten. Seine herausragende wissenschaftliche Betreuung kam mir durchgehend zu Gute und so manche wissenschaftliche Stolperfalle blieb mir damit erspart. Sein enormes persönliches Engagement und seine große Begeisterung für die verschiedenen Projekte haben mich immer wieder aufs Neue motiviert und angespornt zu mehr Leistung und Durchhaltevermögen. Die vielen fruchtbaren Diskussionen über meine Resultate haben mir ein tieferes Verständnis und neue Einsichten ermöglicht, auch zu Themen außerhalb des universitären Lebens.

Des weiteren Danke ich **Prof. Dr. Wolfgang Zinth**, der im Rahmen des institutsinternen Seminars die Fortschritte meiner Arbeit stets mit Interesse verfolgt hat und mir gerne hilfreiche Kommentare gegeben hat.

Auch die Kollegen und Kooperationspartner seien hier noch mal ausdrücklich erwähnt, ohne die die interessanten Resultate nicht möglich gewesen wären:

Herrn **Prof. Dr. Wolfgang Domcke** und **Dr. Maxim Gelin** danke ich für die Rechnungen zu den Doppelimpulsmessungen und ganz besonders für die Bereitschaft mir in Besprechungen die theoretische Seite der Spektroskopie zu vermitteln.

Für die theoretischen Berechnungen zu den Benzhydrylchlorid-Messungen möchte ich Frau **Prof. Dr. Regina de Vivie-Riedle** und den **Mitarbeitern** ihrer Gruppe danken.

Meinen großen Dank möchte ich **Dr. Igor Pugliesi** aussprechen, der nicht nur wissenschaftlich einen wichtigen Teil zu meiner Entwicklung beigetragen hat sondern auch als Büro-Nachbar im Büro viel von meiner Unruhe abgefedert hat, wenn es mal in den Projekten nicht so lief wie gewollt. Aber dafür konnte er mich dann beim gemeinsamen Aikido schwungvoll auf die Matte befördern.

Dr. Jürgen Hauer und **Dr. Peter Baum** danke ich für die initiale Einarbeitung in die experimentelle Arbeit im Labor und die vielen Diskussionen und Beiträge zu den technischen und spektroskopischen Fragestellungen und Lösungen speziell zu den Doppelimpulsmessungen und den Grundlagen der 2-dimensionalen Spektroskopie.

Christian Homann danke ich für die schöne und stets fruchtbare Zusammenarbeit, z.B. an der Entwicklung des Autokorrelators, und die vielen kleinen schnell beantworteten physikalischen Fragen. „Und danke das du meine Begeisterung am Klettersport geweckt hast."

Spezieller Danke geht auch an **Christian Sailer**, dessen tiefes molekülphysikalisches Verständnis mir die klare Interpretation der Messungen am Benzhydrylchlorid näher gebracht hat.

Ich danke **Rafael Probst**, der im Rahmen seiner Diplomarbeit mit viel Einsatzbereitschaft entscheidend an den Erfolgen im Bereich der Impulsformung beigetragen hat.

Maximilan Bradler danke ich für die Messdaten der Malachitgrün-Messung und für die stets gute Laune, die immer wieder alle Mitarbeiter angesteckt hat.

Für die tatkräftige Unterstützung im Labor und die daraus gewonnen Ergebnisse danke ich „meinen" Bachelor-Studenten: **Trung Thuan Doan**, **Niko Heinrichs**, **Rudolf Reiel** und **Lothar Maisenbacher**.

An dieser Stelle möchte ich noch weitere Kollegen explizit nennen, die mich bei Themen zur experimentellen Technik und Molekülphysik sowie auch aus dem privaten Bereich mit viel Elan beraten haben. Mein Dank gilt unter anderem **Dr. Christian Schriever**, **Dr. Uwe Megerle**, **Elias Eckert**, **Franziska Graupner** und **Matthias Himmelstoß**.

Ich danke **Rudi Schwarz**, **Alfons Stork** und **Christian Hausmann** von der Werkstatt für ihr hochpräzisen und schnell bereitgestellten Bauteile jeglicher Form und Komplexität. Des weiteren möchte ich mich bei **Harald Hoppe** für die mir angepassten Optiken bedanken.

Ich danke auch den Mitarbeitern der Firma Horiba Jobin Yvon, vor allem **Gerald Jung** und **Dr. Hans-Erik Swoboda** für die technische Betreuung des Herzstücks all meiner Arbeit, den CPA-Laser und für die Möglichkeit im Namen der Firma optische Komponenten für andere Arbeitsgruppen bauen zu können.

Zu guter Letzt möchte ich mich herzlich bei meiner **Familie** und **Freunden** für die grenzenlose Unterstützung im nicht-wissenschaftlichen Teil meines Lebens bedanken. Hervorheben möchte ich dabei noch **Gabi Moll**, die mich zeitweise begleitet hatte.

Glossary

List of abbreviations

2D	2-dimensional
2P1P	strong-pulse double-pump single-probe
4WM	4-wave-mixing
5,6DPBC	2,2-diphenyl-5,6-benzo(2H)chromene molecule
5,6DPMC	5,6-benzo(2H)chromene molecule
AC	autocorrelator
AOPDF	acousto-optical dispersive filter (pulse shaper)
BBO	Beta barium borate (crystal)
CC	cross-correlation
CCD	charge-coupled device
DNA	desoxy-ribonucleic acid
DPMC	benzhydryl chloride molecule
ESA	Excited-state absorption
FC	Franck-Condon
FROG	Frequency resolved optical grating
FWHM	Full-width half-maximum
GGG	gadolinium gallium garnet (crystal)
GSB	Ground-state bleach
HBT	2-(2'-hydroxyphenyl)benzothiazole molecule
IBW	intermediate beam waist (Gaussian optics)
IR	infrared
KDP	potassium dihydrogen phosphate
LCD	Liquid crystal display
NOPA	noncollinear optical parametric amplifier
PO	Perylene orange molecule
QCS	Quantum control spectroscopy
RMS	root-mean-square value
SD	self-diffraction
SE	Stimulated emission
SHG	Second harmonic generation
SPM	self-phase modulation
UV	ultraviolet
VIS	visible
ZAP-SPIDER	zero-additional phase spectral phase interferometry for direct electric field reconstruction

Most frequently used parameters

$S_{2D}^{P^{(3)}}$	pure 2D signal ($\propto P^{(3)}$)
$S_{2D}^{\Delta OD}$	pure 2D signal ($\propto \Delta OD$)
$2D_{OD}$	processed data of a 2D measurement ($\propto \Delta OD$)
$2D_{raw}$	raw data of a 2D measurement
c_{educt}	concentration of absorbing molecules
d	thickness
D_{pu} (D_{pr})	diameter of pump (probe) beam in the sample
E	electric field
$E^{(3)}_S$	emitted third-order electric signal field
f	focal length
I(t)	temporal pulse intensity
I*	probe intensity after sample with pump ≡ Sig*
I_0	probe intensity after sample without pump ≡ Sig_0
k	wavevector
n	refractive index
n_0	linear refractive index
n_2	nonlinear refractive index
N_{hv}	number of photons
N_{hv}^{total}	total number of photons in a pulse
n_{ph}	photon density
OD	optical density value
$P^{(3)}$	third-order polarization
PE	pulse energy
P_{exc}	excitation probability
q	imaginary Gaussian beam parameter
Q	(product) quantum yield
R	Gaussian beam curvature
$R^{(3)}$	third-order molecular response
RMS	root mean square value

Sig	probe intensity at the signal spectrometer
Sig^{pump} (Ref^{pump})	probe int. at signal (reference) spectrometer with double pump
Sig^{nopump} (Ref^{nopump})	probe int. at signal (reference) spectrometer without dou. pump
Sig* (Ref*)	probe int. at signal (reference) spectrometer with pump
Sig_0 (Ref_0)	probe int. at signal (reference) spectrometer without pump
Sig_{TA}	transient absorption contribution detected at probe spectrometer
Sig_{2D}	2D contribution detected at probe spectrometer
Sig^0 (Ref^0)	probe int. at the signal (reference) spectrometer with $\Delta\Phi = 0$
Sig^π (Ref^π)	probe int. at the signal (reference) spectrometer with $\Delta\Phi = \pi$
T	population time (pump-probe delay)
x	(propagation) distance
z_0	Rayleigh length
ΔOD, ΔOD_{pp}	change in optical density for pump-probe
ΔOD_{2D}	projected ΔOD in 2D (intergrated pump axis)
Δt	interpulse delay
Δt_v	additional pump-probe delay of individual probe freq.
$\Delta\Phi$	interpulse phase
$\Delta\Phi_{AOPDF}$	interpulse phase set in the pulse shaper software
$\delta\omega(t)$	nonlinear frequency shift
ε	molar extinction coefficient
γ	Pearson-coefficient
λ	wavelvength
ν	optical frequency
σ	absorption cross-section
τ	coherence time
τ_p	ultrashort pulse length (FWHM)
ω	optical angular frequency
ω_{AOPDF}	central frequency set in the pulse shaper software
ω_t	Fourier transformed frequency (related to Δt axis)